Alloy and microstructure design for additive manufacturing

Hossein Eskandari Sabzi

Engineering Department

Lancaster University

A thesis submitted for the degree of *Doctor of Philosophy*

May 26, 2022

Declaration

I declare that the work presented in this thesis is, to the best of my knowledge and belief, original and my own work. The material has not been submitted, either in whole or in part, for a degree at this, or any other university. This thesis does not exceed the maximum permitted word length of 80,000 words including appendices and footnotes, but excluding the bibliography.

Hossein Eskandari Sabzi

Abstract

There is a need for theoretical and numerical approaches to describe microstructure-property relationships in metal additive manufacturing (AM). Such relationships are particularly unclear as a function of alloy composition. In this work, a variety of computational models have been developed to optimise the chemical composition, process parameters and mechanical properties of alloys for laser powder bed fusion (LPBF). A computational framework combining genetic algorithms and the calculation of phase diagrams (CALPHAD) methodology is developed to design new alloys with minimum susceptibility to solidification cracking. A methodology to control process parameters to prevent porosity and defect formation during LPBF is also presented. The models are validated using 316L stainless steel (SS), one of the most accepted grades by industry. Metallurgical models are presented to describe the yield strengthening mechanisms during LPBF processing of IN718, Ti-6Al-4V, and 316L SS. It has been shown that dislocation multiplication/annihilation processes such as dynamic recovery and recrystallization are paramount in controlling yield strength of LPBFed alloys. The numerical models have been complemented by detailed advanced microstructural characterisation methods such as electron backscattered diffraction (EBSD), and transmission electron microscopy (TEM). A classical Zener-Hollomon and a modified thermostatistical approach are used to interpret microstructural evolution phenomena during LPBF of 316L SS under various building conditions, improving the understanding of yield strength control in such LPBFed alloys. Furthermore, the important role of low-angle grain boundaries (LAGBs) in strengthening of

LPBFed 316L SS has been revealed quantitatively. A unified Hall-Petch relationship is proposed, for the first time, to relate the yield strength of LPBFed 316L SS to the subgrain size (the size of the grains with LAGBs). An alloy and process design framework is presented to maximise yield strength of austenitic SSs through grain boundary engineering. The contribution of various deformation mechanisms such as dislocation hardening, twinning-induced plasticity, dynamic recrystallization, as well as dislocation types in the strain hardening behaviour of LPBFed 316L SS is modelled.

List of publications

Journals publications:

1. H. Eskandari Sabzi, X. Li, Ch. Zhang, H. Fu, and P. E.J. Rivera-Díaz-del-Castillo. On the strain hardening of a twinning-induced plasticity stainless steel produced by laser powder bed fusion: Importance of dislocation impingement. *Under Review*.

2. H. Eskandari Sabzi, X. Li, Ch. Zhang, H. Fu, D. San-Martín, and P. E.J. Rivera-Díaz-del-Castillo. Deformation twinning-induced dynamic recrystallization during laser powder bed fusion. *Scripta Materialia* 207 (2022) 114307.

3. J. Zhao, Q. Yang, H. Eskandari Sabzi, W. Wen, and P. E.J. Rivera-Díaz-del-Castillo. Modelling stress relaxation after hot deformation: microstructure-property relationships. *International Journal of plasticity* 151 (2022) 103219.

4. H. Eskandari Sabzi, E. Hernandez-Nava, X. H. Li, H. Fu, D. San-Martín, and P. E. J. Rivera-Díaz-del-Castillo. Strengthening control in laser powder bed fusion of austenitic stainless steels via grain boundary engineering. *Materials and Design* 212 (2021) 110246.

5. H. Eskandari Sabzi, N. T. Aboulkhair, X. Liang, X. Li, M. Simonelli, H. Fu, and P. E. J. Rivera-Díaz-del-Castillo. Grain refinement in laser powder bed fusion: The influence of dynamic recrystallization and recovery. *Materials and Design* 196 (2020) 109181.

6. H. Eskandari Sabzi, and P. E. J. Rivera-Díaz-del-Castillo. Composition and process parameter dependence of yield strength in laser powder bed fusion alloys. *Materials and Design* 195 (2020) 109024.

7. H. Eskandari Sabzi, S. Maeng, X. Liang, M. Simonelli, N. T. Aboulkhair, and

P. E. J. Rivera-Díaz-del-Castillo. Controlling crack formation and porosity in laser powder bed fusion: alloy design and process optimisation. *Additive Manufacturing* (2020) 101360.

8. H. Eskandari Sabzi and P. E. J. Rivera-Díaz-del-Castillo. Defect prevention in selective laser melting components: compositional and process effects. *Materials* 12 (2019) 3791.

9. H. Eskandari Sabzi. Powder bed fusion additive layer manufacturing of titanium alloys. *Materials Science and Technology* 35 (2019) 875-890.

Book chapters:

10. H. Eskandari Sabzi and P. E. J. Rivera-Díaz-del-Castillo. Modelling solidification from ingots to additive manufacturing. *Encyclopedia of Materials*, Elsevier (2021).

11. H. Eskandari Sabzi and P. E. J. Rivera-Díaz-del-Castillo. Microscopy techniques for additive manufacturing. *Encyclopedia of Materials*, Elsevier (2021).

Acknowledgment

This work is the result of the three years and nine months research work carried out at the Engineering department of Lancaster University, United Kingdom. I would like to thank the following people, without whom I would not have been able to complete this research.

My very special gratitude goes to my main supervisor Professor Pedro Rivera, whose insight and knowledge into the subject steered me through this research. He provided me the best guidance and feedback throughout this project. His support, encouragement and patience taught me how to find my way to overcome the challenges during this project. I genuinely enjoyed all the scientific and non-scientific discussions that we had either during formal or informal meetings. I am absolutely grateful that not only has he guided me academically but also, through his wisdom, taught me invaluable lessons that have lifelong influence. I will be indebted to him for giving me the opportunity to study abroad and improve my skills as a researcher. Gracias Pedro.

The second person I would like to thank is my second supervisor, Doctor Wei Wen. I appreciate his support and guidance through our useful discussions and meetings. I would also thank Doctor Marco Simonelli and Doctor Nesma Aboulkhair from The University of Nottingham, due to their help and support towards additive manufacturing of some of the samples presented in this thesis in Centre for Additive Manufacturing, The University of Nottingham. A special thanks goes to Professor Hanwei Fu and his research group in Beihang University, China for their help towards advanced characterisation of the samples presented in this thesis. I am very grateful to Doctor David San-Martin at the Spanish National Centre for Metals Research for

Contents

List of Figures

List of Tables

xxiv

List of symbols

D	Spot size
P	Laser power
v	Scan speed
t	Layer thickness
h	Hatch distance
D_m	Melt pool depth
W	Melt pool width
E_D	Energy density
H_n	Normalised enthalpy
h_s	Enthalpy at melting temperature
A	Absorptivity
d	Thermal diffusivity
$\dot{\epsilon}$	Strain rate
T	Temperature
Z	Zener-Hollomon parameter
Q	Activation energy for recrystallization
R	Universal gas constant
ϵ_c^c	Critical strain for activation of DDRX through cell formation
B	Materials' constant
n^*	Materials' constant
a	Materials' constant
b^*	A fraction of normalised enthalpy
ϵ_c^T	Critical strain for activation of DDRX through thermostatistical theory

b Magnitude of the Burgers vector

ΔS Dislocation entropy

μ Shear modulus

ν Poisson's ratio

k_B Boltzmann constant

$\dot{\epsilon}_0$ Maximum strain rate

c Speed of sound in the material

ρ_Y Dislocation density at yield point

ϑ number of atomic sites a vacancy jumps per second

E_m Vacancy migration energy

$\dot{\epsilon}_c^T$ Critical strain rate for activation of CDRX

λ Length scaling constant

x Solute concentration in molar fraction

l^* Dislocations' distortion length

ΔG_{sys} Gibbs free energy of the alloy, representing the energy barrier accounting for the possible atomic arrangements in the lattice

ϵ_T Critical strain for activation of DRX

α_{CTE} Coefficient of thermal expansion

T_L Liquidus temperature

T_S Solidus temperature

σ_t Thermal stress

E Young's modulus

PI Performance index

F Crack prevention factor

σ_Y Yield strength

σ_{gb} Grain boundary strengthening

σ_{pr} Precipitation strengthening

σ_{ss} Solid solution strengthening

σ_d Dislocation strengthening

k_{ss} Solid solution strengthening coefficient

T_b Boiling temperature

T_m Melting temperature

C_p Heat capacity

L Melt pool length

ρ_b Density of the bulk

M_s Martensite start temperature

A_s Temperature at which austenite starts to form from δ-ferrite

M_f Martensite finish temperature

A_f Temperature at which all δ-ferrite transforms to martensite

r^* Critical precipitation radius

σ_i Interfacial energy

ΔG_v Driving force of precipitates

N_P Number density of precipitates

VF Volume fraction of precipitates

SF Strengthening factor

Ac_1 Temperature at which ferrite/martensite transforms to austenite

Ac_3 Temperature at which ferrite/martensite finish transforming to austenite

d_G Actual grain size

d_c Dislocation cell size

G Temperature gradient

T_{peak} Peak temperature

T_0 Powder bed temperature

k Thermal conductivity

ϵ_p Plastic residual strain

ϵ_t Thermal strain

CR Cooling rate

ρ_c Critical dislocation density for twin formation

ρ_c^T Critical dislocation density for twin formation trough three-layer mechanism

ρ_c^P Critical dislocation density for twin formation trough deviated Pole mechanism

b_1 Magnitude of the Burgers vector of twin source

M Taylor factor

α Constant of Taylor relationship

n_s Number of Shockley partials

r_{part} The distance between partial dislocations

γ_{DRX}^* Critical shear strain for activation of DRX

L_0 Length of the twin source

$\tau_c^{P/T}$ Critical shear stress for twin formation through three-layer or deviated Pole mechanisms

a^* Size of a twin nucleus

γ_c^{*t} Critical shear strain for twinning-induced DRX activation

ϵ_c^{*t}	Critical normal strain for activation of twinning-induced DRX
N	Dislocation impingement effect
μ_0	Shear modulus at 0 K
ρ	Dislocation density
k_1	Dislocation multiplication coefficient
f	Dislocation annihilation coefficient
H_m	Enthalpy of melting
l	Total length of laser track
m	Mass
X_{LAGB}	Fraction of low-angle grain boundaries
d_{LAGB}	Subgrain size
X_{HAGB}	Fraction of high-angle grain boundaries
n	Instant strain hardening exponent
f_{tw}	Volume fraction of twins
$d\epsilon_{dis}$	Increase in strain due to dislocation hardening
df_{tw}	Increase in twin volume fraction
Γ	Dislocation mean free path
D_s	Subgrain size
L^*	Intertwin spacing
e	Twin thickness
f_{DRV}	Coefficient of dynamic recovery
f_{DRX}	Coefficient of dynamic recrystallization
F_0	Maximum twin volume fraction
β_0	Twinning kinetic parameter

m^* A fixed exponent

σ_D Contribution of dislocations into strain hardening

x Solute concentration in molar fraction

ρ_{GND} Density of geometrically necessary dislocations

ρ_{SSD} Density of statistically stored dislocations

ϵ_T^{crit} Critical strain for twin formation

σ_T Contribution of twins into strain hardening

β Geometric constant

V Volume of the system per mole

N_A Avogadro's number

V Volume of the system per mole

w_a Materials' atomic weight

U_{form} Energy related to dislocation formation

U_{mig} Energy related to dislocation migration

U_d Energy related to initiation of dislocation glide

G^* Dislocation annihilation energy

A_{act} Activation area for annihilation

Chapter 1

Introduction

Additive manufacturing (AM), also known as three dimensional (3D) printing is a relatively new manufacturing technique that has piqued industry's interest. AM is a layer-by-layer material build-up process for producing near-net shape metals and alloys directly from a computer-aided design (CAD) model. Metal AM is gaining increased attention; the global market demand has surpassed £1.8bn in 2019 [29], and is expected to grow to £5.3bn by 2024 [30]. AM is a key low-carbon manufacturing technology incorporating net-shaping whilst avoiding complex process chains [31]. As a result, it has been promoted to combat greenhouse gas emissions [32]; its implementation will result in energy savings of 5-25% in the aerospace sector and 4-21% in feedstock and transportation [33]. Because of its geometrical and production versatility, AM will help to simplify design and manufacturing processes. AM has demonstrated its dominance in producing complex-structured components to meet urgent demands in the recent effort to resolve the COVID-19 crisis. Furthermore, because of its versatility in proptotyping and remote manufacturing, AM is a vital technology for accelerating the growth of Internet of Things [34]. AM is at the

forefront of industrial growth because of these exciting features. This manufacturing technique is appealing for a variety of applications, including aerospace, oil, gas, marine, automotive, biomedical and nuclear, due to advantages such as component design freedom, component complexity, light weighting, toolless nature, part consolidation, design for feature, and less material waste [35]. However, if the processing is not optimised, the performance of AM components may be inferior to their cast or forged counterparts [36]. Moreover, many high-performance alloys are not amenable to most AM techniques because of the repeated rapid melting and solidification inherent to this manufacturing processes [1]. To overcome the performance limitations and to take advantage of the alloy design opportunities provided by AM technology, a new generation of alloys suitable for AM is needed. In addition to this, optimising process parameters and microstructure evolution during AM can lead to improved mechanical and corrosion properties, among other benefits.

1.1   Alloys for additive manufacturing

One of the current challenges with metal AM is that only a few traditional alloys are available in powder form and suitable for AM. As a result, developing alloys that are specifically designed for metal AM is a crucial step in the advancement of metal AM. Figure 1.1 shows a schematic road map for the design of alloys suitable for AM.

There are four groups of AM alloys: steels, titanium-, nickel- and aluminium-based. So far, only one conventional alloy from each family has been successfully printed with minimal defects, and with mechanical properties comparable or even superior to their wrought counterparts: 316L stainless steel (SS), Ti-6Al-4V, IN718, and Al-Si-Mg [37]. Even though the mentioned alloys can be printed successfully, there
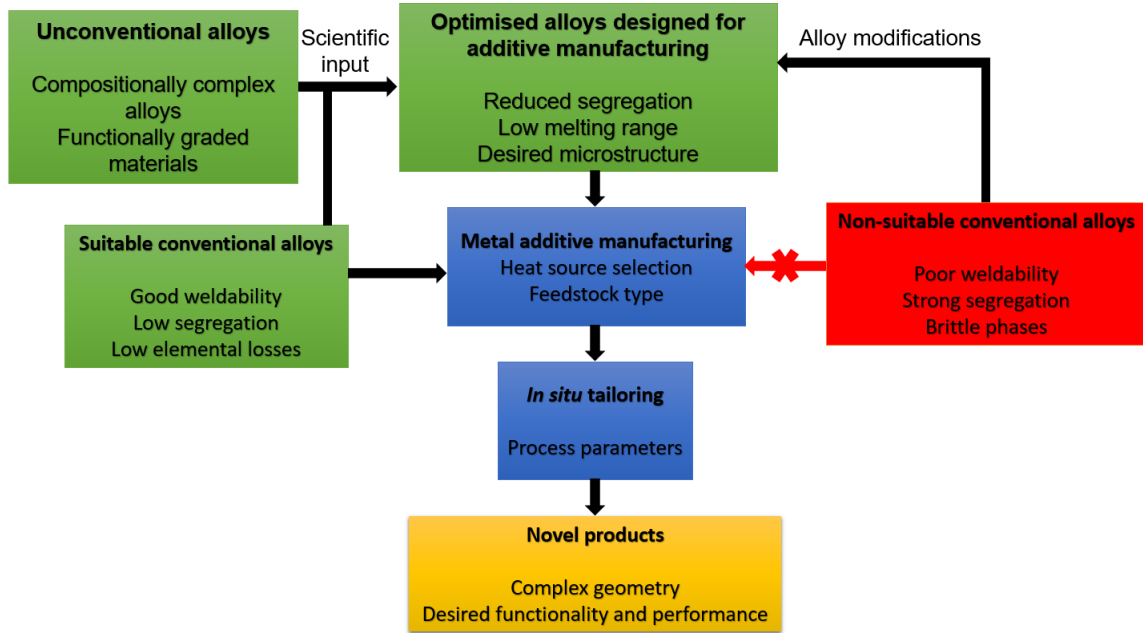
Figure 1.1: Schematic showing the need for alloy and process design for additive manufacturing. Adapted from [1].

is still a wide range of possible mechanical properties resulting from the application of AM processing parameters, demanding the need for alloy and process optimisation to maximise their properties [38].

A set of physical and thermodynamic properties, such as microsegregation, solidification temperature range and weldability must be optimised in order to fabricate an alloy using AM [39]. Therefore, not all alloys suitable for wrought processing can be successfully produced through AM. In general, alloys with good weldability, low segregation, low elemental losses, and no brittle phases during solidification are good candidates for AM. However, most commercial alloys such as nickel superalloys and automotive steels, suffer from at least one of these issues. Microstructure control is difficult during AM due to its non-equilibrium nature (ultra-fast heating and cooling), in contrast to wrought processing, where the microstructure can be carefully

controlled through subsequent thermo-mechanical processing.

Furthermore, depending on their application, AM alloys should be optimised for enhanced properties. Aerospace systems, for example, necessitate the highest strength, hardness and toughness properties, as well as high temperature stability, all while minimising weight to reduce the environmental impact [40]. As a result, alloys with lower properties but higher processability are preferred. The growing demand for biomedical applications is almost entirely driven by increased flexibility and biocompatibility, necessitating design-driven alloy growth [41]. Recyclability adds difficulty to the problem, as the chemical composition cannot be changed as freely as it can with primary elemental additions [42]. For example, the recyclability rate of elements such as V, Zr, Hf, and Ta is less than 1%, whereas that of elements such as Fe, Mn, Ti, Cr and Ni is more than 50% [43].

Before the advent of AM techniques, casting and powder metallurgy, as well as welding, were widely thought to be near-net shape processing. AM has similarities to casting from the point of view of processing issues such as porosity and hot cracking [44]. Most of the AM techniques use powder as the feedstock, which makes them similar to powder metallurgy [45]. But, the most similar technique to AM is welding, as AM processing can be regarded as welding of subsequent metallic layers depending on the shape of the final product. The heat source, heating and cooling rates, and solidification process in AM are quite similar to welding processes [37]. Therefore, AM can borrow from the rich welding conventional alloys databases and make them AM processable.

1.2 Alloy and microstructure design for additive manufacturing

Alloy design for AM should be guided by component operation conditions (e.g. temperature or stress), size and build topology, service environment conditions (e.g. wear, corrosion, static or dynamic loading), as well as the type of AM machine and infrastructure, including post-processing steps such as hot isostatic pressing (HIP) and/or heat treatment. All these should be balanced and a business case produced [46]. Similar to conventional materials processing approaches such as casting and forging, a given alloy can be fabricated through AM with acceptable levels of defects, which must be balanced with properties needed for a specific application.

Determining the main process parameters to minimise the probability of defect formation is a major challenge for researchers working on AM. Experimental advances have been achieved through trial and error methods, which are costly and time consuming. *In situ* defect identification using imaging techniques as a strategy to track the AM process is a common approach [47]. This method is useful for detecting crack and pore formation, but fails to establish a direct correlation with AM machine process parameters and feedstock compositions, which have been adjusted through trial and error. Computational approaches describing processing and composition are a powerful tool for AM advancement. Designing alloys less susceptible to AM variations, and therefore less vulnerable to defect formation, is a promising approach from a materials standpoint.

1.3   Scope and outline of the thesis

This work aims to design alloys suitable to AM processing, leading to optimal microstructures of improved mechanical behaviour. The proposed alloy design approach is based on a framework incorporating optimised solidification and controlled thermal stress formation. For this purpose, a number of metallurgical criteria for crack prevention will be introduced. This results in a crack prevention factor to define safe regions in compositional space for microcrack prevention upon AM of alloys. A genetic algorithm (GA), combined with thermodynamic calculations will be used to optimise and choose the new alloys. Then, a comprehensive analytical model will be proposed to estimate safe process parameters for AM of defect-free components. This incorporates material properties to avoid the formation of process-induced porosity in the as-built part.

It will be demostrated that restoration mechanisms such as dynamic recovery (DRV) and dynamic recrystallization (DRX) play a significant role in the microstructural evolution of AM alloys. The conditions for the activation of DRX and DRV during AM will be examined using both classical and a more recent thermostatistical theories. Thermal analysis will be carried out using empirical and simulation results to describe the thermal cycles during layering in AM. Experiments with various process parameters will be carried out to investigate the possibility of activating DRX and DRV during AM, and their impact on the microstructure and tensile properties of the as-built samples. A composition-independent methodology will be proposed to control microstructural evolution during AM and enhance the build mechanical properties.

Succint expressions for the yield strength prediction of different types of alloys

produced by AM will be presented in this work. Experimental work on 316L SS, IN718 and Ti-6Al-4V demonstrates that the yield strength of as-built fully-dense AM components correlates with the heat input via the normalised enthalpy, which incorporates both the AM process parameters and the alloy physical properties. The contribution of various mechanisms governing strengthening in AM alloys will be revealed using analytical models.

A unified relationship for the prediction of the yield strength in AM alloys, considering the role of low- and high-angle grain boundaries will be presented. Criteria to control restoration processes and maximise the yield strength by controlling both process parameters and alloy composition will be suggested. As the micrsotructure of the as-built AM alloys are unique and different from their wrought counterparts, their deformation behaviour will also be modelled using plasticity modelling approaches.

The outline of this thesis is as follows: in **Chapter 2**, different additive manufacturing techniques are reviewed, LPBF is described in detail as the main AM technique studied in this work. Processing defects such as cracks and porosity, and criteria to prevent their formation, are introduced. Optimisation methods for alloy design are presented, and the main microstructural development theories for AM alloys are reviewed. The yield strengthening theories for AM alloys are finally provided.

Chapter 3 presents the main alloy design approach to produce crack- and defect-free AM components. This approach has been applied to various steel families such as 316L and 17-4 precipitation hardening stainless steels, as well as a Formetrix maraging steel. LPBF process parameters have been optimised via empirical models to minimise porosity formation. The mechanical properties of 316L SSs produced with various porosity contents are also presented in this chapter. Microstructural investi-

gations to interpret the variations in mechanical properties are presented in **Chapter 4**. DRX and DRV during LPBF are modelled using two approaches.

Mechanical properties of LPBF alloys are modelled and optimised using various metallurgical theories in **Chapter 5**. The role of low-angle grain boundaries and a unified Hall-Petch-type relationship considering the role of subgrains in yield strengthening are described for 316L SS. Other contributors to the yield strengthening in LPBF alloys are also discussed in this chapter. In **Chapter 6** the deformation behaviour of defect-free LPBF 316L SS is investigated and modelled based on advanced microscopy observations. Following this, concluding remarks and a summary of this thesis are presented in **Chapter 7**.

Chapter 2

Literature review

AM techniques are introduced in this chapter, with a focus on LPBF, as the main technique used in this work. LPBF processing defects including cracks and pores are presented, and the possible approaches to minimise them are discussed. Computational alloy design principles for AM are described. Microstructure and mechanical properties of LPBF alloys are reviewed. Various approaches to model thermal cycling, restoration mechanisms and yield strengthening during LPBF are presented. Special emphasis is made on 316L SS, as experimental attempts for model validation have been performed on this alloy.

2.1   Additive manufacturing techniques

The American Society for Testing and Materials (ASTM) (ASTM F42 – Additive Manufacturing) published a set of standards in 2010 that divided AM techniques into seven categories: (i) Vat photopolymerisation, (ii) material jetting, (iii) binder jetting, (iv) material extrusion, (v) powder bed fusion (PBF), (vi) sheet lamination, and (vii)

directed energy deposition (DED). PBF and DED are the most common metals and alloys based manufacturing techniques. PBF and DED are powder bed or powder fed AM techniques, respectively. PBF methods can be categorised as laser powder bed fusion (also known as selective laser melting), and electron beam melting (EBM) [6]. The most important DED method for metal AM is laser metal deposition (LMD) [48].

Metal AM techniques are classified and schematically depicted in Figure 2.1. In LPBF, a laser beam with a fixed spot size (usually smaller than 100 μm) and a scan speed of around 1 m/s fuses several layers of powder with a pre-specified thickness (a few tens of microns) to build a part of desired geometry. After a layer has solidified, a new powder layer is added with a roller and the process is repeated until the entire product is constructed. LPBF processing is characterised by small melt pools with large thermal gradients and cooling rates of 10^5-10^6 K/s. Usually, the chamber is filled with nitrogen or argon to protect the component from oxidation and to clear any spatter produced by the scanning laser [49, 50].

As compared to LPBF, EBM is an AM technique for producing components with minimal support structures and needing less post-processing, leading to less residual stresses and higher productivity rates. The mechanics of EBM technology are similar to LPBF, but it has a vacuum chamber and melts powder layers with an electron beam rather than a laser. A rake is used to disperse the powder on the substrate. This technology also allows for the preheating of the powder bed to temperatures of up to 900 °C [51, 52]. Firstly, the powder bed is preheated via the electron beam. In the melting stage a beam current of 5-20 mA and scan speeds of 0.1-1 m/s are applied. EBM is more complicated than LPBF, as it requires the optimisation of more process

parameters [53].

LMD is a powder-fed system in which metal powders contained in one or more nozzles are directed coaxially or laterally into the interaction zone between the laser and the substrate through deposition nozzles, where they are fused by the laser beam to create a metallic bed. This process is repeated layer by layer (with a pre-specified layer thickness, which is typically higher than LPBF and EBM) until the entire part is constructed [54].
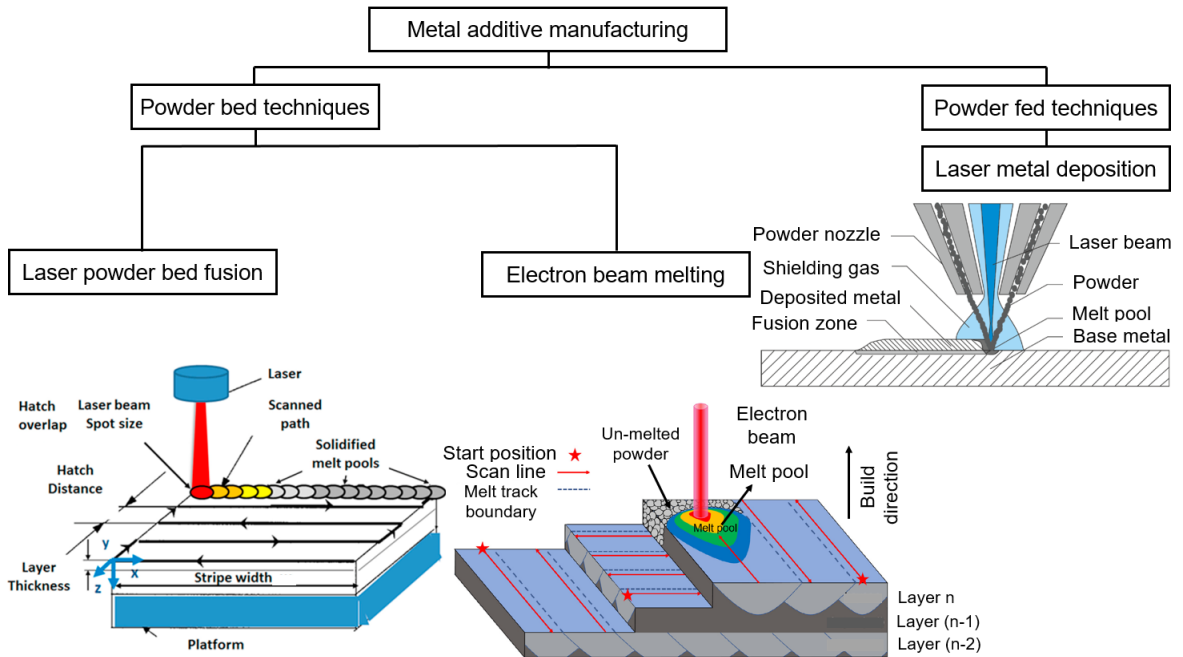
Figure 2.1: Schematics of metal AM techniques.

Similar to every manufacturing technique, AM has advantages and limitations compared to more conventional manufacturing techniques such as casting and forging; these include: (i) complex 3D geometries with internal features can be printed in the absence of tooling; (ii) there is no need for coarse machining after AM, minimising waste; (iii) the components can be printed directly from the 3D computer model; (iv)

11

faster prototyping in AM allows designers to evaluate multiple iterations, resulting in a shorter design cycle process; (v) functionally graded materials can be printed more conveniently compared with conventional manufacturing methods; (vi) mechanical properties of AM alloys are usually superior.

Limitations of AM can be summarised as: (i) since this technology is quite recent, the industrial building process is slow and expensive; (ii) owing to the high cost of equipment, manufacturing costs are high; (iii) depending on the AM technique and the type of the alloy, different post-processing treatments may be required; (iv) in comparison to other manufacturing part sizes, such as casting and forging, the build volume is small; (v) some alloys cannot be produced with AM with superior mechanical properties compared to their wrought counterparts; (vi) poor surface finish and texturised microstructures are produced, with the latter resulting in anisotropy in mechanical properties.

Since LPBF currently dominates commercial PBF and DED systems, the emphasis of this thesis will be on LPBF rather than EBM or LMD.

2.1.1   Laser powder bed fusion

LPBF, also known as selective laser melting (SLM) is a metal AM process with a capability for producing near fully-dense structures without the need for post-processing [50]. A number of research studies have been published on its application, process improvement, parameter optimisation, and numerical modelling to predict the temperature gradients, the occurrence of melting and evaporation, as well as the analysis and prediction of resulting microstructures [55, 56, 57, 58, 59, 39, 60].

To gain a better understanding of LPBF processing of alloys, laser characteristics,

process parameters, and resulting microstructures must all be studied together. Most laser characteristics such as maximum power, wavelength, spot size (diameter, D), and beam energy distribution are unique to the laser equipment and cannot be changed by the user. However, a set of laser processing parameters such as laser power (P), scan speed (v), hatch distance (the distance between the centres of the two adjacent powder layers, h), and layer thickness of the powder spread into powder bed (t) can be controlled and varied to achieve the best combination of part density and mechanical properties [50]. Table 2.1 summarises the common variation ranges of LPBF processing parameters.

Table 2.1: Typical processing parameters including laser power (P), scan speed (v), layer thickness (t), and hatch distance (h) used for LPBF processing.

P (W)	v (m/s)	t (μm)	h (μm)	D (μm)
80-400	0.1-2	20-50	50-150	30-200

In addition to these, the laser scan strategy can also be changed to control texture and residual stress evolution, and localised heat input during LPBF [61]. The most common LPBF scan strategies are meander, chessboard and stripe. They are depicted schematically in Figure 2.2. Among these, it has been reported that meander scan strategy with a 67° rotation after each layering leads to the minimum residual stresses and a uniform thermal field [62].

The effects of the mentioned process parameters, in combination with powder characteristics such as its size, distribution, and morphology on variations in the quality of the built component in terms of density, mechanical properties, residual stress, surface roughness, and defects are not yet well known. Metal component production with LPBF is rapidly increasing. However, the transition of this technology from prototype to critical component production is hampered by the uncertainties affecting
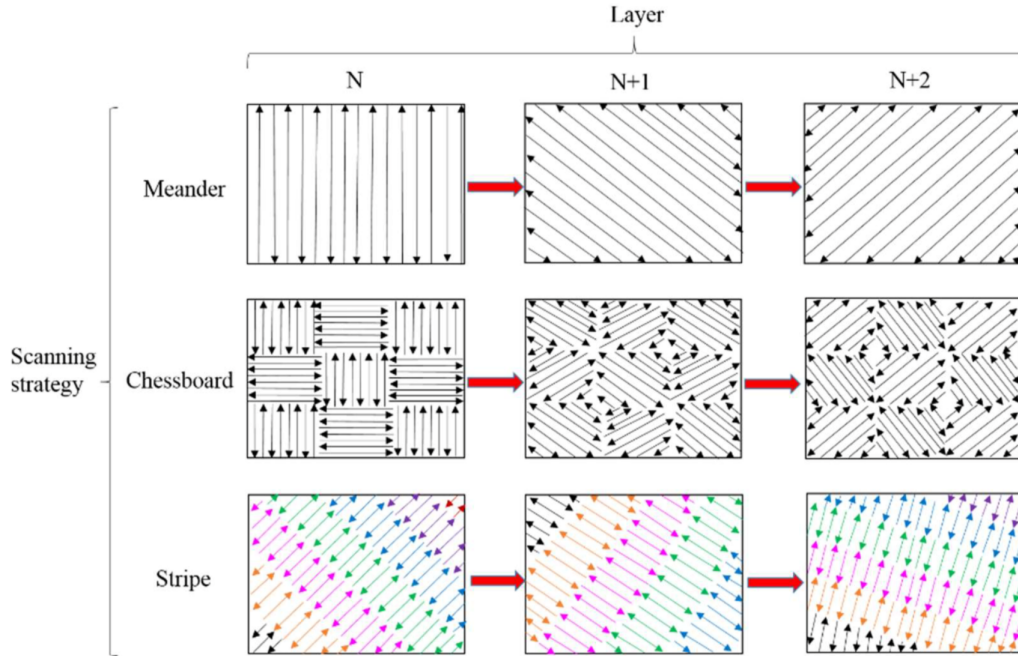
Figure 2.2: Common LPBF scan strategies. Adopted from [2].

the part quality. A basic understanding of the physics of this technique can be used to enhance its reliability. It is widely agreed that modelling and simulation can increasingly be used to achieve this understanding. However, the large range of length and time scales as well as temperature ranges associated with LPBF pose major physics, computational, and materials challenges. For example, melt pool instabilities, material spattering and balling problems, lack of fusion, rapid material evaporation, and keyhole-induced pore formation can occur as a result of the high/low energies applied to the powder bed with high/low power laser beam [62]. These phenomena and the solutions to control them must be understood via combining metallurgical knowledge and computational tools to simulate complex physical phenomena.

2.2 Laser powder bed fusion processing defects

In AM, printability refers to a feedstock's ability to be effectively deposited as a bulk material on a substrate while preventing major defects and achieving desired mechanical properties [63, 8]. Printability is similar to the principle of weldability, which illustrates the ability and ease with which alloys can be welded together. However, in contrast to welding, there is no systematic approach for determining a material's printability under various metallurgical and process conditions.

Hot (solidification) cracks and porosity are the two most common processing defects in LPBF alloys. When the stress caused by solidification shrinkage and thermal contraction exceeds the alloy's elastic/plastic deformation, hot cracking occurs [64]. This typically happens at the end of the solidification process, when there is not enough liquid left in the interdendritic regions [65, 3]. Because of differences in solidification characteristics such as solidification temperature range and solid fraction change upon cooling from liquidus and solidus temperatures; this phenomenon is highly influenced by alloy composition [64].

The alloy solidification sequence is schematically represented in Figure 2.3. The first solid forms from liquid and acts as a nucleus for solid phase growth, forming a dendrite (Figure 2.3a). The size of the dendrite increases in subsequent stages of solidification, before grains are formed (Figure 2.3b, c). Owing to the fact that alloys solidify within a range of temperatures, the first metal to solidify has the highest melting point composition, while the last has the lowest eutectic composition. As a result, the alloy fraction with the lowest melting point is moved ahead of the solidifying dendrite until it becomes stuck between the grain boundaries (Figure 2.3d). Therefore, a significant difference in melting points between the eutectic and the bulk

alloy increases the susceptibility to solidification (hot) cracking [66].
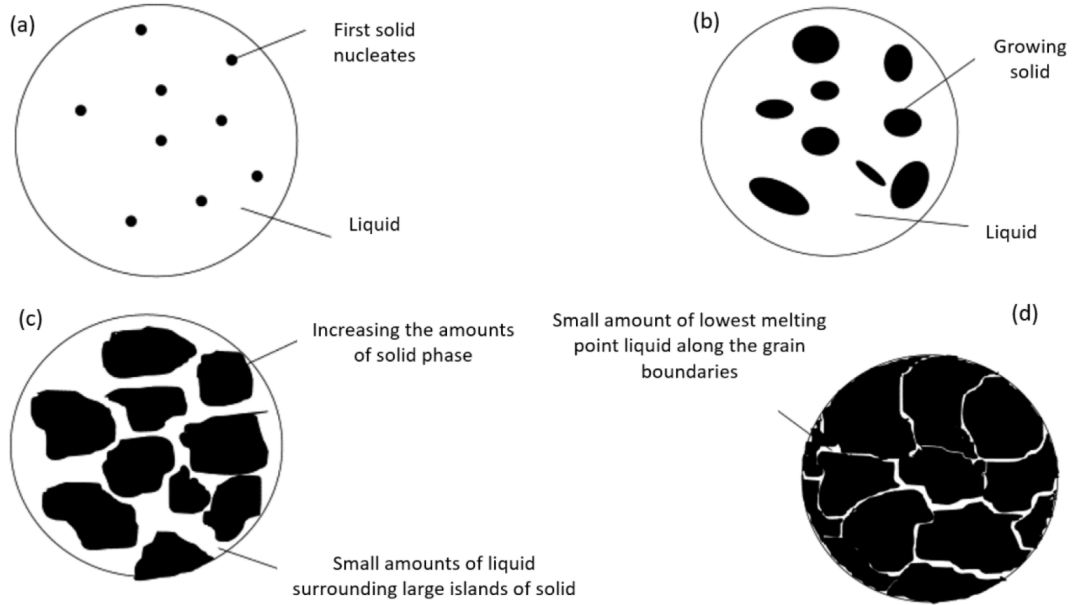
Figure 2.3: Schematic showing how an alloy solidifies. (a) The beginning of solidification (near liquidus temperature), (b) solid phase grows through the liquid phase, (c) the amount of solid increases by decrease in temperature, (d) latest stages of solidification, where low amounts of liquid remained along the solidified grain boundaries. Adapted from [3].

Porosity may have a negative impact on mechanical properties. Spherical and irregular shapes are the two major types of pores. Gas entrapment during powder processing causes spherical pores [67], which are thought to be permissible at the component scale, with a maximum acceptable volume of ~0.7% [68]. Lack of fusion, keyhole-induced pore, and balling are three distinct types of irregularly formed pores. The lack of fusion pores are caused by the melt pool not penetrating far enough into the previous layer (Figure 2.4a) [69]. The keyhole-induced pore is mainly caused by extremely high heat inputs, which can result in vapourisation and the creation of deep V-shaped melt pools, as shown in Figure 2.4b [70]. Balling is a frequent shift

in the size and shape of the solidified track caused by melt pool instabilities due to capillarity. This phenomenon can create voids and make it difficult for subsequent layers of powder to spread uniformly (Figure 2.4c) [3].
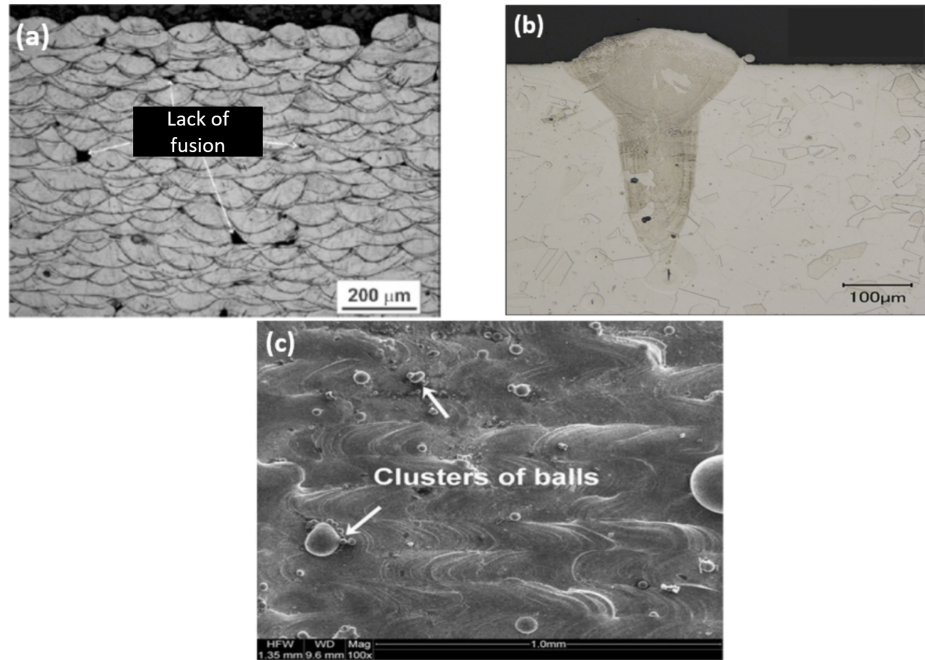
Figure 2.4: (a) Micrograph showing lack of fusion pores; (b) keyhole-induced porosity [4]; (c) balling defect [5]. Adopted from [6].

Khairallah *et al.* [71] combined X-ray synchrotron experiments with predictive multi-physics models to better understand the causes of defect formation during LPBF. One of their aims was to demonstrate how energy is consumed during printing of powder layers. They found that a significant number of pores and defects were caused by simple spatter, where process-ejected particles interfere with newly deposited material. They further showed that by carefully monitoring the laser power, much of the spatter and resulting defects in the as-built component could be reduced significantly.

Microscopy techniques for porosity and crack characterisation can be categorised in

four main methods: optical microscopy (OM), scanning electron microscopy (SEM), X-ray computed tomography (XCT) and synchrotron X-ray computed tomography (sXCT) [72]. OM and SEM are frequently used to measure the AM components density by characterising the number of pores. Using these two techniques, crack and pore characteristics such as their size distribution and uniformity, shape irregularities, interconnectivities, and their size can be determined in two dimensions [73, 74]. The limitation is that typical metallography (OM and SEM) uses a small number of 2D images and does not include bulk 3D images or statistically relevant quantitative data. However, this approach is the most common in porosity and crack characterisation.

XCT and sXCT are non-destructive volumetric charcterisation techniques, as they provide 3D images used for studying internal material features [72]. The same features of pores and cracks can be revealed using these two techniques, but the data are more comprehensive due to the larger specimen volume covered by their detectors compared with OM and SEM. Due to partial coherence, high beam brilliance, and adjustability of the experimental setup, sXCT has major advantages over XCT. These include fewer artefacts, improved contrast, refined spatial resolution below 1 μm, and faster capture rates, which allow *in situ* measurements of pores and cracks during AM [72]. Examples of the application of XCT and sXCT in AM can be found in [75, 76, 77, 78].

In order to limit pore formation during LPBF, processing parameters must be chosen carefully. Keyhole-induced pores and lack of fusion are two most common defects observed and reported during LPBF of metals and alloys [7]. A number of criteria help to avoid keyhole-induced pores and lack of fusion during LPBF, which depend on both process parameters and physical properties of the alloy. In the case of lack of fusion, if there is enough overlap between melt pools to ensure that all areas

18

are melted at least once, the lack of fusion boundary can be calculated. Gordon *et al.* [7] implemented a criterion to avoid lack of fusion during LPBF by controlling melt pool geometry, which depends on the process parameters (hatch distance, h, and layer thickness, t):

$$\left(\frac{h}{W}\right)^2 + \left(\frac{t}{D_m}\right)^2 \leq 1, \tag{2.1}$$

where W is the melt pool width and D_m is the melt pool depth. Zhu *et al.* [79] used a modified criterion for lack of fusion prevention during LPBF:

$$\left(\frac{h}{W}\right)^2 + \frac{t}{t + D_m} \geq 1. \tag{2.2}$$

Seede *et al.* [80] simply considered melt pool depth and layer thickness as the most important variables to control lack of fusion. They suggested that if the melt pool depth is greater than or equal to the layer thickness, complete melting occurs. In a similar approach, Johnson *et al.* [8] considered a certain criterion of $D_m/t > 1.5$ as a reliable assumption for lack of fusion prevention. It should be noted that most of these criteria come from welding literature, as some physics of LPBF such as high heat input and rapid heating/cooling rates are similar to welding. Therefore, these criteria need to be tested, verified and modified for application in LPBF.

Keyhole-induced pore boundary should be determined based on the instabilities in deep keyholes that cause pores to pinch off. Similar to lack of fusion, keyhole-induced pore formation is also a common issue during laser welding of metals and alloys. Therefore, some concepts in welding can also be applied to AM. Most of the previous reports suggest that there is a certain threshold for melt pool width to depth ratio that prevents formation of keyhole-induced pores. This threshold is reported to

19

be 2, 1.5 or even 1.2 [8, 80, 7]. Furthermore, as keyhole-induced pores are the result of the evaporation of the metal powder, the heat input must also be controlled. There are two approaches to estimate LPBF heat input: (i) energy density (E_D, equation 2.3) [69], and (ii) normalised enthalpy (H_n, equation 2.4) [81].

$$E_D = \frac{P}{vht}.$$ (2.3)

$$H_n = \frac{AP}{h_s\sqrt{\pi vdD^3}},$$ (2.4)

where h_s is the enthalpy at the melting temperature, A is the absorptivity, and d is the thermal diffusivity.

There are several reports showing that E_D cannot be correlated with keyhole-induced pore formation probability [21, 82, 83, 84]; conversely, threshold values have been reported for H_n to prevent the formation of keyhole-induced pores [4, 81].

To sum up, some studies used a combination of melt pool geometry criteria to find optimal process parameters windows (e.g. P and v) to prevent defect formation. However, the development of these approaches is at its onset and more efforts are needed to build a comprehensive methodology for defect formation prevention. Examples of recent attempts to find the optimal LPBF process windows are shown in Figure 2.5.

2.3   Alloy design approaches

Although porosity formation can be mainly controlled via processing parameters optimisation, cracking largely depends on finding the best chemical composition. Ap-
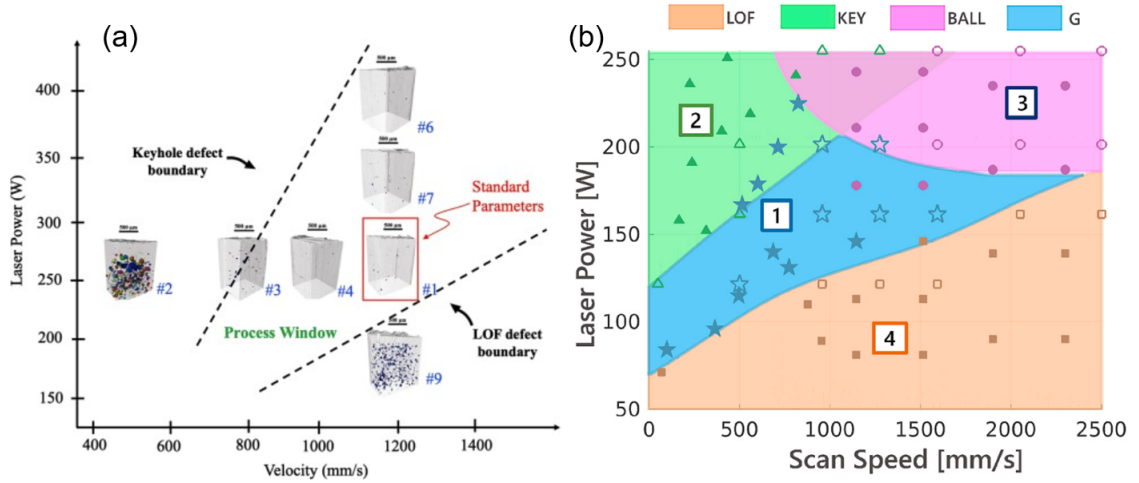
Figure 2.5: (a) Defect structure process map of LPBF Ti-6Al-4V, showing regoins of keyhole-induced pores and lack of fusion (LOF) formation, as well as the process window for defect-free components. Adapted from [7]. (b) Printability map showing regions of defect-free (1, G), keyhole-induced pores (2, KEY), balling (3, BALL), and lack of fusion (4, LOF) in LPBF Ni-5wt.%Nb. Adapted from [8].

proaches for alloy design optimisation are summarised as follows.

2.3.1   Optimisation methods

The conventional method for alloy design is to create a distinct set of ingots with different compositions, which is a time-consuming and expensive process. The complexity of industrial alloys, which often contain ten or more alloying elements that interact with one another during processing, demands the need for computer-based optimisation methods.

In materials science and metallurgy, developing methodologies for accelerated alloy design has become more relevant since the advent of the Materials Genome Initiative in 2011 [85]. However, one challenge is that the properties of structural materials are not only influenced by their composition, but also by their microstructure (phase

fraction, size, shape, chemistry), which is based on both composition and processing parameters through phase transformations and their kinetics at the nanoscale [9].

There are two key steps in an accelerated alloy design strategy: (i) developing metallurgical criteria to predict the structure, microstructure and properties of alloys in order to minimise the number of experimental trials for alloy development; (ii) exploring the alloy design space with high-throughput experimental and numerical methods for finding the optimal alloy grade composition [9].

Combining computational thermodynamics using the calculation of phase diagrams (CALPHAD) method, physical metallurgy modelling, and optimisation using multi-objective genetic algorithms is one method for alloy design in a multi-dimensional variable space.

2.3.2   Genetic algorithms

Alloy design space includes a near-infinite number of alloys and compositions. Metallurgical problems are non-linear and strongly coupled, making it difficult to explore all grades without mathematical optimisation tools such as genetic algorithms (GAs) [9]. Figure 2.6 illustrates the principles of GA optimisation. GA incorporates a population of individuals (alloy compositions), each of which represents a possible solution. A population of individuals (alloys) is generated at random and goes through a cycle of selection, reproduction and mutation. Each cycle results in the birth of a new generation. A fitness function measures the performance of each generation based on the expected characteristics to be optimised and a set of constraints known as go/no-go criteria. The objective is to find individuals that, over a number of generations, come close to an optimal solution [86].
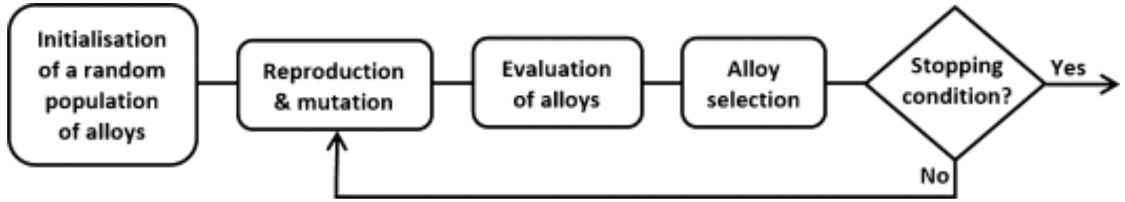
Figure 2.6: Flowchart showing how genetic algorithm optimisation works. Adopted from [9].

Various parameters must be optimised as a function of composition in order to design a new alloy with a GA. Therefore, models that can accurately predict various properties are needed. There are numerous modelling approaches for predicting alloy properties as a function of composition and processing parameters. The most common tools include density functional theory, Monte Carlo simulations, molecular dynamics, computational thermodynamics and kinetics, finite element method, and phase field simulations [87].

In order to make an optimisation process efficient, the optimisation time must be fast. Millions of different alloys must be investigated over the process of a GA optimisation; if the optimisation takes a month to complete, this approach cannot meet the needs of industry. As a result, time-consuming modelling methods are not favourable for alloy design. Therefore, three types of predictive tools have been commonly used in the computational alloy design approach by combinatorial optimisation [9]: (i) those with physical models that can be solved with simple equations; (ii) thermodynamics-based approaches (CALPHAD methodology); (iii) machine learning tools. Depending on the problem to be solved, all three approaches will reduce optimisation time to a fraction of a second, minutes or several hours. Because the alloy design approach that has been used in this research is based on CALPHAD methodology, this method will be presented in detail in the next section.

2.3.3 CALPHAD methodology

CALPHAD is a semi-empirical method for predicting and calculating thermodynamic and kinetic properties (as well as associated properties) of multicomponent systems. It is based on phase equilibrium, beginning with pure elements and progressing to binary, ternary, and multicomponent systems. CALPHAD can predict the properties of higher order alloys, such as engineering materials, by extrapolating and interpolating thermodynamic data [88]. Thermodynamic properties are modelled in CALPHAD as a function of composition, temperature, and in some cases pressure (or strain). This, coupled with the use of different thermodynamic models, allows one to extrapolate data from binary and ternary systems to higher order systems, which is rarely available through experiments or handbooks. Since phases are the fundamental building blocks of a material, the CALPHAD method is truly a Materials Genome approach [89].

This approach has applications that go beyond conventional thermochemistry. CALPHAD can calculate/predict a variety of properties. Phase equilibrium properties such as the phase fraction, constitute concentration, driving forces, phase and Pourbaix diagrams, physical/thermodynamic properties calculations such as enthalpy, entropy, specific heat, heat capacity, heat of formation, interfacial energy, density, coefficient of thermal expansion, lattice parameters, viscosity, and surface tension of liquid, thermal conductivity, resistivity, and diffusivity make this approach very popular for optimising for desirable properties. Using CALPHAD, one can also predict kinetic coefficients such as atomic mobility, tracer and intrinsic diffusion, and interdiffusion, as well as non-equilibrium solidification properties such as liquidus, solidus, incipient melting temperature, solidification temperature range, fraction of solid curves,

solidification path, eutectic fraction, microsegregation, partitioning coefficients, and latent heat of melting [90, 91]. This is very useful to model the possible solidification routes during AM, to minimise crack formation, and to optimise the microstructure evolution and subsequent mechanical properties.

The parameters employed in CALPHAD are stored in databases. Using Thermo-Calc Software, one use CALPHAD methodology whilst incorporating a range of databases. Additionally, mobility databases generate kinetic data to match the thermodynamic and properties database. All database development uses the same methodology, but there are differences in the models that are applied to the data [92]. Each of these databases are developed for a range of alloy families including steels and iron alloys, nickel-, aluminium-, magnesium-, copper-, and titanium- based alloys, as well as high entropy alloys [92].

CALPHAD methodology consists of four main steps (selection and evaluation of input data, selection of models for the Gibbs free energy, optimisation of model parameters, and calculation and comparison), which lead to a variety of applications [10]. The whole procedure is schematically summarised in Figure 2.7.

Collecting experimental data on the materials system of interest is the first step in CALPHAD modelling. Data sources can be phase equilibrium experiments, thermochemical properties including enthalpy of mixing or formation energies, and crystal structures. When experimental data is inaccessible, software such as Thermo-Calc can incorporate *ab initio* calculations. Machine learning and empirical relations are also used with Thermo-Calc to estimate model parameters for systems with few or uncertain data.

Second step is the critical assessment and pre-processing of the collected data to
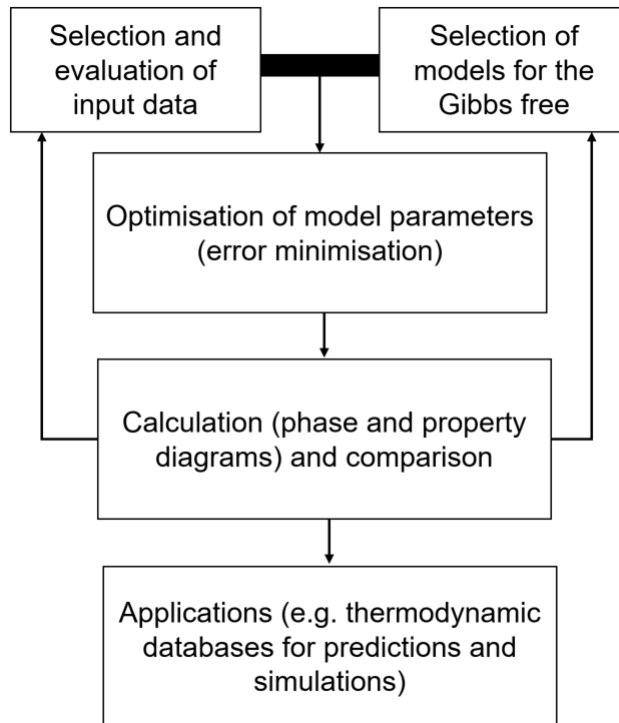
Figure 2.7: Flowchart illustrating the core of CALPHAD methodology. Adapted from [10].

calculate and model the Gibbs free energy. There are a variety of possible phases in a phase diagram assessment of a given thermodynamic system with two components. Depending on the crystal structure of each of these phases, a model for the Gibbs free energy is allocated. The Gibbs free energy is typically a polynomial function of the chemical composition, temperature and pressure.

The third step is optimisation, which includes adapting the model's parameters to the input data obtained in the first step. An error minimisation technique, such as non-linear least squares, is used to test empirical parameters.

The Gibbs free energy functions containing the newly optimised parameters are then used to measure phase and property diagrams, which can then be compared to

known data. In metastable conditions, metastable equilibria and the related thermo-dynamic functions must also be verified.

2.3.4 Computational alloy design by combinatorial optimisation

In the previous section, it has been shown that CALPHAD can be used to propose new alloy compositions based on desired microstructural features. But for these features, even if involved in attaining desired properties (for example crack prevention), there is no guarantee that they provide the optimal solution. Therefore, it is important to combine CALPHAD methodology with an optimisation approach such as GA.

This has been done successfully for wrought alloys to design new compositions that yield certain target properties. Aristeidakis *et al.* [93] combined CALPHAD and GA optimisation to design medium-Mn steels to optimise the chemical composition and heat treatment process to obtain desired microstructural features. A similar approach has been used to design new maraging steels [94, 95, 96, 97, 98, 99, 100, 101, 102, 103], high entropy alloys [104, 105, 106, 107], and nickel superalloys [108, 109, 110].

The general optimisation approach used in previous research can be summarised in Figure 2.8 [109]: (i) a set of initial parents (the number of parents depends on the number of genes) is generated with random genes (original composition space); (ii) parents reproduce at random and generate children; each child inherits half of its parent's genes, which are selected randomly; (iii) for each child, a fitness criterion or multiple fitness criteria are calculated to be minimised. These criteria are based on the optimisation objective (for example alloy cost, crack prevention, or mechanical properties), as well as Thermo-Calc predictions, which have specific stability and

processability constraints; (iv) the best of the generated children are chosen to become parents of the next generation, while avoiding individuals with similar genes; (v) after the predetermined number of generations is reached, the algorithm returns to step (i).
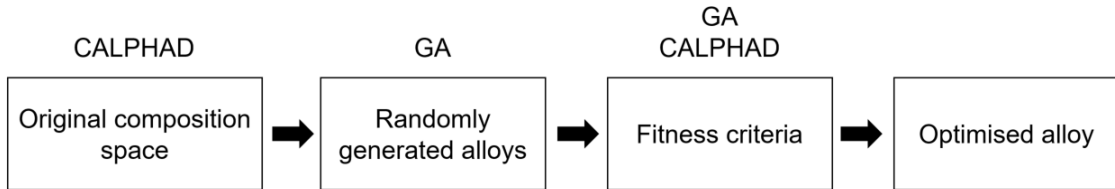
Figure 2.8: Flowchart of the applied computational alloy design, combining CAL-PHAD and GA.

2.4 Microstructural evolution during laser powder bed fusion

Since LPBF alloys are exposed to intense heating and cooling rates as well as thermal strains, they usually have microstructures that vary from their wrought counterparts [38]. The quick layer-by-layer scanning of the laser beam during LPBF results in a non-equilibrium process [111]; this leads to short interaction times between the powder and the laser beam, as well as localised high heat inputs. As layering progresses, complex cycles of heating above the melting point, cooling, and solidification occur in parts of the powder bed, which are repeated as the laser moves away. This results in the development of solidification-enabled cellular structures, low angle grain boundaries, high dislocation densities, as well as a greater chance of martensitic transformation when the material is cooled [17, 112, 19]; as a result, most LPBF alloys have high yield strengths. Figure 2.9 depicts a typical microstructural features of LPBF alloys. Figure 2.9 also displays transmission electron microscopy (TEM) micrographs of the

three most common LPBF alloys. The key feature of the LPBF 316L SS (Figure 2.9a), Ti-6Al-4V (Figure 2.9b) and IN718 (Figure 2.9c) is the high dislocation density caused by dislocation multiplication/annihilation at high temperatures and thermal strains. As another significant microstructural feature, α'-martensite laths can be seen in the microstructure of Ti-6Al-4V (Figure 2.9b). Figure 2.9d shows in the as-built 316L SS the cellular structure [11], while Figure 2.9e depicts the same features within an IN718 processed by LPBF [13].
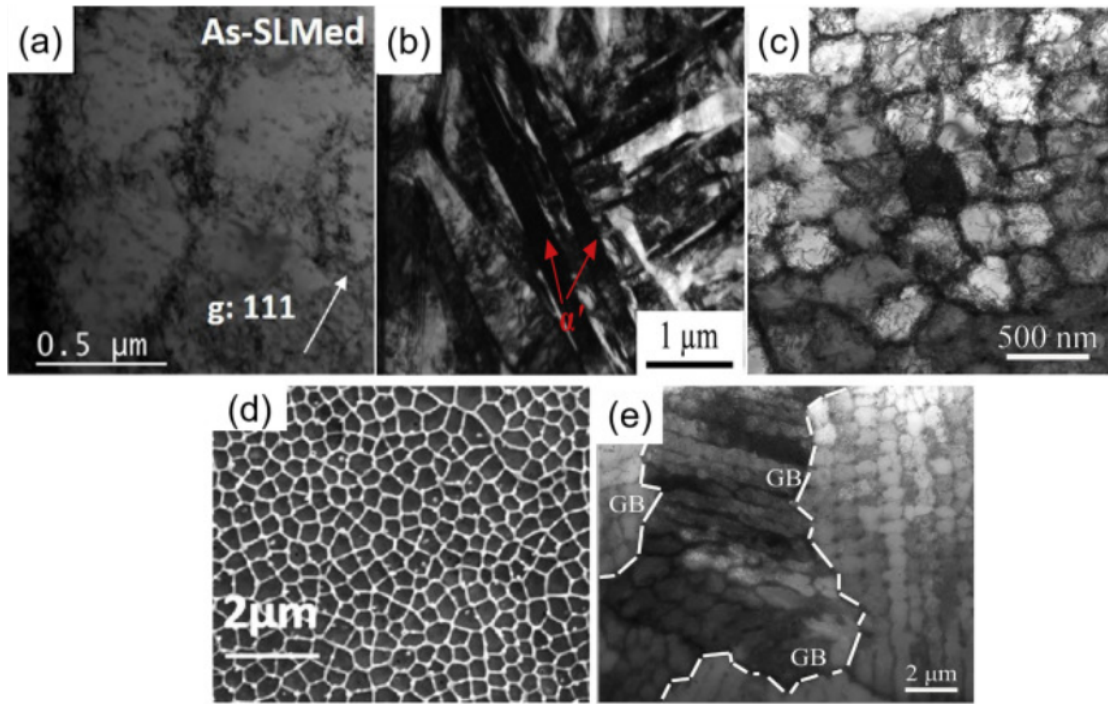
Figure 2.9: Representative bright field TEM images of the LPBF processed (a) 316L SS [11], (b) Ti-6Al-4V [12] and (c) IN718 [13]. (d) Scanning electron microscope image of the microstructure of a LPBF processed 316L SS showing cellular structures [11]. (e) Bright field TEM image showing the cellular structure inside a grain (GB indicates the grain boundaries) in LPBF-processed IN718 [13].

Since these microstructural features are specific to LPBF, a summary of the modelling approaches that could be used to control/predict microstructural evolution will

be provided here.

2.4.1   Thermal cycling inherent to laser powder bed fusion

Because of the complex thermal cycles that a component experiences during layer-by-layer melting and solidification, the microstructures of LPBF-fabricated parts are peculiar. As a result, the material may go through several solid-solid, liquid-solid, and solid-liquid phase transformations. An example of the temperature-time profile for a layer of LPBF-processed Ti6Al4V is shown in Figure 2.10a. In this case, the alloy has experienced two rapid melting/solidification and two $\beta \rightarrow \alpha$ transformations. Therefore, LPBF processing generates metastable microstructures that differ in each layer of the as-built component [14].

Hussein *et al.* [15] implemented a 3D finite element simulation to predict the temperature-time profile of a layer during LPBF of IN718 (Figure 2.10b). As can be seen in Figure 2.10b, the material experiences two rapid melting/solidification, as well as three subsequent cycles that the material is prone to solid state phase transformations, precipitation or even restoration processes such as DRX and DRV.

A similar trend can be observed in DED of 316L SS (Figure 2.10c). Figure 2.10c shows that each layer of 316L undergoes three thermal cycles during DED, in which the material is prone to restoration processes at the second and third thermal cycles.

The underlying physical process behind the evolution of these subsequent thermal cycles is heat conduction. Since the melt pool is formed in a conductive metallic medium, not only the temperature of the region under the laser beam but also the temperature of the surrounding material rises during the heating stage and melt pool formation. Because of the larger temperature drop, the newly deposited layer is prone
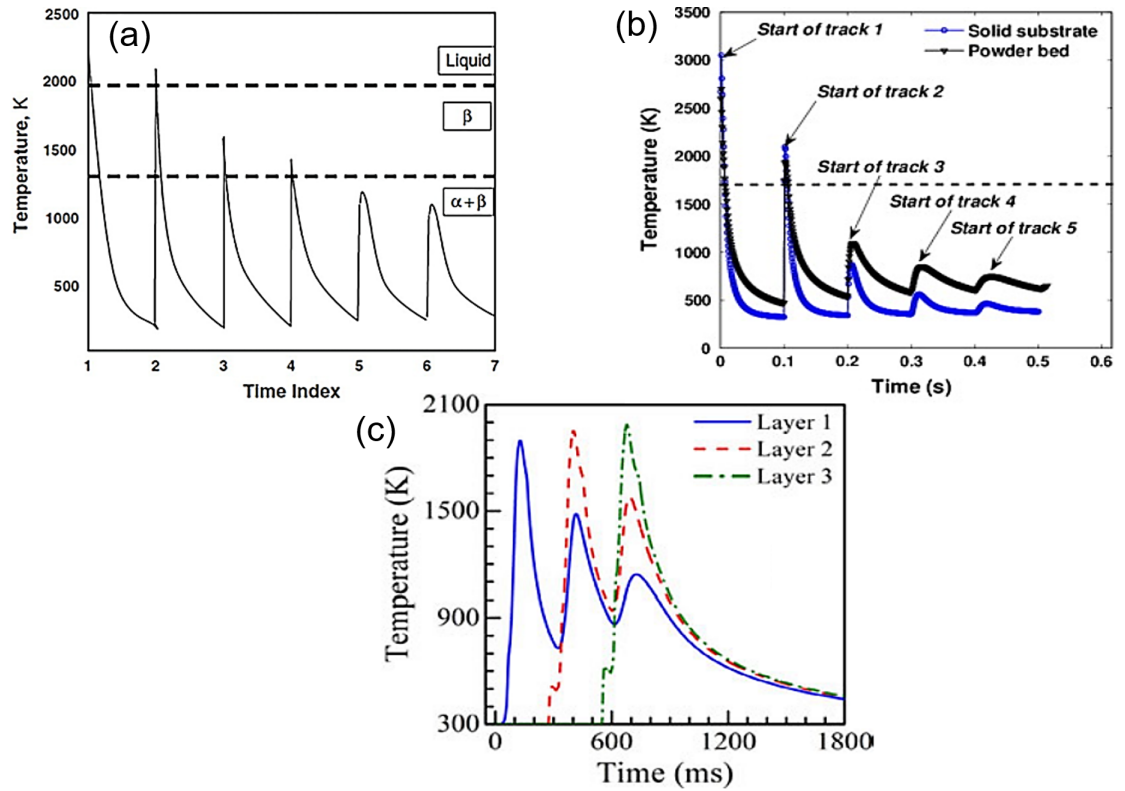
Figure 2.10: (a) Schematic representation of temperature-time profile of an AM processed Ti-6Al-4V, adopted from [14]. (b) Temperature-time profiles of the first scan track of a LPBF IN718, simulated via finite element method. Adopted from [15]. (c) Thermal cycles at three monitoring locations in the first three layers in a DED 316L SS, adopted [16].

to a higher solute concentration during cooling. The regions further away from the laser beam restrain the deposited layer's contraction due to their lower contraction capability [113]. This will result in the generation of thermal and plastic strains during LPBF. This generated strain, combined with subsequent heating/cooling cycles lead to several *in situ* thermo-mechanical processes, which can affect the microstructural evolution and subsequent mechanical properties of the as-built LPBF alloys. The thermo-mechanical phenomena and approaches to control them will be described in the next section.

31

2.4.2 Background on restoration mechanisms

Restoration mechanisms such as DRV and DRX can occur during hot deformation, resulting in increased formability at high temperatures. DRX and DRV are crucial aspects influencing the mechanical properties of wrought alloys because of their impact on texture, grain size and morphology [114]. LPBF is a process with high strain rate with the build experiencing cyclic heating and cooling. As a result, when the thermo-mechanical conditions are appropriate, DRX and DRV can be activated.

DRV is the primary restoration mechanism in alloys where dislocation cross-slip and climb processes are common [115]. The density of dislocations increases as a result of deformation, increasing the driving force for DRV [116]. Figure 2.11 illustrates the various restoration processes that occur during thermo-mechanical processing. Microstructural characteristics such as the formation of low-angle grain boundaries (LAGBs) and subgrains can be used to detect the incidence of DRV (Figure 2.11a). In this thesis, the grains are divided into two categories: (i) actual grains surrounded by high-angle grain boundaries (HAGBs), as shown in Figure 2.11c, and (ii) subgrains surrounded by LAGBs, as shown in Figure 2.11b, centre panel. It is worth mentioning that subgrains themselves have a high density of dislocation cells (Figure 2.11a). Such subgrains, according to Humphreys [117], have high dislocation contents in their boundaries, which are LAGBs. Subgrains may thus play an important role in the strengthening of alloys that have undergone DRV.

When recovery processes are sluggish during high-temperature processing, DRX can occur once a critical strain and strain rate is reached [118]. Continuous dynamic recrystallization (CDRX) and discontinuous dynamic recrystallization (DDRX) are two major mechanisms of DRX. When the subgrains produced during DRV processes

Dislocation tangles/pile-ups

Subgrains containing
dislocation cells

—— LAGBs
—— HAGBs
----- Dislocation cell walls
⬭ New dislocation-free
grains

(a)

DRV

Strain
increase

$\dot{\varepsilon} > \dot{\varepsilon}_c^T$

Formation of HAGBs
by CDRX

(b)

CDRX

Strain
increase

Strain
increase

$\dot{\varepsilon} < \dot{\varepsilon}_c^T$

Actual grains with HAGBs

Formation of HAGBs by DDRX

(c)

DDRX

Strain
increase

Strain
increase

$\varepsilon > \varepsilon_c^{c/T}$
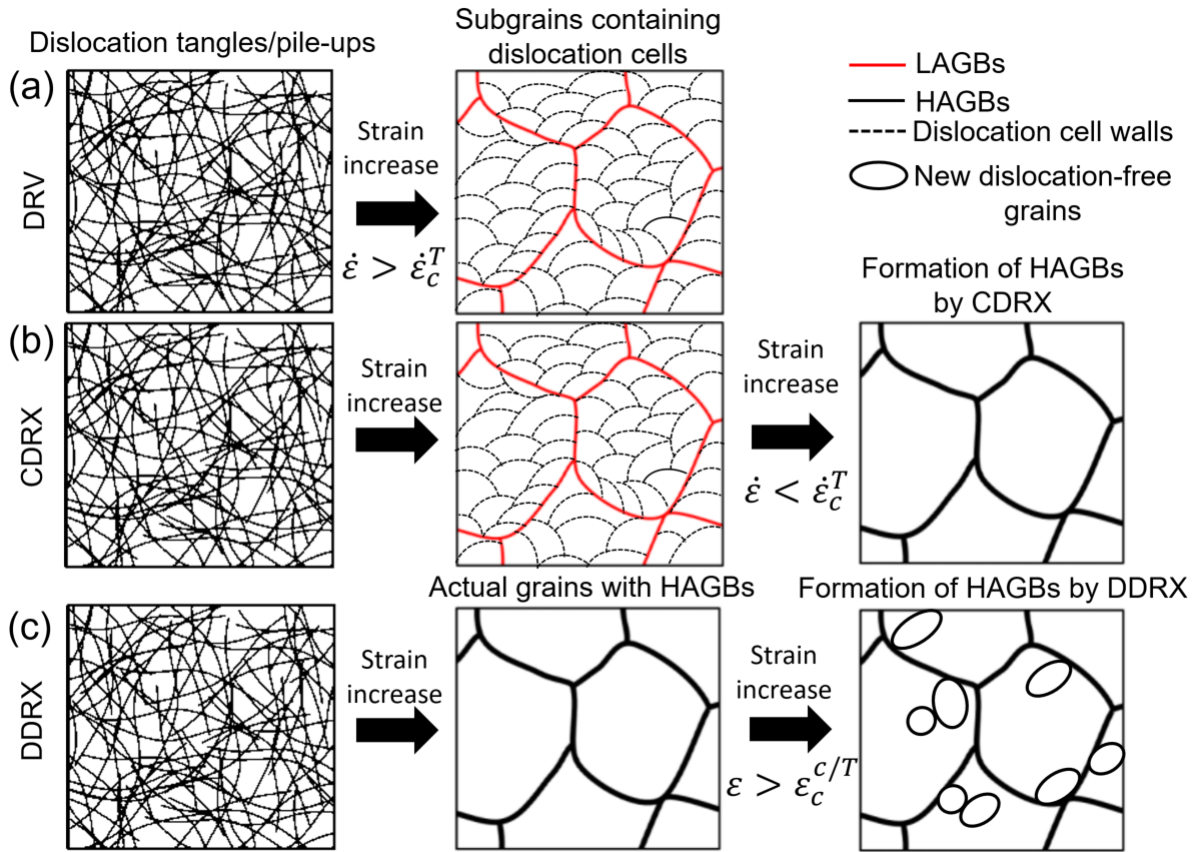
Figure 2.11: Schematic description of restoration processes. (a) DRV, (b) CDRX, and (c) DDRX. Typically, the transition DRV→CDRX→DDRX occurs as temperature is increased.

rotate and increase their misorientation angles as a result of the applied load, HAGBs form, and this mechanism is known as CDRX, as shown schematically in Figure 2.11b [119, 120]. As a result, CDRX requires DRV as a prerequisite. In fact, the consumption of LAGBs as part of the overall strain energy minimisation process has resulted in an increase in the HAGB fraction of the alloy.

In comparison to CDRX, where there is no distinction between nucleation and growth of newly formed DRX grains, new grains (with HAGBs) produced by the DDRX mechanism originate at the old deformed grain boundaries, and thus the nu-

cleation and growth stages are distinct [121]. The development of HAGBs is a crucial microstructural feature of both DDRX and CDRX mechanisms. Unlike CDRX, however, new DDRX grains form at the HAGBs of deformed grains or old DRX grains (Figure 2.11c, right panel). Therefore, the existence of DDRX does not result in the consumption of LAGBs. The accumulation of solutes at the grain boundaries affects the transition between CDRX and DDRX in an alloy. When the boundaries are heavily loaded with solute, they are unable to migrate easily, allowing CDRX to develop more than DDRX [122]. This is a critical factor in LPBF since different process parameters result in different cooling rates, which can cause solute segregation at grain boundaries. The terms DRV, CDRX, and DDRX appear regularly in the literature on wrought alloys, but they are seldom associated with LPBF alloys. One of the aims of this thesis is to demonstrate the impacts of the various restoration mechanisms on controlling the mechanical properties of LPBF alloys, as well as to provide methods to quantify these properties.

2.4.3 Modelling of restoration mechanisms

Restoration mechanisms modelling can be done using both the classical (Zener-Hollomon) and thermostatistical methods. Zener and Hollomon demonstrated that the strain rate ($\dot{\epsilon}$) and deformation temperature (T) can describe the hot deformation of steels using a parameter known as the Zener-Hollomon parameter (Z) [123]:

$$Z = \dot{\epsilon} \exp\left(\frac{Q}{RT}\right), \tag{2.5}$$

where Q is the activation energy for triggering deformation and R=8.314 J/mol is the universal gas constant. DRX is more likely to occur in low and medium Z values;

otherwise, DRV is more likely to be the main restoration mechanism. DDRX can be triggered when a critical strain is reached, according to several studies, resulting in a very fine grain microstructure [124, 122, 119, 125]. The critical strain (ϵ_c^c) for the activation of DDRX can be estimated from [126]:

$$\epsilon_c^c = BZ^a, \tag{2.6}$$

where B and a are material's dependent constants.

Another approach for modelling restoration mechanisms is provided by the thermostatistical theory, developed by Galindo-Nava and Rivera-Díaz-del-Castillo [127]; it takes into account not only process parameters such as strain rate and temperature, but also the physical properties of the material. This method is based on the dislocations' degree of freedom during deformation. As a result, the critical strain for DDRX activation based on thermostatistical theory ϵ_c^T can be calculated as follows [128]:

$$\epsilon_c^T = \frac{\frac{1}{2}\mu b^3 - \left(1 + \frac{1}{k_c}\right)T\Delta S}{\frac{1}{2}\mu b^3}, \tag{2.7}$$

where μ is the shear modulus, b is the magnitude of the Burgers vector, ΔS is the statistical entropy of dislocations and $k_c = \frac{12\pi(1-\nu)}{(2+\nu)}\left(1 + \frac{T\Delta S}{\mu b^3}\right)$ [128], where ν=0.3 is the Poisson's ratio. The dislocation statistical entropy can be calculated via:

$$\Delta S = k_B \ln\left(\frac{\dot{\epsilon}_0 + \vartheta}{\dot{\epsilon}}\right), \tag{2.8}$$

where k_B=1.38×10^{-23} J/K is the Boltzmann constant, $\dot{\epsilon}_0 = cb\rho_Y$ is a limiting strain rate related to the speed of sound c, and ρ_Y is the dislocation density at the yield point

$(\rho_Y = \left(0.9\sigma_Y/\mu b\right)^2)$, where σ_Y is the material's yield strength [128]); $\vartheta = 10^{13} \exp\left(-\frac{E_m}{RT}\right)$ is the frequency of atomic jump of vacancies and E_m is the vacancy migration energy.

The activation of CDRX and DRV through the critical processing strain rate $(\dot{\epsilon_c}^T)$ can also be predicted by the thermostatistical theory [127]:

$$\dot{\epsilon}_c^T = (\dot{\epsilon}_0 + \vartheta) \exp\left(-\frac{\frac{\lambda}{2}\mu b^3 - \frac{2xl^*}{bk_c}\Delta G_{sys}}{k_B T}\right), \tag{2.9}$$

where λ=0.6 [127] is a length scaling constant, x is the solute concentration in molar fraction $(0 \leq x < 0.5)$, $l^* = 12.5b$ is the dislocations' distortion length, which accounts for 98% of the total strain field induced by dislocations and ΔG_{sys} is the Gibbs free energy of the alloy, representing the energy barrier accounting for the possible atomic arrangements in the lattice. ΔG_{sys} expressions for various alloy grades can be found in [127]. If $\dot{\epsilon} < \dot{\epsilon}_c^T$, then CDRX takes palce. Otherwise, DRV is the main restoration process [127].

2.5 Mechanical properties of additively manufactured alloys

To tailor mechanical properties in engineering alloys, a fundamental understanding of the process-structure-property relationships is needed. Many attempts have been made to explain the exceptional mechanical properties of LPBF alloys, but changes in process parameters or chemical composition of the powder have an effect on the mechanical properties including yield strength [129, 130, 69, 131, 17, 132]. Many researchers have used the energy density concept to try to link the yield strength of LPBF alloys to the heat input, but there is no clear correlation [49, 37]. However,

the heat input can play a significant role in determining the yield strength via dislocation multiplication and annihilation processes since the material undergoes several thermal cycles during LPBF. Dislocation climb and cross-slip commonly occur in alloys such as 316L SS. At high temperatures, DRV and cell formation occur, resulting in microstructural restoration [133]. When a critical strain is reached in alloys with slow recovery rate, such as IN718, DRX may occur, with new grains originating at old grain boundaries; however, for longer deformation times, further strain causes an increase in dislocation density of certain grains [134]. The initial dislocation density of the parent phase at high temperatures determines the strength of alloys prone to martensitic transformation such as Ti-6Al-4V during LPBF [135]. Depending on the heat input, each of the hot deformation (thermo-mechanical processing) mechanisms introduced in the previous sections can be triggered during LPBF, which affect mechanical properties of the as-built parts significantly.

Electron backscatter diffraction (EBSD) micrographs of a LPBF as-built 316L SS [17] are shown in Figures 2.12a-c. The occurrence of DRV during LPBF of 316L SS can be supported by orientation gradients inside the grains in the inverse pole figure (IPF) map (Figure 2.12a), the evolution of LAGBs inside the grains (Figure 2.12b), and the fact that the dislocation density is very high, particularly in coarse grains (kernel average misorientation (KAM) map shown in Figure 2.12c). Furthermore, the activation of DRX may be linked to the evolution of very fine grains with HAGBs, though this mechanisms is less prevalent in 316L SS than DRV. However, the occurrence of DRV and DRX has not been confirmed in that original research [17].

The yield strength of Ti-6Al-4V can be determined by restoration mechanisms

that govern the thickness and fraction of the martensite laths. Figure 2.12d shows a fine martensitic microstructure that has been processed by LPBF.

Figure 2.12e shows the IPF map of the LPBF as-built IN718 reported in [19], which supports the existence of very fine grains, which can be attributed to DRX activation, although this also has not been confirmed.
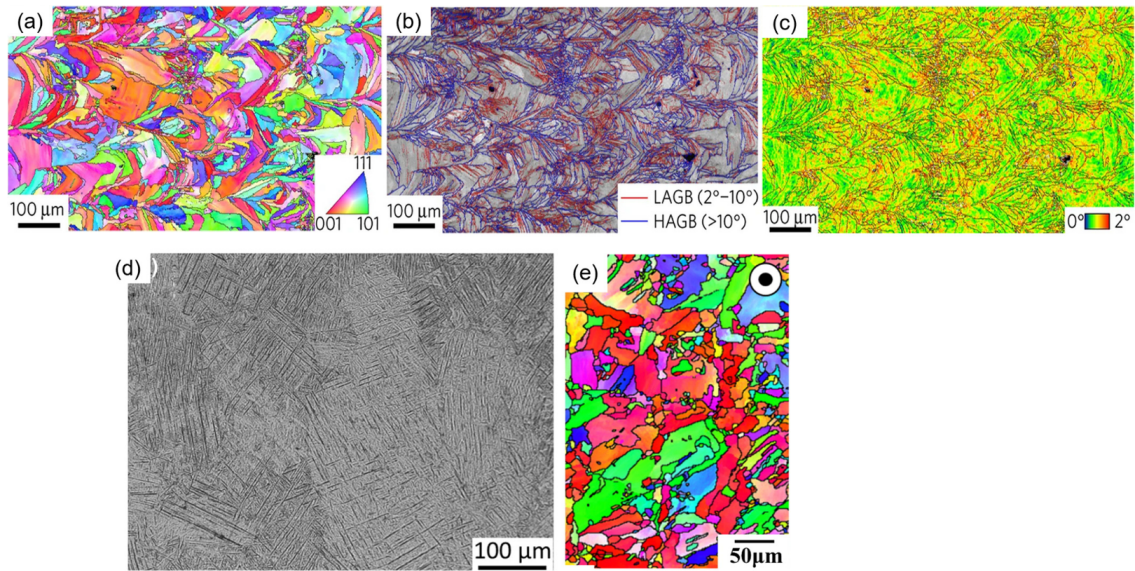
Figure 2.12: (a) Inverse pole figure, (b) grain boundary and (c) kernel average misorientation maps for the as-built 316L SS adopted from [17]. (d) Optical micrograph showing fine martensite laths in an LPBF Ti-6Al-4V. Adapted from [18] (e) Inverse pole figure map showing very fine grains that can be the result of activation of DRX during LPBF of IN718. Adapted from [19].

To evaluate the process-microstructure-property relationships in LPBF, the weighted contribution of the dense cellular structure (mentioned as one of the most important microstructural features of LPBF alloys, Figure 2.9) and the restoration mechanisms is needed.

The Hall-Petch effect is a primary strengthening mechanism in wrought components [136]. It takes into account the effects of HAGBs as effective dislocation barriers.

A dislocation hardening concept based on a Taylor relationship is added to the Hall-Petch contribution for alloys that experience significant deformations such as severe plastic deformation [137]. The same has been used to model the yield strength of LPBF processed alloys [138, 139, 140, 141], but these approaches are not appropriate for process parameter optimisation because adjusting the LPBF process parameters makes it difficult to control both grain size and dislocation density. As opposed to wrought products, where only equiaxed grains are present in their microstructure, LPBF components may contain two possible grain morphologies: equiaxed and columnar [142]. Therefore, to model grain boundary engineering, Jia *et al.* [143] proposed a modified Hall-Petch relationship that takes into account the combined effects of equiaxed and columnar grains. Yanushkevich *et al.* [144] suggested a modified comprehensive Hall-Petch-type relationship for wrought products that included both the effects of actual grains and contributions from dislocation substructures. Since it only depends on the grain size as a variable, which can be controlled via DRX and DRV during processing, this approach is suitable for alloy design and process parameter optimisation. In LPBF alloys, however, there is no sufficient data to model the relationships among dislocation cell size, grain size, and dislocation density. Complex microstructural transitions occur during LPBF, resulting in a significant fraction of grains with LAGBs. As compared to conventional substructured grains from wrought products, these substructures have a higher dislocation density [145, 146]. To explain and quantify the role of LAGBs and HAGBs in LPBF alloy strengthening, a grain boundary engineering approach is needed. In this thesis, a unified Hall-Petch-type relationship, which is based on grain boundary engineering, will be presented for LPBF 316L SS as a representative of a single-phase alloy without phase transformations

during LPBF.

Processes such as cold working, annealing, and severe plastic deformation are well known for improving the strength of wrought alloys while degrading ductility [147, 148]. AM alloys made with LPBF, such as 316L austenitic SS, have promising mechanical properties with a good balance of strength and ductility [146, 11]. The existence of LAGBs, dislocation decorated cellular structures, and the production of twins during deformation are reported to be the major contributors in LPBFed 316L SS maintaining a good balance of strength and ductility [17, 149].

Activation of DRX has been reported during tensile testing of LPBFed 316L SS at room temperature, in addition to dislocation slip and twinning induced plasticity (TWIP) effects [150]. The activation of DRX during deformation is thought to be caused by the existence of a high dislocation density in the as-built samples microstructure [150]. Although previous reports on strain hardening mechanisms of LPBFed SSs are quite useful, there is a lack of approaches to model the room temperature plastic deformation phenomena. This thesis aims to shed light on phenomena such as dislocation hardening, TWIP effect and DRX during deformation of LPBFed 316L SS, providing quantitative tools for their description.

2.6   Summary

A systematic work to create methodologies to design novel alloy compositions, as well as to optimise microstructure, and subsequent mechanical properties for AM alloys has never been attempted. In general, AMed metals and alloys have superior mechanical properties compared with their wrought counterparts, but no reports quantitatively link the unique microstructural features of AMed alloys with mechanical

properties such as yield strength. Compared to wrought products, AM components possess distinct features such as a high dislocation density, a distinct texture with desired contents of dislocation cells and low-angle grain boundaries, a fine regular grain structure, an undesired porosity, voids and micro-cracks, and residual stress. The key hypothesis of this work is to control those features through modelling to design novel alloys minimising defects, as well as maximising strength.

This thesis aim is to model, design and produce printable (AM components without processing defects) alloys, with a focus on the most common group of alloys available for AM: austenitic stainless steels. The key objectives are:

  i Integrate modelling approaches to predict the condition under which cracks and defects such as keyhole-induced pores and lack of fusion can form during LPBF AM.

  ii Determine key processing parameters to produce components free of cracks and porosity.

  iii Develop an integrated approach for combining printability and properties modelling.

  iv Verify modelling approaches through experiments.

  v Quantitatively describe the microstructural evolution phenomena during LPBF.

  vi Link the microstructure and process parameters to mechanical properties of LPBF alloys.

  vii Develop a unified approach to estimate yield strength of LPBFed alloys.

  viii Understand the deformation behaviour of LPBFed alloys.

Chapter 3

Controlling crack and porosity formation during laser powder bed fusion

In this chapter, a computational approach is proposed for designing alloys with lower susceptibility to solidification cracking while preventing the formation of porosity and defects during LPBF is proposed. The method was validated for austenitic stainless steels, which have a wealth of data available due to numerous crack and pore/defect formation conditions that have been published. The model is based on an alloy design methodology that combines thermodynamic calculations with a genetic algorithm to discover novel austenitic stainless steel compositions; the new alloys are expected to be crack-free while displaying increased strength. To link composition to solidification cracking formation, a new crack prevention factor is proposed. The solidification temperature range, the performance index (ratio between yield stress and coefficient of thermal expansion), and the solidification path are all quantified in this factor. Over-

all, literature results on 316L austenitic SS validates the design methodology. While 316L SS usually does not crack during LPBF, it is an excellent choice for demonstrating the conditions under which cracks develop. This methodology has also been applied to two other steel families that are more susceptible to solidification cracking during LPBF: 17-4 precipitation hardening (PH) stainless steel and a maraging steel called Formetrix, and optimised alloys are found. In terms of preventing porosity and defects, it is demonstrated that this can be accomplished by supplying enough energy to melt the powder bed and regulating the melt pool geometry; such parameters differ from those stated in the literature review section. Based on the proposed criteria, process maps have been created to show the effects of process parameters on the formation of pores and defects. The model is used to optimise certain parameters in order to manufacture 316L austenitic SS, and it is demonstrated that a defect-free LPBF SS can be produced, which mechanical performance is superior than its wrought counterparts during tensile testing.

3.1 Alloy design methodology for crack prevention in austenitic stainless steels

First, the microstructural and mechanical requirements for austenitic SSs are addressed, as well as their relationship to alloy composition. Then, the same methodology is applied to two other types of steel, using additional criteria to optimise the microstructure as well.

Due to high residual stresses generated during LPBF, an inadequate amount of liquid in the melt pool filling the interdendritic regions of the solidifying metals can

cause solidification cracking. Following are three criteria for reducing the incidence of solidification cracks during LPBF.

3.1.1 Solidification temperature range

Via equation 3.1, the cumulative thermal strain (ϵ_T) of a solidifying alloy during LPBF can be related to the coefficient of thermal expansion (α_{CTE}) and solidification temperature range (STR) of the alloy [151]:

$$\epsilon_T = \alpha_{CTE}(T_L - T_S), \tag{3.1}$$

where T_L and T_S are liquidus and solidus temperatures for the corresponding composition, respectively. Therefore, the solidification cracking susceptibility can be directly related to the STR, which can be defined as $T_L - T_S$. The STR for a given alloy can be affected by even small changes in the chemical composition. During solidification, at low temperatures, a thin layer of solute-rich liquid persists because low melting point constituents are rejected by solidifying dendrites. A crack forms when this can no longer withstand the shrinkage strain (ϵ_T) [152]. The STR can be increased by adding certain elements such as S, P, and Si, which increase the probability of solidification cracking [153, 154, 26]. However, due to complex thermodynamic interactions of various alloying elements, there is no clear relationship between adding or eliminating certain elements to control the STR. To reduce solidification cracking susceptibility during LPBF, STR must be minimised.

3.1.2 Performance index

In addition to STR, the LPBF's unique features will also influence the alloy cracking behaviour. LPBF as-built components are exposed to high thermal stresses due to the layer-by-layer nature of the process, which imposes extreme temperature fluctuations from the melting area to the far-field powder bed temperature (examples of temperature time-profiles of LPBF are presented in Figure 2.10). Thermal stress contraction causes plastic deformation and the generation of residual stresses, which can result in microcracks in the as-built component [155]. Equation 3.2 can be used to calculate the thermal stresses (σ_t) produced during LPBF [156]:

$$\sigma_t = \left[\frac{E\alpha_{CTE}}{2(1-\nu)}\right]\Delta T, \tag{3.2}$$

where E is the Young's modulus, ΔT is the temperature difference between the melt pool (working temperature) and the powder bed, and ν is the Poisson's ratio. As the proposed model in this work is aimed at alloy design through composition tailoring, it should be considered that the Young's modulus varies moderately in response to changes in alloy composition. In comparison, α_{CTE} has a much larger dependency on compositional changes when thermal stress is generated during LPBF. As a result, alloys with lower α_{CTE} produce less thermal stress. Alloys with higher yield strength (σ_Y)at high temperatures, on the other hand, perform better under rapid cooling and heating conditions. As a result, the ability of different alloys to withstand cracking is represented by the performance index (PI); thus, maximising PI is the second criterion for LPBF alloy design:

$$PI = \frac{\sigma_Y}{\alpha_{CTE}}. \tag{3.3}$$

3.1.3 Solidification path

Solidification path is the third factor that must be optimised to design alloys against solidification cracking. Austenitic SSs can have different solidification paths depending on the alloy composition. The primary phase produced from the eutectic reaction, which is the transformation of liquid phase into austenite and δ-ferrite ($L \rightarrow \gamma + \delta$) is primarily dependent on the chromium and nickel equivalent content ratio. The ratio of chromium and nickel equivalent, Cr_{eq} and Ni_{eq}, respectively is used as a solidification path criterion in multicomponent systems. Although there are several relationships, Hull has presented the most comprehensive expressions for Cr_{eq} and Ni_{eq} [157]:

$$Cr_{eq} = W_{Cr} + 1.21W_{Mo} + 0.48W_{Si} + 0.14W_{Nb} + 2.2W_{Ti} + 0.72W_W + 0.21W_{Ta}$$
$$+ 2.27W_V + 2.48W_{Al} \tag{3.4}$$

$$Ni_{eq} = W_{Ni} + 0.11W_{Mn} + 24.5W_C + 18.4W_N + 0.44W_{Cu} + 0.41W_{Co} \tag{3.5}$$

where W_i, with i =Cr, Mo, Si, W, Nb, ... is the $wt.\%$ of element i. Based on the subsequent solid-state transformations, there are four solidification paths in austenitic SSs (Figure 3.1) [153]:

(i) Austenitic (A) ($L \rightarrow L + \gamma \rightarrow \gamma$)

(ii) Austenitic-ferritic or primary austenitic (AF) ($L \rightarrow L + \gamma \rightarrow L + \delta + \gamma \rightarrow \gamma + \delta$)
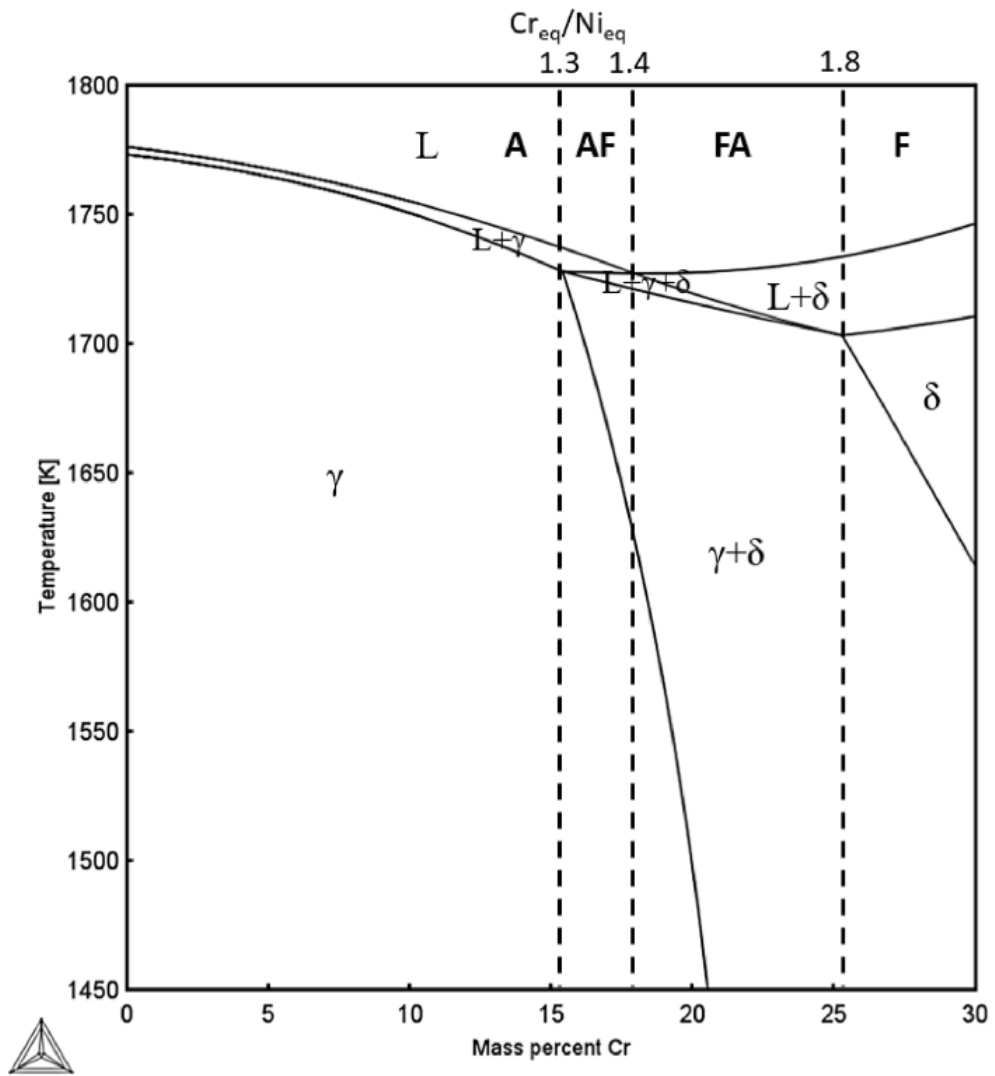
Figure 3.1: The pseudobinary part of the Fe-Cr-Ni ternary phase diagram at 70 wt.% iron shows various solidification paths (A, AF, FA, and F) based on the related Cr_{eq}/Ni_{eq} values.

(iii) Ferritic-austenitic or primary ferritic (FA) ($L \rightarrow L + \delta \rightarrow L + \delta + \gamma \rightarrow \gamma + \delta$)

(iv) Ferritic (F) ($L \rightarrow L + \delta \rightarrow \delta \rightarrow \delta + \gamma$)

Cr_{eq}/Ni_{eq} has been commonly used to predict which path dominates during solidification since it determines the stability of δ-ferrite and austenite (γ) during solidification. Although LPBF kinetics do not obey equilibrium conditions, Figure 3.1 can be used to estimate a threshold for the presence of δ-ferrite during solidification. Even small amounts of δ-ferrite in the austenitic matrix are known to mitigate the negative effects of impurity elements such as Si, P, and S, which have a higher solubility in δ-ferrite than in austenite (Table 3.1), resulting in less segregation to grain boundaries once solidification is completed [158].

Table 3.1: Partition coefficient of the most important impurity elements in austenite and δ-ferrite [26].

Impurity element	Partition coefficient in γ	Partition coefficient in δ
Sulphur	0.035	0.091
Phosphorus	0.13	0.23
Silicon	0.52	0.77

Furthermore, since δ-ferrite pins the austenite grain boundaries, cracking paths are more complicated than in fully austenitic microstructures [159]. During solidification, a two-phase solidification front of δ-ferrite/austenite effectively improves the interphase interfaces between austenite and ferrite while reducing the area of austenite/austenite and ferrite/ferrite grain boundaries. Since austenite and ferrite have different crystal structures, liquid does not easily wet phase boundaries between them, as it wets grain boundaries between two identical lattices such as austenite/austenite boundaries. As a result, crack propagation in a ferritic-austenitic-solidifying material is more difficult than in an austenitic-solidifying material [26]. Therefore, the third criterion for alloy design against cracking is based on the presence of δ-ferrite during

solidification.

Path A of solidification (austenitic) is activated when $Cr_{eq}/Ni_{eq} < 1.3$. The existence of δ-ferrite during solidification is guaranteed when $Cr_{eq}/Ni_{eq} > 1.3$ [160]. Since LPBF's rapid cooling rates increase the stability of austenite during solidification [161], there is no upper limit for Cr_{eq}/Ni_{eq} in the alloy design methodology. As a result, $Cr_{eq}/Ni_{eq} > 1.3$ is the third criterion for alloy design.

3.1.4 Computational tools

As summarised in section 2.3.4, a combination of optimisation tools, as well as thermodynamic calculations can be used to find new alloys satisfying the defined requirements for certain applications. In this thesis, ThermoCalc software was used in conjunction with the TCFE9 database, which was accessed using TC Matlab toolbox. To restrict the composition of alloys and keep their constitution within design requirements, the optimisation algorithm used ThermoCalc data as input. To optimise compositions, a multiobjective GA was used.

The fitness scores are made up of STR and PI. Compositions of printed 316L austenitic SSs reported in the literature are specified in Table 3.2 to find metrics for these scores to be used as constraints for the alloy design approach. This methodology will also be applied on other steel families that are more vulnerable to crack formation during LPBF in the next sections. As shown in Figure 3.2, the first three alloys in Table 3.2 (shown in bold) have microcracks in their as-built states. The majority, on the other hand, have been successfully printed by changing the chemical composition by trial and error. The lowest STR measured from the presented data in Table 3.2 is 32 K, and the highest PI measured in 1.46×10^6 MPa·K. Therefore, (1) STR (measured

by ThermoCalc) should be less than 32 K; (2) PI (equation 3.3) should be greater than 1.46×10^6 MPa·K; and (3) Cr_{eq}/Ni_{eq} (equations 3.4 and 3.5) should be greater than 1.3 for each candidate solution. These criteria have been defined as go/no-go. Figure 3.3 depicts the methodology algorithm for designing 316L SS compositions against cracking during LPBF based on these criteria. It should be noted that instead of using equations 3.4 and 3.5 for Cr_{eq}/Ni_{eq} measurements, ThermoCalc databases can be used to estimate the existence of δ-ferrite. However, this results in a much longer calculation time; the current algorithm requires more than three days to complete the optimisation (An Intel(R) Xeon(R) CPU E3-1240 v6 at 3.70 GHz with a 32 GB RAM was used for optimisation).

Table 3.2: Chemical compositions of 316L SS in wt.%, produced by LPBF. The units of STR and PI are K and MPa·K, respectively. Fe valuse are balanced. F is the crack prevention factor.

Cr	Ni	Mn	Mo	C	N	Si	P	S	STR	$PI\times10^6$	Cr_{eq}/Ni_{eq}	F	Ref.
16.17	**12.57**	**0.23**	**2.33**	**0.09**	**-**	**0.6**	**0.014**	**0.014**	**50**	**1.32**	**1.28**	**1.53**	**[20]**
17	**12**	**2**	**2.5**	**0.03**	**0.1**	**1**	**0.045**	**0.03**	**60**	**1.45**	**1.51**	**1.58**	**[21]**
17.26	**11.48**	**1.41**	**2.32**	**0.01**	**-**	**0.71**	**0.01**	**0.01**	**39**	**1.19**	**1.68**	**1.54**	**[22]**
17.34	10.74	1.14	2.28	0.01	0.1	0.63	0.026	0.014	43	1.36	1.57	1.63	[162]
17.5	11.5	2	2.25	0.03	0.11	1	0.045	0.03	57	1.45	1.54	1.6	[163]
17.42	12.53	0.6	2.36	0.02	0.06	0.51	0.01	0.01	32	1.36	1.45	1.82	[164]
17	12	1	2.5	0.01	0.05	0.5	0.023	0.01	38	1.35	1.51	1.69	[165]
17.75	12.75	1.5	2.4	0.02	-	-	0.01	0.001	33	1.24	1.49	1.7	[166]
16.7	11.9	0.6	2.5	0.02	-	0.6	0.01	0.02	33	1.22	1.61	1.69	[167]
16.7	10.3	0.99	2.2	0.01	-	0.69	0.02	0.05	37	1.12	1.85	1.53	[168]
17.9	12.8	1.15	2.35	0.01	0.09	0.66	0.01	0.004	33	1.42	1.4	1.82	[169]
17.5	11.2	2.2	2.3	0.03	-	-	0.05	0.03	61	1.22	1.67	1.37	[170]
16.3	10.3	1.31	2.09	0.02	-	0.49	0.026	0.006	44	1.14	1.72	1.44	[171]
18.43	12.2	1.86	2.46	0.02	-	0.75	0.032	0.01	54	1.26	1.69	1.44	[172]

The yield strength and coefficient of thermal expansion for each candidate alloy must be determined before PI can be calculated. σ_Y can be written as:

$$\sigma_Y = \sigma_{gb} + \sigma_{pr} + \sigma_d + \sigma_{ss}, \tag{3.6}$$
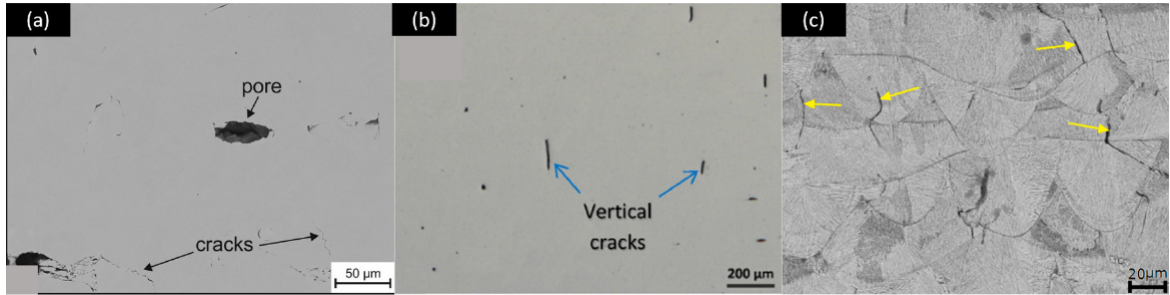
Figure 3.2: Microstructures of the 316L SS samples that were cracked during LPBF. Reproduced from (a) [20], (b) [21], and (c) [22].
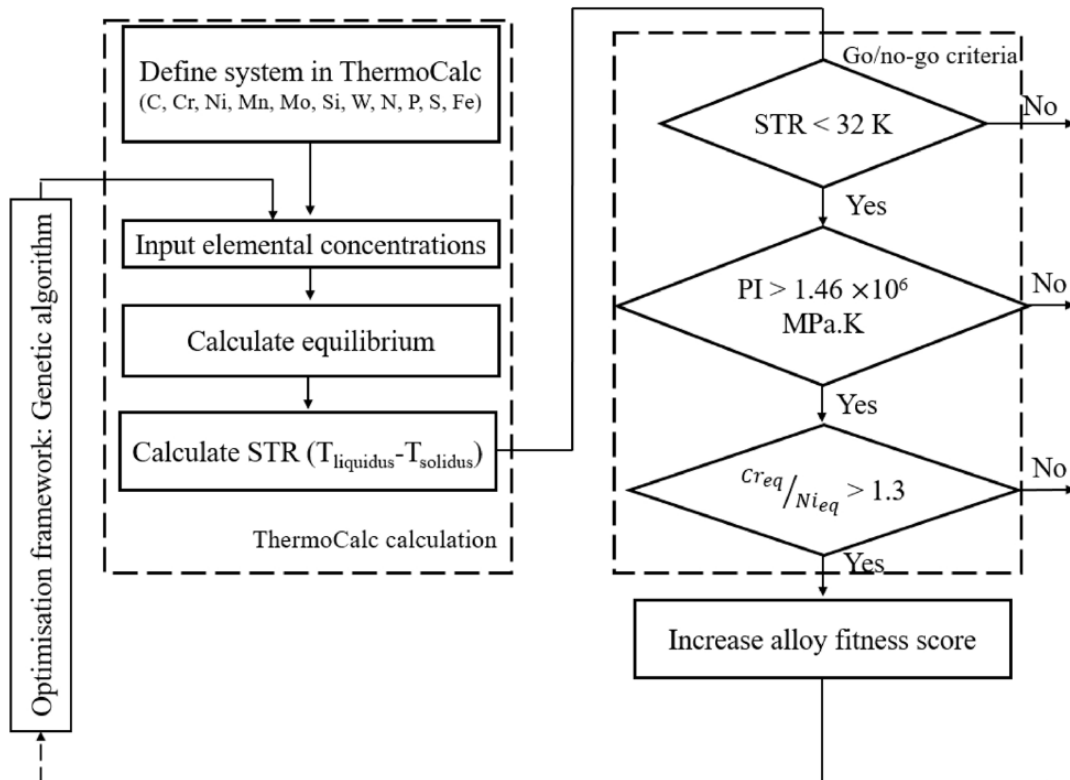
Figure 3.3: Algorithm combining thermodynamic calculations and optimisation method for designing crack-free 316L SS for LPBF.

where σ_{gb} is the grain boundary strengthening (Hall-Petch relationship [173]), σ_{pr} is the precipitation strengthening, σ_d is the dislocation strengthening (Taylor relationship), and σ_{ss} is the solid solution strengthening. The most important term for alloy design in the absence of precipitates and for coarse grain sizes upon solidification and similar processing parameters, which yield similar dislocation densities is σ_{ss}, which can be expressed as [27]:

$$\sigma_{ss} = \left[\sum_i (k_{ss,i}^{\frac{3}{2}} c_i) \right]^{\frac{2}{3}}, \tag{3.7}$$

where $k_{ss,i}$ is the coefficient of solid solution hardening for element i and c_i is the concentration of each element in the matrix in at.%. k_{ss} of different elements in austenitic matrix are listed in Table 3.3. The α_{CTE} of an alloy can be measured using the rule of mixtures [174]. Table 3.3 also includes α_{CTE} values for various elements near their melting points.

Table 3.3: Coefficients of solid solution strengthening for different elements (i) in austenitic matrix [27] and their thermal expansion coefficient near their melting points [28].

i	Cr	Ni	Mo	Mn	Cu	W	C	N	Si	Nb	Fe
k_{ss}[MPa.at%$^{-3/2}$]	101.71	112	637	101	600	826	1984	1984	200	1106	-
α_{CTE} [10^{-6}·K^{-1}]	19	20.3	16.5	-	25.8	11.6	-	-	3.8	10.1	23.3

To design new 316L SS-type alloys, the alloy design framework consists of ten alloying elements: C, Cr, Ni, Mn, Mo, Si, W, N, P, and S, with the quantities of P and S being set (because these are the most important impurity elements). Table 3.4 shows the concentration ranges used in the optimisation procedure for each element in wt.%. The model uses the optimisation criteria provided in this chapter to search the entire composition ranges in Table 3.4.

Table 3.4: Concentration ranges of all alloying elements employed in the optimisation (wt.%).

	Cr	Ni	Mo	W	C	N	Si	Mn	P	S
Min	12	8	0.3	0	0.01	0	0.1	0.2	0.03	0.001
Max	21	13	2.5	1	0.03	0.11	0.5	2.2	0.03	0.001

3.1.5 Crack prevention factor

A crack prevention factor (F) proposed for the alloys mentioned from literature and shown in Table 3.2 based on the factors influencing solidification cracking in austenitic SSs:

$$F = \sqrt{1500(STR^{-1})^2 + PI^2}. \tag{3.8}$$

This is based on a Pythagorean relationship between the PI and the reciprocal of the STR (lower STRs are better). This relationship has been proposed to match literature data (Table 3.2) and include a rule of the thumb approach for alloy selection for printability. The derived coefficients used in equation (3.8) are the results of fitting to the experimental results. Maximising the crack prevention factor, based on equation (3.8), would result in a material that is more resistant to crack formation. The experimental findings on LPBF of 316L SS (Table 3.2) indicate a crack susceptibility resistance threshold of F=1.6. LPBF produced austenitic SSs with $F > 1.6$ are crack-free. The solidification path, on the other hand, plays an important role in crack resistance as well. Alloys with an F less than 1.6 but a Cr_{eq}/Ni_{eq} greater than 1.69 avoid crack formation during LPBF. As a result, Figure 3.4 shows a process map for F and Cr_{eq}/Ni_{eq} based on literature data (Table 3.2). Figure 3.4 shows that the alloy that will be used in this project has the optimised crack prevention factor and

Cr_{eq}/Ni_{eq}.
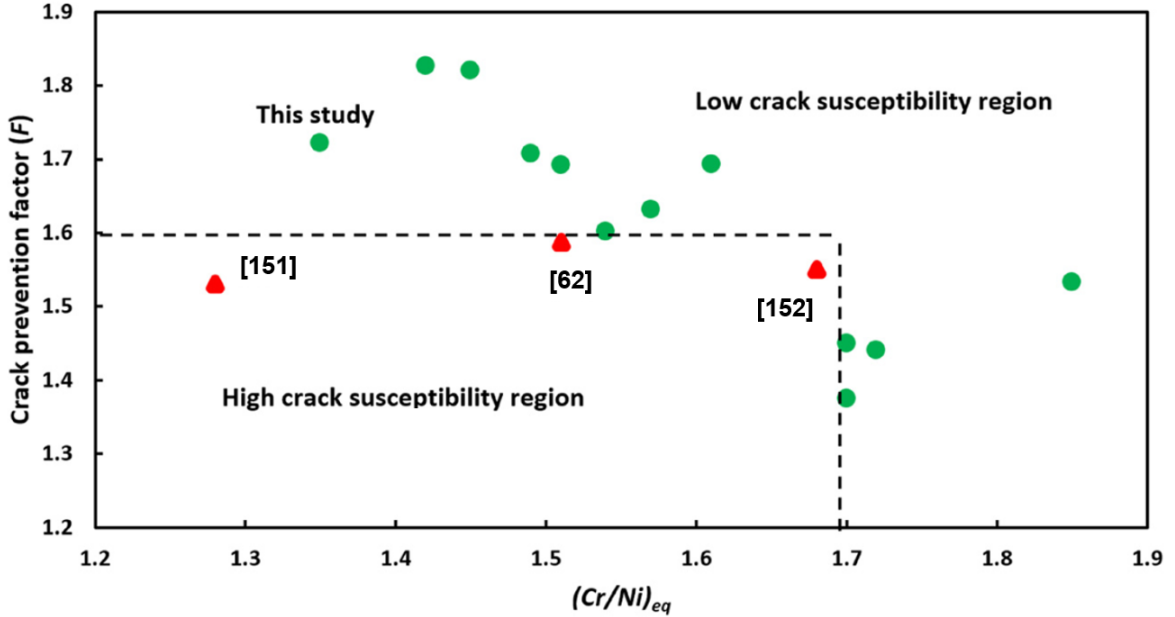
Figure 3.4: Process map for LPBF austenitic SSs shows the safe area from solidification cracks. The alloy that will be used in this thesis is also shown. The red triangles represent solidification cracking during LPBF, while the green circles represent no-crack alloys; references are mentioned in Table 3.2.

To sum up, the criteria that are proposed for the first time to avoid microcrack formation during LPBF of austenitic SSs are presented in Table 3.5.

Table 3.5: Summary of microcrack prevention criteria proposed in this thesis for LPBF of austenitic SSs.

Phenomenon	Criteria	Notes
Microcracks	STR minimisation	To reduce formation of low melting point eutectics
	PI maximisation	For thermal shock resistance
	Presence of δ-ferrite during solidification	Alleviating detrimental effects of impurity elements

3.2 Model for defects and porosity prevention

3.2.1 Keyhole-induced pores

A high laser energy input on a small volume causes keyholes, which result in the creation of a narrow and deep melt pool. As mentioned in section 2.2, melt pool geometry optimisation plays a key role in controlling keyhole-induced pore formation. $W/D_m > 2$ is the keyhole-induced pore prevention criterion considering the melt pool geometry that is used in our work.

Furthermore, the amount of energy used to melt the powder should be optimised: low energies result in lack of fusion, while high energies result in keyhole-induced pore formation. Adopting the normalised enthalpy (H_n, equation 2.4) concept, introduced by King *et al.* [4], is one way to take into account of both LPBF process parameters and material properties to optimise the energy input. When using the normalised enthalpy concept for 316L-type of SSs to prevent keyhole-induced pore formation, the following conditions must be met:

$$H_n \leq \frac{\pi T_b}{T_m} = 5.5 \qquad (3.9)$$

where T_b is the boiling temperature and T_m is the melting temperature of the alloy.

3.2.2 Lack of fusion

Insufficient melting between two neighbouring layers, both in the width and height directions, is the definition of lack of fusion. To prevent lack of fusion based on melt pool geometry, two conditions have been suggested by Johnson *et al.* [8]: (1) $D_m/t > 1.5$ and (2) $h/W < 1$. The width of the melt pool can be calculated using the

55

following equation [175] to predict the maximum hatch distance for LPBF process:

$$W = \sqrt{\frac{8}{\pi \cdot e} \frac{AP}{\rho_b C_p v (T_m - T_0)}}$$ (3.10)

where, ρ_b is the density, C_p is the heat capacity, and T_0 is the powder bed temperature. To avoid keyhole-induced pore formation, the maximum depth of the melt pool must not exceed half of the melt pool width, as mentioned in section 3.2.1. As a result, based on the first criterion for lack of fusion, the maximum layer thickness of LPBF can also be estimated.

3.2.3 Balling

Creation of non-stabilities in the melt pool as a result of the incidence of laser with the powder bed may cause balling. Both low and high laser energies are thought to cause balling defects. They can cause formation of discontinuous scan lines, which will have a major impact on overlapping of the melt pools. $L/W < 2.3$ is the melt pool geometry criterion for preventing balling [8]. Rubenchik *et al.* [176] proposed a numerical equation for predicting melt pool length. The length of the melt pool is determined by the laser spot size and to dimensionless parameters (a and b^*) that depend on the material properties. The dimensionless parameter a depends on the thermal diffusivity, laser scan speed, and laser spot size:

$$a = \sqrt{\frac{d}{v\sigma}}.$$ (3.11)

If $a < 1$, the thermal diffusion length (D/v) is smaller than the beam size during the laser dwell time. Therefore, the melt pool is shallow and long. This is char-

Table 3.6: Summary of the defects and pores appearing during LPBF and the criteria proposed in this study for avoiding them. The references and how this the criteria modified to be used in this study are also provided.

Phenomenon	Criteria	Ref.	Notes
Lack of fusion	$D_m/t > 1.5$	[177]	A ratio of 1.1 has been suggested by Mukherjee *et al.*
	$h/W < 1$	[69]	Tang *et al.* claimed the criteria for lack of fusion prevention is $(h/W)^2 + (t/D)^2 \leq 1$
Keyhole-induced pores	$W/D_m > 2$	[8]	Johnson *et al.* suggested a ratio of 1.5 rather than 2
	$\Delta H/h_s < 5.5$	[4]	King *et al.* suggested a threshold of 30 rather than 5.5
Balling	$L/W < 2.3$	[178]	-

acteristic of low thermal conductivity materials such as SSs. b^* is a fraction of the normalised enthalpy for these materials:

$$b^* = \frac{H_n}{2^{3/4}\pi}. \tag{3.12}$$

Finally, the melt pool length can be estimated via [176]:

$$L = \frac{\sigma}{a^2}\left[0.0053 - 0.21a + 1.3a^2 + (-0.11 - 0.17b^*)a^2 \ln a + b^*(-0.0062 + 0.23a + 0.075a^2)\right]. \tag{3.13}$$

To summarise, Table 3.6 lists the defects mentioned above, as well as the methods for preventing them. All the criteria have been modified compared to their original form that have been used previously in the literature, with the exception of balling prevention criterion, which is the same as stated in the literature. The criteria stated in the literature for lack of fusion have been simplified to two distinct criteria. The proper use to the normalised enthalpy and the right threshold of it have been provided here for keyhole-induced pore prevention.

3.3 Application of the alloy design and defect prevention methodology to 316L stainless steel

3.3.1 Experimental procedure

The material used for model validation is 316L SS. Carpenter Additive supplied the pre-alloyed powder, which was made by gas atomisation. Table 3.7 shows the chemical composition of the powder (in wt.%) used for LPBF. For this alloy, the STR, PI and Cr_{eq}/Ni_{eq} are 44 K, 1.48×10^6 MPa·K, and 1.35, respectively. Despite its STR, which is higher than the criterion imposed in alloy design approach, this commercial alloy stands well in the safe region from cracking (shown as 'this study' in Figure 3.4), based on the crack prevention factor concept. Therefore, this alloy has been chosen to validate the presented methodology. The as-received powder has mainly a spherical morphology with some satellites, as shown in Figure 3.5. The particles size distribution is in the range of 15-45 μm with an average particle size of 38 μm.

Table 3.7: Chemical composition of the powder used in the present investigation in wt.%.

Fe	Cr	Ni	Mo	Mn	Si	P	S	N	C	Cu
Bal.	17.75	12.75	2.38	2	0.75	0.025	0.01	0.1	0.03	0.5

Table 3.8 shows the physical properties (at melting temperature) of the alloy used in this analysis, which were measured using ThermoCalc software and the TCFE9 database for steels and Fe alloys [92].

A Renishaw plc (UK) AM125 LPBF system (in The University of Nottingham) with a laser spot size of 35 μm was used to fabricate samples with a tensile testing specimen shape with the dimensions shown in Figure 3.6. To reduce the scan vector
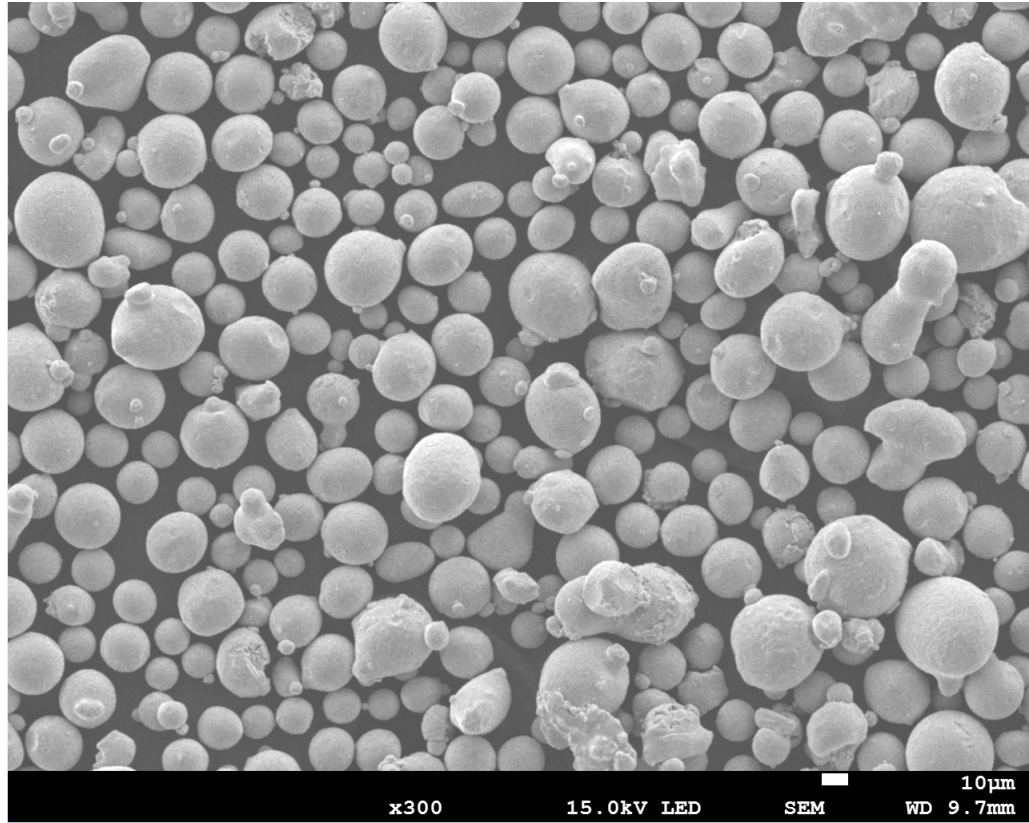
Figure 3.5: SEM micrograph showing 316L SS powder used as feedstock for LPBF in this study.

Table 3.8: Material properties used in the physical model for porosity prevention in 316L SS. All the thermophysical properties have been calculated using ThermoCalc at liquidus temperature.

Material properties	Value at liquidus temperature
A	0.36
h_s (J/m^3)	7.764×10^9
d (m^2/s)	6.052×10^{-6}
T_b (K)	2885
T_m (K)	1647
ρ_b (kg/m^3)	6922
C_p (J/kg·K)	663.614

length and application of supports, all of the samples were aligned at a 5° angle over the substrate (ISO/ASTM 52921 standard [179]). A 200 W D-series redPOWER ytterbium fibre continuous wavelength (CW) laser from SPI laser (UK) with a near infrared wavelength of 1070 nm equips the platform. The AM125 has a 125 mm^3 build volume with an 80°C base plate heater that was maintained during the build process. The oxygen content was held below 900 ppm using a vacuum and argon purge; however, the oxygen content was below 100 ppm in the actual processing conditions. The substrate was 304 SS. Samples were fabricated by the machine operator in The University of Nottingham.
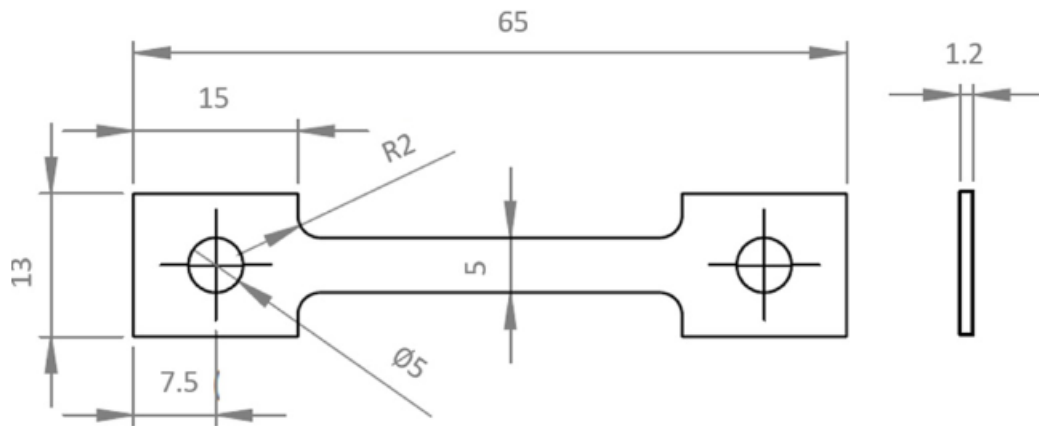
Figure 3.6: Tensile testing specimen geometry designed to be fabricated by LPBF. All the values shown are in mm.

The different sets of experiments with different process parameters (shown in Table 3.9) were built. The first batch parameters set was intuitively selected to induce keyhole and lack of fusion defects into the structure. The second batch has a layer thickness that is slightly higher than the optimised layer thickness (it will be defined in the next section). Based on what will be addressed in the next section, the third batch was generated with the optimised process parameters. To reduce residual stresses, a

meander scan strategy with a 67° rotation at the end of each layering process was used.

Table 3.9: LPBF main process parameters that have been used for 316L SS builds.

	P (W)	v (m/s)	h (μm)	t (μm)
Batch 1	200	1	110	50
Batch 2	100	1	70	30
Batch 3	100	1	70	20

The longitudinal section of as-built samples was ground on SiC paper followed by mechanical polishing, for cracks/porosity characterisation. The Leica DFC295 was used to capture optical microscopy images. Image analysis using ImageJ software [180] was used to determine porosity in micrographs taken from various locations for each sample.

Tensile tests were conducted at room temperature using an Instron 3382 universal testing machine at a strain rate of 10^{-4} s^{-1} [181] with the load axis parallel to the building direction, to investigate the mechanical properties of the LPBF-produced 316L alloy and compare the results with the wrought 316L SS.

3.3.2 Crack-free high strength austenitic stainless steels

Three new austenitic SSs are proposed that are designed to solidify at lower temperature ranges, have higher strengths (solid solution strengthening) and lower thermal expansion capability, and solidify through the proper solidification path. The optimised alloys should outperform the most common austenitic SS, 316L, which used as the baseline alloy, in terms of the properties and characteristics. There are 38 optimised alloys after running GA optimisation for Table 3.4 compositional variations. From the standpoint of the three parameters stated earlier, Figure 3.7 shows a con-

trast between the optimised alloys and the three 316L SSs that have been printed with microcracks in the literature [20, 21, 22]. Since all of the designed alloys have a STR less than 32 K and a PI greater than 1.46×10^6 MPa·K, and solidify in a ferrite + austenite path, they should perform better than the three cracked 316L SSs. Three alloy examples are proposed among the 38 optimal alloys: Alloy 1 is optimised for the lowest STR; Alloy 2 is optimised for the highest PI; and Alloy 3 is optimised for a compromise between all the three criteria. Table 3.10 lists the chemical compositions of each of the proposed alloys.
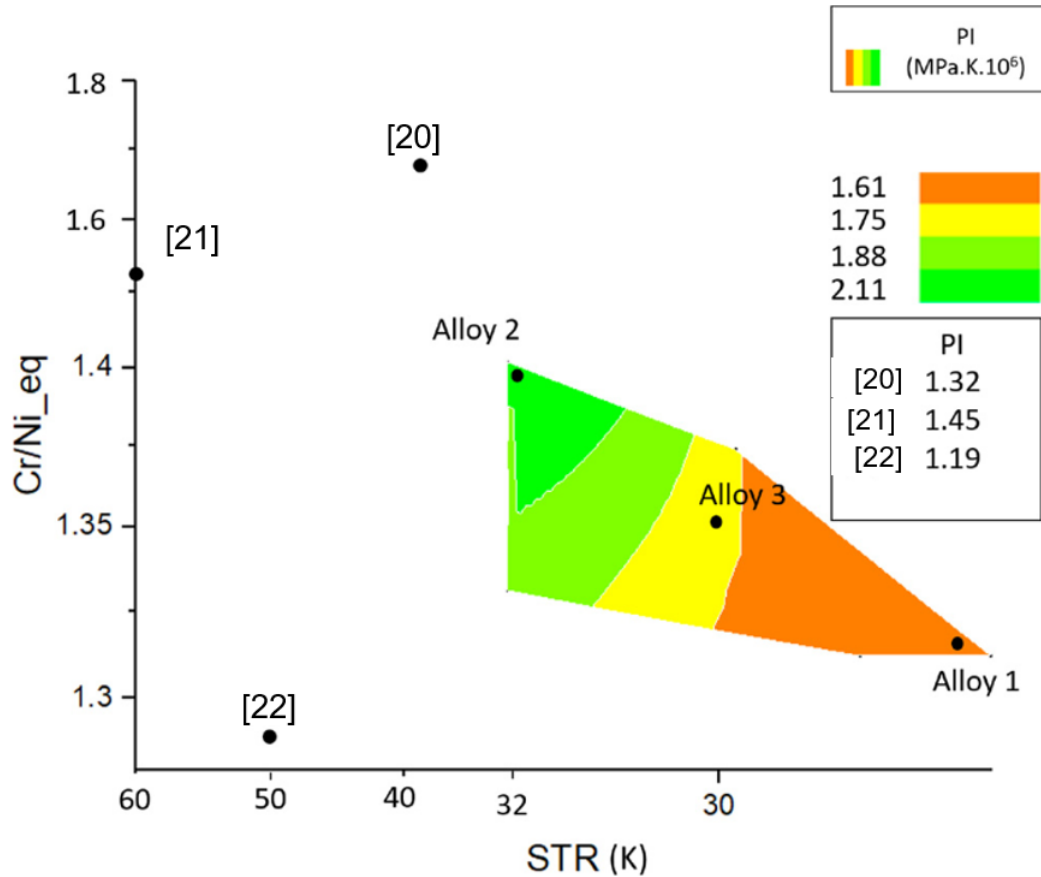
Figure 3.7: The optimum space and the baseline alloys (316L SSs) are compared. Alloys 1-3 are three proposed alloys that have been shown. As shown in Figure 3.2 the alloys [20], [21], and [22] crack.

Table 3.10: Chemical composition of the designed alloys. All the contents are provided in wt.%. In all three alloys, P and S are 0.03 and 0.001 wt.%, respectively. STR and PI are in K and MPa·K, respectively.

Alloy	C	Cr	Ni	Mn	Mo	Si	W	N	STR	$PI\times10^6$	Cr_{eq}/Ni_{eq}
Alloy 1	0.02	14.50	10.37	1.08	0.88	0.43	0.36	0.07	28.13	1.68	1.31
Alloy 2	0.01	15.03	10.88	1.92	1.45	0.23	0.92	0.06	31.64	2.11	1.40
Alloy 3	0.02	15.83	11.23	1.06	1.09	0.3	0.44	0.07	29.88	1.87	1.35

Scheil simulation for the designed alloys and three cracked 316L alloys were carried out to show the solidification path, assuming constitutive segregation, in order to explain the impact of each of the three criteria given in this thesis on crack susceptibility resistance (Figure 3.8). C and N are considered as fast diffusers in these simulations. The STR has been extended to larger ranges to account for the effects of element segregation. Alloys 1-3 have STRs of 147, 157, and 153 K, respectively. For the three alloys reported with cracks after LPBF the STR is 143 K [20], 172 K [21], and 113 K [22].

For the composition reported in [20], despite the fact that the STR in paraequilibrium conditions is lower than that of the designed alloys, austenite dominates the solidification mode (because its Cr_{eq}/Ni_{eq} is less than 1.3). Furthermore, during solidification, the undesirable MnS phase will be stable for more than 100 K, which is difficult to dissolve in austenite. The STR of the alloy printed by Sun *et al.* [21] is too high in both equilibrium and non-equilibrium conditions, and this cannot be compensated by high Cr_{eq}/Ni_{eq} values. As a result, cracks formed during LPBF process. In non-equilibrium, the third alloy, which was printed by Chen *et al.* [22], has a very low STR, showing the low tendency of the elements for segregation. However, the formation of the cracks during LPBF is caused by a very low PI (1.19×10^6 MPa·K). Therefore, a compromise between the criteria proposed in this thesis is needed to
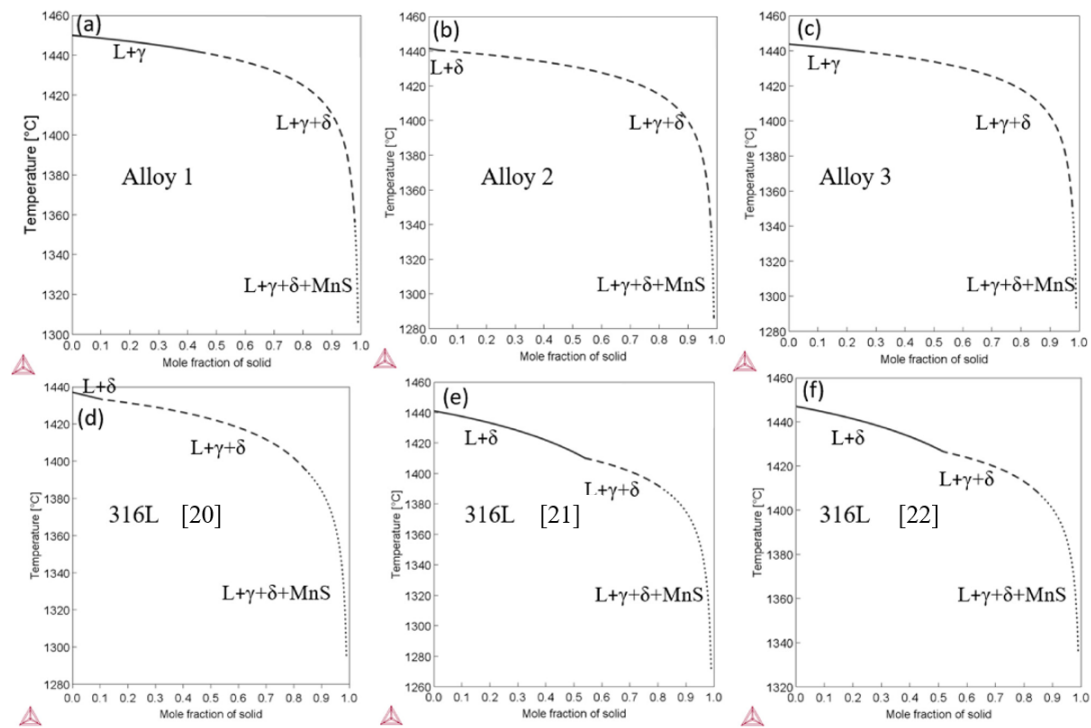
Figure 3.8: (a)-(c) Scheil simulation for the designed, and (d)-(f) for three cracked 316L SS reported in the literature. C and N are considered to be fast diffusers in all simulations. ThermoCalc was used to perform calculations, which were based on the TCFE9 database.

achieve a crack-free austenitic SS. Although the three designed alloys have not a very low STR in non-equilibrium conditions, their higher PI and lower MnS stability during solidification make them more resistant to crack formation during LPBF.

While phase field (PF) modelling may be used to obtain more precise results, since our aim is alloy design and some of the PF variables, such as interfacial energy and diffuse interface thickness, have unknown compositional dependencies, PF may not be a computationally feasible method for alloy design.

3.3.3   Porosity-free 316L stainless steel

The first step in producing a component free of defects and porosity is to determine the normalised enthalpy (energy transferred to the powder bed) for various laser powers and scan speeds in order to determine safe regions free of keyhole-induced pore formation. With the material properties from Table 3.8, equation 2.4 and 3.9 can be used to evaluate two areas of safe and keyhole-induced pore regions, as shown in Figure 3.9. For 316L SS, the normalised enthalpy threshold is about 5.5 (based on equation 3.9). For a constant laser spot size of 35 μm, all combinations of P and v that result in normalised enthalpies lower than 5.5 are safe from keyhole-induced pore formation (Figure 3.9). The process maps were plotted using a variety of laser powers (100-300 W) and scan speeds (0.1-2.5 m/s). Using higher powers and slower scan speeds increases the risk of keyhole-induced pore formation due to overheating, which causes the powder bed temperature to reach the alloy's boiling point. According to Figure 3.9, for a machine with a spot size of 35 μm, laser powers greater than 150 W cannot be used for LPBF of 316L SS. Machines with larger spot sizes can be used to increase the process efficiency (by using higher laser powers without producing

keyhole-induced pores). In this case, the keyhole-induced pore region (P=200 W and v=1 m/s) was chosen as the first experimental parameters set to produce batch one specimens. The second and third batches were produced with a safe P and v (100 W and 1 m/s, respectively) combination.
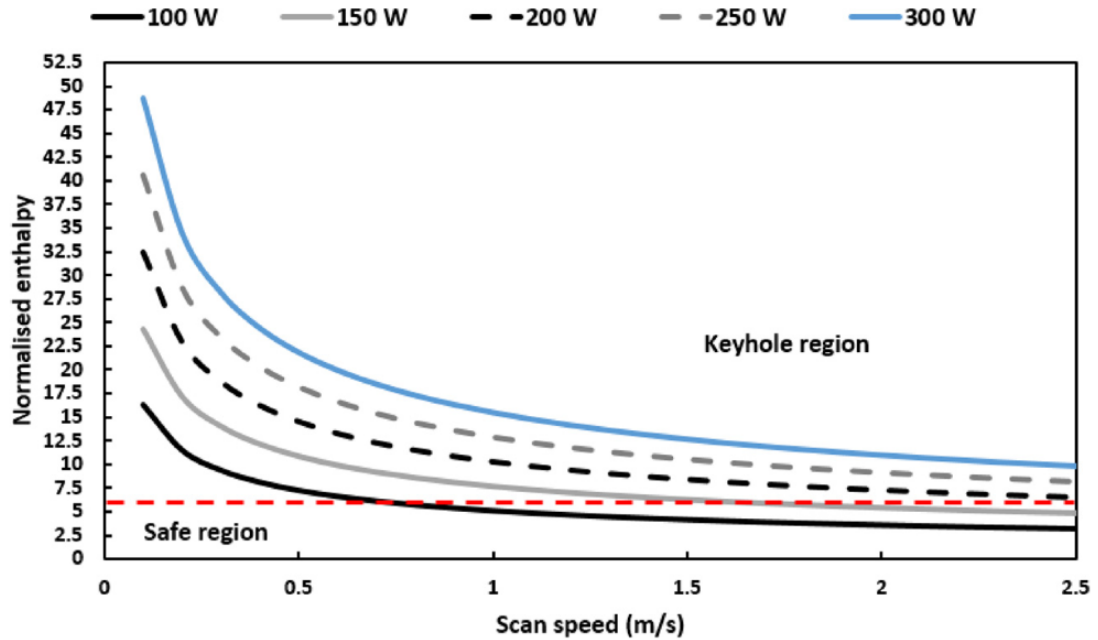
Figure 3.9: Keyhole-induced pore and safe regions, based on various combinations of P and v for LPBF of 316L SS with a laser spot size of 35 μm.

The second step is to prevent lack of fusion defects, which are determined by the process hatch distance and layer thickness. The melt pool width (W) is the maximum hatch distance (h) of the process, based on the second criterion for lack of fusion prevention. Therefore, using equation 3.10, the maximum h for various combinations of P and v is shown in Figure 3.10a. When higher powers and slower scan speeds are used, the hatch distance must be increased (Figure 3.10a). However, in this case, the maximum hatch distance is determined to be 105 μm for the first batch. The experimental h is set to 110 μm in order to produce lack of fusion in this study. The

maximum h is 75 μm when P is reduced to 100 W for the next two batches. As a result, a hatch distance of 70 μm was used for these two batches. Knowing the depth of the melt pool allows an optimal layer thickness to be selected based on the first criterion for lack of fusion prevention. W/D_m should be higher than 2 according to the keyhole-induced pore formation criterion. Thus, the maximum D_m is equal to half of W. Since D_m/t should be greater than 1.5, the maximum layer thickness for LPBF of 316L SS is plotted for different combinations of P and v for a machine with a laser spot size of 35 μm and shown in Figure 3.10b. Layer thicknesses of less than 80 μm are clearly ideal for a laser power of 100 W. The maximum allowable layer thickness in this study is 35 μm for P=200 W (first batch). Therefore, for this batch, a t=50 μm was used to induce lack of fusion deliberately. The maximum t for the second and third batches is 25 μm. A t=30 μm is used for the second batch to induce lack of fusion without keyhole-induced pore formation, and a t=20 μm is used for the third batch to ensure sufficient melting.

The third step is to ensure that there is no balling defects. When the L/W ratio exceeds 2.3 balling occurs. Figure 3.11a depicts the expected melt pool length (L) for various P and v combinations. When the scan speed is increased and laser power is reduced, L decreases. In Figure 3.11b, the balling criterion for various combinations of P and v is also shown. Balling is thus not a significant issue during LPBF of 316L SS with a machine with a spot size of 35 μm. The melt pool stability is high enough to avoid any balling defects even at high powers and scan speeds. As a result, for the three batches listed, the process parameters remain the same as before.

Since the powder was gas atomised under argon atmosphere, internal porosity in the powder particles can often be found when the built is fabricated by LPBF. This
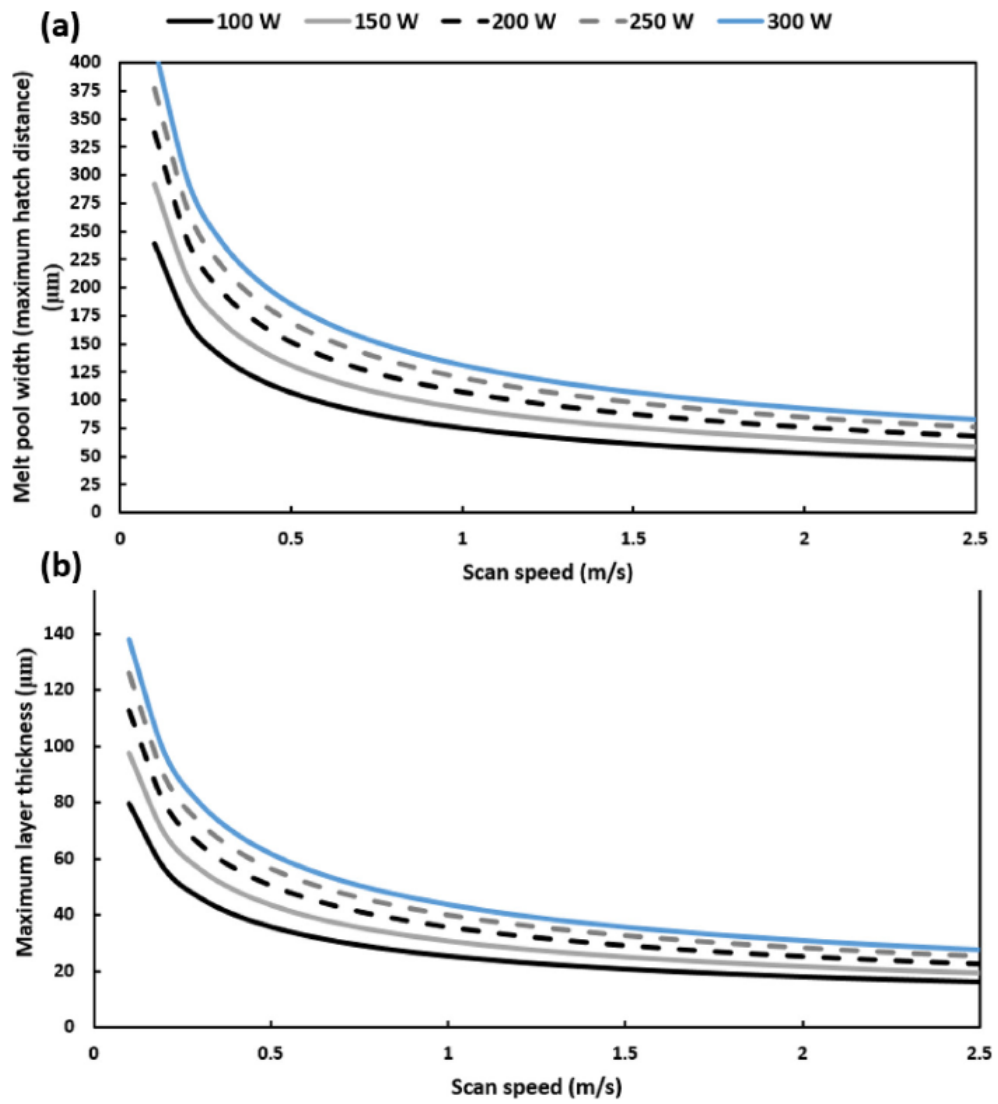
Figure 3.10: (a) Maximum hatch distance, and (b) maximum layer thickness for the experimental 316L SS for different combinations of P and v with a laser spot size of 35 μm.
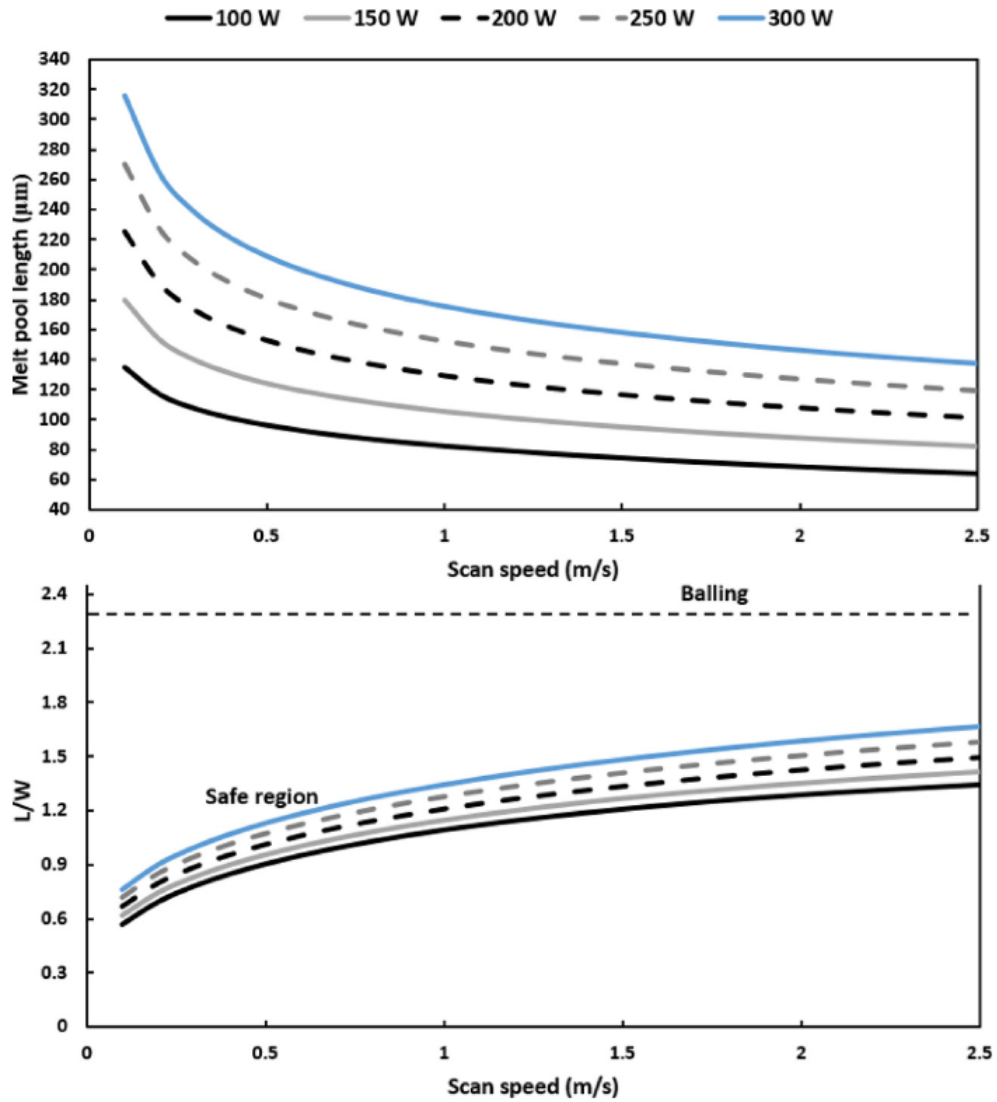
Figure 3.11: (a) Melt pool length and (b) balling criterion for different combinations of P and v with a laser spot size of 35μm for the experimental 316L SS.

type of porosity can be avoided if argon is given enough time to escape from the melt [78]. However, since these types of pores have no negative effects on mechanical properties [18], no attempt has been made to optimise against their formation in this study.

Optical microscopy is used to characterise crack/porosity contents after the samples have been produced using LPBF. The representative optical micrographs of the samples from different batches are shown in Figure 3.12. A black and white contrast of the optical micrographs using ImageJ software are shown in Figure 3.13. Those images (only three representatives are presented here) have been used to measure the average porosity contents of the samples from different batches. After LPBF, the optical micrographs display no solidification cracks, as predicted given the alloy's high F (F=1.72, equation 3.8). Micrographs from samples built in batch one with unoptimised process parameters show the existence of keyhole-induced pores and lack of fusion defects, as predicted by the presented methodology in this thesis (Figure 3.13a). This specimen has an average porosity content of 1.11±0.4 %. This batch has been produced with a normalised enthalpy of 10.2, which is higher than the threshold for keyhole-induced pore formation (the threshold is 5.5). This causes the powder bed to be overheated, resulting in evaporation. Based on its near-circular morphology, the smallest keyhole-induced pore found is around 3 μm. With layer thickness and hatch distances higher than the maximum values predicted by our model, it was also expected to produce some lack of fusion defects. The smallest lack of fusion defect identified in this study is approximately 10 μm. Since lack of fusion defects are larger than keyhole-induced pores, they are expected to have a greater impact on mechanical properties. Gas entrapment pores are also identified in this study,

but they are much smaller, measured around 1 μm in diameter. By optimising the process parameters and decreasing the normalised enthalpy value to 5.1, there is no significant evidence of keyhole-induced pores in samples from batch 2 and 3, as shown in Figures 3.12b and c, and Figures 3.13b and c. Samples from these two batches have average porosity levels of 0.03$\pm$0.02 %. Some lack of fusion defects can be found in Figure 3.13b, which is due to the unoptimised layer thickness that was chosen for fabricating of this batch. However, this has not influenced the average population of pores compared to batch 3, thus it can be assumed that exceeding slightly from layer thickness maximum (from 25 μm as the maximum to 30 μm) has no serious impacts on the density of the as-built parts. The only type of pores present in the as-built samples from batch 3 are gas entrapped pores, which may be related to the powder atomisation process. Therefore, the methodology presented in this thesis can lead to production of porosity-free components by LPBF.

This study also shows that the volumetric energy (heat input) is not a useful tool for predicting the density of LPBF-produced components. For the batches 1-3 produced in this study, using equation 2.3, E_D is 36, 47.61, and 71.42 J/mm^3, respectively. Based on this approach, the samples produced with the lowest amount of heat input (batch 1 samples) underwent evaporation and subsequently keyhole-induced pore formation, although higher heat inputs did not lead to evaporation. Furthermore, while the average porosity contents in batches 2 and 3 are the same, E_D is totally different for these two batches. These results show that, in comparison to previous approaches published in the literature [182, 183, 72], the proposed model in this thesis works well in achieving fully-dense LPBF as-built components.
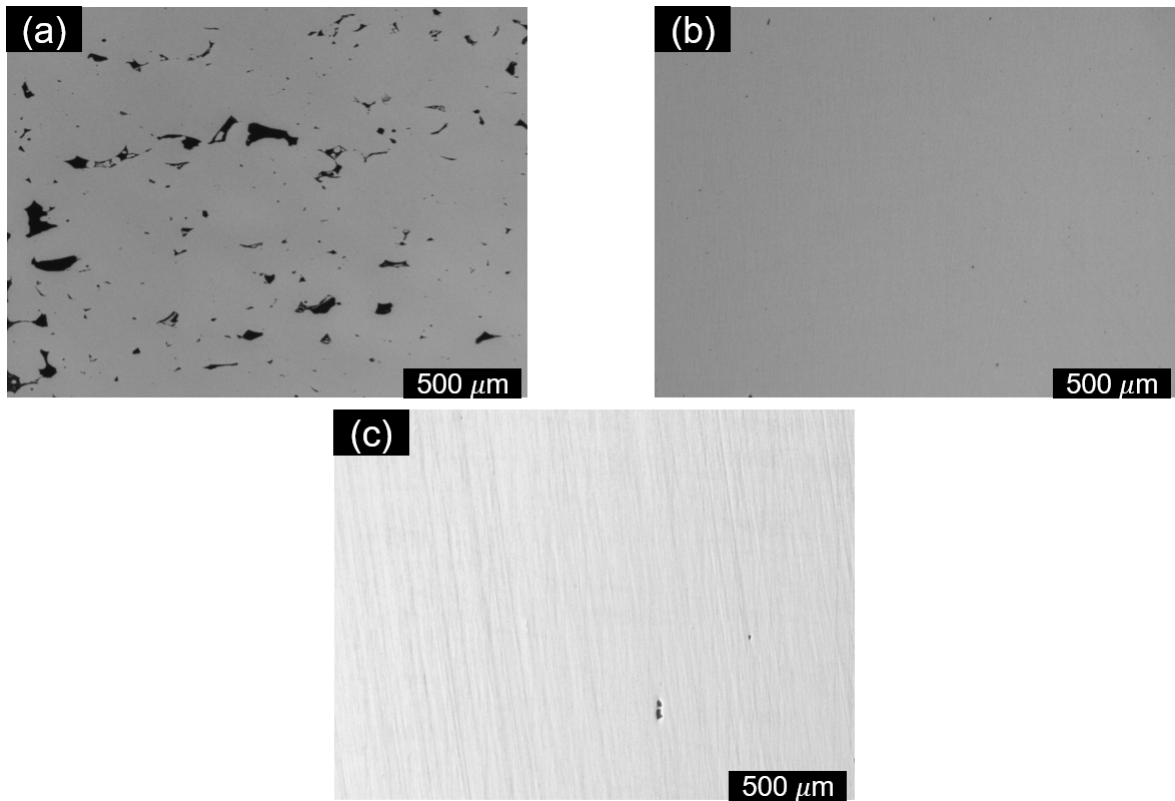
Figure 3.12: Representative optical micrographs showing the presence of pores in samples from (a) batch 1, (b) batch 2, and (c) batch 3.
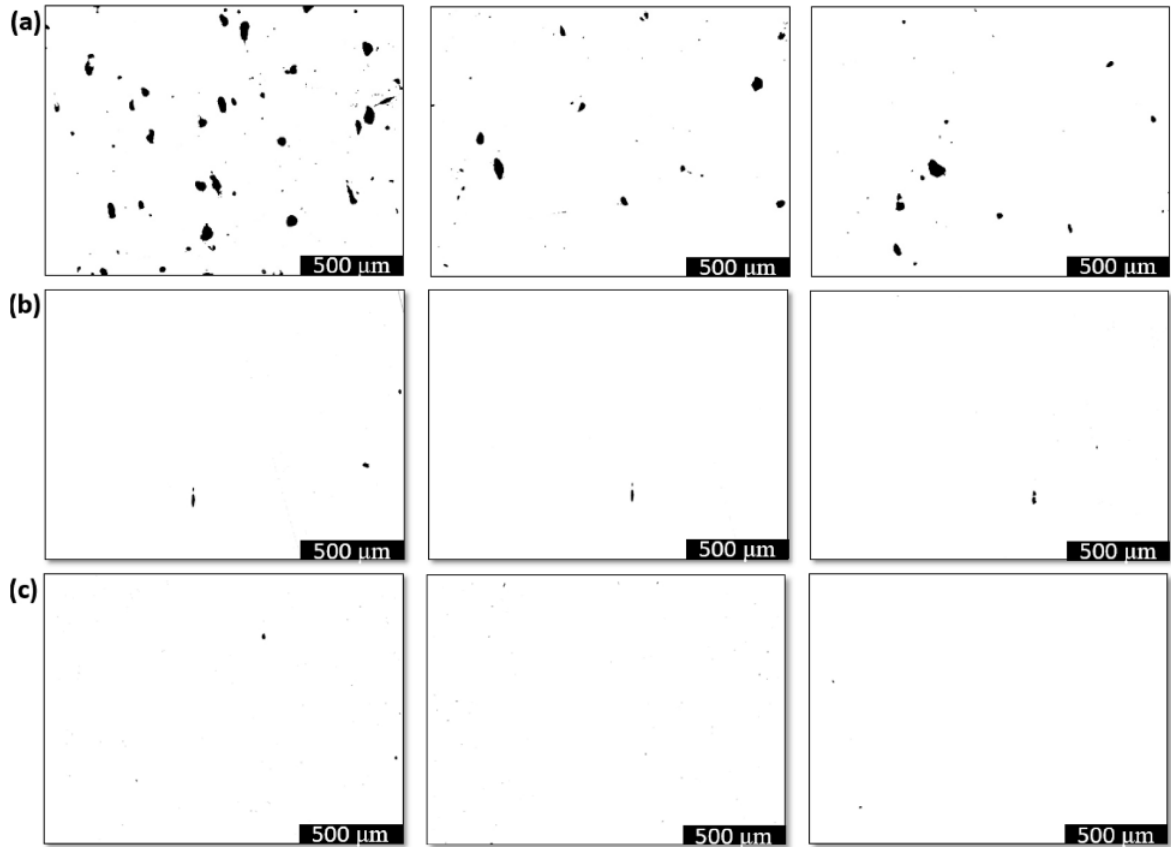
Figure 3.13: Representative black and white contrast of the optical microscopy images processed with ImageJ software: (a) sample from batch 1 showing keyhole-induced pores and lack of fusion defects, (b) and (c) samples from batch 2 and 3, respectively displaying no keyhole-induced pores and lack of fusion defects (only spherical gas-entrapped pores can be found).

3.3.4 Mechanical properties

The tensile properties of the LPBF as-built 316L SS samples fabricated using various process parameters are shown in Figure 3.14. In addition, based on ASM standard [184], the mechanical property specifications for 316L SS in two states of cold-finished wrought (black dashes in Figure 3.14) and hot-finished wrought (blue dashes in Figure 3.14) are shown in Figure 3.14. It is worth noting that tensile properties of samples with equal void density are very similar. Due to its relatively high porosity, the sample from batch 1 has the lowest yield, tensile strength and elongation values compared to other high density LPBF produced samples. However, although its yield and ultimate tensile strength meet the 316L SS specifications, its elongation is around 10% lower than the cold-finished wrought and 32.5% lower than the hot-finished wrought samples. But the fully-dense samples from batches 2 and 3 have higher strengths and compared ductility values to hot-finished wrought samples. In comparison to the high porosity sample, these samples have higher strength and they are more ductile. Fully-dense samples have a 47% higher yield and a 12% higher ultimate tensile strength than wrought samples. It is also worth noting that the ductility values for fully-dense LPBF-built samples are slightly lower than those for cold-finished wrought alloy and slightly higher than those for hot-finished wrought alloy.

The results of this study show that LPBF processing can improve the formability of 316L SS as well, by using optimised alloy compositions and process parameters. Due to a higher dislocation density resulting from the high cooling rates and thermal strain generated during LPBF, the yield strength of both defect-free and high porosity samples produced by LPBF is superior to that of wrought alloys [185]. Another potential explanation for the LPBF component's superior yield strength may be the
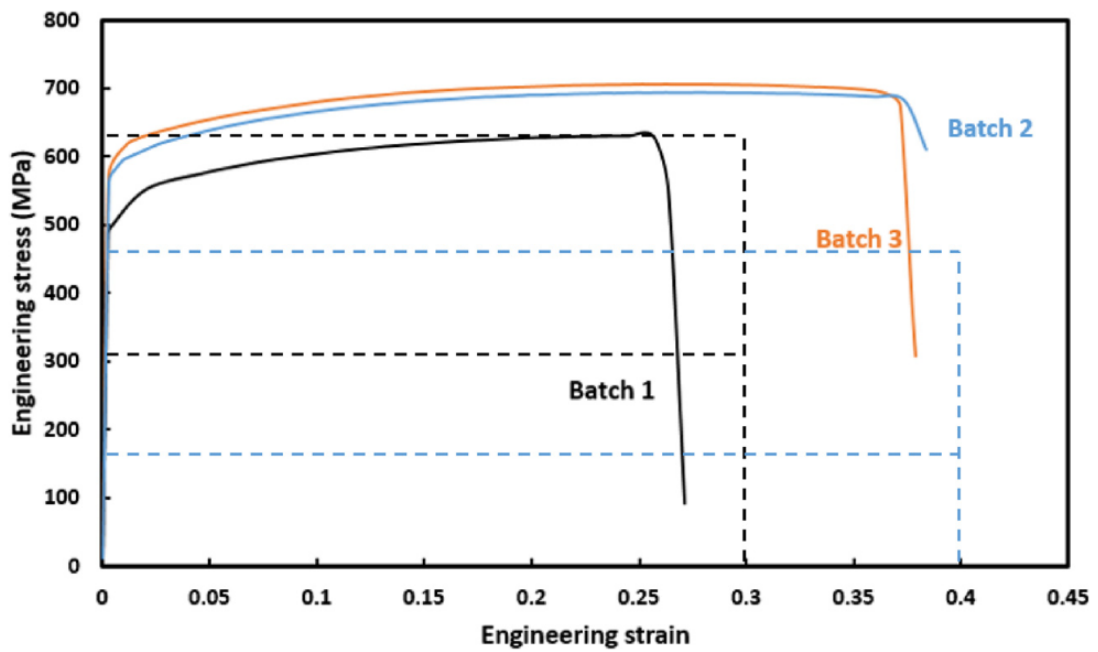
Figure 3.14: Engineering stress-strain curves for various LPBF-built 316L SS samples. The requirements for the tensile properties (the yield strength, ultimate tensile strength, and elongation) for cold-finished and hot-finished wrought samples are indicated in black and blue dashes, respectively.

development of solidification-enabled cellular structures with average submicron sizes during processing [185]. The details of mechanisms for yield strengthening of LPBF 316L SS will be discussed in the next chapters. The defect-free LPBF-built samples have higher ultimate tensile strength and ductility than the sample with porosity. The existence of keyhole-induced pores and lack of fusion was thought to reduce the material's tensile strength and ductility. Furthermore, the presence of pores reduced the yield strength of the LPBF-built samples. However, to verify the effects of pores on the mechanical properties, more samples processed with more variations in process parameters will be investigated in the next chapters.

When comparing the formability index (ultimate tensile strength×elongation) [186] of the LPBF-built samples to the wrought alloys, the formability index of the LPBF samples indicates a substantial improvement from 18,690 to 19,200 MPa% for wrought alloys to 27800-28280 MPa% for batches two and three, respectively. Due to its moderate stacking fault energy, it is thought that dislocation slip and deformation twinning govern the deformation mechanisms of wrought 316L alloy [187]. Although the formation of twins does not result in a high strain hardening rate in the LPBF as-built samples in here, the deformation twins may be responsible for the high ductility of fully-dense samples. This will be investigated in detail in the next chapters. This large improvement in the formability index demonstrate how optimising both the composition and process parameters of LPBF will result in the development of significantly better alloys while also lowering the cost of heat treatments and forming processes.

3.4 Application of alloy design methodology to other alloying systems

17-4 PH SS is commonly used in a number of applications such as aerospace, chemistry, medical, and food industries [188, 189, 190, 191] due to its high strength and excellent corrosion resistance. The martensitic structure and incorporation of fine Cu-rich precipitates during ageing heat treatment results in its superior mechanical properties [36, 192]. The fabrication of 17-4 PH SS builds using LPBF has gained a lot of interest [193, 194, 195, 196].

Unlike their wrought counterparts (which have a fully-martensitic structure), the LPBF as-built 17-4 PH SS parts have a microstructure that is a mixture of austenite, δ-ferrite, and martensite. The differences between LPBF and wrought component microstructures have been attributed to the atomising medium, build chamber atmosphere, build orientation, process heat input, scan strategy and laser beam settings [197, 198, 199, 200, 194]. Furthermore, the LPBF build microstructures are difficult to be predicted due to complicated interactions between alloying elements and the difference in precipitate formation in austenite, δ-ferrite, and martensite. Sun *et al.* [201] reported that LPBF as-built components had a fully-ferritic microstructure, and had a lower hardness than the wrought component with a fully martensitic structure. The microstructure changed to nearly fully martensitic after solution annealing, making the hardness comparable to the wrought component after the same heat treatment. The hardness of the LPBF-produced specimen improved significantly and surpassed that of its wrought counterparts after ageing, which was due to finer martensite blocks after solution annealing, resulted in the formation of finer precipi-

tates. Therefore, eliminating the solution annealing stage and obtaining a martensitic microstructure in the LPBF as-built condition will reduce manufacturing costs. Several factors can influence the phase transformation paths during LPBF solidification. The martensitic start temperature (the temperature at which austenite fully transforms to martensite, M_s) [202], the austenite start temperature (the temperature at which δ-ferrite fully transforms to austenite, A_s) [193], and the solidification mode, which can be quantified by the Cr_{eq}/Ni_{eq} value, all influence martensite formation during high cooling rate solidification.

Microcracks and porosity (keyhole-induced pores and lack of fusion) can also negatively affect mechanical properties in addition to the lack of a fully-martensitic microstructure [203, 48, 204]. In order to solve the problem of printability of such precipitation hardening steels, a new class of maraging steels called Formetrix alloy has been developed recently [205]. Although this alloy is printable from the point of view of crack prevention, the microstructure of the as-built parts does not meet the fully-martensitic requirement, leading to lower mechanical properties compared to similar wrought maraging steels. Therefore, the methodology to control crack formation has been updated and criteria for improvement of mechanical properties have been added to our methodology to redesign 17-4 PH SS and Formetrix alloy-type compositions suitable for LPBF.

3.4.1 Criteria to obtain martensitic microstructure upon printing

Three factors influence phase transformations during solidification of 17-4 PH SS and Formetrix alloy: (i) martensite start temperature (M_s), (ii) solidification path, and

(iii) Austenite start temperature (A_s). Different criteria have been identified and outlined in here in order to achieve a martensitic microstructure upon printing.

M_s temperature

The M_s, which is primarily composition dependent, determines the ability to form a fine lath martensitic microstructure during high cooling rate solidification (a cooling rate of 10^6 K/s is considered in here to resemble LPBF processing) . When quenching to room temperature from solution treatment temperature, experimental results on various types of steels have shown that a M_s temperature above 150°C is needed to obtain an approximately fully-martensitic microstructure [206]. A decrease in the M_s temperature results in an increase in the fraction of retained austenite and coarsening of the martensitic microstructure. Ishida proposed a model to predict the effects of alloying elements on M_s temperature, which agrees well with experimental findings [207]:

$$M_s(°C) = 545 - 330W_C + 2W_{Al} + 7W_{Co} - 14W_{Cr} - 13W_{Cu} - 23W_{Mn} - 5W_{Mo}$$
$$-4W_{Nb} - 13W_{Ni} - 7W_{Si} + 3W_{Ti} + 4W_V$$

$$(3.14)$$

where W_i, i= C, Al, Co, ... are the weight percentage of each alloying element. Table 3.11 shows a list of alloys (17-4 PH and Formetrix compositions) produced by LPBF in previous studies. For all such alloys, M_s temperature is calculated via equation (3.14) and shown in Table 3.12. Alloys L-1 to L-11 refer to 17-4 PH SS variations and alloys L-12 to L-23 refer to the Formetrix alloy variations. In the case of 17-4 PH

SS, except from L-1, L-2, and L4, which have $M_s \geq 211°C$, martensite has not been reported as the main phase in the microstructure of the as-built specimens. Xu *et al.* [100] suggested that a marageing steel with a minimum M_s temperature of 200°C can exhibit a fully-martensitic structure after solution annealing and subsequent quenching. Therefore, the first criterion for obtaining a martensitic transformation for 17-4 PH-type of steel is $M_s \geq 200°C$. In the case of Formetrix alloy, M_s is in a higher level (L-12 to L-23, Table 3.12), thus a minimum of 240°C has been chosen to redesign Formetrix alloy for LPBF.

Table 3.11: Chemical compositions of 17-4 PH SS (L-1 to L-11) and Formetrix alloy (L-12 to L-23) produced by LPBF in the literature in wt.%.

Alloy	C	Cr	Cu	Mn	Ni	P	S	Si	Nb	N	Mo	Ref.
L-1	0.011	15.87	3.63	-	3.98	-	0.005	-	0.57	0.058	-	[208]
L-2	0.02	15.85	3.21	0.02	4.18	-	-	0.78	0.19	0.007	-	[193]
L-3	0.01	16.58	4.58	0.23	4.24	-	-	0.43	0.3	0.031	-	[193]
L-4	0.01	15.09	3.23	0.56	4.51	-	-	0.38	0.24	0.036	-	[193]
L-5	0.035	16.7	4.2	0.48	4.2	0.02	0.003	0.67	1.8	0.11	-	[209]
L-6	0.035	16.7	4.2	0.48	4.2	0.02	0.003	0.67	0.33	-	-	[201]
L-7	0.05	15.4	4	0.6	4.3	0.02	0.01	0.7	0.27	-	-	[36]
L-8	0.054	16.51	3.97	0.18	4.16	0.011	0.005	0.41	0.42	-	-	[200]
L-9	0.037	16.23	4.06	0.392	3.42	0.02	0.005	1	0.308	-	-	[210]
L-10	0.066	15.06	4.14	0.576	4.55	0.015	0.006	0.628	0.232	-	-	[210]
L-11	0.04	15.06	4.14	0.576	4.55	0.01	0.006	0.628	0.232	-	-	[210]
L-12	0.16	10.64	0.54	-	1.96	-	-	0.19	0.03	0.07	1.48	[205]
L-13	0.25	11.5	0.5	-	1	-	-	0.25	0.03	0.05	1.5	[205]
L-14	0.2	11.5	0.5	-	1	-	-	0.25	0.03	0.05	1.5	[205]
L-15	0.16	11.5	0.59	-	1.05	-	-	0.18	0.04	-	1.51	[205]
L-16	0.21	11.21	0.12	-	1.93	-	-	0.19	0.03	0.04	1.7	[205]
L-17	0.21	15.55	0.55	-	0.88	-	-	0.16	0.03	0.07	0.89	[205]
L-18	0.21	11.69	2.56	-	0.94	-	-	0.17	0.06	0.08	1.47	[205]
L-19	0.1	10.56	0.56	-	-	-	-	0.14	0.04	0.14	1.61	[205]
L-20	0.17	11.01	-	-	1.85	-	-	0.53	0.04	0.074	0.95	[205]
L-21	0.12	10.55	0.55	-	-	-	-	0.39	0.08	0.14	1.52	[205]
L-22	0.11	11.03	-	-	-	-	-	0.2	0.08	0.16	1.38	[205]
L-23	0.23	10.6	0.69	1.74	-	-	-	0.39	0.04	0.133	1.99	[205]

Table 3.12: Characteristics of interest for the alloys printed and reported in the literature. L-1 to L11 refer to 17-4 PH SS compositions (see Table 3.11), and L-12 to L-23 refer to Formetrix alloy compositions (see Table 3.11).

Alloy	M_s (°C)	Cr_{eq}/Ni_{eq}	A_s (°C)	STR (°C)	PI$\times 10^6$ (MPa·K)
L-1	212	2.3	1235	68	1.55
L-2	216	2.61	1221	61	1.34
L-3	185	2.37	1270	63	1.58
L-4	211	2.21	1317	69	1.41
L-5	167	1.92	1182	70	2.29
L-6	174	2.45	1220	68	1.56
L-7	187	2.14	1323	65	1.52
L-8	177	2.31	1220	75	1.56
L-9	193	2.72	1193	68	1.53
L-10	180	1.91	1376	62	1.54
L-11	189	2.07	1358	61	1.50
L-12	301	1.69	1339	73	1.32
L-13	272	1.62	1313	80	1.36
L-14	289	1.90	1273	79	1.31
L-15	300	2.56	1191	88	1.18
L-16	282	1.69	1304	76	1.25
L-17	233	2.21	1090	102	1.30
L-18	257	1.56	1357	75	1.71
L-19	347	2.38	1255	75	1.28
L-20	302	1.68	1336	76	1.11
L-21	339	2.18	1269	78	1.35
L-22	345	2.27	1250	76	1.15
L-23	258	1.53	1331	75	1.62

Solidification path

δ-ferrite in the LPBF as-built 17-4 PH SS microstructures is reported frequently to be present [193, 201], As it is known to deteriorate the mechanical properties, it is important to control the solidification path in order to avoid δ-ferrite. Both in welding and AM processed 17-4 PH SS, a primary ferritic path of solidification has been reported [208, 211], because of the high Cr_{eq}/Ni_{eq} values (higher than 1.9), which is typical of the nominal compositions of 17-4 PH SS (Table 3.12). When the cooling rate is slow (lower than 1 K/s), δ-ferrite has enough time to be transformed to austenite and subsequently to martensite (if M_s temperature is high enough). However in LPBF, which is a high cooling rate process (cooling rates up to 10^5 K/s), the transformation from δ-ferrite to austenite can be suppressed fully or partially, which leads to fully ferritic or duplex or even triplex microstructures. Recently, Vunnam *et al.* [193] showed that when Cr_{eq}/Ni_{eq}=2.36, the LPBF as-built 17-4 PH SS exhibited a microstructure containing 75% of martensite, 20% austenite and just 5% of δ-ferrite. As lower Cr_{eq}/Ni_{eq} values can lead to lower retained δ-ferrite after processing, based on the information from Table 3.12, the maximum Cr_{eq}/Ni_{eq} should be 1.9 and 1.53 for 17-4 PH- and Formetrix-type of alloys, respectively.

A_s temperature

In both 17-4 PH SS and Formetrix alloy, due to their high ferrite stabiliser elements, in non-equilibrium conditions, the primary solid phase which is formed from liquid is δ-ferrite, and the secondary phase is austenite. Due to the microsegregation of alloying elements, ferrite may remain stable even at temperatures far lower than the solidus temperature. Because of high cooling rates in LPBF, if the A_s temperature is very

82

low, there is not enough time for δ-ferrite to be transformed to austenite completely. This will lead to stabilisation of δ-ferrite after the part is built. As is shown in Table 3.12, the highest A_s temperature for the reported 17-PH SS and Formetrix alloy is 1376°C, and 1357°C, respectively. Therefore, the third criterion for microstructure optimisation to redesign 17-4 PH SS and Formetrix alloy is $A_s \geq 1376°C$ and $A_s \geq 1357°C$, respectively.

Crack prevention

As described in section 3.1, crack prevention during LPBF of austenitic SSs depends mainly on three concepts: STR, PI and solidification path. Solidification path optimisation was important to obtain martensitic matrix, thus the go/no-go criteria are the same as described previously for both alloys. STR and PI of the printed alloys from literature are also listed in Table 3.12. It can be deduced from the data provided in Table 3.12 that the new designed alloys should have STRs lower than 61°C, and 75°C for 17-4 PH- and Formetrix-type of alloys, respectively. The average PI for reported 17-4 PH and Formetrix alloy are 1.55×10^6 MPa·K, and 1.33×10^6 MPa·K, respectively. Therefore, the newly designed alloys for both cases should exceed the mentioned average PIs.

Ageing optimisation

The strengthening of PH alloys and maraging steels is achieved by ensuring a homogeneous distribution of precipitation during ageing heat treatment. In the case of 17-4 PH SS, Cu precipitates, and in the case of Formetrix alloy, both Cu and $M_{23}C_6$ carbides are responsible for strengthening. Assuming that the precipitates have a

spherical morphology, the critical radius for nucleation of a spherical precipitate (r^*) can be estimated as [212]:

$$r^* = -\frac{2\sigma_i}{\Delta G_V},\tag{3.15}$$

where σ_i is the precipitate/matrix interfacial energy per unit area and ΔG_V is the precipitation driving force per unit volume. Equation (3.15) shows that the initial size of the precipitate decreases with increasing the precipitate driving force. As the finer precipitates contribute to higher strengthening, a high precipitation driving force is needed to maximise precipitation hardening.

In addition to the precipitate size and driving force, the number density of precipitates also contributes in strengthening [98]. Assuming that the precipitate size is in the range of a few nanometres, the precipitates will approach their critical nucleation radius (r^*), while their volume fraction approaches equilibrium. Therefore, the total number of precipitates (N_P) can be approximated via [212]:

$$N_P = \frac{VF}{\frac{4}{3}\pi(r^*)^3},\tag{3.16}$$

where VF is the equilibrium volume fraction of the precipitate. Therefore, to maximise the strengthening contribution of the precipitates, both the driving force for precipitation and their equilibrium volume fraction must be maximised. In a previous research, Xu et $al.$ [100] used the following relationship for approximation of the strengthening factor (SF) to design maraging steels for wrought processing:

$$SF \approx (VF)^{1/2}r^{*-1/2} \approx (VF)^{1/2}(\Delta G_V)^{1/2}.\tag{3.17}$$

84

Therefore, the first ageing optimisation criterion is to maximise the SF for each composition. Both VF and ΔG_V can be calculated using ThermoCalc software.

In addition to strengthening contribution of precipitates, it is important to preserve the corrosion resistance upon ageing heat treatment in 17-4 PH SS. The formation of a Cr-rich passive oxide film is necessary to maintain the ability of both types of the alloys to be stainless. This can be ensured by imposing a criterion of at least 12 wt.% of Cr in the martensitic matrix at the ageing temperature. This can also be enforced via ThermoCalc calculations.

3.4.2   Redesigned 17-4 PH stainless steel and Formetrix alloy for LPBF

A GA optimisation framework combined with thermodynamic calculations has been used to discover new alloy compositions. The GA was linked with ThermoCalc using TCMatlab toolbox. The concentrations of all alloying elements defining the search ranges to redesign 17-4 PH SS and Formetrix alloy are presented in Table 3.13 and Table 3.14, respectively. The general optimisation algorithm is similar to that presented for austenitic SSs (section 3.1.4) is shown in Figure 3.15 and 3.16 for 17-4 PH SS- and Formetrix-type alloys, respectively. For each candidate solution the criteria mentioned in the previous section is applied:

i The system is defined in ThermoCalc, and the thermodynamic data are obtained from TCFE9 database. The ageing temperature is fixed to 482°C, as it is reported as the optimised ageing temperature of both 17-4 PH SS and Formetrix alloy [208, 205].

ii Using the concentration of a candidate alloy, STR and PI are calculated for crack prevention. Alloys are limited corresponding to the relevant go/no-go criteria shown in Figures 3.15 and 3.16.

iii For obtaining a martensitic matrix, thermodynamic calculations are performed to find the A_s temperature. The M_s temperature and Cr_{eq}/Ni_{eq} value are calculated from equations (3.14), (3.4) and (3.5), respectively, for each alloy candidates. Go/no-go criteria defined in Figures 3.15 and 3.16 limits the candidate alloys to printable alloys with a martensitic matrix upon printing.

iv A thermodynamic equilibrium calculation is performed at the ageing temperature (482°C). Equilibrium volume fraction of the desirable precipitates, which are Cu precipitates and $M_{23}C_6$ carbides are recorded for each candidate alloy. All the undesirable phases, precipitates and carbides are kept under 0.1 wt% in ThermoCalc. The driving force for the desirable precipitates and carbides are also calculated via ThermoCalc. Using GA, the alloys with maximum SF are chosen. Simultaneously, an equilibrium calculation at ageing temperature with a condition for ensuring the presence of Cr in the martensitic matrix (at least 12 wt%) is performed for 17-4 PH SS-type of alloys.

Table 3.13: Concentration ranges of all alloying elements to redesign 17-4 PH SS in wt.%.

	C	Cr	Cu	Mn	Ni	Si	Nb
Min	0.01	13	2	0.01	2	0.01	0.1
Max	0.03	19	6	2	6	1	0.6

As a result of the optimisation process, three 17-4 PH SS- and five Formetrix-type of alloys are chosen as the best alloys. The exact composition of the alloys cannot

Table 3.14: Concentration ranges of all alloying elements to redesign Formetrix alloy in wt.%.

	C	Cr	Ni	Cu	Nb	Mo	Si
Min	0.1	10.5	0	0	0.03	0.8	0.1
Max	0.25	12	2	6	0.08	2	0.6
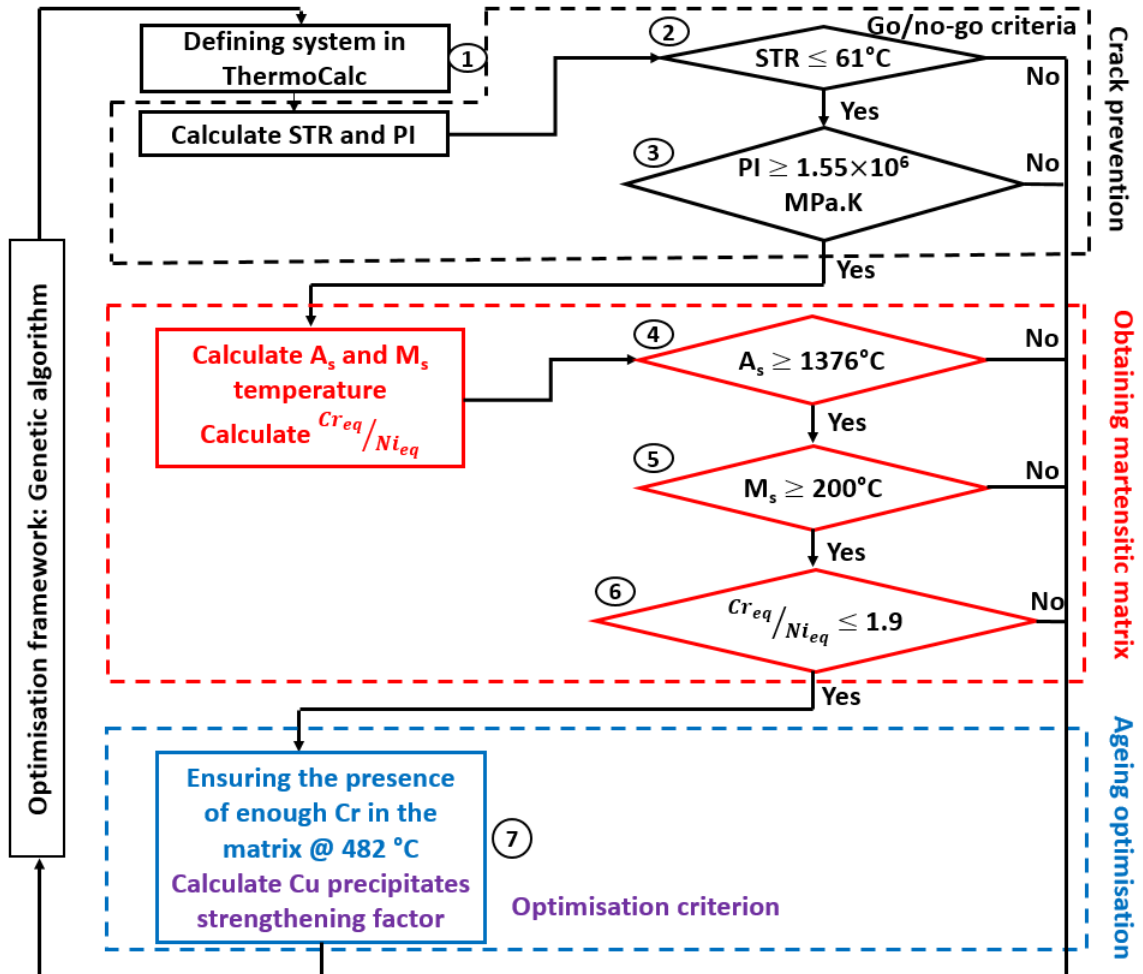
Figure 3.15: Algorithm used for redesigning 17-4 PH SS for LPBF.
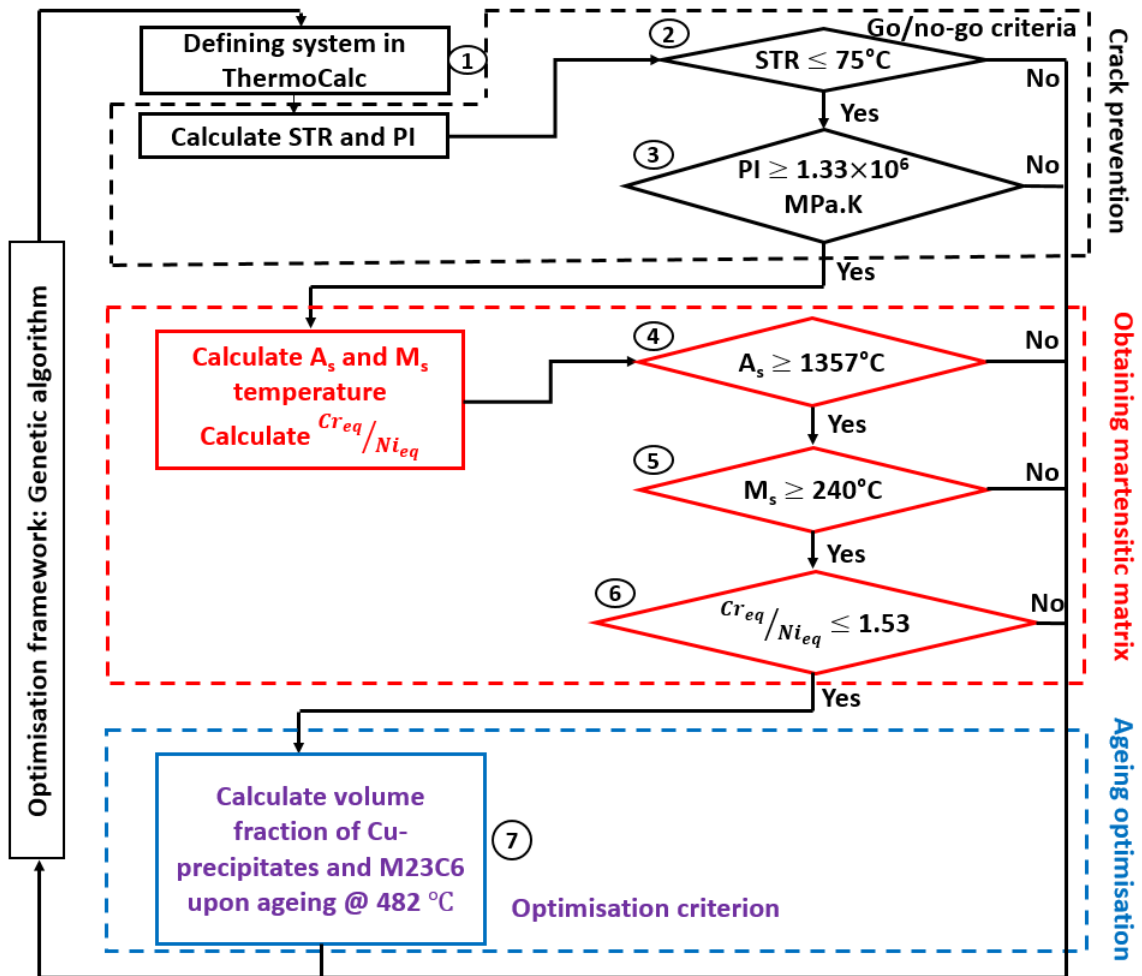
Figure 3.16: Algorithm used for redesigning Formetrix alloy for LPBF.

be reported due to patenting purposes. Table 3.15 lists the key characteristics of the designed alloys for crack prevention and obtaining a martensitic matrix upon printing. Compared to the printed alloys printed from literature (Table 3.12), all the designed alloys met the criteria defined for both crack prevention and martensitic matrix. To compare and predict the precipitation hardening contribution of the designed alloys with the reported alloys in the literature, SF was calculated via ThermoCalc for L-1 to L-11 alloys, and SS1-SS3 (newly designed alloys) and listed in Table 3.16. In the case of Formetrix alloy, since they are strengthened by two types of precipitates (Cu-precipitates and carbides), SF cannot be predicted directly, therefore, the individual equilibrium volume fraction of Cu-precipitates and $M_{23}C_6$ carbides in the martensitic matrix at the ageing temperature are captured by ThermoCalc and listed in Table 3.17. Cr content in the martensitic matrix at the ageing temperature of the newly designed and previously reported 17-4 PH SSs are also presented in Table 3.16. Table 3.16 shows that the strengthening contribution of Cu-precipitates increased significantly for SS1-SS3. The presence of more than 12 wt.% of Cr in martensite upon ageing also ensures the stainless nature of the newly designed alloys. Table 3.17 shows that the new modified Formetrix alloys contain significantly more Cu-precipitates upon ageing, which in contribution with carbides can induce extraordinary combinations of strength and ductility after heat treatment. Considering the fact that most of the variations of Formetrix alloys can only be strengthened via carbide formation (Table 3.17), the modified versions of this alloy should have a superior performance, based on metallurgical predictions.

Table 3.15: Composition of the optimised 17-4 PH SS (SS1-SS3) and Formetrix alloy (F1-F5) in wt.%. For each composition, the STR (°C), PI (MPa·K), M_s (°C), A_s (°C), and Cr_{eq}/Ni_{eq} are also presented.

	STR	$PI \times 10^6$	M_s	A_s	Cr_{eq}/Ni_{eq}
SS1	58	1.7	236	1394	1.87
SS2	60	1.77	212	1387	1.76
SS3	54	1.62	201	1399	1.62
F1	69	1.87	242	1393	1.18
F2	69	1.73	257	1401	1.33
F3	65	1.73	257	1405	1.27
F4	69	1.97	258	1392	1.48
F5	65	1.75	258	1399	1.51

Table 3.16: Comparison of the strengthening factor (SF) of the Cu-precipitates and the Cr content in the martensitic matrix at the ageing temperature for the newly designed 17-4 PH SSs and similar alloys reported previously in the literature.

Alloy	SF (kJ$^{1/2}$)	Cr @ 482°C (wt.%)
SS1	56.87	13.5
SS2	56.66	13.8
SS3	54.6	14
L-1	45.16	16
L-2	39.64	15.9
L-3	49.04	16.7
L-4	41.18	15.3
L-5	50.36	16.9
L-6	44	16.9
L-7	43.3	15.7
L-8	43.45	16.8
L-9	42.98	16.5
L-10	44.14	15.3
L-11	44	15.3

Table 3.17: Comparison of the equilibrium volume percentage of Cu-precipitates and $M_{23}C_6$ carbides at the ageing temperature (482 °C) for the newly designed and previously reported Formetrix alloys.

Alloy	Cu-precipitates (%)	$M_{23}C_6$ (%)
F1	2.6	4.8
F2	3	4.8
F3	2.4	4.8
F4	5	2.2
F5	3.2	3.8
L-12	0.4	3.2
L-13	0.4	5
L-14	0.4	4
L-15	0.4	3.2
L-16	0.06	4.2
L-17	0.4	4.1
L-18	2.2	4.2
L-19	0.4	1.9
L-20	0	3.3
L-21	0.4	2.3
L-22	0	2.1
L-23	0.5	4.6

3.4.3   Model validation

The designed alloys were prepared via vacuum suction casting as rods of 6.2 mm in length and 2.93 mm in diameter. Because the cooling rate of suction casting is in the range of 10^2-10^3 °C/s, the initial microstructure of the cast samples are expected to be martensitic. In order to measure the critical transformation temperatures such as martensitic start (M_s), martensitic finish (M_f), as well as ferrite to austenite transformation temperatures (Ac_1 and Ac_3), high-resolution dilatometry (dilatometer model used: DIL 805 A/D Quenching and Deformation dilatometer from TA instruments) was used in Materalia Research Group, National Center for Metallurgical Research (CENIM, Spain) (Experimental dilatometry tests were performed by the operator in CENIM, but analysis and figures are produced by the author of the thesis). To estimate the critical temperatures under conditions as close as possible to LPBF, a high heating rate of 10 °C/s was employed in the dilatometer to reach a full austenitisation at 1050 °C for SS1-SS3, and at 1000 °C for F1-F5. Thermodynamic calculations were carried out using ThermoCalc to predict and compare Ac_1 and Ac_3 temperature with the simulated LPBF condition. After austenitisation for 1 h (SS1-SS3) and 1.5 h (F1-F5), the samples were quenched to room temperature at a high rate of 100 °C/s to capture M_s and M_f temperatures. Figure 3.17 schematically shows the austenitisation and quenching procedure for both sets of designed steels.

Figures 3.18 and 3.19 depict the temperature evolution of the relative change in length during the heat treatment illustrated in Figure 3.17. According to Figures 3.18 and 3.19, the initial microstructure (martensite) expands during heating from room temperature up to a temperature Ac_3 where a contraction due to reversion of martensite to austenite occurs. The estimated Ac_1 and Ac_3 temperatures from dilatometry
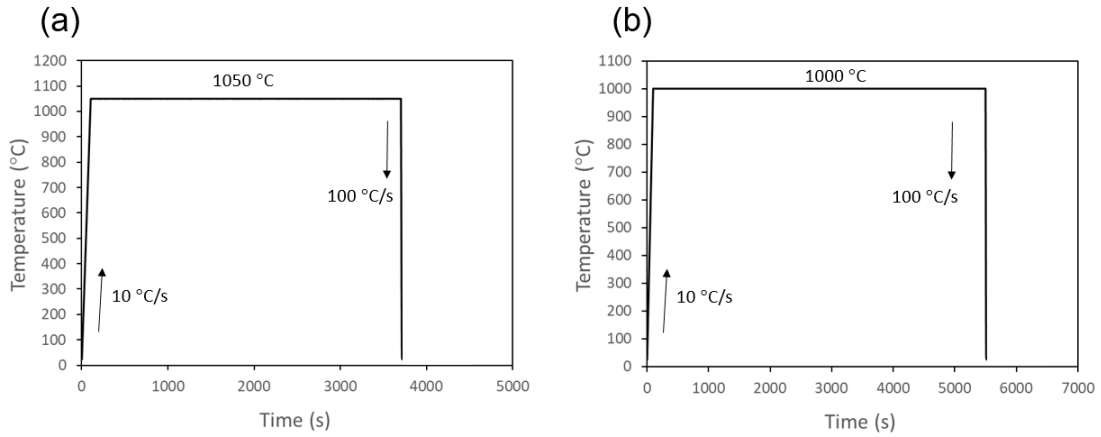
Figure 3.17: Schematics showing austenitisation and quenching for (a)SS1-SS3, and (b) F1-F5.

are reported in Table 3.18. During cooling, all alloys experience a continuous contraction down to the M_s temperature, where an expansion occurs at the beginning of martensitic transformation. When the transformation is completed at M_f temperature, alloys resume contraction down to room temperature. Estimated M_s and M_f temperatures measured from dilatometry results are also reported in Table 3.18. It can be seen that even after cooling at a rate of 10 °C/s, the alloys are expected to possess a fully-martensitic microstructure. Regarding ultra-high cooling rates of LPBF ($\sim 10^5$-10^6 °C/s), the designed alloys are expected to exhibit a fully-martensitic microstructure after LPBF, which can eliminate the need for austenitisation heat treatment after LPBF, and also improve the potential for age hardening because no retained austenite/δ-ferrite are expected.

A comparison between the experimental M_s and predicted M_s from the alloy design methodology shows a good agreement. Only F3 has a meaningful discrepancy from the modelling predictions. A magnified view of the evolution of the relative change in length during cooling around M_s temperature for F3 alloy is represented in Figure
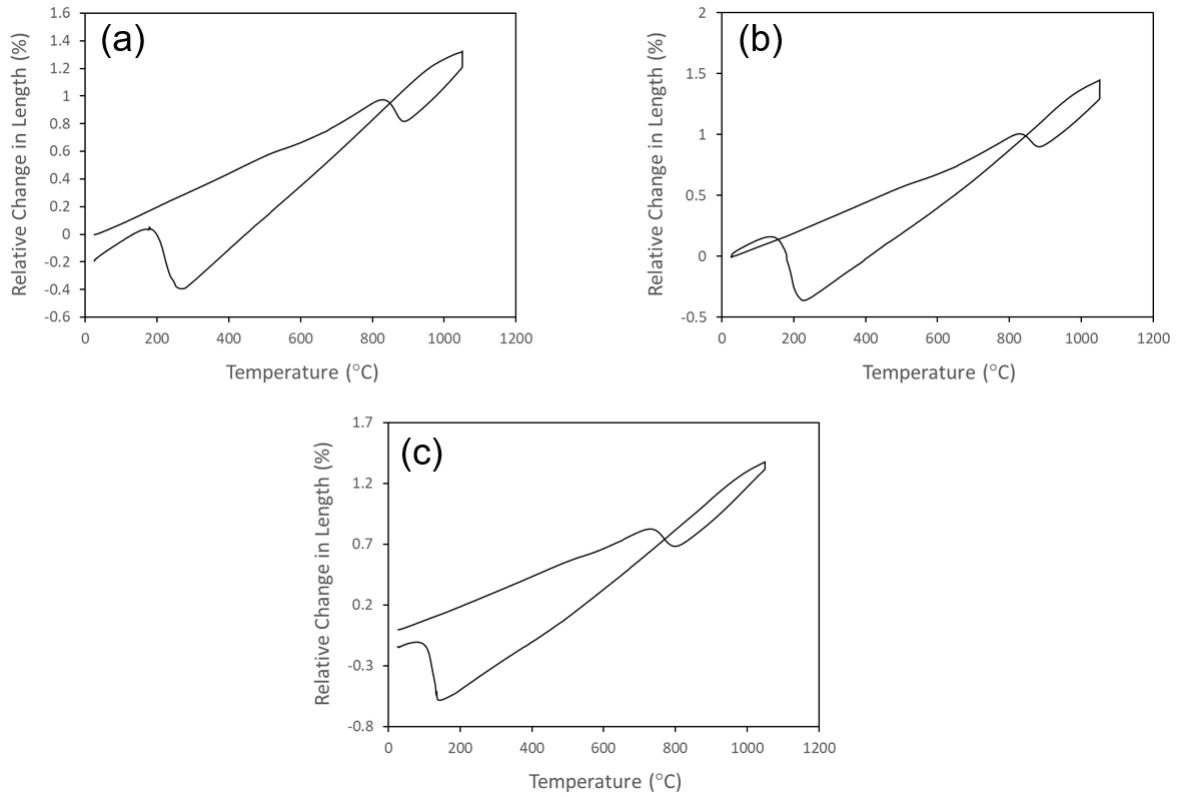
Figure 3.18: Temperature evolution of the relative change in length during continuous heating and cooling of (a) SS1, (b) SS2, and (c) SS3.

Table 3.18: Ac_1 and Ac_3 temperatures estimated using dilatometry. To compare with modelling, the predicted M_s temperatures are also presented.

Alloy	Ac_1 (°C)	Ac_3 (°C)	M_s (°C)	M_f (°C)	Predicted M_s (°C)
SS1	785	915	290	175	236
SS2	780	890	250	150	212
SS3	705	825	180	80	201
F1	820	920	230	90	242
F2	820	905	270	110	257
F3	810	885	330	170	257
F4	810	900	280	160	258
F5	800	880	235	100	258
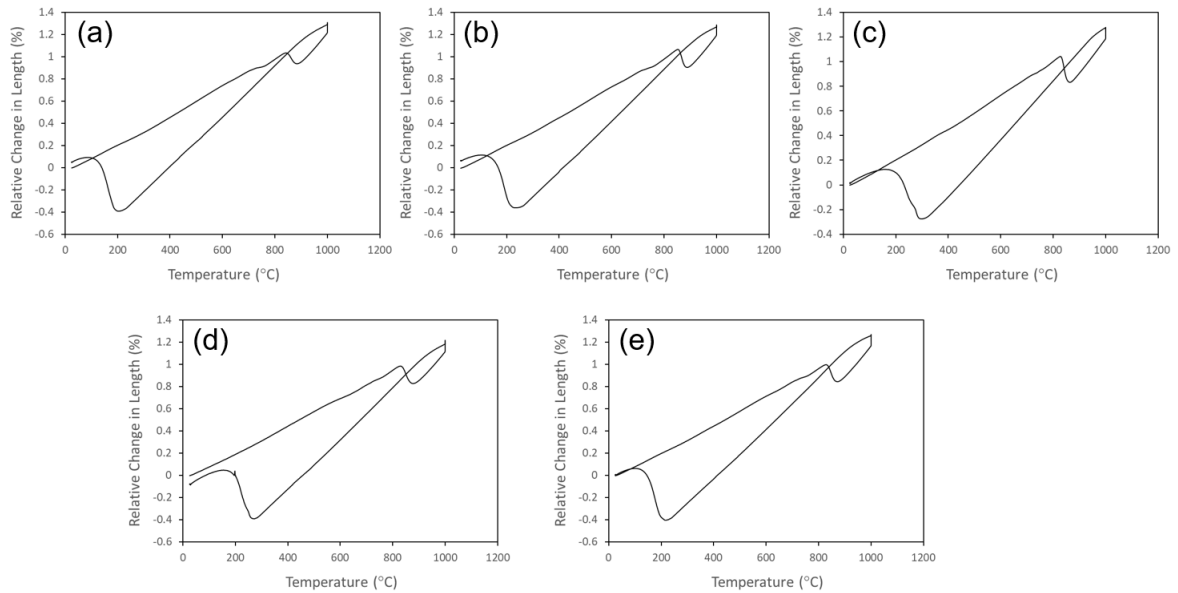
Figure 3.19: Temperature evolution of the relative change in length during continuous heating and cooling of (a) F1, (b) F2, (c) F3, (d) F4, and (e) F5.

3.20. Figure 3.20 shows that martensitic transformation starts at around 340 °C, but another inflection in the curve is shown with the red circle suggests that actually it is possible that most of the martensitic transformation occurs from 270 °C down to the M_f temperature. This could be due to the possible segregation of the alloying elements that leads to inhomogenities in the chemical composition, which leads to a local increment in the M_s temperature. However, as during LPBF the cooling rates are at least 10,000 times faster than the cooling rate applied during dilatometry, this double transformation is expected to disappear.

Ageing of the newly designed alloys

To investigate the precipitation hardening behaviour of the newly designed steels, dilatometry experiments have been carried out using a slower heating rate, comparable with controlled heat treatments in industry followed by rapid quenching. With this
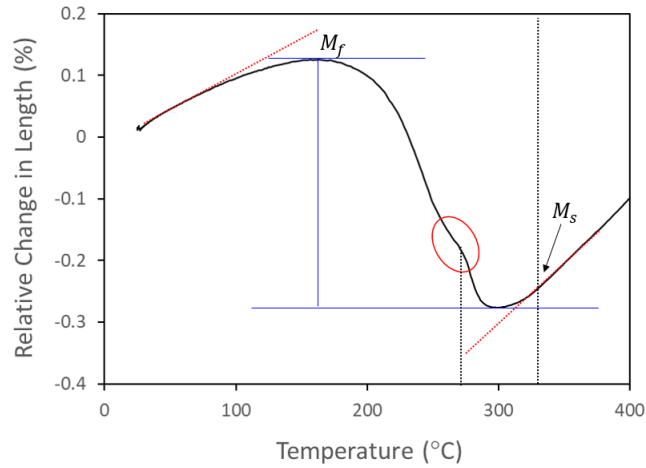
Figure 3.20: Magnified representation of the evolution of the relative change in length for F3 during cooling around M_s temperature.

aim, the cast rods with the same dimensions that was reported before in section 3.4.3 were austenitised at 1050 °C for 60 minutes (alloys SS1–SS3) and at 1000 °C for 90 minutes (alloys F1–F5) using a slow heating rate of 0.05 °C/s. This heating rate typically is regarded as quasi-equilibrium condition. Then, all samples were quenched rapidly with a cooling rate of 100 °C/s. The schematics of the new heat treatment scheme are shown in Figure 3.21.

Figures 3.22 and 3.23 depict the relative change in length as a function of temperature during the slow heating and rapid cooling treatment to capture the contribution of precipitations and determine the ageing temperature. Figures 3.22 and 3.23 show that both alloys experience a change in the slope of the relative change in length during heating at around 500 °C (shown in red in Figures 3.22 and 3.23). This change in the slope is more pronounced in F1–F5 alloys (Figure 3.23) and the slope changes more than once in those alloys. These changes in the slope could be related to precipitation reactions during heating of the alloys.

96
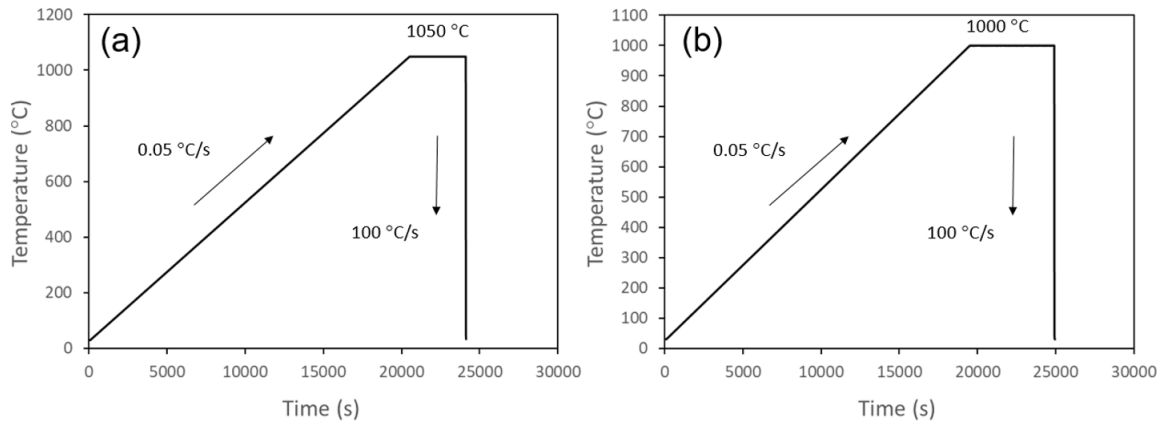
Figure 3.21: Schematics showing slow austenitisation and rapid quenching for (a)SS1-SS3, and (b) F1-F5.
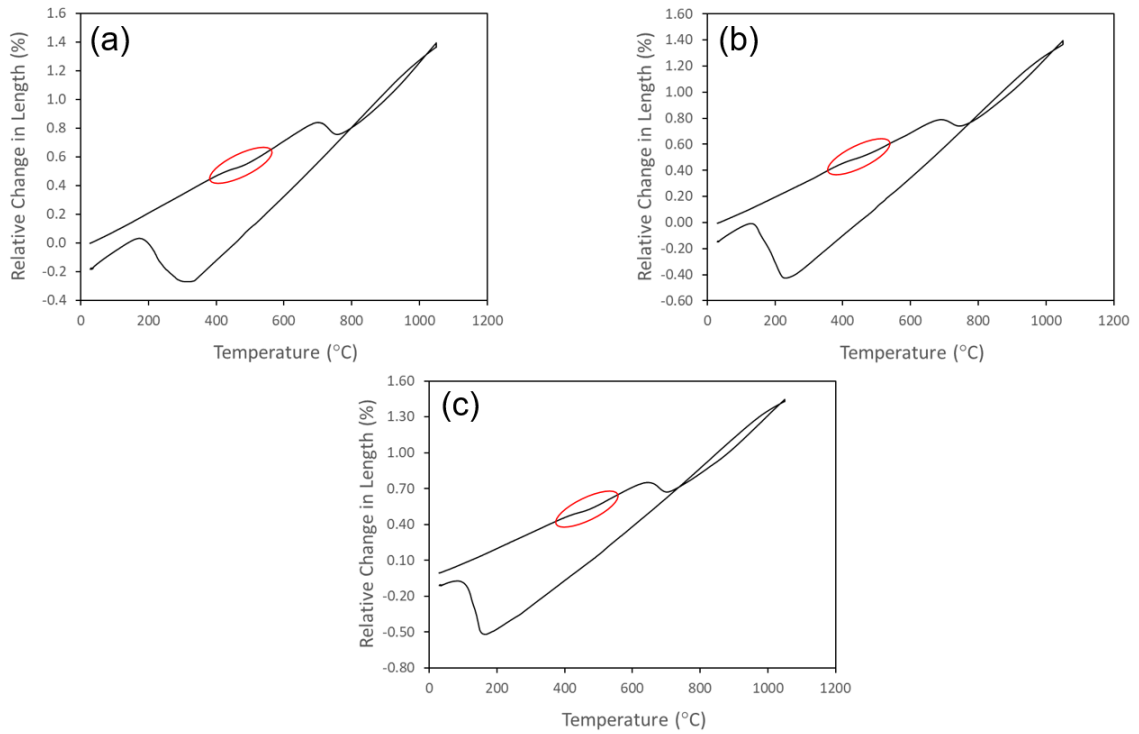
Figure 3.22: Relative change in length during slow heating and rapid cooling of (a) SS1, (b) SS2, and (c) SS3.

97
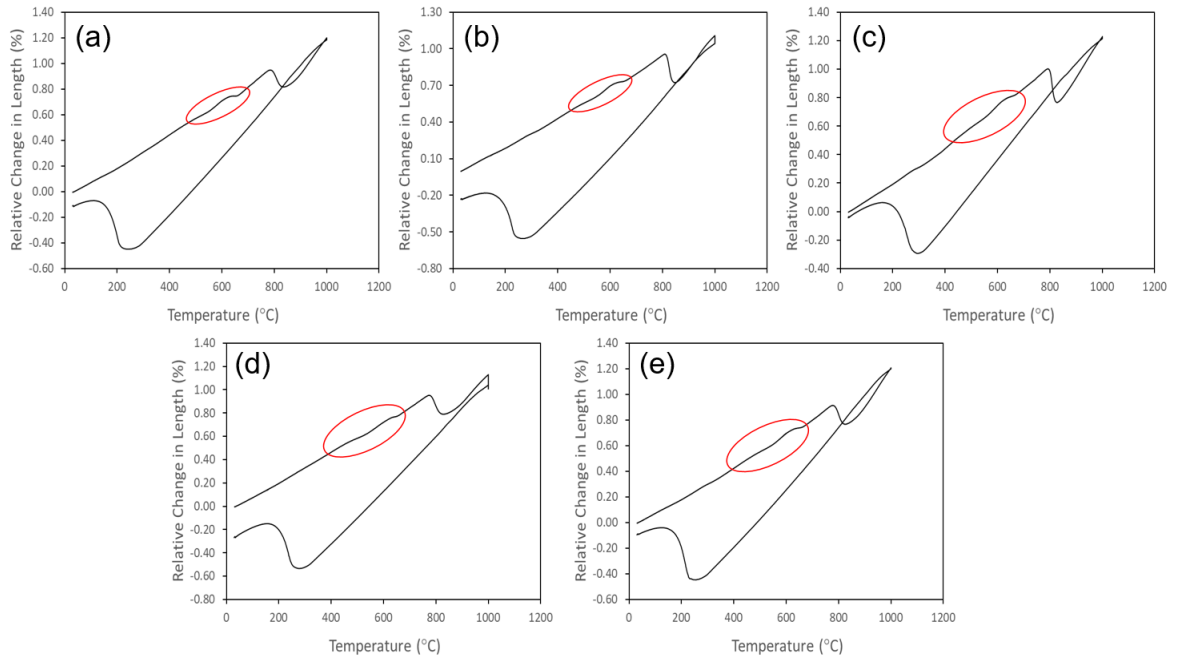
Figure 3.23: Relative change in length during slow heating and rapid cooling of (a) F1, (b) F2, (c) F3, (d) F4, and (e) F5.

In order to capture the precipitation temperatures more accurately, the relative change in length (RCinL) and its variations with temperature (d(RCinL)/dT) are simultaneously plotted as a function of temperature and presented in Figures 3.24 and 3.25 for SS1–SS3 and F1–F5, respectively. Any drops in the derivative of the relative change in length with temperature can be related to a phase transformation or a significant change in physical properties of the material. Figure 3.24 shows that there is a phase transformation starting from around 390 °C and ending at around 510 °C in SS1 and SS3 (orange rectangles, α'+p, in Figures 3.24a and c). It can be related to precipitation of Cu particles in the martenstic (α') matrix. This precipitation seems to take place with two stages in SS2, as there are two distinct changes in the derivative of the relative change in length as a function of temperature; the first clear change in the slope is similar to SS1 and SS2, but the second change is located between around

98

530 °C and 600 °C (two orange rectangles, $\alpha'+p_1$ in Figure 3.24). Upon further slow heating, the next visible peak for all 17-4-type alloys relates to the Curie temperature (Curie T), which is the temperature above which steels lose their magnetic properties. In other words, it is the beginning of austenite (γ) formation, which is shown in Figures 3.24 a-c with a pink rectangle. After transformation of martensite to austenite, there would be a continuous raise in the derivative of the relative change in length with temperature, suggesting that no other phase transformation takes place.
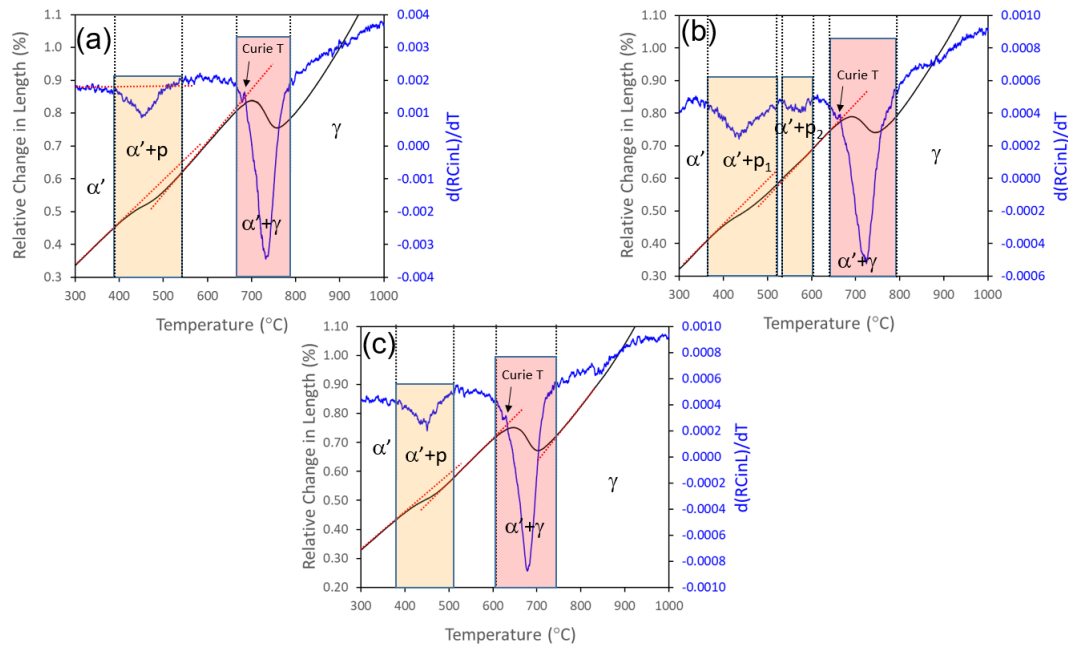
Figure 3.24: Relative change in length (RCinL) and its temperature derivative for (a) SS1, (b) SS2, and (c) SS3.

Figure 3.25 suggests that the phase transformations and physical properties variations are more complicated for F1–F5. The first visible drop in the derivative of the relative change in length with temperature in F1 (Figure 3.25a) occurs in the range of 420 °C – 580 °C, which can be related to precipitation of Cu particles and/or $M_{23}C_6$ carbides, because these steels are designed to be hardened with these two types of
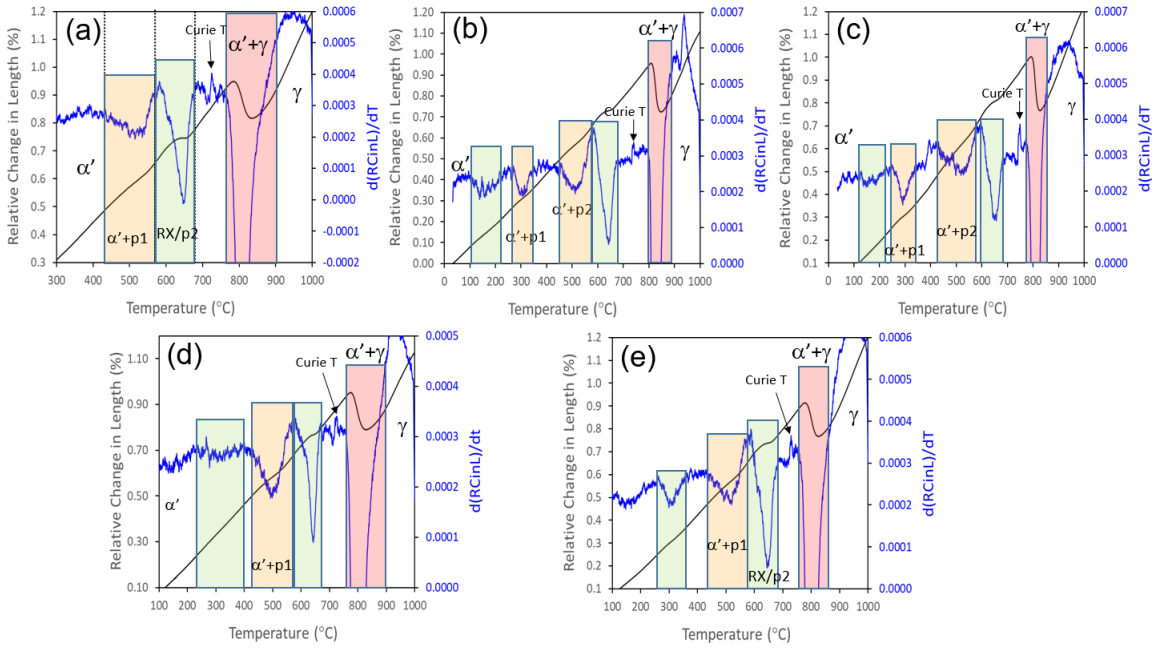
Figure 3.25: Relative change in length (RCinL) and its temperature derivative for (a) F1, (b) F2, (c) F3, (d) F4, and (e) F5.

precipitates upon ageing. The second sharp drop in d(RCinL)/dT (green rectangle in Figure 3.25) occurs at higher temperatures ranging from 580 °C to 680 °C. This could be either because of the second stage of the precipitation and/or the recrystallization (RX) of the martenstic matrix. After that, the Curie temperature can be observed, and then, austenite starts to form from the martensitic matrix upon further heating. F2 and F3 behaviour is similar in the sense that there is a slight drop in d(RCinL)/dT at temperatures around 100 °C – 200 °C (the first green area in Figures 3.25b and c), which could be due to the beginning of precipitation reactions. The second sharp drop in d(RCinL)/dT (the first orange area in Figures 3.25b and c) could be related to the first stage of precipitation, followed by another sharp drop in d(RCinL)/dT at temperatures around 450 °C – 580 °C (the second orange area in Figures 3.25b and c). The second green area in Figures 3.25b and c may be related to recrystal-

lization of martensite and/or the coarsening of the precipitates that formed at lower temperatures. Then, the Curie temperature appears followed by the fully reversion of martensite to austenie upon further heating. Alloys F4 and F5 also behave similarly starting with a stage prior to the main precipitation reactions, followed by recrystallization of martensite and/or precipitation coarsening, and reversion of martensite to austenite (Figures 3.25d and e).

Therefore, based on the dilatometry curves that are presented in this section, an ageing temperature of 450 °C for 4 hours is chosen for SS1 – SS3 alloys. For F1 – F5 alloys an ageing temperature of 500 °C for 4 hours has been chosen. It is worth noting that those ageing temperatures and times are chosen as a starting point for heat treatment optimisation.

Table 3.19 shows the average microhardness of the newly designed marageing steels after ageing heat treatment. The average microhardness of the commercial wrought 17-4 PH SS varies from 310 HV to 430 HV, depending on various solutionising and ageing treatments [196]. It can be seen that even without an optimised heat treatment scheme, the average hardness of the alloys SS1–SS3, which are designed based on the 17-4 PH SS surpass the original existing alloy. This confirms the applicability of the optimisation procedure that has been used in this thesis to design new marageing steels with superior performance. It can be expected that after optimisation of the heat treatment scheme, the hardness could be increased as well. Moreover, as printed alloys have the advantage of higher dislocation density compared to wrought products, it can be expected that the hardness of the printed SS1–SS3 alloys would be increased significantly. The average microhardness of the Formetrix marageing steels after printing, solutionising and ageing is reported to vary between 424 HV–549

HV [213]. The modified Formetrix alloys that are designed in this thesis (F1–F5) in the as-cast + solutionised + aged condition (it is worth noting that the ageing treatment is not optimised) show hardness values of 480 HV–563 HV, which can be improved after ageing optimisation, and especially after printing. This also confirms that the methodology presented in this thesis to design maraging steels with superior mechanical properties is valid.

Table 3.19: Average microhardness of the newly designed maraging steels after ageing heat treatment.

Alloy	Average hardness (HV)
SS1	472±4
SS2	493±7
SS3	486±8
F1	563±10
F2	554±7
F3	506±5
F4	480±8
F5	534±9

3.5   Summary and conclusions

To predict printability of austenitic SSs, a general theory-guided computational alloy design methodology is presented, along with a physics-based model. To prevent formation of solidification cracks during austenitic SS printing, three variables were controlled: the solidification temperature range, the performance index, and the solidification path. Three austenitic stainless steels were designed and compared to existing 316L alloys in order to reduce the development of solidification cracks during laser powder bed fusion. Furthermore, a new crack prevention factor has been identified to predict crack susceptibility.

To avoid defects and porosity during laser powder bed fusion, physics-based models have been combined to estimate melt pool geometry and optimise process parameters while taking into account the material's physical properties. In various combinations of laser powder bed fusion process parameters, process maps have been drawn to identify the safe regions from different types of pores and defects.

To validate the printability model, a 316L alloy with an optimised composition (high crack prevention factor) was chosen. As compared to samples with pores and wrought versions of the same alloy, the formability of the defect-free laser powder bed fusioned 316L alloy was substantially improved. The results of this study will be useful for other types of metallic alloys for production of high-performance parts using laser powder bed fusion. A promising approach for overcoming the long-standing strength-ductility problem in metallic materials is to optimise the chemical composition of the alloy as well as process parameters. The metallic parts or components formed by laser powder bed fusion will become safer when used in heavy load-bearing structures, and less material will be required to achieve the same goal without the need for post-processing. The results presented in this chapter can aid in the expansion of metal additive manufacturing industrial applications.

The requirements for expanding this technique to other alloying systems including maraging steels and precipitation hardening stainless steels have been discussed. Two precipitation hardening alloys of 17-4 PH SS and Formetrix alloy are redesigned to be suitable for laser powder bed fusion, with the same methodology that has been used for designing austenitic stainless steels. Crack prevention, obtaining martensitic matrix upon printing and maximisation of mechanical properties and corrosion resistance are merged together in one single optimisation framework. Eight new alloys with

predicted superior mechanical properties are designed. It has been shown that even the hardness of the cast new alloys without an optimised heat treatment scheme surpasses the hardness of the original existing based alloys. This methodology has also the capability of being applied to various alloying systems such as nickel and high entropy alloys to optimise the chemical composition for laser powder bed fusion.

Chapter 4

Grain refinement mechanisms during laser powder bed fusion

This chapter describes the microstructural features of LPBFed 316L SS developed and produced via the methodology presented in chapter 3. The powder bed undergoes multiple thermal cycles involving complex thermo-mechanical processing during LPBF. At different thermal cycles, different restoration mechanisms such as DRV, DRX, and grain growth can be enabled, resulting in a very fine average grain size. This is modelled via classical and thermostatistical approaches for 316L SS. In addition to the samples introduced in Chapter 3 (Table 3.9), seven more samples are produced with various process parameters and heat input to reveal the role of microstructural evolution on mechanical properties of LPBFed 316L SS. Microstructural features are characterised using OM, SEM, TEM, and EBSD. Each grain experiences different microstructural evolution as a result of several subsequent thermal cycles in each layer. The development of a highly deformed cellular microstructure and the formation of deformation nanotwins are caused by the high cooling rate solidification in the first

thermal cycles. To induce grain refinement, the next thermal cycles activate CDRX, DDRX, and DRV.

4.1 Introduction

Owing to the heating and cooling cycles, dislocation multiplication and thermally activated softening or restoration processes (DRV and DRX) occur during LPBF [214]. The well-known Kocks-Mecking equation [137, 112] can be used to model and explain these phenomena. A plastic strain is imposed on the material at high temperatures in thermo-mechanical processes such as hot rolling or forging, and DRX may occur when a critical strain is reached [126]. The classic Zener-Hollomon analysis [123] and the thermostatistical method suggested by Galindo-Nava and Rivera-Díaz-del-Castillo [128, 127] provide analytical expressions for calculating this critical strain as a function of strain rate and temperature. They have been described in section 2.4.3 and they will be used to model DRX and DRV in this chapter. Variations in flow stress caused by DRX softening can directly influence yield strength at room temperature through the final dislocation density [112].

The occurrence of DRX during LPBF has never been previously investigated comprehensively. As heat is dissipated during cooling, it causes extreme plastic deformation, which, when combined with the high temperatures during LPBF processing, can be treated as a thermo-mechanical process with ultra-high strain rates. The activation of DRX and DRV during LPBF is investigated in this chapter using both classical and thermostatistical theories. To explain the thermal cycles during layering in LPBF of 316L SS, thermal analysis is carried out using empirical and simulation results. Experiments are carried out with and without optimised process parameters

to see if DRX and DRV can be enabled during LPBF and what effect this has on the microstructure of the as-built samples.

4.2   Experimental procedure

In Chapter 3, it has been mentioned that three batches of 316L SS were produced with LPBF with various process parameters. The samples from batch 3 (see Table 3.9) showed full density and the best mechanical properties. Therefore, those samples are chosen for microstructural investigations. In addition to these samples, to spread a range of heat inputs and microstructures, a new set of samples with various process parameters have been produced with a Renishaw plc (UK) AM125 machine equipped with a laser spot size of 70 μm in an argon atmosphere (in the University of Sheffield; samples produced by the operator in The University of the Sheffield). Cubic samples of size 3×3×3 mm^3 are produced for microstructural characterisation, using the process parameters and corresponding heat inputs (determined by normalised enthalpy, H_n) listed in Table 4.1. All the samples were produced with a meander scan strategy with a 67° rotation after each layer is built. The powder bed temperature was kept at 80°C during LPBF to reduce residual stresses.

Microstructural characterisation was performed on the cubic samples from macro to nano-scale using a variety of characterisation tools. For porosity characterisation, unetched optical micrographs (OM, Leica DFC295) are used. OM images were processed with ImageJ software to quantify porosity contents. Moreover, Aqua Regia etchant, which is a mixture of hydrochloric acid, nitric acid and water, has been used to etch the samples for microstructural investigations through optical microscopy. SEM (Tescan Mira 3 LMHP field emission SEM) was used for characterisation of

Table 4.1: Processing parameters including laser power (P), scan speed (v), layer thickness (t) and hatch distance (h) used for LPBF processing. The corresponding H_n for each experimental set is also shown.

Sample	P (W)	v (m/s)	t (μm)	h (μm)	H_n
S1	100	1	20	70	5.1
S2	200	0.33	50	110	6.32
S3	200	0.30	50	110	6.62
S4	200	0.56	50	110	4.85
S5	200	0.47	50	110	5.3
S6	200	0.45	50	110	5.4
S7	200	0.40	50	110	5.74
S8	200	0.66	50	110	4.46

solidification cellular structures, and morphology of grains. SEM equipped with an EBSD detector (OXFORD Instrument symmetry) at a scanning step size of 0.8 μm was used to reveal orientation of grains, texture, characteristics of the grain boundaries, and recrystallized fraction. SEM and EBSD characterisation was done in The Beihang University, China. EBSD analysis were performed using HKL Channel 5 software (by the author of the thesis). Three mm diameter disks were machined out of the samples and ground to a thickness of 50 μm and then thinned using the Gatan 691 Type Ion Beam Thinner for TEM. The specimens were examined using a TECNAI G20 TEM operated at 200 kV. TEM characterisation was also done in the Beihang University, China, and the analysis performed by the author of the thesis.

To estimate the critical strain for the activation of DRX, tensile testing was performed using flat tensile samples produced with the same process parameters listed in Table 4.1 with a gauge length of 35 mm and thickness of 1.2 mm. Tensile testing was done under a strain rate of 10^{-4} s^{-1} at room temperature using an Instron 3382 universal testing machine with load axis parallel to the build direction. Yield strength of the samples were correlated with hardness to estimate the residual plastic strain in

LPBFed samples. The Vickers hardness testing was performed with a load of 300 g.

4.3 Microstructural characterisation of the LPBF as-built samples

4.3.1 Porosity characterisation

Porosity characterisation has been done using optical micrographs of the polished samples before etching. Figures 4.1-4.8 show various optical unetched micrographs that have been used to measure porosity contents in S1-S8 statistically. All the images are taken from the surface of the sample along various directions compared to the building direction, BD (three directions of BD, transverse direction (TD), and normal direction are shown in Figures 4.1-4.8).

After post-processing the images shown in Figures 4.1-4.8 from ImageJ software, the porosity contents of the LPBFed samples are summarised in Table 4.2. In here, only S1 has produced with the optimised parameters, so that a fully-dense material can be compared with other samples with various contents of pores.

Table 4.2: Porosity contents of the LPBFed samples produced with various process parameters.

Sample	Porosity (%)
S1	0.03±0.01
S2	1.51±0.19
S3	1.19±0.11
S4	2.12±0.11
S5	0.62±0.04
S6	1.26±0.1
S7	1.41±0.12
S8	2.93±0.16
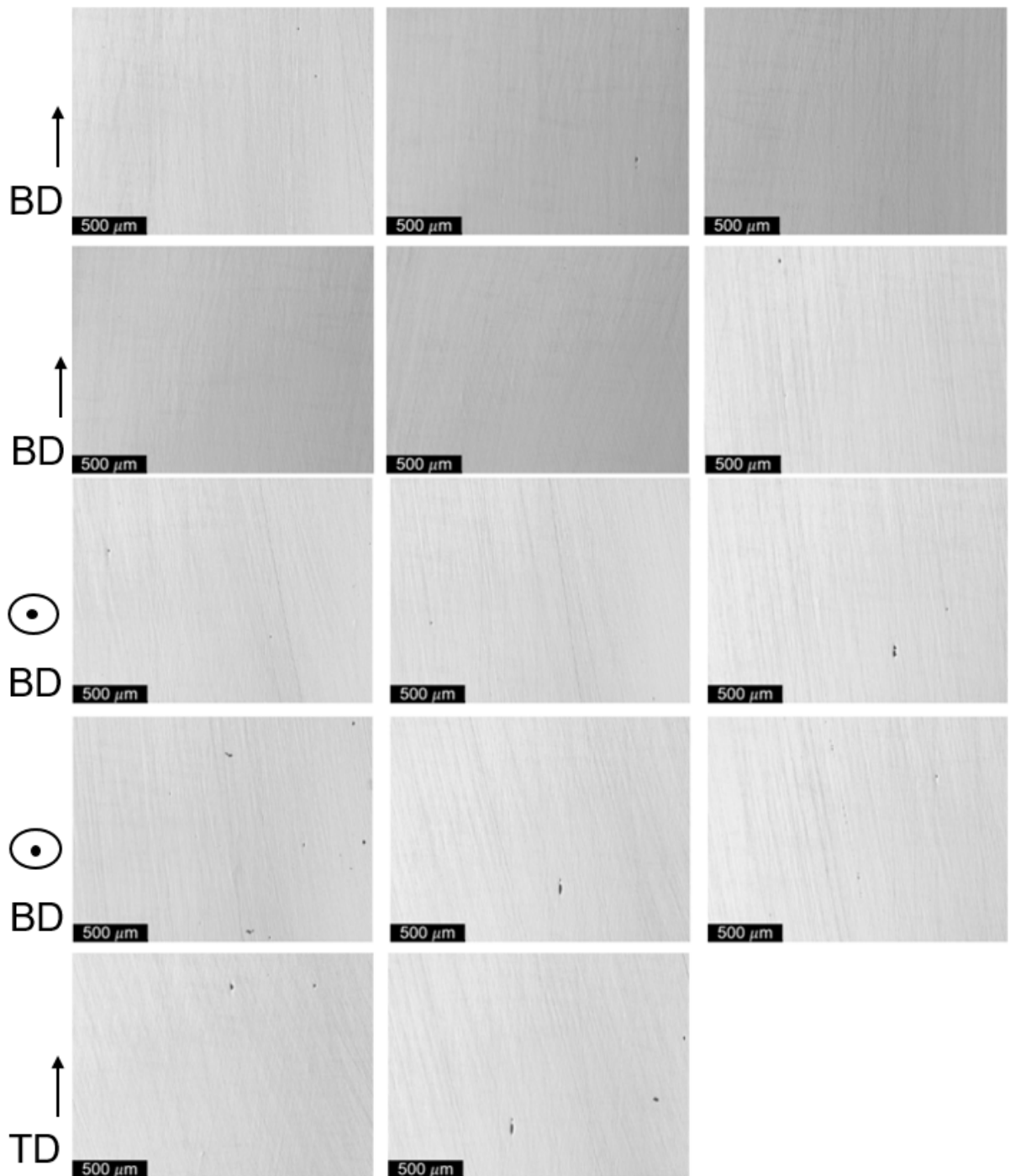
Figure 4.1: Optical micrographs of polished S1 used for porosity measurements.
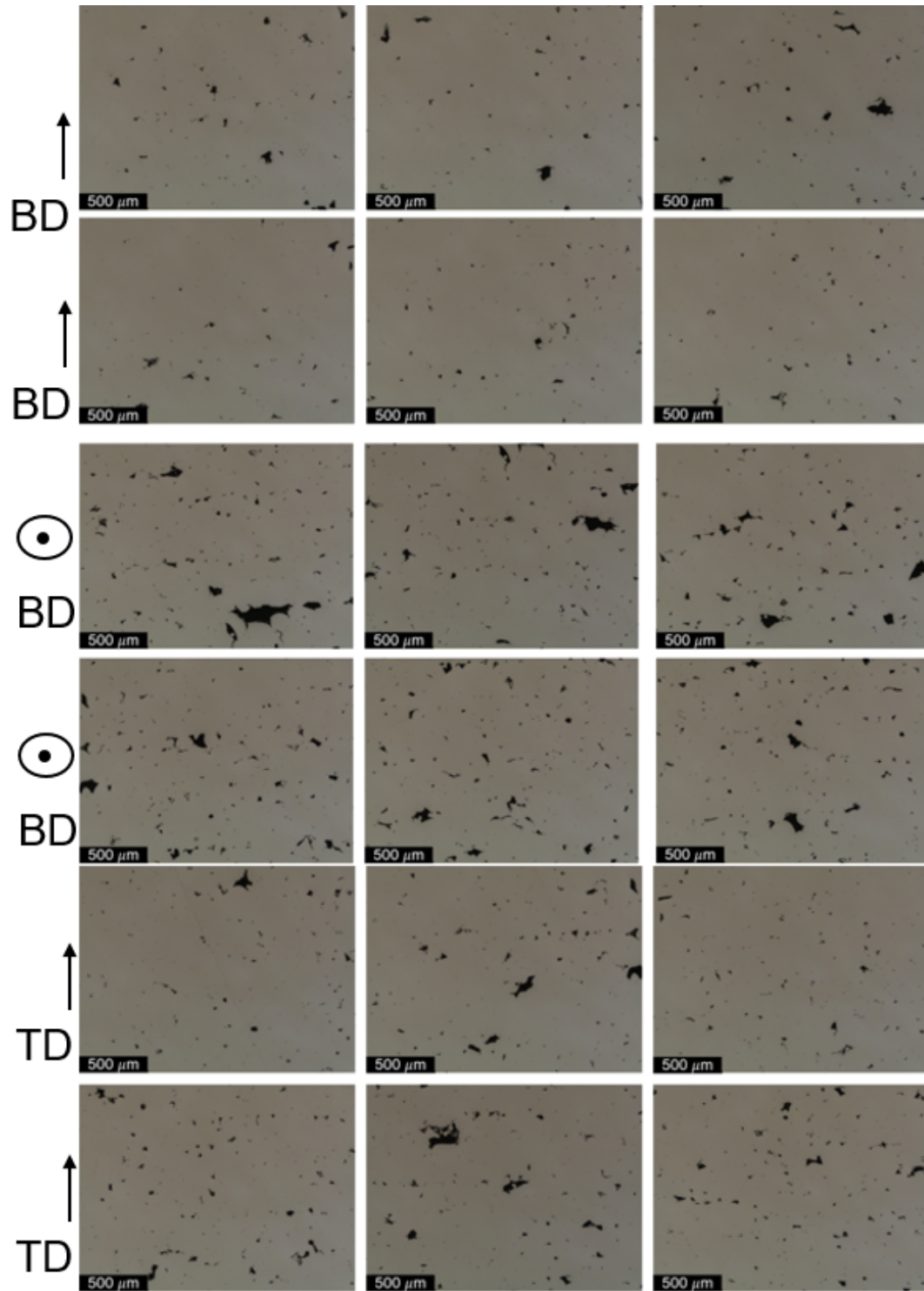
Figure 4.2: Optical micrographs of polished S2 used for porosity measurements.
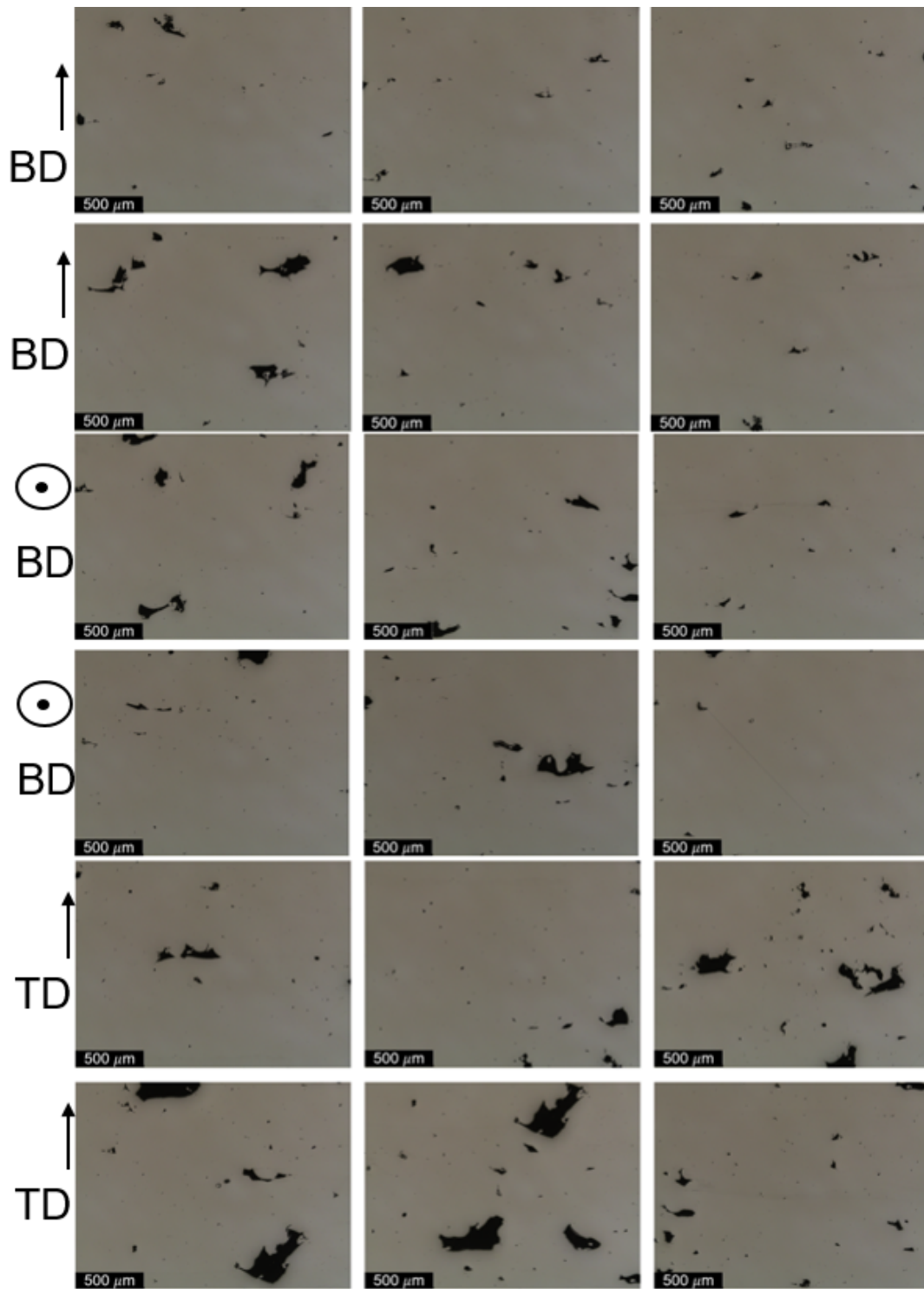
Figure 4.3: Optical micrographs of polished S3 used for porosity measurements.
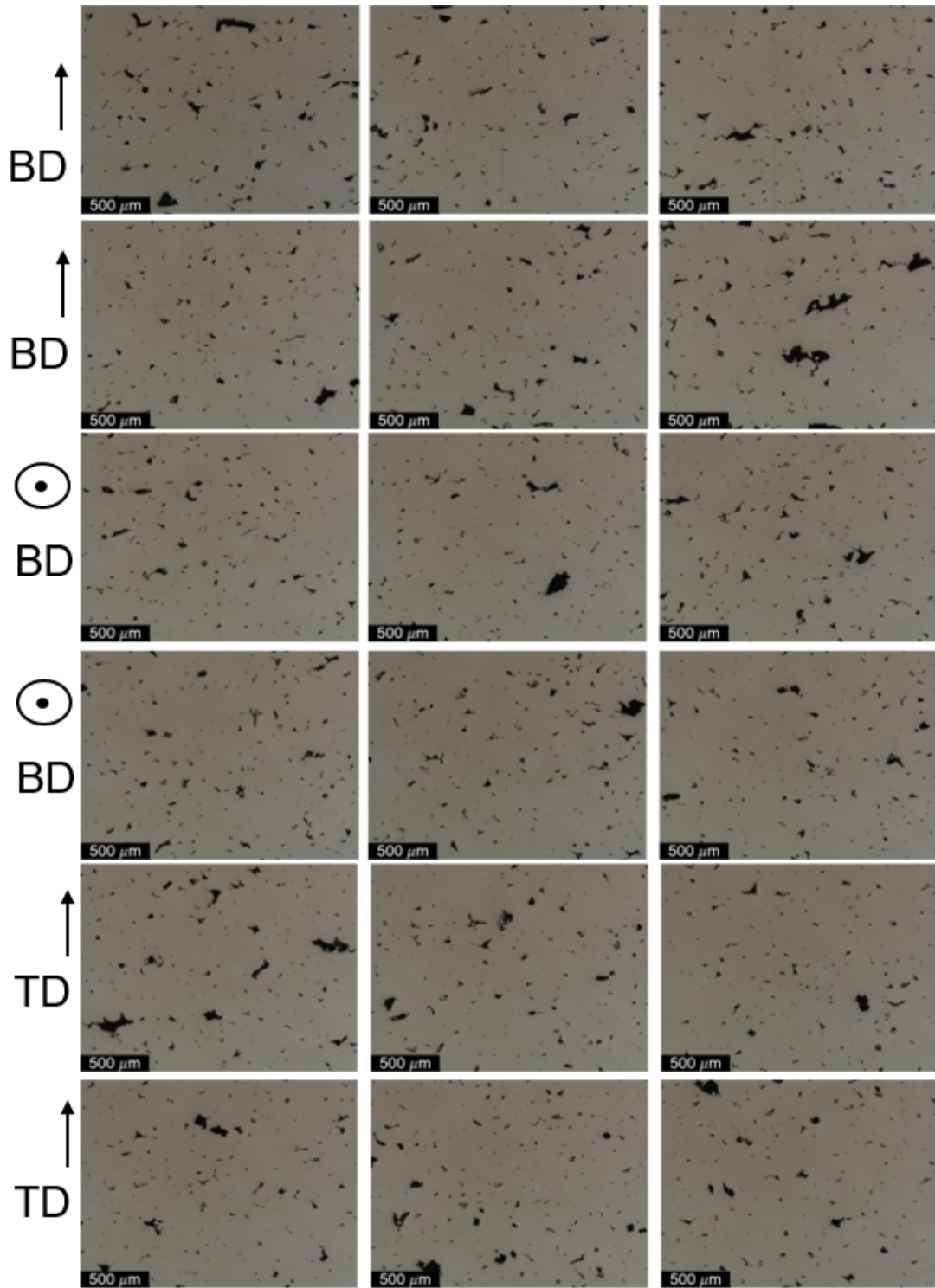
Figure 4.4: Optical micrographs of polished S4 used for porosity measurements.
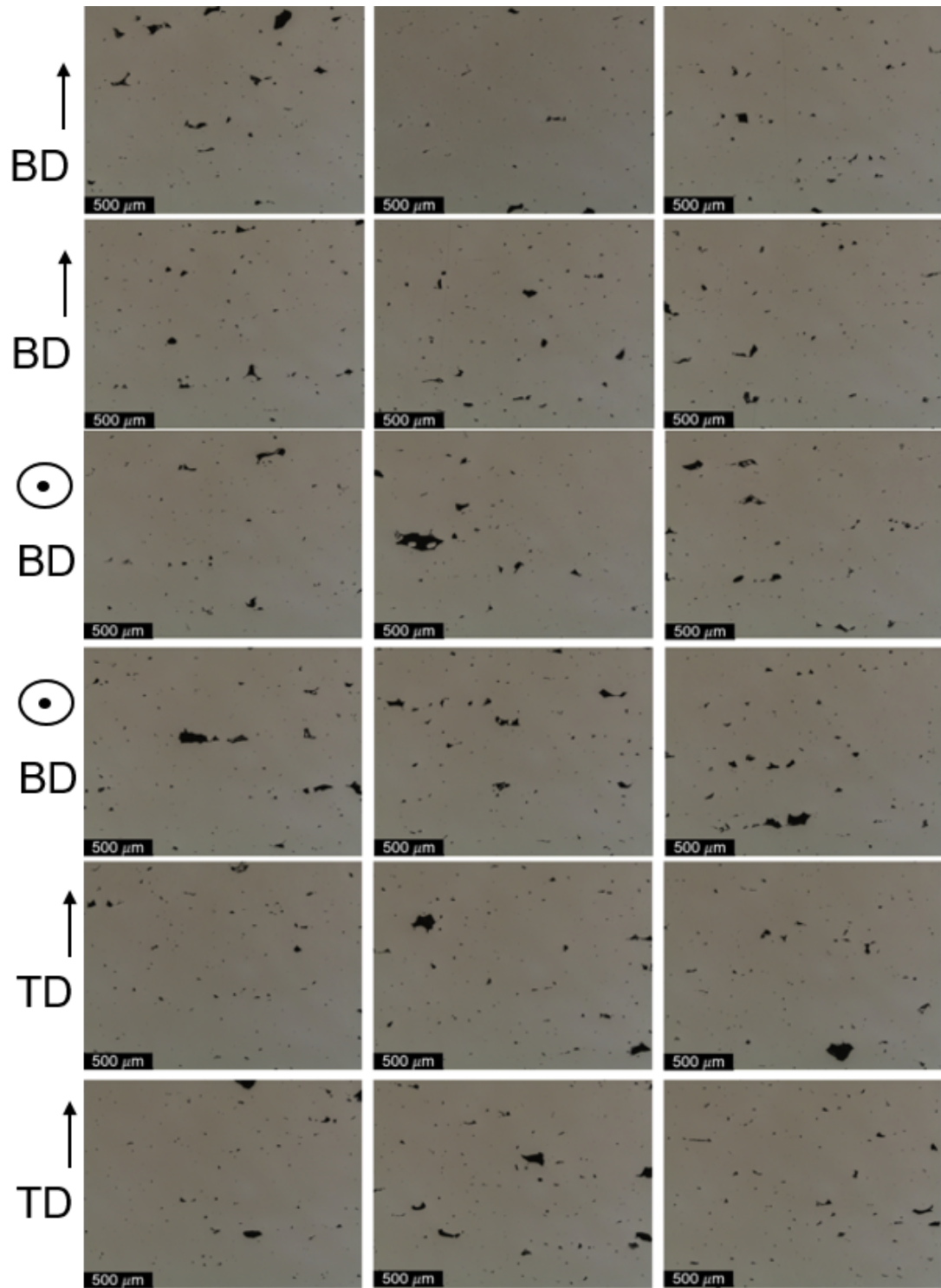
Figure 4.5: Optical micrographs of polished S5 used for porosity measurements.
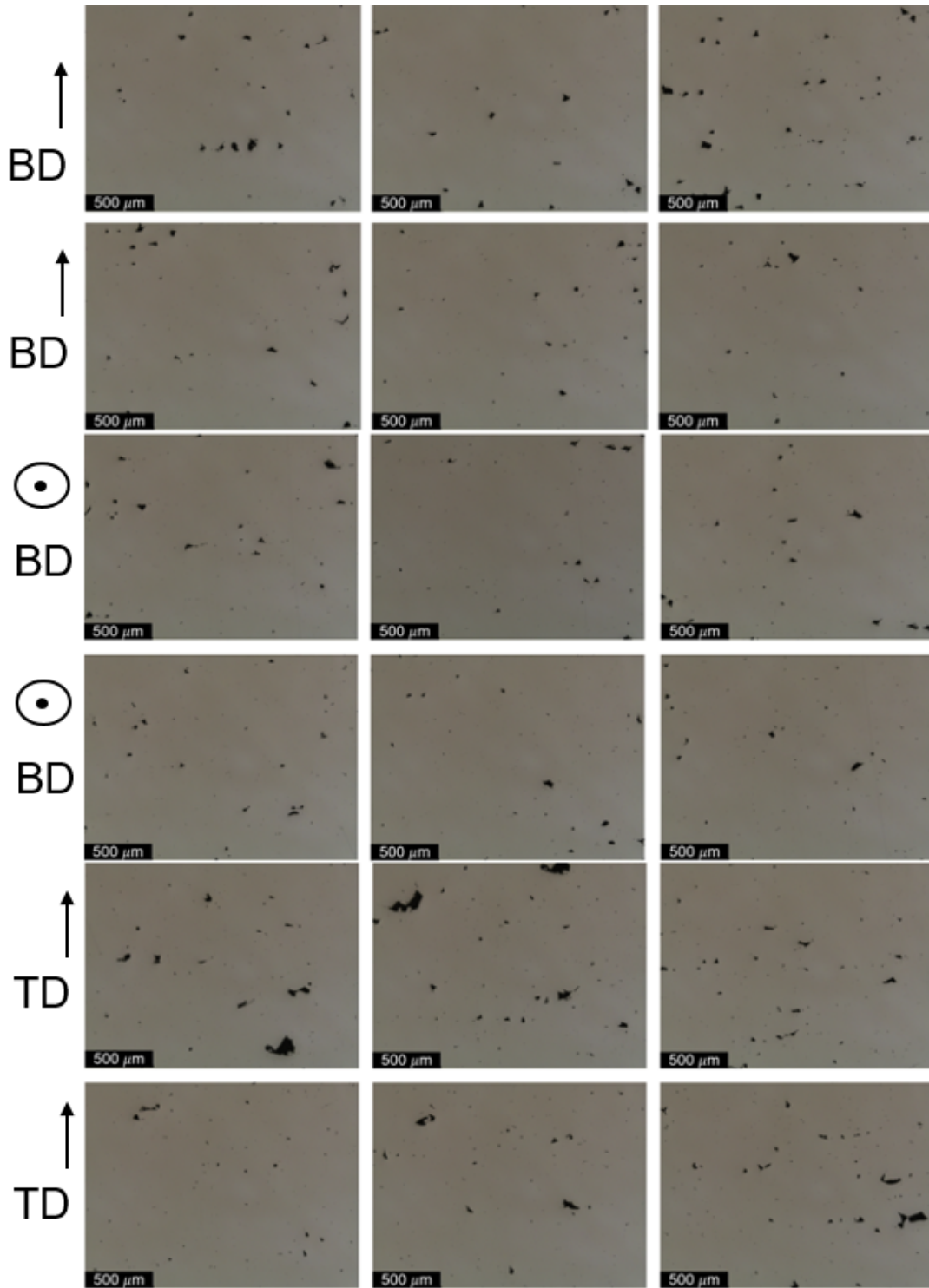
Figure 4.6: Optical micrographs of polished S6 used for porosity measurements.
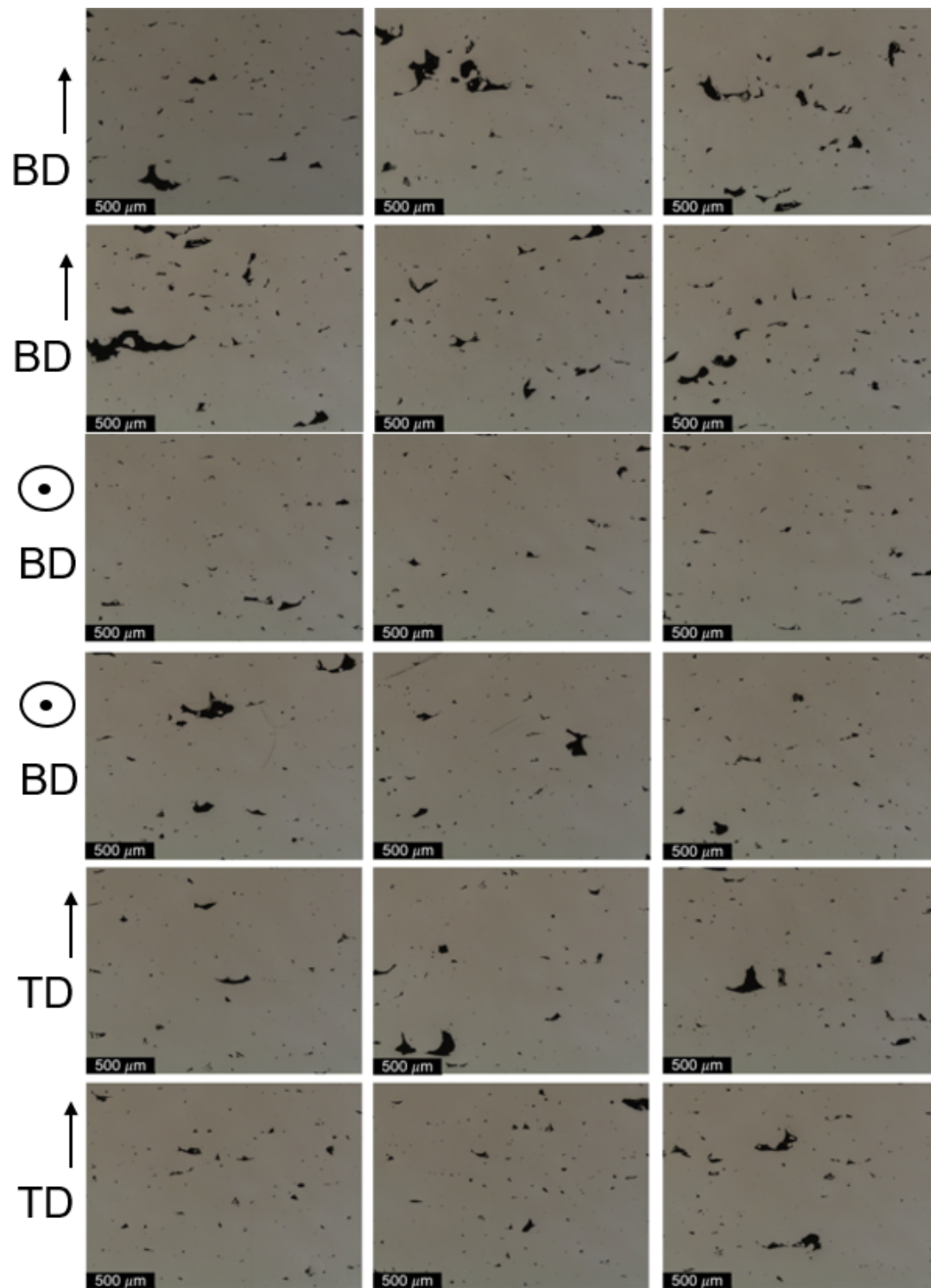
Figure 4.7: Optical micrographs of polished S7 used for porosity measurements.
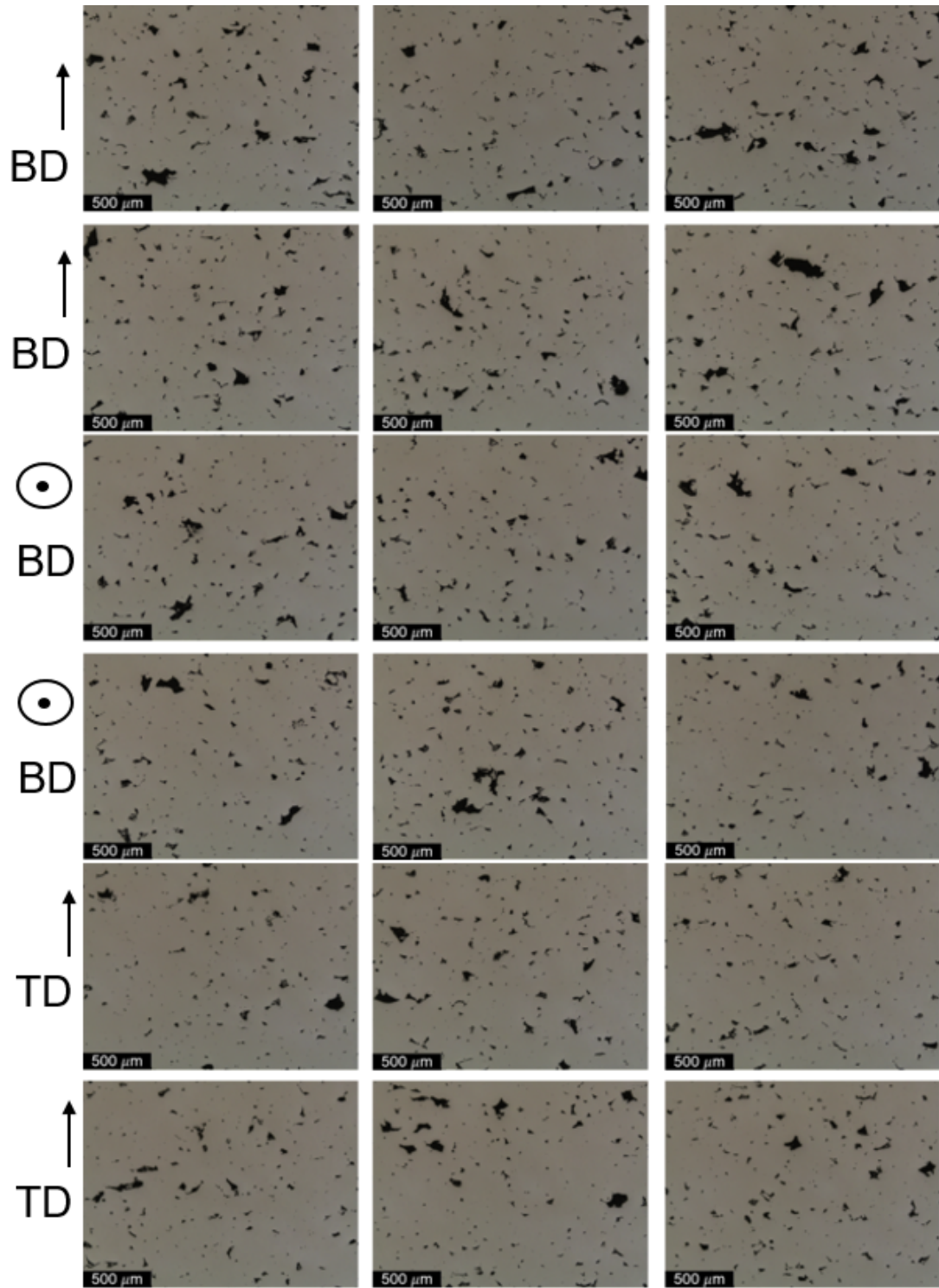
Figure 4.8: Optical micrographs of polished S8 used for porosity measurements.

4.3.2 Optical microscopy

In Figure 4.9, optical microscopy analysis of 316L SS samples after LPBF, and perpendicular to build direction reveals visually distinct melt pools, which reflect the solidification pattern during LPBF. Solidification occurs along the heat gradient within each melt pool. A columnar grain growth pattern is also visible across melt pools, except from S4, in which a columnar dendritic growth dominates solidification morphology. Such columnar grains result from epitaxial solidification in a layer-by-layer manner during LPBF. The presence of columar dendritic structure in S4 can be related to its lower heat input compared to other samples (see Table 4.1), where the branching activity and tip interaction are reduced, resulting in cellular like dendritic arrays with a high degree of disorder.
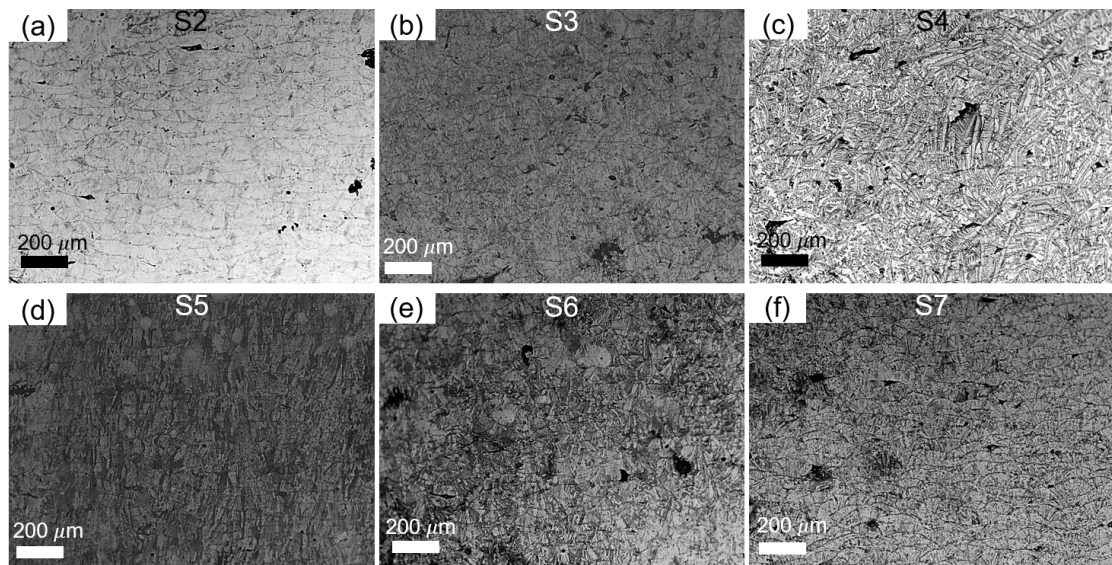
Figure 4.9: Optical micrographs of etched samples perpendicular to build direction. (a) S2, (b) S3, (c) S4, (d) S5, (e) S6, and (f) S7.

The presence of pores can also be recognised after etching the samples. Due to their H_n, S2, S3, and S7 (Table 4.1) are prone to keyhole-induced pore formation

(based on the modelling approach presented in Chapter 3). Keyhole-induced pores, which have a spherical morphology can be observed in Figure 4.1a, 4.1b, and 4.1f, which represent S2, S3, and S7 microstructures. Spherical pores are rarely seen in the other samples with normalised enthalpies less than 5.5, however, some keyhole-induced pores can be recognised in S5 and S6 (Figures 4.1d and 4.1e, respectively) as their H_n (5.3 for S5 and 5.4 for S6) are close to the critical H_n for keyhole-induced pore formation. Lack of fusion pores with irregular morphology can also be seen in S2-S7, which can be attributed to very high layer thickness. It has been reported that the presence of lack of fusion has detrimental effects on the ductility of LPBF alloys [58]. This will be investigated in the next chapter. Despite the overall information about the morphology of grain growth, solidification characteristics and pore morphology and content, optical microscopy revealed no major microstructural changes resulted from the variation in processing parameters.

4.3.3   Scanning electron microscopy

SEM microstructural analysis of as-built samples in a cross-section perpendicular to the building direction (BD, indicated by the white arrow in Figure 4.10a) reveals a sub-grained cellular microstructure, as shown in Figure 4.10. During LPBF, ultra-fast cooling rates prevent the formation of equiaxed grains that are observed in conventionally-manufactured alloys, resulting in this cellular pattern [185, 163]. This typical microstructure has been frequently reported for LPBFed 316L SS [215, 17]. Long columnar grains can be observed in the building direction. The temperature gradient during processing causes the austinite favoured $< 001 >$ growth path during solidification, and epitaxial grain growth from the grains of the previous layer all

contribute to the formation of such long columnar grains [216, 217]. Due to their preferred growth path, columnar and cellular solidification substructures within columnar grains are thought to be primary dendrites without secondary arms (Figure 4.10). On the cross section, cells with a diameter less than 1 μm expand cylindrically in different directions. Different morphologies of solidification cellular structures are evident in Figure 4.10a and 4.10d.
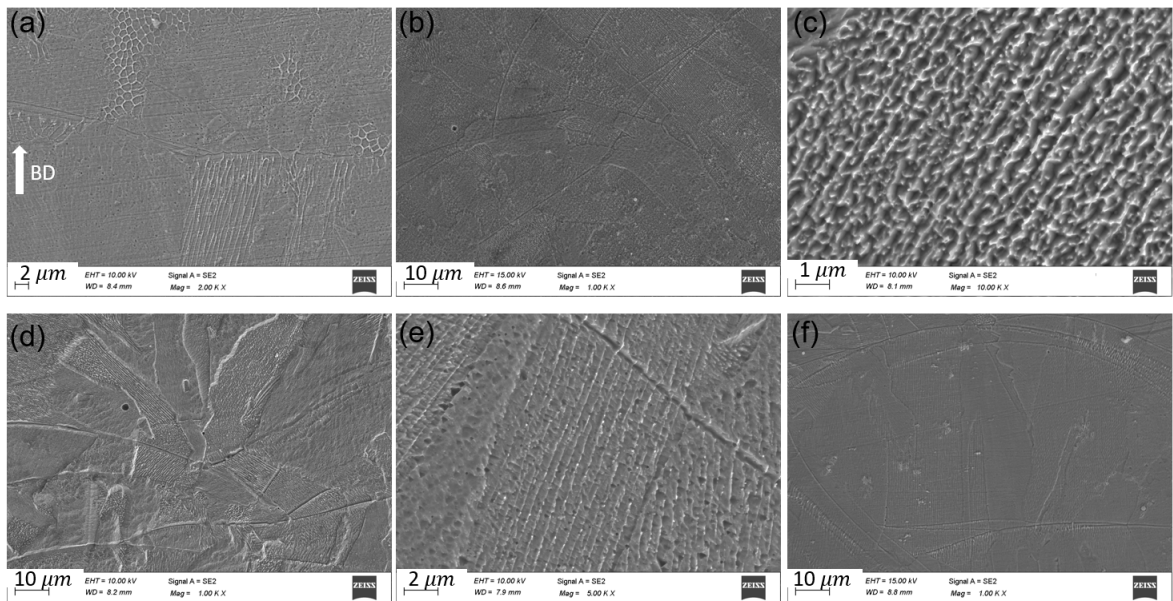
Figure 4.10: SEM micrographs of the as-built samples. (a) S2, (b) S3, (c) S4, (d) S5, (e) S6, and (f) S7.

4.3.4 Electron backscattered diffraction

In order to reveal the microstructural evolution of the as-built samples, EBSD analysis is performed. Figure 4.11 shows a representative EBSD inverse pole figure (IPF) map of 316L SS after LPBF processing with various parameters from the centre of cubic samples. All the samples showed a mixture of equiaxed and columnar grains

with no orientation preference, and a bimodal grain size distribution. The average grain size of the samples are measured at least from two EBSD images per sample, containing more than 1000 grains per image. The average grain size of the samples, considering both LAGBs and HAGBs, and without considering LAGBs (actual grain size, d_G) are measured and listed in Table 4.3. The large variations between the average grain size and the actual grain size indicates the pronounced role of LAGBs in the microstructure of the LPBFed samples. It should be noted that in EBSD measurements, all LAGBs, including the complete and incomplete boundaries are taken into account. The respective aspect ratio of the samples are also listed in Table 4.3. This indicates that S2-S8 are more equiaxed and S4 underwent a more inhomogeneous grain refinement mechanism.
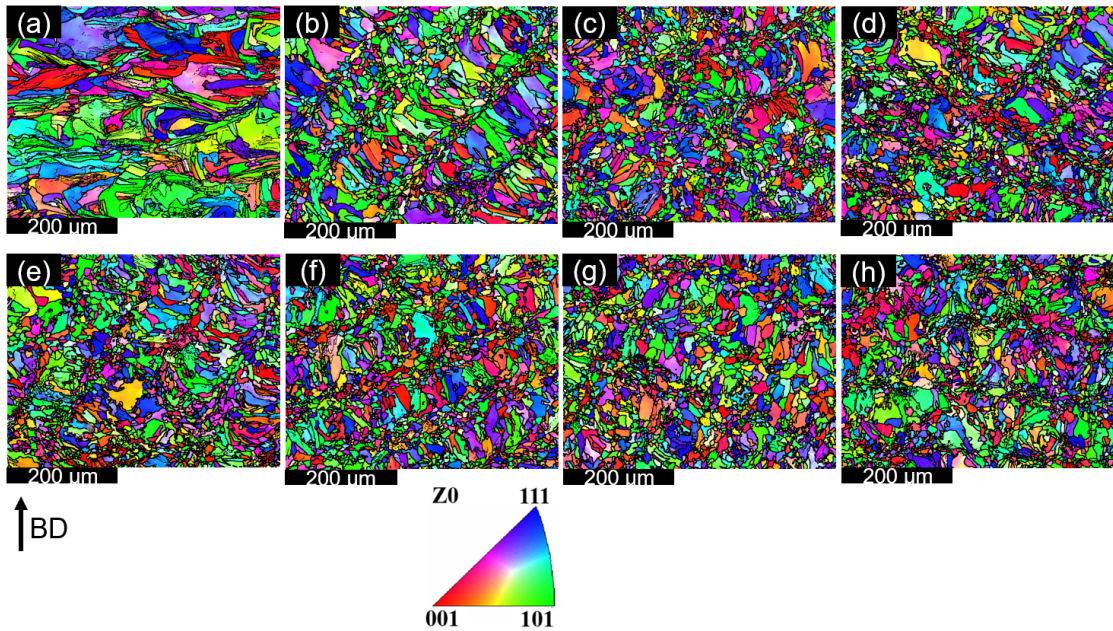
Figure 4.11: EBSD IPF micrographs of 316L SS built with different process parameters: (a) S1, (b) S2, (c) S3, (d) S4, (e) S5, (f) S6, (g) S7, (h) S8.

In order to reveal the nature of the grain refinement mechanism during LPBF,

Table 4.3: Average grain size, actual grain size, and average aspect ratio of the grains of different LPBFed as built samples.

Sample	Average grain size (μm)	Actual grain size, d_G (μm)	Aspect ratio
S1	4.7±2	35±9	2.45
S2	13±3	27±4	1.8
S3	11.2±5	22±5	1.8
S4	8±3	19±10	2
S5	16±5	33±2	2
S6	6±4	35±2	2
S7	8±3	30±2	1.9
S8	5.3±4	20±9	2

recrystallized maps were produced for various samples. A representative of the recrystallized fraction map of various LPBFed as-built samples is shown in Figure 4.12. Fully recrystallized, substructured, and deformed (heavily dislocated) grains are displayed as blue, yellow, and red, respectively. The internal average misorientation angle within each grain is measured by Channel 5 software, and if it exceeds 15°, the grain is considered as deformed. A grain is classified as substructured if it has internal misorientation of less than 15° but misorientation through subgrains of more than 15°. The grains that remain are classified as recrystallized. From Figure 4.12, the fraction of recrystallized, substructured, and deformed grains of the as-built samples are listed and presented in Table 4.4. From Table 4.4, it can be seen that recrystallized fraction is more pronounced in S3-S8, while there is only 5 and 7% of recrystallized grains in the microstructure of S1 and S2. The deformed structure, on the other hand is more pronounced in S1 and S2 compared to the rest of samples. All samples contain high contents of substructured grains, which underwent DRV/partial recrystallization and believed to have dislocation densities in between the recrystallized (very low dislocation density), and deformed (heavily dislocated) grains. This suggests that restoration mechanisms played a significant role during LPBF of 316L SS, resulting

in grain refinement in all samples.
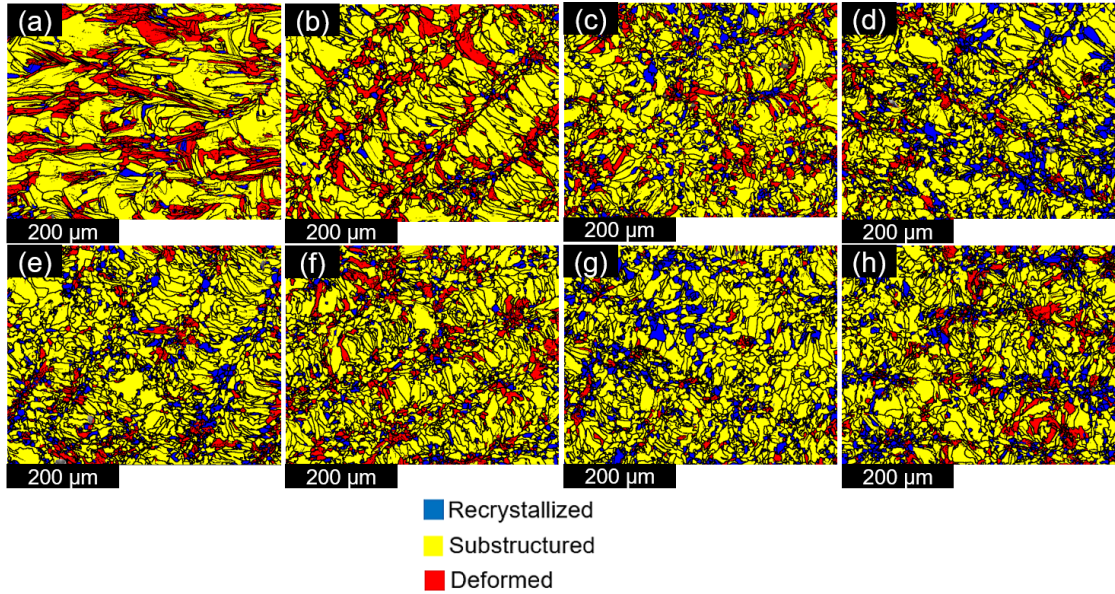
Figure 4.12: Recrystallization maps of the as-built samples: (a) S1; (b) S2; (c) S3 and (d) S4; (e) S5; (f) S6; (g) S7; (h) S8. Blue, yellow and red represent recrystallized, substructured and deformed grains, respectively.

Table 4.4: Average fraction of recrystallized, substructured, and deformed grains of the LPBFed as-built samples.

Sample	Recrystallized fraction	Substructured fraction	Deformed fraction
S1	0.05	0.59	0.36
S2	0.07	0.66	0.27
S3	0.13	0.68	0.19
S4	0.18	0.7	0.12
S5	0.16	0.71	0.13
S6	0.12	0.69	0.19
S7	0.18	0.77	0.05
S8	0.16	0.69	0.15

Since recrystallized and recovered/partially recrystallized (substructured) grains can be seen in the LPBFed samples, further research has been done to establish the presence, sequence, and nature of DRX and DRV. Figure 4.13 illustrates the

distribution of LAGBs (boundaries with misorientations between 2° and 15°), and HAGBs (boundaries with misorientations ≥15°) in all samples. The respective volume fraction of LAGBs and HAGBs of each sample are reported in Table 4.5. Table 4.5 shows that the majority of boundaries are HAGBs in S3-S8. LAGBs and HAGBs are equal in S2, but 70% of the total grain boundaries in S1 are LAGBs. All samples have numerous incomplete LAGBs (indicated by white arrows in Fig. 4.13) within the grains with HAGBs, which is a characteristic of CDRX [218, 144]. In general, DRX structures have such a wide distribution of LAGBs and HAGBs fractions [219]. When comparing Figures 4.12a and 4.13a, it can be seen that the majority of the deformed grains have a high density of substructures (LAGBs), which may contribute significantly to strengthening mechanisms in S1. LAGBs of this type can be seen in S2-S8 (Figures. 4.13b-h), but to a lesser extent.
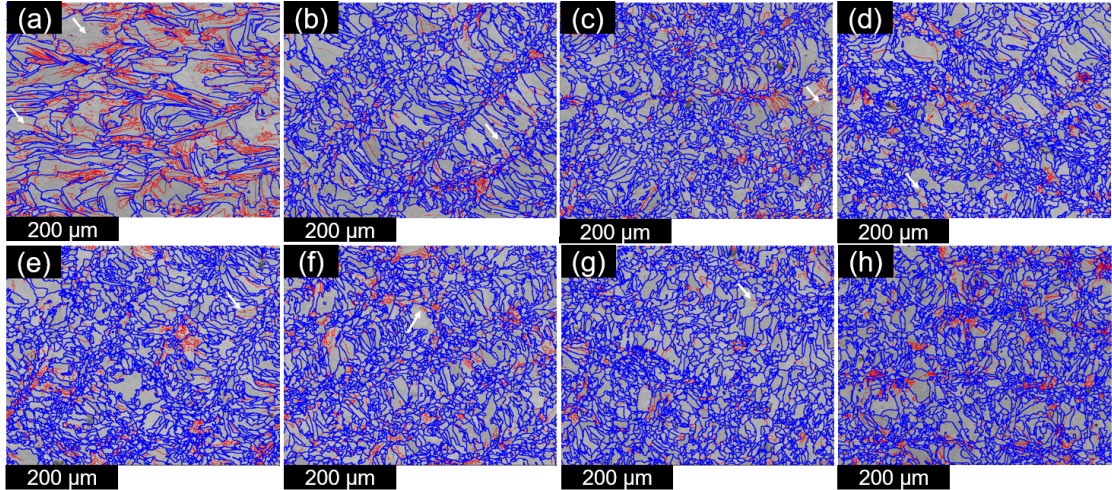
Figure 4.13: LAGB and HAGB distribution map of (a) S1, (b) S2, (c) S3, (d) S4, (e) S5, (f) S6, (g) S7, and (h) S8. LAGBs (<15°) are coloured red and HAGBs (≥15°) are coloured blue. White arrows show incomplete LAGBs.

During thermo-mechanical processing, FCC alloys are prone to formation of annealing twins, after restoration mechanisms such as DRV and DRX are activated; this

Table 4.5: Volume fraction of LAGBs, HAGBs, and annealing twins of the LPBFed as-built samples.

Sample	LAGBs fraction	HAGBs fraction	Annealing twins fraction
S1	0.7	0.3	0.02
S2	0.5	0.5	0.12
S3	0.45	0.55	0.12
S4	0.38	0.62	0.12
S5	0.4	0.6	0.13
S6	0.4	0.6	0.14
S7	0.39	0.61	0.15
S8	0.38	0.62	0.14

is a part of grain growth [220]. The distribution of $\Sigma 3$ boundaries (twin boundaries) in the as-built samples is shown in Figure 4.14. During processing, extreme twinning occurred in S2-S8 ($\sim$ 0.12-0.14 of the total boundaries). In S1, however, the existence of annealing twins is minimal. Table 4.5 also lists the fraction of twin boundaries in different samples. The twins were not uniformly distributed in the S2-S8 samples; they were mostly found in the recrystallized regions and fine deformed areas (Figures. 4.12b-h and Figures. 4.14b-h). The formation of such high number of annealing twins and large fractions of HAGBs during LPBF in samples S2-S8, as well as the absence of annealing twin boundaries and evolution of large fraction of LAGBs in S1 can be attributed to the various DRX mechanisms activated during LPBF of 316L SS with various process parameters.

The microtexture of the grains in S1 is shown in Figure 4.15 since texture evolution is thought to be affected by DRX and DRV [221]. With a volume fraction of 32%, the most dominant texture is $< 110 >$-fibre (green). $< 111 >$-fibre (blue), $< 100 >$-fibre (red), and the Cube (pink) are next, with percentages of 23, 18, and 10%, respectively. It can be seen that no particular texture is associated with any specific grain form, implying that DRX mechanisms are activated during LPBF of 316L SS, as DRX is
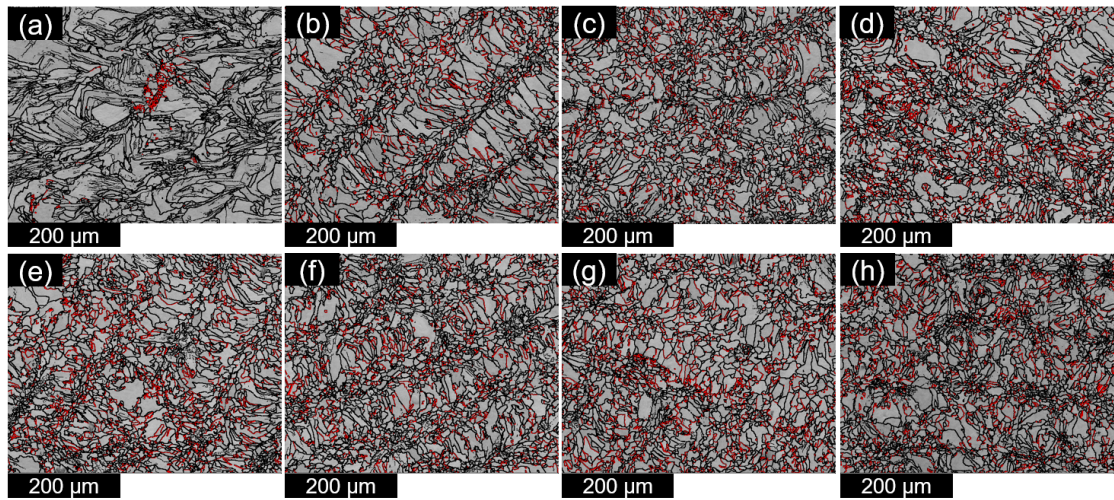
Figure 4.14: Distribution of twin boundaries (red boundaries) in (a) S1, (b) S2, (c) S3, (d) S4, (e) S5, (f) S6, (g) S7, and (h) S8.

believed to randomise the texture after thermo-mechanical processing is done [221].
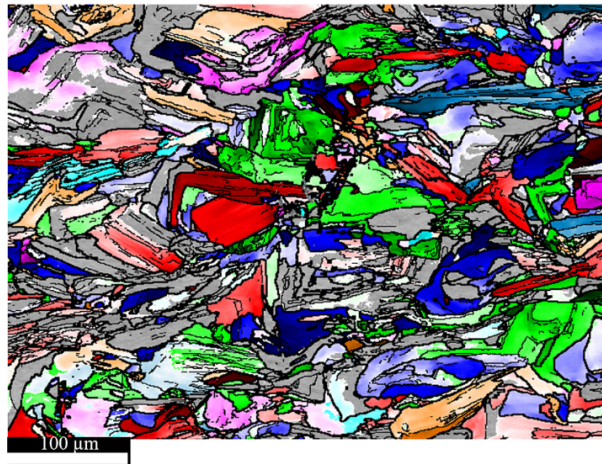
Figure 4.15: Texture component map of S1 showing the grains with different textures. $< 110 >$-fibre in green, $< 111 >$-fibre in blue, $< 100 >$-fibre in red and Cube component in pink. The rest of the grains (shown in gray) have a random texture with a volume fraction lower than 10%.

4.3.5 Transmission electron microscopy

TEM characterization was used to further investigate the microstructure. TEM images of the as-built samples (Figures 4.16) reveal the dislocation features including dislocation cells, walls, lines, and tangles. For brevity purposes, only representative TEM images from different samples are shown here, however, the microstructural features of interest were present in all samples (S1-S8). Generally, a high density of dislocations can be observed in the cell walls, which is in agreement with previous findings of LPBFed 316L SS [17, 222, 223].
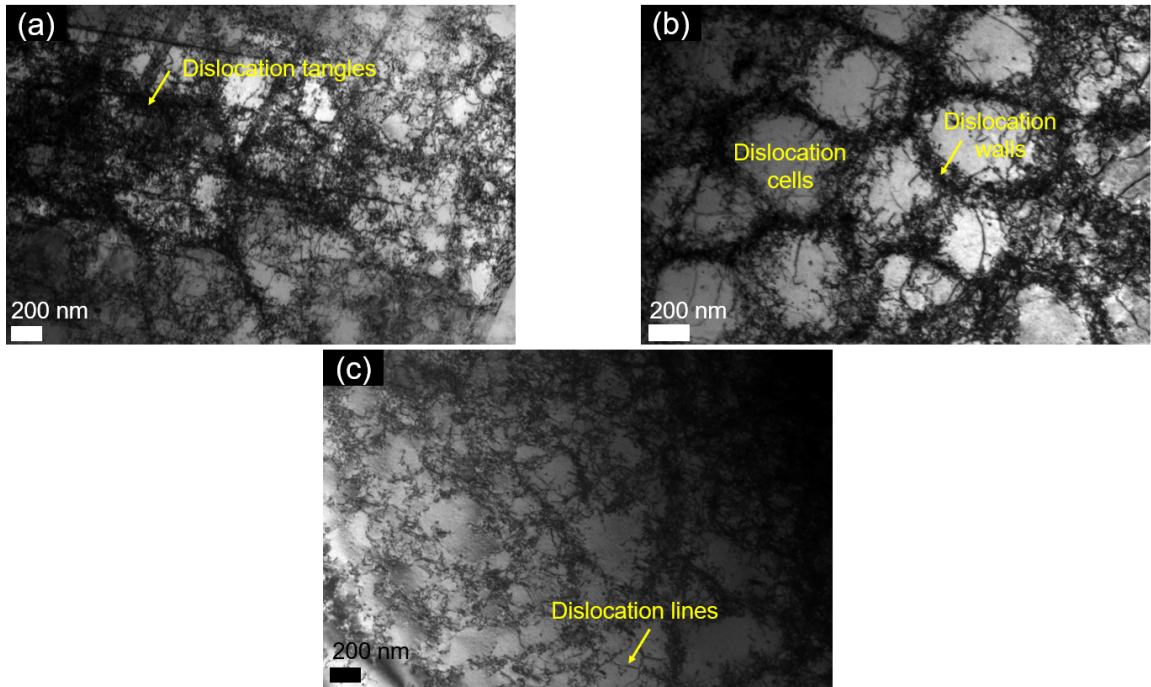
Figure 4.16: Bright field TEM images showing dislocation features, including dislocation cells, lines, tangles, and lines (indicated in the images) in (a) S2, (b) S4, and (c) S6.

The average diameter of the dislocation cells (d_c) is measured from several TEM micrographs and listed in Table 4.6; a representative image showing the clear distri-

bution of dislocation cells in each sample is presented in Figure 4.17. There is no clear correlation between process parameters and the dislocation cell size, as the variations of the cell size are not in a visible order with neither scan speed nor the normalised enthalpy.
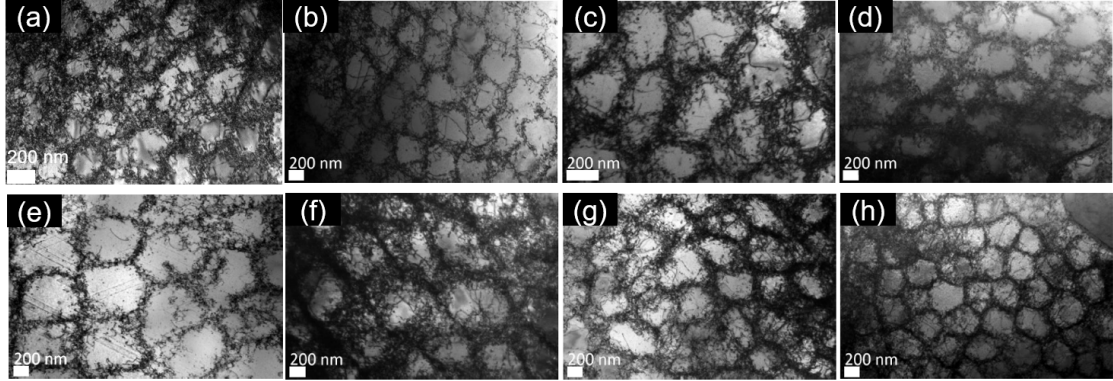
Figure 4.17: Bright field TEM images showing dislocation cells of LPBFed as-built 316L SS with different process parameters.(a) S1, (b) S2, (c) S3, (d) S4, (e) S5, (f) S6, (g) S7, (h) S8.

Table 4.6: The average dislocation cell size (d_c) of different samples with various process parameters.

Sample	d_c (μm)
S1	0.40±0.08
S2	0.30±0.04
S3	0.33±0.05
S4	0.39±0.05
S5	0.57±0.05
S6	0.59±0.10
S7	0.51±0.17
S8	0.34±0.04

Another important microstructural feature of the LPBFed 316L SS is the presence of stacking faults (SFs). Figure 4.18 shows the presence of SFs in LPBFed as-built samples, representatively. Observation of SFs led to deeper microstructural investi-

gations to look for traces of deformation twins in the LPBFed as-built 316L SS, since SFs are the precursor for formation of deformation twins.
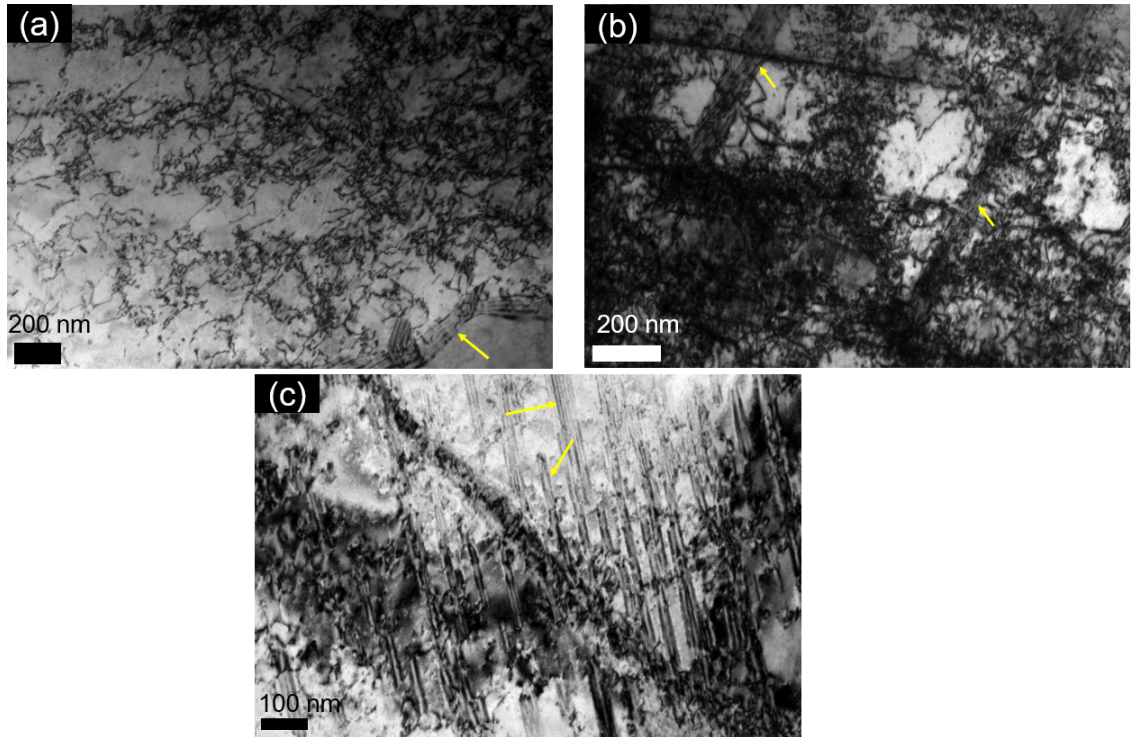
Figure 4.18: Bright field TEM images showing stacking faults in (a) S1, (b) S2, (c) S4.

Charcterisation of deformation nanotwins

To improve the mechanical properties of wrought 316L SS, thermo-mechanical processing such as cold rolling and subsequent annealing has traditionally been used to activate deformation-induced phenomena such as mechanical twinning, or strain-induced martensitic transformations [224, 225]. Wang *et al.* [226] demonstrated that nanotwins formed by pre-deforming 316L SS can provide additional nucleation sites for recrystallization during the annealing process, improving strength and ductility

through grain refinement.

Deformation nanotwins have also been shown to increase yield stress and dislocation recovery, resulting in strain hardening improvement [227]. LPBF can combine hot/cold working and subsequent annealing steps due to the fast heating and cooling cycles that induce repetitive strains (this will be discussed in the next sections) [146, 58]. As a result, embedding nanotwins as precursors for recrystallization and recovery should be possible without post-treatment using LPBF. According to Gao *et al.* [228] deformation twins formed during compression of an LPBFed 316L SS facilitated recrystallization during subsequent annealing. However, the results of our EBSD studies confirm the occurrence of DRX and DRV during LPBF, without any post-treatment. Li *et al.* [229] reported the presence of nanotwins in a LPBF processed high entropy alloy with an intermediate stacking fault energy (SFE); and it is known that deformation nanotwins can be thermally stable up to 1000°C for several minutes during annealing [226], making it possible to characterise those twins after LPBF builds are fabricated.

Numerous planar dislocation structures can be seen in the as-built structures of S1 and S3, as shown in Figure 4.19. They are present in all samples S1-S8, but only representative images from different samples are presented here for brevity purposes. The as-built samples showed nanoscale deformation bands with a higher dislocation density, compared to the matrix (Figures 4.20a and b). Using the selected area diffraction patterns (SADP) shown in Figures 4.20c and d, these bands were confirmed as deformation twins. Deformation twins with a thickness of several nanometres were found in all eight samples in the LPBF as-built state, and they are referred to as nanotwins. Planar dislocations are required before nanotwins can be formed; planar

dislocations reduce the material's ability to cross-slip and thus cause deformation twinning. Nanotwins have previously been charcterised in the microstructure of severely plastic deformed 316L SS [230, 231], but this is the first time they have been identified in the LPBF as-built microstructure of 316L SS, without any post-processing or subsequent deformation.
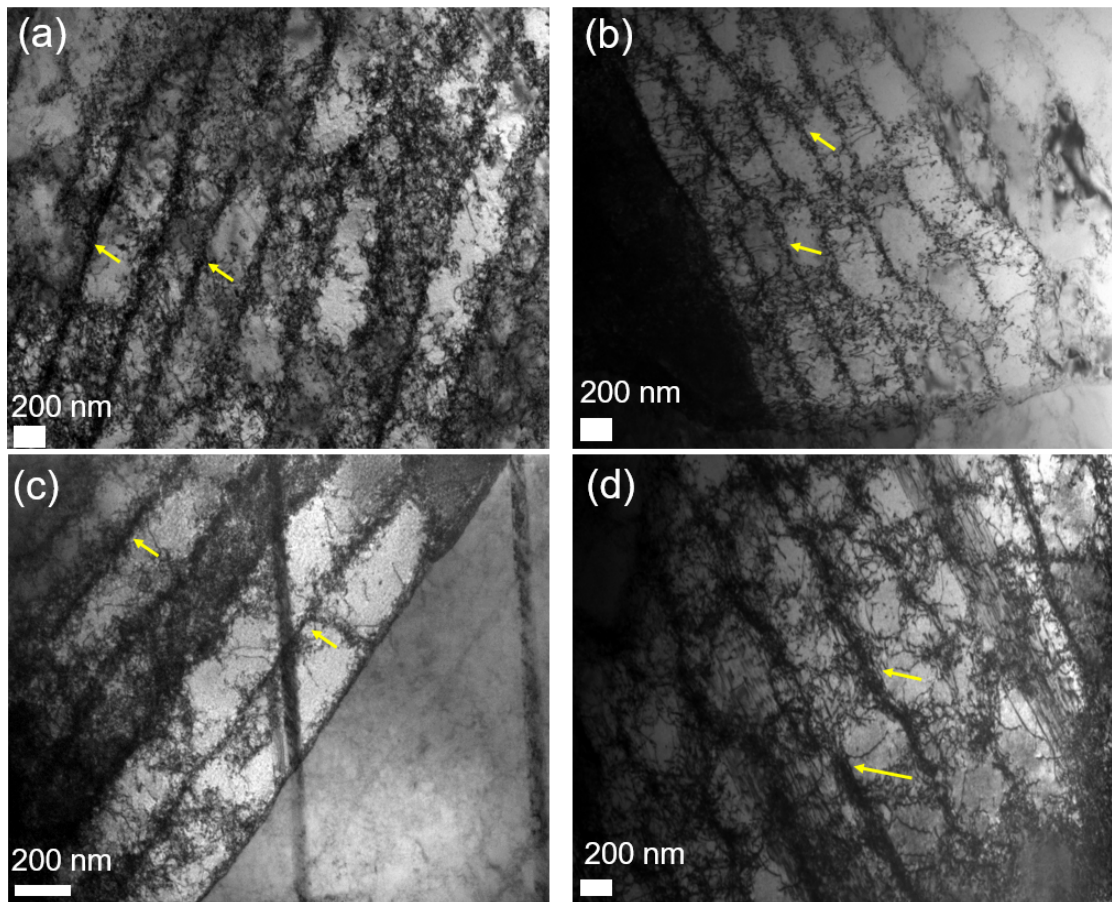
Figure 4.19: Bright field TEM images showing planar dislocation structures (some of them are indicated with yellow arrows) in (a) S1, (b) S3, (c) S7, and (d) S8.
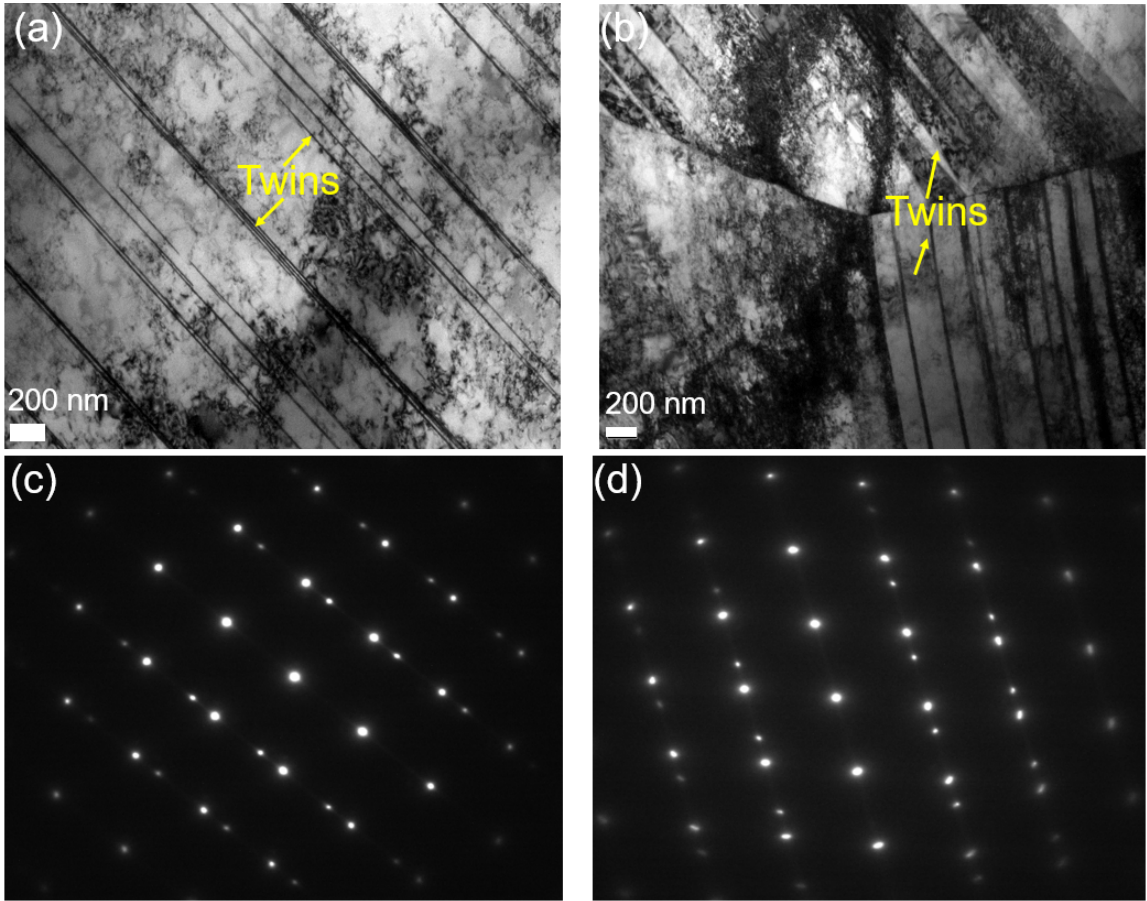
Figure 4.20: Bright field TEM images showing deformation bands in the LPBFed as-built structure of (a) S5, (b) S7. Corresponding SADP of the deformation bands in (c) S5, and (d) S7, confirming those bands are mechanical twins.

4.4 Modelling of restoration mechanisms during laser powder bed fusion

4.4.1 Thermal model

In order to model restoration mechanisms as the main microstructural evolution phenomena, temperature gradients (G [K/mm]) during LPBF for all samples are calculated using an empirical thermal model established by Bertoli *et al.* [162]:

$$G = 10570\left(\frac{P}{v}\right)^{-0.42}.$$ (4.1)

According to equation 4.1, the temperature variations caused by laser penetration are highly dependent on scan speed. Even a small change in scan speed from 0.3 m/s (S3) to 0.45 m/s (S6) will result in a large difference in temperature gradient of $1.25{\times}10^4$ K/mm to $1.48{\times}10^4$ K/mm, (about 18% change). Equation 4.1 also demonstrates that temperature fluctuations during LPBF are not dependent on the LPBF system machine, but rather on the process parameters such as laser power and scan speed. This supports the comparison of findings from two different laser systems with various laser spot sizes used to build the samples in this study.

The temperature decay during layering should be calculated in order to obtain the temperature-time profiles of the samples processed with different parameters. Figure 4.21 depicts a schematic of the LPBF processing (the schematic of the process is adapted from [232]). To emphasise the effect of layer thickness and hatch distance, the build has been divided into cubes. The temperature rises to T_{peak} when the laser interacts with the powder bed/building component at point a (melting starts at the

layer). T_{peak} during LPBF can be estimated via [38]:

$$T_{peak} = \frac{H_n T_b}{H_n^{max}}, \tag{4.2}$$

where T_b=2885 K is the boiling temperature of 316L SS and H_n^{max}=5.5 is the maximum allowable heat input before the onset of evaporation in 316L SS. The laser moves at a specific time, depending on the scan speed, to point b in the x-direction, the magnitude of which is determined by the hatch distance, and this is repeated until a layer is created. The laser then pushes a layer thickness in the z-direction. When this occurs, multiplying the hatch distance (see Table 4.1) by the temperature gradient measures the temperature decay at point b:

$$\Delta = G \times h. \tag{4.3}$$
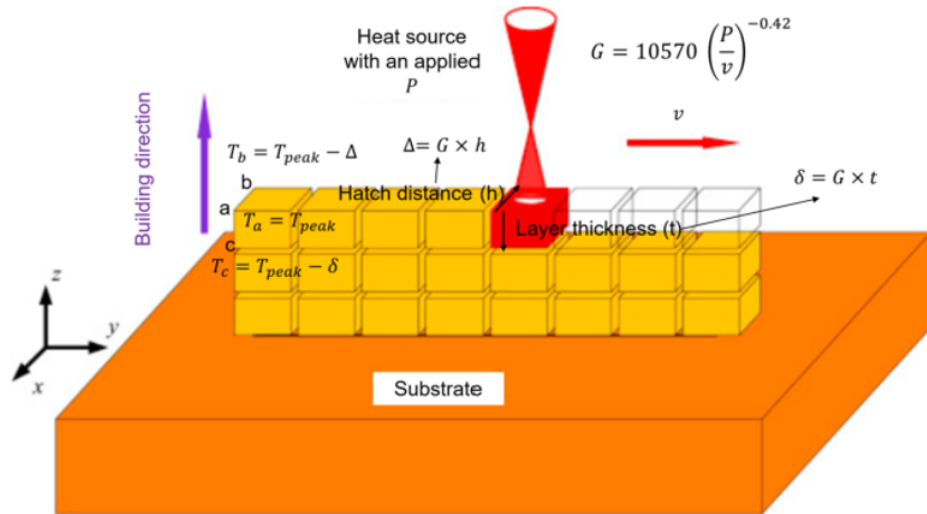
Figure 4.21: A schematic of LPBF showing how the thermal model works.

The temperature in the previous layer (first layer) decreases to $T = T_{peak} - \Delta$

134

when the second layer is deposited. The temperature at point c can be determined in a similar way by multiplying the layer thickness (see Table 4.1) by the temperature gradient:

$$\delta = G \times t. \tag{4.4}$$

As a result, $T_{peak} - \delta$ is the maximum temperature of the first layer during the deposition of the second layer; this is repeated for the deposition of the next layers. The related temperature-time profiles that each layer experiences during LPBF for different samples are plotted in Figure 4.22. A thermal cycle is described as each of the temperature rises and drops in Figure 4.22. The minimum temperature of the melt pool is considered to be the same as the previous thermal cycle when $T_{peak} - \Delta \leq T_0$, where T_0 is the powder bed temperature. The reciprocal of the strain rate $(1/\dot{\epsilon})$, where $\dot{\epsilon}$ at each thermal cycle is calculated via equation (4.5) can be used to estimate the corresponding time during layering.

$$\dot{\epsilon} = \frac{kT_{peak}v}{P}, \tag{4.5}$$

where k is the thermal conductivity, and T_{peak} is the maximum temperature at each thermal cycle. Equation 4.5 is proposed in this thesis to estimate the strain rate originated by a laser beam, which speed (v) causes a maximum temperature (T_{peak}) leading to an amount of energy dissipated into the powder bed at a rate dictated by thermal conductivity (k), but which magnitude is determined by P.

During LPBF, the samples go through a variety of thermo-mechanical processing schemes, which are dependent on the process parameters (see Figure 4.22). The deposited layers in S2 and S3 experience three consecutive rapid melting and two
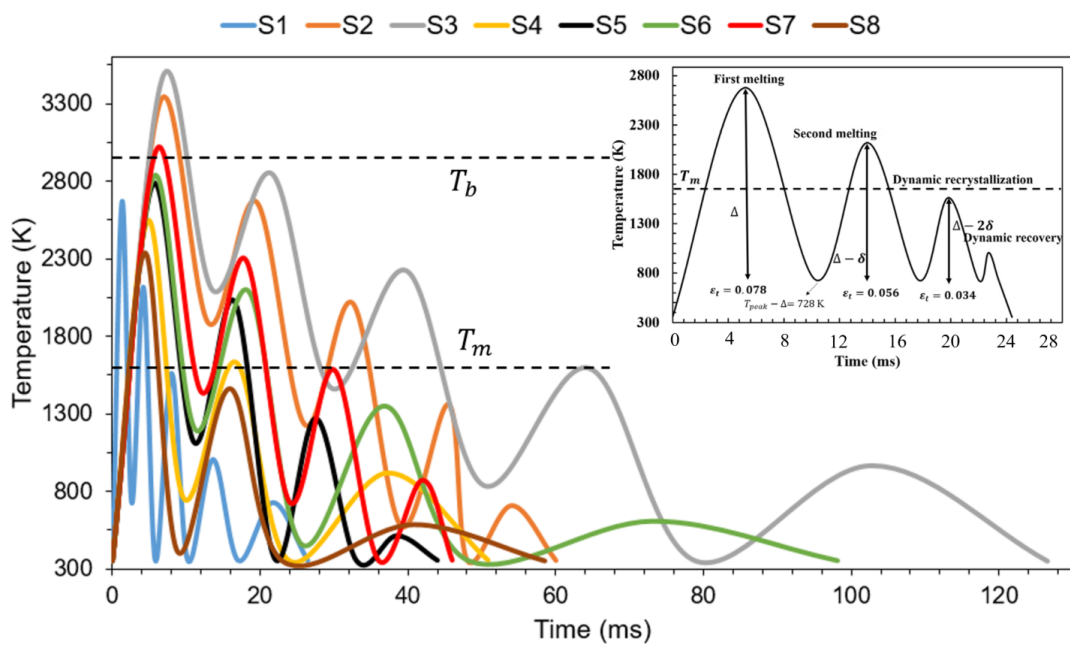
Figure 4.22: Temperature-time profiles for each layer during LPBF of samples with various process parameters. The inset shows temperature-time profile of S1, with Δ and δ being schematically defined.

rapid solidification processes during LPBF. They also undergo two thermal cycles at temperatures that are prone to DRX and DRV (temperatures above $0.5T_m$, i.e above 833 K for 316L SS). Deposited layers in S1, S4, S5, S6, and 7 S1 experience only two fast melting and solidification stages. Only S1 and S7 undergo DRX/DRV at their corresponding third and fourth thermal cycles, but the rest of them only experience one DRX/DRV stage. S8 layers just experience two thermal cycles during LPBF, in which one can be related to rapid melting/solidification and the other to DRX/DRV.

4.4.2 Estimation of thermal and plastic strains

The thermal and plastic strains induced by LPBF layering should be estimated in order to predict what restoration mechanisms are active during LPBF of different samples. Thermal strain (ϵ_T), which is caused by repeated expansion and contraction during heating and cooling cycles, can be calculated using the following formula:

$$\epsilon_T = \sum_i \alpha_{CTE} \Delta T_i, \tag{4.6}$$

where α_{CTE}=20.21×10^{-6} K^{-1} [92], and ΔT_i is the difference between the peak temperature at each heating/cooling thermal cycle and its corresponding minimum temperature (see Figure 4.22). Table 4.7 lists ϵ_T values for various samples. Thermal strain is not a residual strain; it only influences microstructural evolution during the layering process.

Furthermore, large thermal gradients are created in the bulk as a result of the localised and subsequent heating and cooling cycles during LPBF, which can cause severe plastic deformation of the as-built component during processing. Residual strains grow as a result of the induced plastic deformation. When these are large,

Table 4.7: Thermal, plastic and total strain induced by LPBF of 316L SS.

Sample	ϵ_T	ϵ_p	ϵ_t
S1	0.18	0.14	0.32
S2	0.19	0.05	0.24
S3	0.20	0.04	0.24
S4	0.13	0.05	0.18
S5	0.18	0.05	0.23
S6	0.19	0.04	0.23
S7	0.18	0.05	0.23
S8	0.13	0.03	0.16

the high temperature cycles will activate restoration mechanisms through thermo-mechanical processing. Elmesalamy *et al.* [23] found a correlation between the residual plastic strains (ϵ_p) formed during laser welding of 316L SS and the bulk material's hardness (Figure 4.23). We adopted this approach to find residual plastic strains in laser welding in our LPBF calculations. The measured hardness values for various samples are listed in Table 4.8 (they are also shown in Figure 4.23). Therefore, the corresponding ϵ_p for each sample is shown in Figure 4.23 and listed in Table 4.7. Thus, total strain induced by LPBF is $\epsilon_t = (\epsilon_T + \epsilon_p)$, which is also listed in Table 4.7.

Table 4.8: Hardness of the various LPBFed as-built samples, used for measurement of the residual plastic strain.

Sample	Hardness (HV)
S1	237±4
S2	198±6
S3	192±5
S4	196±5
S5	195±6
S6	193±5
S7	196±3
S8	186±12
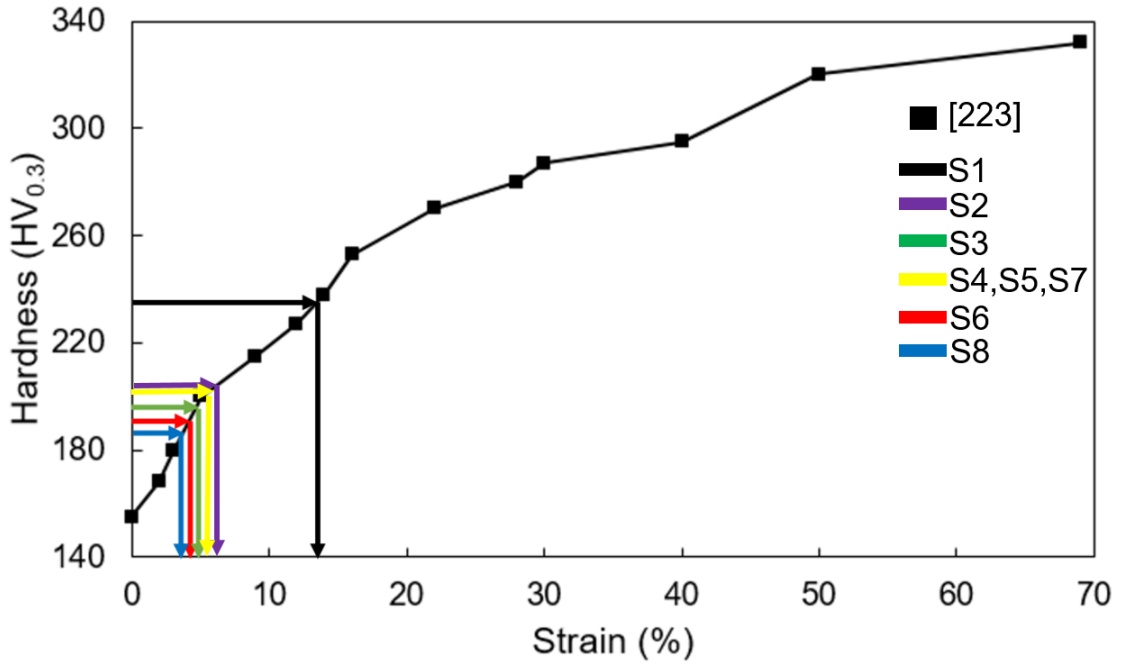
Figure 4.23: Correlation between the hardness and the residual plastic strain of 316L SS adopted from laser welding [23].

4.4.3 Activation of dynamic recrystallization and recovery

Two methods are used to predict DDRX activation: classical (Zener-Hollomon) and thermostatistical approaches. Table 4.9 summarises the phenomenon triggered at each thermal cycle during layering of each sample based on temperature-time profiles (Figure 4.22). In here, the thermal cycles with a maximum temperature above 0.8 T_m=1333 K are considered as DRX cycle and the cycles with maximum temperatures between 0.8 T_m and 0.5 T_m (833 K) are considered as DRV cycles. The thermal cycles prone to DRX and their respective $\dot{\epsilon}$ and temperatures are indicated in Table 4.9.

Table 4.9: Phenomena activated during various thermal cycles (Figure 4.22) in each layer in the studied samples. RM and RM/S represent the rapid melting and rapid melting/solidification, respectively.

Sample	1st cycle	2nd cycle	3rd cycle	4th cycle	5th cycle
S1	RM/S	RM/S	DRX ($\dot{\epsilon}$=454 s^{-1}, T=1563 K)	DRV	-
S2	RM	RM/S	RM/S	DRX ($\dot{\epsilon}$=152 s^{-1}, T=1359 K)	DRV
S3	RM	RM/S	RM/S	DRX ($\dot{\epsilon}$=145 s^{-1}, T=1594 K)	DRV
S4	RM/S	RM/S	DRX ($\dot{\epsilon}$=163 s^{-1}, T=950 K)	-	-
S5	RM/S	RM/S	DRX ($\dot{\epsilon}$=181 s^{-1}, T=1268 K)	-	-
S6	RM/S	RM/S	DRX ($\dot{\epsilon}$=177 s^{-1}, T=1350 K)	-	-
S7	RM/S	RM/S	DRX ($\dot{\epsilon}$=167 s^{-1}, T=1584 K)	DRV	-
S8	RM/S	DRX ($\dot{\epsilon}$=223 s^{-1}, T=1563 K)	-	-	-

Classical approach

To determine ϵ_c^c (equation 2.6), Z values must be calculated using equation (2.5). Q=460 kJ/mol (for 316L SS deformed at around 1522 K) is assumed as the activation energy to trigger deformation [233]. Wang *et al.* [17] demonstrated that LPBF of 316L SS causes Cr and Mo to segregate into solidification cell boundaries, resulting in high austenite stability. They also discovered that process parameters such as laser power and scan speed have a significant impact on elemental segregation. Suppression of elemental segregation in 316L SS can be achieved by lowering laser power and scanning speed [17, 39]. Sun *et al.* [187, 21] also claimed that ultra-fast LPBF cooling rates ($\geq 10^5$ K/s) significantly suppress elemental segregation. LPBF cooling rate (CR) can be correlated to the dislocation cell size (d_c) for 316L SS via [162]:

$$d_c = 80(CR)^{-0.33}. \tag{4.7}$$

Using d_c values listed in Table 4.6, the average cooling rates for various samples during LPBF are all larger than 10^6 K/s, which means that Q=460 kJ/mol can be used as the activation energy for deformation during LPBF of 316L SS, as no significant segregation that can change the austenite stability is predicted. Based on the temperatures and strain rates that are shown in Table 4.9, Zener-Hollomon parameter (Z) has been calculated for different specimens and are shown in Table 4.10. The critical strain for the activation of DDRX (equation 2.6) at the corresponding thermal cycles determined in Table 4.9 are also calculated and listed in Table 4.10. In equation (2.6), a=0.084 for 316L SS [126]. Comparing ϵ_c^c with the values of ϵ_t (Table 4.7) shows that DDRX only can happen in S1. Total strain generated during LPBF of S2-S8 was insufficient to trigger DDRX in these samples, through the well-known dislocation cell formation mechanism.

Table 4.10: Zener-Hollomon parameter and corresponding ϵ_c^c for different LPBFed as-built samples.

Sample	Z (s^{-1})	ϵ_c^c
S1	1.07×10^{18}	0.29
S2	7.29×10^{19}	0.25
S3	1.72×10^{17}	0.40
S4	3.2×10^{27}	0.21
S5	1.67×10^{21}	0.52
S6	1.11×10^{20}	0.40
S7	2.46×10^{17}	0.25
S8	5.27×10^{17}	0.32

Thermostatistical approach

From equation (2.7), the critical strain for DDRX can also be estimated, adopting the thermostatistical theory of plastic deformation. When dislocation cell formation is responsible for grain boundary bulging, equation (2.7) can be used to model hot

deformation of engineering alloys. The constants and physical properties values that should be used for calculation of ϵ_c^T are listed in Table 4.11. To calculate the dislocation density at the yield point (ρ_Y), tensile testing was performed on all the LPBFed as-built samples. The yield strength (σ_Y) values are reported in Table 4.12. Thus ϵ_c^T for various samples are listed in Table 4.13. It can be seen that the calculations from thermostatistical theory are in agreement with the classical Zener-Hollomon approach, and with a comparison between Table 4.13, and 4.7, it is revealed that only S1 is prone to DDRX, if the dislocation cells are responsible for triggering DRX.

Table 4.11: Physical properties and constant used for calculation of ϵ_c^T for 316L SS.

Properties	Value	Reference
μ (GPa)	74×10^9	[234]
b (m)	2.54×10^{-10}	[235]
c (m/s)	5280	[236]
E_m (J/mol)	73×10^3	[237]

Table 4.12: Tensile yield strength of the various LPBFed as-built samples, used for measurement of the dislocation density at the yield point.

Sample	σ_Y (MPa)
S1	600±5
S2	520±6
S3	518±1
S4	504±5
S5	424±6
S6	432±14
S7	409±3
S8	400±5

As is shown in section 4.3.5, deformation nanotwins are characterised in all the LPBFed as-built samples; they can also act as precursors for new dislocation-free DRX grains and lower the critical strain needed for activation of DDRX. Ultra-fast

Table 4.13: Critical strain for activation of DDRX through thermostatistical approach.

Sample	ϵ_c^T
S1	0.31
S2	0.26
S3	0.42
S4	0.23
S5	0.54
S6	0.42
S7	0.26
S8	0.34

solidification during LPBF resembles cyclic deformation at a high strain rate, which can result in a high density of deformation nanotwins in 316L SS (Figure 4.20). This is analogous to the formation of twins in face-centred cubic (FCC) materials as a result of shock loading [238, 239]. In FCC alloys, there are four main mechanisms for deformation twin formation [240]: (1) The pole mechanism proposed by Venables where a perfect twin structure without stacking faults will form and grow [241]; (2) a deviation from the pole mechanism (by Cohen and Weertman) where a perfect dislocation decomposes into a Frank and a Shockley partial when the dislocation meets a barrier such as a Lomer-Cottrel lock [242]; (3) the stair-rod cross-slip mechanism (by Fujita and Mori) in which multiple glide, high stress concentration and the formation of ϵ-martensite as an intermediate phase occurs [243]; (4) the three-layer mechanism (by Mahajan and Chin) in which a twin may evolve if three layers of stacking faults composed of three Shockley partials grow into each other [244]. The deviated pole mechanism and the three-layer mechanism are possible twin formation mechanisms because the deformation nanotwins tend to be composed of many stacking faults (Figure 4.18), and exhibit discontinuous, and there is no traces of ϵ-martensite.

The dislocation density-based method proposed by El-Danaf *et al.* [245] is used to

demonstrate the formation of deformation nanotwins. Deformation twins can develop when a critical dislocation density (ρ_c) is reached, and they can grow or be stopped by obstacles such as grain boundaries. Based on the three-layer mechanism (ρ_c^T) and the deviated pole mechanism (ρ_c^P) [245]:

$$\rho_c^{P/T} = \frac{(SFE)^2}{n_S^2 \mu^2 b_1^2} \cdot \frac{1}{(M\alpha b - n_S b_1)^2},\tag{4.8}$$

where SFE is the stacking fault energy of the alloy, b_1=0.14 nm is the magnitude of the Burgers vector of the twin source, M=3 is the Taylor factor, α=0.24 is the constant of the Taylor relationship, b=0.25 nm is the magnitude of the Burgers vector, and n_S is the number of Shockly partial dislocations responsible for twin formation. n_S=1 for the deviated pole mechanism and n_S=3 for the three-layer mechanism. TEM observations of the distance between the partial dislocations (r_{part}) allow the calculation of SFE (Table 4.14) [246]:

Table 4.14: The measured values of SFE, critical dislocation density for both twinning mechanisms (P stands for deviated pole and T stands for three-layer mechanism) and the dislocation density upon rapid solidification (calculated from the solidification thermal cycle of each sample, provided in Figure 4.22).

Sample	SFE (mJ/m^2)	$\rho_c^P \times 10^{14}$ (m^{-2})	$\rho_c^T \times 10^{14}$ (m^{-2})	$\rho \times 10^{14}$ (m^{-2})
1	17	8.2	15.5	204
2	14	6.5	10.5	134
3	23	25	28.5	124
4	6	9.5	22	124
5	15	3	13	181
6	11	3.4	6.5	174
7	11	11	6.5	161
8	20	5.6	21.5	242

Table 4.14 shows that both deviated pole and three-layer mechanisms can be activated during LPBF of 316L SS.

Previous studies in the literature suggested that deformation twinning could induce DRX and DRV in 316L SS [226, 227, 247, 228]. Shear banding can be activated in an area of high density nano-scale twins as the twin density approaches saturation and further twinning is unable to accommodate subsequent strain. Elongated nano-scale dislocation cells can arrange along the shear direction as the twin structure is deformed, as shown in Fig. 4.24. With more deformation, these elongated cells will disintegrate into roughly equiaxed subgrains with increasing misorientations, gradually evolving into randomly oriented recrystallized grains (Figure 4.25) [247]. Partial recrystallization occurs in all samples as a result of the build cyclic deformation after solidification, and deformation nanotwins were retained in the microstructure unless they were consumed by the growth of the recrystallized grains (Fig. 4.25d). Twin discontinuities, on the other hand, suggest LPBF detwinning (Figures 4.20a, 4.22d, and 4.25a), resulting in a decrease in dislocation density, as seen in the dark-field TEM images in Fig. 4.26. It can be concluded that, in comparison to wrought alloys, deformation nanotwins cannot contribute much to yield strengthening of LPBF 316L SS due to their low dislocation density compared to subgrain boundaries. Therefore, they are thought to be important in the evolution of low- and high-angle grain boundaries, which may control yield strengthening in LPBFed 316L SS. Yield strengthening mechanisms in LPBFed alloys will be discussed in detail in the next chapter.

To determine the critical shear strain needed for DRX through deformation twinning, a thermostatistical framework is used. The critical shear strain for DRX (γ_{DRX}^*) was originally calculated with dislocation cell formation as a prerequisite for DRX (equation 2.7). However, though equation 2.7 considers dislocation cells to be a DRX motivator, deformation twins can also serve as DRX nucleation sites [226, 247]. A
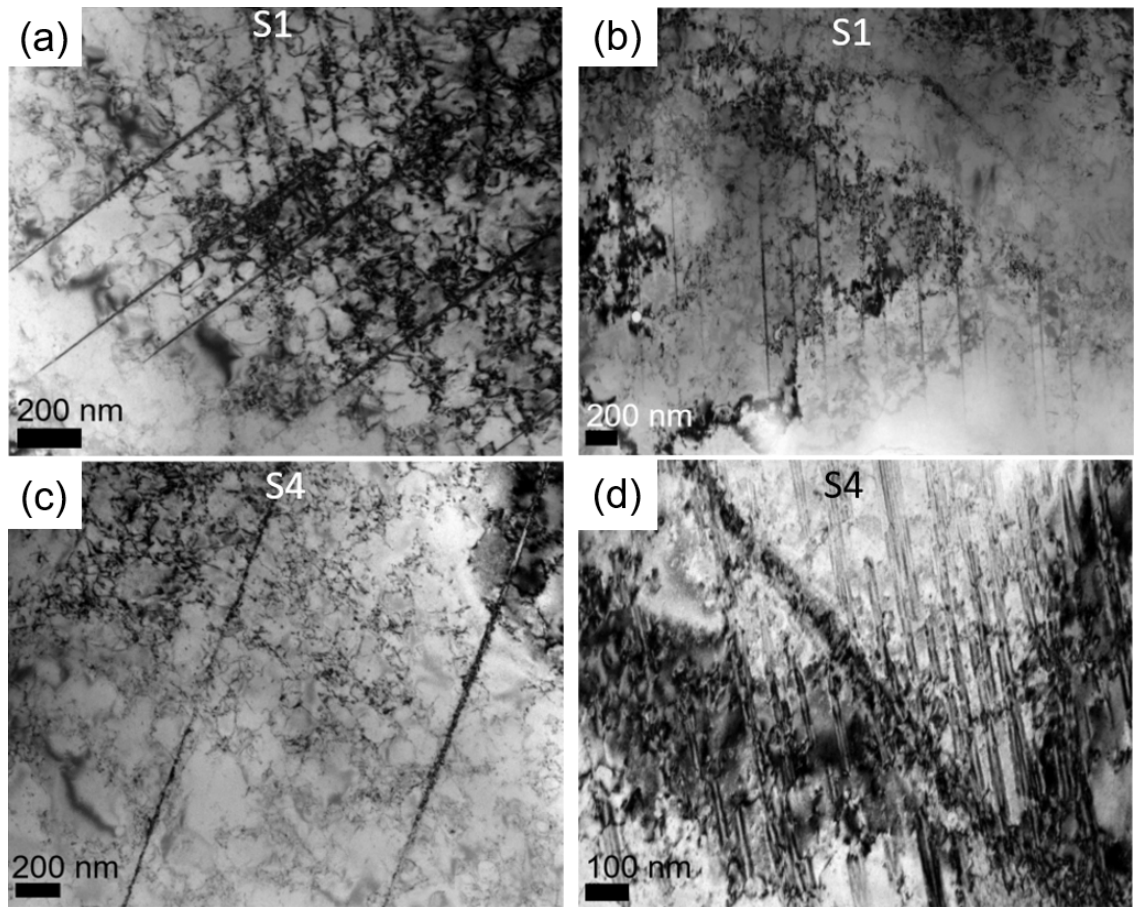
Figure 4.24: Bright field TEM micrographs showing formation of nano-scale dislocation cells at the vicinity of deformation nanotwins in (a), (b) S1, and (c), (d) S4..
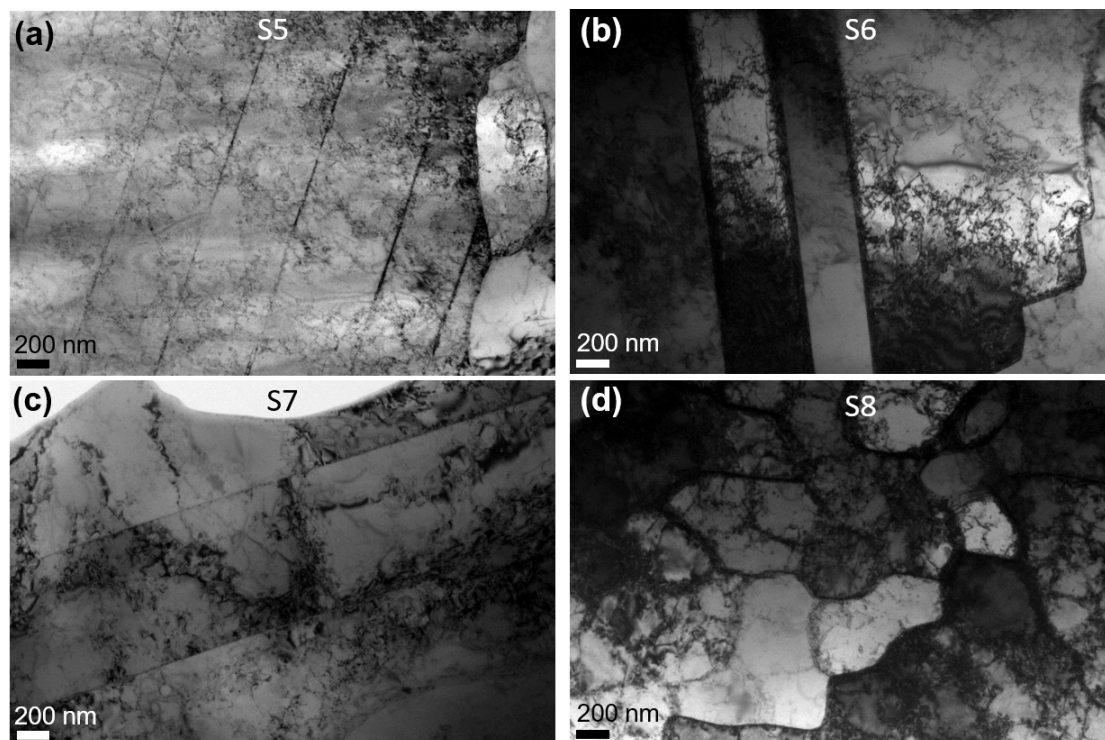
Figure 4.25: Bright field TEM micrographs showing the presence of nanotwin bundles, nano-scale dislocation cells and ultrafine recrystallized grains mixed together in (a) S5, (b) S6, (c) S7, and (d) S8.
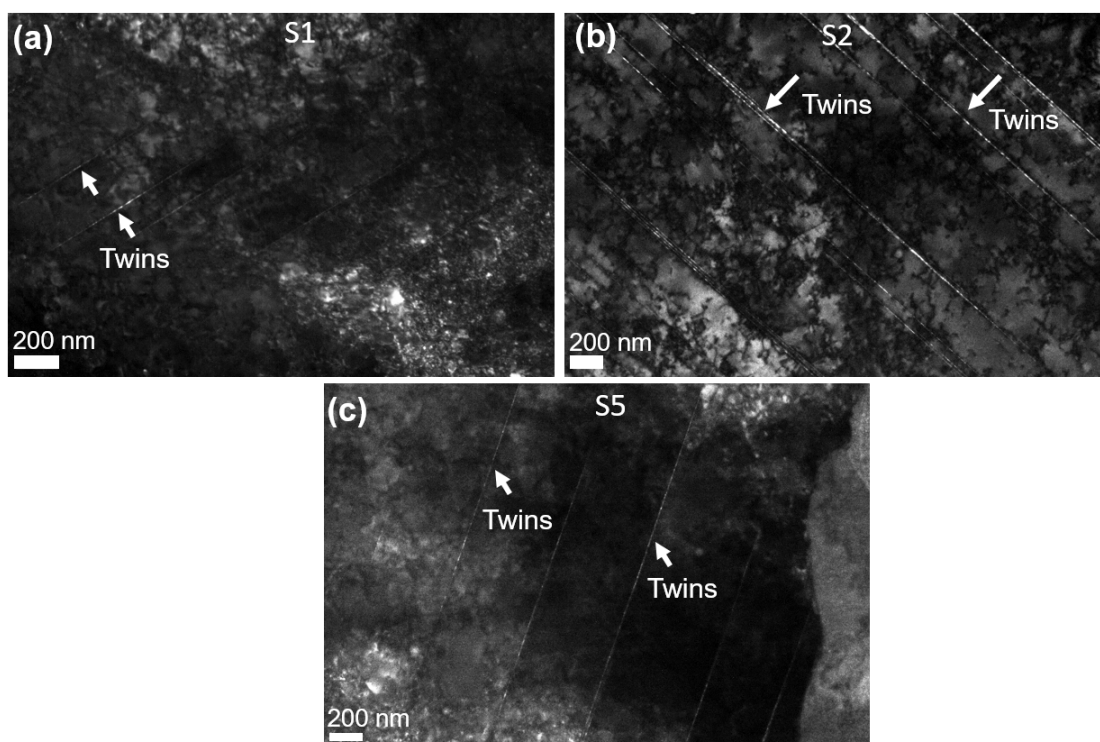
Figure 4.26: Dark field TEM micrographs showing low dislocation density along the nanotwins (a) S1, (b) S2, (c) S5.

critical resolved shear stress must be overcome in order to form deformation twins using either the deviated pole (P) or the three-layer mechanism (T):

$$\tau_c^{P/T} = \frac{SFE}{n_S b_1} + \frac{n_S \mu b_1}{L_0}, \tag{4.9}$$

where L_0 is the length of the twinning source, and estimated here to be around 200 nm [248]. The energy to form a deformation twin nucleus via said mechanisms can be estimated as $\tau_c^{P/T} a^{*3}$, where a^* is the size of a twin nucleus, assumed to be 1 nm. In order to consider only the fraction of twins that leads to bulging, the twin energy must be scaled as $\tau_c^{P/T} a^{*3} \left(\frac{T \Delta S}{\mu b^3} \right)$. Therefore, the critical shear strain for twinning-induced DRX (γ_c^{*t}) can be written as:

$$\gamma_c^{*t} = \frac{\frac{1}{2} \mu b^3 - T \Delta S + \tau_c^{P/T} a^{*3} \left(\frac{T \Delta S}{\mu b^3} \right)}{\frac{1}{2} \mu b^3}, \tag{4.10}$$

where $\Delta S = k_B \ln \left(\frac{\dot{\epsilon}_0 + \vartheta}{\dot{\epsilon}} \right)$, k_B is the Boltzmann constant, $\dot{\epsilon}_0 = cb\rho_Y$ is a constant related to the speed of sound (c=5280 m/s [236]), $\rho_Y = (0.9\sigma_Y/\mu b)^2$ is the dislocation density at the yield point, σ_Y is the yield strength (the values for yield strength are listed in Table 4.12), $\dot{\epsilon} = \frac{kvT_{peak}}{P}$ [38] is the LPBF strain rate, with k=29 W/m·K being the average thermal conductivity of 316L SS at high temperatures [249], $\vartheta = 10^{13} \exp\left(-\frac{E_m}{RT}\right)$ is the vacancy jump frequency, E_m=73 kJ/mol [237] is the vacancy migration energy, R=8.314 J/mol·K is the universal gas constant, and T is the maximum temperature at the corresponding thermal cycle (in here restoration mechanisms temperature). Using the Taylor factor $\gamma = M\epsilon$, the critical normal strain to trigger DRX by the formation of deformation twins can be obtained by:

$$\epsilon_c^{*t} = \frac{\frac{1}{2}\mu b^3 - T\Delta S + \tau_c^{P/T} a^{*3}\left(\frac{T\Delta S}{\mu b^3}\right)}{\frac{3}{2}\mu b^3}. \tag{4.11}$$

The values of $\epsilon_c^{*t}(P)$, $\epsilon_c^{*t}(T)$, ϵ_t and ϵ_c^T (critical normal strain for the activation of DRX via formation of dislocation cells) are listed in Table 4.15. In all samples, ϵ_t reaches the critical strain for DRX activation by both twinning mechanisms (except from the deviated pole mechanism in S8, where the critical and total strain are equal). This means that after rapid solidification during LPBF, deformation nanotwins can form, and they can cause DRX during subsequent LPBF thermal cycles, resulting in the microstructural evolution scenarios previously discussed.

Table 4.15: Critical strain for twinning induced DRX in LPBF 316L SS. Total strain accumulated in each sample during LPBF is also reported. P stands for deviated pole and T stands for three-layer mechanism.

Sample	$\epsilon_c^{*t}(P)$	$\epsilon_c^{*t}(T)$	ϵ_t	ϵ_c^T
S1	0.18	0.15	0.32	0.31
S2	0.16	0.17	0.24	0.26
S3	0.13	0.13	0.24	0.42
S4	0.11	0.12	0.18	0.23
S5	0.18	0.18	0.23	0.54
S6	0.16	0.17	0.23	0.42
S7	0.12	0.13	0.23	0.26
S8	0.16	0.15	0.16	0.34

In order to confirm the validity of the current approach to estimate the critical strain for activation of twinning induced DRX, tensile testing at room temperature is conducted on S1. EBSD micrographs in Figure 4.27 display recrystallized, deformed, and substructured grains before and after tensile testing. After tensile testing, the fraction of recrystallized grains increased dramatically from 5% to 23% (Table 4.16). Deformation twinning during tensile testing of S1 activated DRX at high strain levels,

even at room temperature, since the critical strain for activation of twinning-induced DRX is 0.26 and 0.23 for deviated pole and three-layer mechanisms, respectively. Since the critical strain for twinning-induced DRX is based on both composition-dependent properties such as shear modulus, yield strength, and SFE, as well as process-dependent variables such as temperature and strain rate, this opens up new possibilities for alloy and process design.
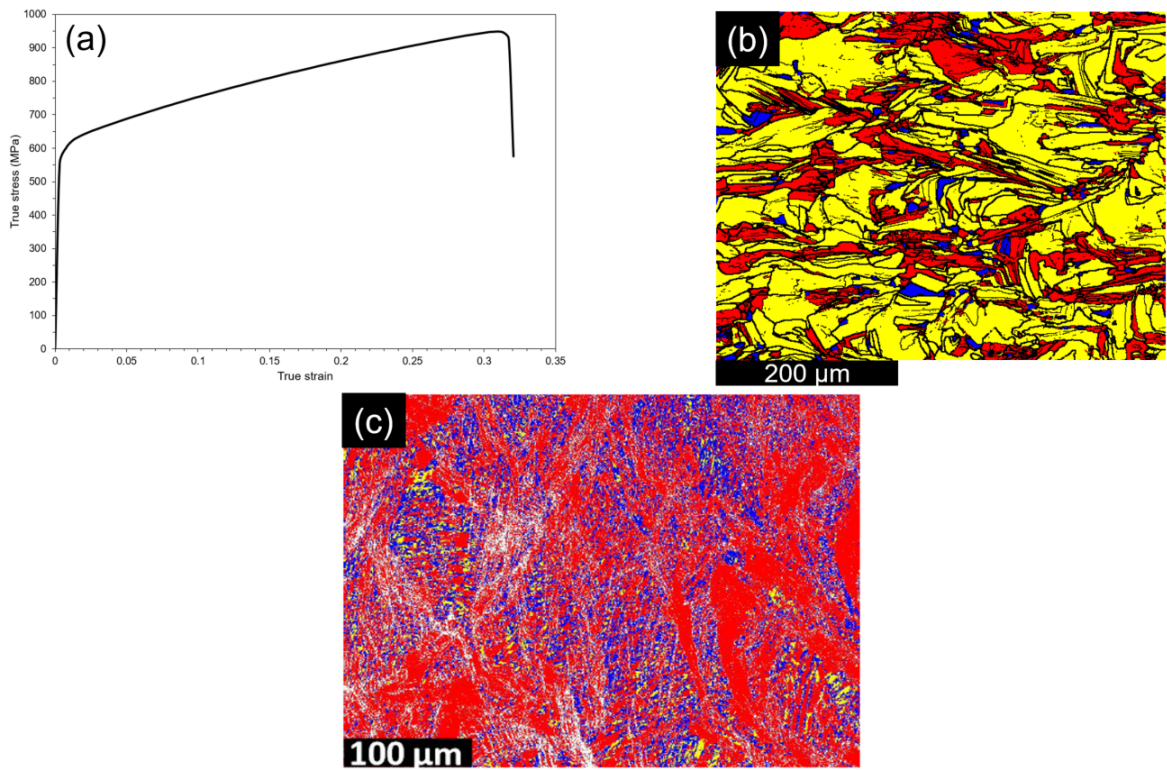
Figure 4.27: (a) Tensile true stress - true strain curve of S1. Representative EBSD re-crystallization map of S1 (b) prior, and (c) after tensile testing. Grains are categorised as deformed (red), recrystallized (blue), and substructured (yellow).

In addition to DDRX activation, the possibility of occurrence of CDRX can also be modelled with thermostatistical theory. The $\dot{\epsilon}_c^T$ for the activation of CDRX can be estimated via equation 2.9. To calculate $\dot{\epsilon}_c^T$, ΔG_{sys} (kJ/mol) can be estimated via

Table 4.16: Fraction of deformed, recrystallized and substructured grains before and after tensile testing derived from Figures 4.27b and 4.27c.

Sample	Deformed fraction	Recrystallized fraction	substructured fraction
S1 (before deformation)	0.36	0.05	0.59
S1 (after deformation)	0.72	0.23	0.05

[127]:

$$\Delta G_{sys} = -(1.69 + 0.013T + 3.1 \times 10^{-5}T^2), \qquad (4.12)$$

where T is taken as the peak temperature for each thermal cycle (Figure 4.22, and Table 4.9). Table 4.17 lists $\dot{\epsilon}_c^T$ for the thermal cycles in which the material is prone to DRX and compares it to the corresponding $\dot{\epsilon}$ for that thermal cycle. It can be seen that $\dot{\epsilon}$ is insufficient to activate DRV during the corresponding thermal cycles, indicating that the material is susceptible to DRX. This means that CDRX is prevalent during LPBF of S2-8. However, in S1, the $\dot{\epsilon}$ is nearly identical to the $\dot{\epsilon}_c^T$, indicating that CDRX is not activated. In other words, the thermo-mechanical conditions in the third thermal cycle of S1 cause DRV to occur, but unlike S2-S8, the driving force is insufficient to cause certain dynamically recovered grains to function as CDRX promoters. As discussed in section 2.4.2, DRV is required for the occurrence of CDRX, but CDRX cannot be enabled if the strain rate is too high.

4.5 Discussion

The activation of DRX and DRV controls the microstructural evolution of 316L austenitic SS produced by LPBF. All samples form a highly dislocated (deformed)/ nanotwinned microstructure with a solidification cellular structure after thermal cycles

Table 4.17: Critical strain rate (s^{-1}) for the activation of DRV/CDRX mechanisms during processing at the relevant thermal cycles of different samples. The applied process strain rates are also reported.

Sample	$\dot{\epsilon}_c^T$ at thermal cycle prone to DRX	$\dot{\epsilon}$ at the corresponding cycle
S1	455	454
S2	422	72
S3	495	69
S4	444	85
S5	478	69
S6	400	88
S7	418	74
S8	445	140

with rapid solidification/melting (Figure 4.22). Subsequent thermal cycles of LPBF provides the required stored energy for the activation of restoration mechanisms. Different pathways are involved in thermal cycles that are prone to DRX (Figure 4.22). CDRX, and twinning-induced DRX are the dominant mechanisms in S2-S8, while DDRX, and twinning-induced DRX are triggered in S1. DRV is thought to play a key role in the activation of CDRX in S2-S8 [120]. The key feature of CDRX is the formation of LAGBs with a gradual increase in misorientation [250]. Table 4.5 shows that the proportion of HAGBs increased substantially from 0.3 in S1 to 0.5-0.62 in S2-S8, implying that DRX is more pronounced in S2-S8 than in S1. Since dynamically recovered grains cannot be converted to DRX grains due to a high processing strain rate, the presence of 0.7 LAGBs in S1 is related to CDRX deactivation in its third thermal cycle. Since CDRX is followed by the consumption of LAGBs (Figure 2.11), it is evident that CDRX is not the primary DRX mechanism in S1, as 70% of the grain boundaries are still LAGBs. Both classical and thermostatistical approaches also showed that DDRX, and twinning-induced DRX are active during the third thermal cycle of S1. As is shown in Figure 4.22, S1, S3, and S7 are susceptible to DRV at

their respective final thermal cycles. DRV is performed on the remaining deformed grains, while the DRX grains formed in the previous stage will grow and increase their dislocation density. Furthermore, some solidification cellular structures that do not meet the right conditions for DRX/DRV may coarsen and increase the amount of deformed grains in S1, S3, and S7. As a result, each sample microstructural evolution can be summarised as follows:

- S3: Highly deformed solidification cells and nanotwins were formed during the first three thermal cycles in each layer. During the fourth cycle, CDRX occurred and HAGBs developed in the microstructure. In the fifth cycle, DRV activated and some of the deformed and recrystallized grains also undergo substructure development, resulting in a high fraction of substructured grains.

- S2 and S7: These samples respectively experienced two and one rapid solidification/melting stages leading to the development of a highly deformed structure. They both undergo DRV followed by CDRX at their final thermal cycles.

- S1: Highly deformed cellular structure with a high dislocation density, and a high density of nanotwins formed during the first and second thermal cycles. In the third thermal cycle, DRV activates as a precursor for CDRX, but due to high strain rate in this cycle, most of the grains just undergo DRV developing LAGBs. Twinning-induced DRX was also activated. Finally, the remaining highly deformed structure starts to grow at the fourth thermal cycle, as the conditions are not appropriate for DRX. They remain as deformed grains (red in Fig. 4.12a). Some of the recrystallized grains undergo DRV and become substructured grains (yellow in Fig. 4.12a). The dislocation density increases

154

in these grains. The remaining DRV grains in the previous cycle undergo more DRV and grain growth, increasing the fraction of substructured grains. At the end, only 5% of the grains can be characterised as DRX grains with low dislocation density.

- S4, S5, and S6: All of these samples experienced two rapid solidification/melting stages, followed by a CDRX stage. Absence of a thermal cycle related to DRV is the reason why the fraction of LAGBs is not high in these samples.

- S8: This sample only experienced one rapid solidification and melting, followed by one CDRX stage at each layer. Similar to S4, this sample contain the highest fractions of recrystallized grains, which is due to more pronounced DRX.

4.6 Summary

Eight LPBF 316L SS samples were built with various process parameters. DDRX, CDRX, twinning-induced DRX, and DRV are found to be enabled and control the final microstructure of as-built specimens. The activation of restoration mechanisms is highly influenced by process parameters, as shown by temperature-time profiles. To model the detailed restoration mechanisms, a Zener-Hollomon and a thermostatistical approach were used. In their as-built microstructure, all of the samples had deformation nanotwins. At the high strain rate solidification stage cycles of LPBF, nanotwins form. The occurrence of DRX is aided by deformation nanotwins; but, as the dislocation density of the remained nanotwins after the build is fabricated is lower than the dislocation density at LAGBs, and solidification cellular structures, thsu, deformation nanotwins may not contribute significantly to yield strengthening.

The fraction of DRX grains increased significantly after tensile deformation at room temperature, which is due to the same twinning-induced DRX mechanism. This newly discovered microstructural phenomenon in 316L SS LPBF provides a method for optimising mechanical properties by controlling both composition- and process-dependent properties.

Chapter 5

Yield strength of laser powder bed fusion alloys

Understanding the factors that influence yield strengthening in LPBF alloys is crucial for developing new formulations and predicting the best processing parameters. In this chapter, for a titanium, nickel, and stainless steel alloy (Ti-6Al-4V, IN718 and 316L, respectively), a relationship between heat input and strengthening and softening mechanisms is proposed. In 316L SS, maximum strength is obtained by increasing heat input, while IN718 and Ti-6Al-4V require low heat inputs. The results show that the normalised enthalpy can be used to define yield strength in near fully-dense LPBF alloys. Dislocation multiplication/annihilation at certain processing temperatures and thermal straining, which are alloy dependent, as well as dislocation strengthening and heat dissipation during cooling, which are process dependent, all affect the yield strength of LPBF alloys. Well-known metallurgical approaches are used to model these dependencies. Various strengthening mechanisms' relative contributions are discussed. Based on the choice of LPBF process parameters and chemical composition,

the results of this chapter can be used as a metric for yield strength prediction and further development. To reveal the detailed effects LPBF process parameters and heat inputs on mechanical properties, a series of 316L SS samples are tensile tested at room temperature. It has been shown that DDRX, CDRX, and DRV are three restoration mechanisms that must be balanced to control the strength of LPBF 316L SS. To describe strengthening in LPBF 316L austenitic SS, a unified Hall-Petch-type relationship is proposed. The proposed relationship predicts yield strength in terms of subgrain size rather than actual grain size, which is consistent with experimental findings. The Hall-Petch-type equation for austenitic stainless steels, which has been validated, can be used to improve LPBF alloys by increasing the LAGB fraction (grain boundary engineering). DRV should be promoted as the primary mechanism for inducing LAGBs in order to achieve higher strength. The dependency of yield stress on process parameters and alloy composition is quantitatively described in this chapter.

5.1   Introduction

The use of LPBF as a manufacturing route to improve the mechanical properties of engineering alloys is a promising option [251]. Stainless steels (such as 316L SS), titanium alloys (especially Ti-6Al-4V), and nickel superalloys (IN718) are the most common alloy families used in LPBF [49, 252, 129]. As is shown in previous chapter, LPBF-processed alloys typically exhibit microstructures distinct from their wrought counterparts as they experience extreme heating and cooling rates and thermal strains. This renders LPBF alloys exceptional strength compared to their wrought counterparts (Chapter 3).

In this chapter we present a methodology for predicting yield strength of various types of alloys produced by LPBF. The yield strength of as-built fully-dense LPBF specimens correlates with the heat input through the normalised enthalpy, according to experiments on 316L SS, IN718 and Ti-6Al-4V, Figure 5.1. The process heat input has been quantified using the normalised enthalpy, H_n, which takes into account both the LPBF process parameters and the alloy physical properties [253]. Analytical models are used to show the contribution of various mechanisms governing strengthening in LPBF alloys. The findings presented here shed new light on the alloy and process based mechanisms that can lead to LPBF alloys having maximum yield strength. This can clarify some unresolved findings in the literature regarding process-structure-property correlations, as well as the inadequacy of established single viewpoints for interpreting LPBFed alloy yield strength.

In addition to find a correlation between the heat input and the yield strength in LPBF fully-dense materials, the aim of this chapter is to present a unified relationship for the prediction of the yield strength in LPBF alloys (irrespective of the porosity content), considering the role of LAGBs and HAGBs. 316L SS was selected as a typical representative of a single-phase alloy without precipitation and phase transformations during LPBF processing. The specimens were produced with a wide heat input range in order to obtain various microstructures. Criteria to control restoration processes and maximise the yield strength by controlling both process parameters and alloy composition are suggested.
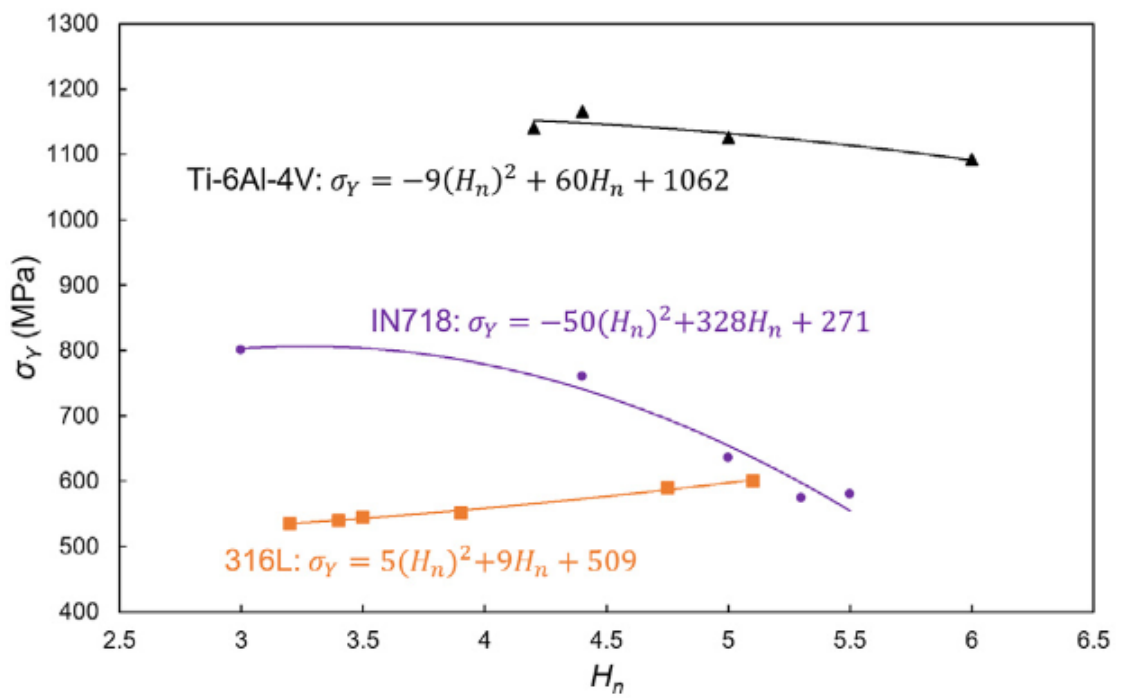
Figure 5.1: Correlation between the yield strength and the normalised enthalpy, H_n for alloys subjected to LPBF.

5.2 Correlation between heat input and yield strength

5.2.1 Materials and processes

Three different alloys have been studied in this chapter: 316L SS, Ti-6Al-4V and IN718. H_n can be calculated via equation 2.4. Table 5.1 shows the decrease in heat input from experimental conditions 1 to 6. (E1 to E6). In addition to sample S1 that has been produced by the author, the literature provided experimental results on the heat input and yield strength [254, 17, 19, 11, 13, 255, 256, 257, 258, 259, 260, 261, 262]. The associated process parameters and materials properties for the H_n calculation are listed in Tables 5.2 and 5.3, respectively. The depicted alloys have enough reduced porosity to eliminate the effects of keyhole-induced pores and lack of fusion on yield strength. The maximum H_n for keyhole-induced pore formation prevention is given from [62], $H_n^{max} = \pi \frac{T_b}{T_m}$; therefore H_n^{max}= 5.5, 6 and 6 for 316L SS, Ti-6Al-4V and IN718, respectively. The melt pool peak temperature is scaled to the boiling and melting temperatures via the ratio between H_n and H_n^{max}, as has been presented in equation 4.2. The estimated T_{peak} for different conditions and materials is presented in Table 5.4.

Table 5.1: H_n values used in this study. H_n^{max} and H_n^{min} are the limits based on boiling and melting points.

Experiment	316L H_n	Ti-6Al-4V H_n	IN718 H_n
H_n^{max}	5.5	6	6
E1	5.1 [62]	6 [254]	5.5 [255]
E2	4.75 [17]	5 [260]	5.3 [256]
E3	3.9 [11]	4.4 [262]	5 [257]
E4	3.5 [258]	4.2 [260]	4.4 [13]
E5	3.4 [259]	-	3 [19]
E6	3.2 [261]	-	-
H_n^{min}	3	3	3

Table 5.2: Process parameters used for H_n calculation for different materials. E1-E6 references appeared in Table 5.1.

Experiment	316L SS			Ti-6Al-4V			IN718		
	P (W)	v (m/s)	D (μm)	P (W)	v (m/s)	D (μm)	P (W)	v (m/s)	D (μm)
E1	100	1	35	170	0.65	100	175	0.62	100
E2	150	0.7	54	240	1	100	250	0.7	100
E3	200	0.85	70	175	0.7	100	285	1	100
E4	175	0.55	100	240	1.4	100	160	0.8	80
E5	300	0.9	100	-	-	-	400	7	100
E6	175	668	100	-	-	-	-	-	-

Table 5.3: Parameters used for solving equations in this study. The shear modulus is approximated at melting temperature. α_{CTE} values are reported values near the melting point.

Parameters	316L SS	Ti-6Al-4V	IN718
A	0.36 [62]	0.7 [263]	0.59 [175]
h_s (J/m^3)	7.76×10^9 [92]	6.15×10^9 [92]	6.81×10^9 [92]
d (m^2/s)	6×10^{-6} [62]	1.07×10^{-5} [264]	6×10^{-6} [265]
μ (Pa)	$(88884.6-37.3T)\times10^6$ [234]	$(49-\frac{4.355}{\exp\left(\frac{198}{T}\right)-1})\times10^9$ [266]	$83100(1-0.5(\frac{T-300}{T_m}))\times10^6$ [267]
b (m)	2.54×10^{-10} [235]	2.9×10^{-10} [112]	2.54×10^{-10} [268]
B	80 [162]	80.9 [269]	34 [270]
n	0.33 [162]	0.34 [269]	0.25 [270]
α_{CTE} (/K)	20.21×10^{-6} [249]	2.11×10^{-6} [271]	17.5×10^{-6} [272]
ν	0.3	0.3	0.3
N	1 [273]	1 [273]	1 [273]
k (W/m·K)	27.8 [249]	27 [274]	29.3 [275]
μ_0 (Pa)	8.88×10^{10}	49.02×10^9	8.31×10^{10}
α	0.3 [276]	0.3 [276]	0.3 [276]
T_b (K)	2885 [92]	3533 [92]	3188 [92]
T_m (K)	1648 [92]	1877 [92]	1528 [92]
c (m/s)	5280 [236]	4898 [236]	5205 [236]
E_m (J/mol)	73×10^3 [237]	121×10^3 [277]	135×10^3 [278]
C_p (J/Kg·K)	663[92]	758 [92]	725 [92]

To prevent lack of fusion, the lower bound to the normalised enthalpy, $H_n = H_n^{min}$, is dictated by $T_{peak} = T_m$. $H_n^{min} = \pi \approx 3$ [4] for all materials. It follows that the process boundary values are delimited by $H_n^{min} < H_n < H_n^{max}$, i.e. when the peak melt pool temperature is above melting but below boiling.

Table 5.4: Estimated values of peak temperature and strain rate during LPBF for different experimental conditions and different materials.

Experiment	T_{peak} (K)			$\dot{\epsilon}$ (s^{-1})		
	316L SS	Ti-6Al-4V	IN718	316L SS	Ti-6Al-4V	IN718
E1	2675	3533	2922	744	365	303
E2	2491	2944	2816	323	331	231
E3	2045	2590	2656	242	279	273
E4	1835	2473	2337	160	389	342
E5	1783	-	1594	149	-	817
E6	1678	-	-	179	-	-

5.2.2 Theory

The relationship between yield strength and normalised enthalpy is shown in Figure 5.1 after tensile testing at room temperature. There are a variety of possible relationships between σ_Y and H_n, but the stated values are the result of process optimisation that resulted in low residual stresses, low porosity (near-full density), and a single phase on which solidification/deformation processes are imposed. As a result, the following theory is only true after such optimisation. In the case of 316L SS, increasing the heat input results in a monotonic hardening response, while the yield strength of IN718 and Ti-6Al-4V is determined by a balance between softening and hardening depending on the heat input. In 316L SS, the highest heat input results in the highest yield strength. Conversely, in IN718 and Ti-6Al-4V, the maximum yield strength occurs for their lowest corresponding H_n.

Inspection of the polynomial forms of σ_Y in Figure 5.1 indicate that the variation of yield stress with normalised enthalpy can be completely determined by $\frac{d\sigma_Y}{dH_n}$ and $\frac{d^2\sigma}{dH_n^2}$. The most conspicuous aspect of LPBF is rapid solidification leading to a severe thermal strain ϵ. Thus, it is postulated that $\frac{d\sigma_Y}{dH_n} = \frac{d\sigma_Y}{d\epsilon}\frac{d\epsilon}{dH_n}$, but

i $\frac{d\epsilon}{dH_n} = \frac{d\epsilon}{dT}\frac{dT}{dH_n}$, where $\frac{d\epsilon}{dT} = \alpha_{CTE}$ is the coefficient of thermal expansion,

ii and $\frac{\mathrm{d}\sigma_Y}{\mathrm{d}\epsilon} = \frac{\mathrm{d}\sigma_Y}{\mathrm{d}\rho}\frac{\mathrm{d}\rho}{\mathrm{d}\epsilon}$, which indicates that the thermal strain ϵ changes yield strength via a variation in dislocation density ρ.

Yield strength variation with normalised enthalpy

The variation of yield strength with normalised enthalpy is therefore expressed as the product of four terms to reveal the contribution of the various hardening and softening mechanisms:

$$\frac{\mathrm{d}\sigma_Y}{\mathrm{d}H_n} = \frac{\mathrm{d}\sigma_Y}{\mathrm{d}\rho}\frac{\mathrm{d}\rho}{\mathrm{d}\epsilon}\frac{\mathrm{d}\epsilon}{\mathrm{d}T}\frac{\mathrm{d}T}{\mathrm{d}H_n}, \tag{5.1}$$

(i) the Taylor strengthening $\frac{\mathrm{d}\sigma_Y}{\mathrm{d}\rho}$, (ii) the Kocks-Mecking contribution $\frac{\mathrm{d}\rho}{\mathrm{d}\epsilon}$, (iii) the thermal straining $\frac{\mathrm{d}\epsilon}{\mathrm{d}T}$, and (iv) the heat dissipation cooling $\frac{\mathrm{d}T}{\mathrm{d}H_n}$. Equation 5.1 uses the chain rule to show that certain variations are dependent on one another. In other words, for a given heat input of H_n, a temperature drop of ΔT occurs as the laser beam moves forward, creating a special strain and a variation in dislocation density to accommodate it. The yield strength can be calculated using the Taylor relationship and the dislocation density obtained from the complex multiplication and annihilation processes.

Yield strength variation with dislocation density

The evolution of strength is first expressed in terms of dislocation density as can be described by the well-known Taylor relationship [279]:

$$\sigma_Y = \alpha M \mu b \sqrt{\rho}, \tag{5.2}$$

where α=0.3 [276] reflects the average strength of dislocation interactions (Taylor constant), M=3 [280] is the Taylor factor and accounts for textural effects, μ is the shear modulus and b is the magnitude of the Burgers vector. Therefore, the dependency of strength with dislocation density can be estimated by:

$$\frac{\mathrm{d}\sigma_Y}{\mathrm{d}\rho} = 0.5\alpha M\mu b\rho^{-0.5}. \tag{5.3}$$

For dislocation density estimation in various experimental conditions, the equations presented by Galindo-Nava $et~al.$ [281, 282] are used for face-centred cubic (FCC) structures (316L SS and IN718) and body-centred cubic (BCC) structures (Ti-6Al-4V above the β-transus temperature), respectively:

$$\rho = \left[\frac{12\pi(1-\nu)}{(2+\nu)} \left(1 + \frac{N^{-1}T\Delta S_{FCC}}{0.5\mu b^3} \right) \right]^2 d_c^{-2}, \tag{5.4}$$

$$\rho = \left[\frac{6\pi(1-\nu)}{(2+\nu)} \left(1 + \frac{N^{-1}T\Delta S_{BCC}}{2\mu b^3} \right) \right]^2 d_c^{-2}, \tag{5.5}$$

where ν is the Poisson's ratio, N is the impingement effect due to the overlapping strain field of contiguous dislocations that alter the possibilities for dislocation slip, ΔS_{FCC} and ΔS_{BCC} are the statistical dislocation entropies of FCC and BCC structures, respectively, T is the peak temperature and d_c is the dislocation cell size. The statistical entropy for FCC and BCC structures is respectively [127, 282]:

$$\Delta S_{FCC} = k_B \ln \left(\frac{\dot{\epsilon}_0 + \vartheta}{\dot{\epsilon}} \right)^N, \tag{5.6}$$

165

$$\Delta S_{BCC} = k_B \ln \left(\frac{\dot{\epsilon}_0 + \vartheta}{\dot{\epsilon}} \right)^{2N}, \tag{5.7}$$

where k_B is the Boltzmann constant, $\dot{\epsilon}_0 = cb\rho$ is a limiting value for the strain rate, and c is the speed of sound in the bulk. $\vartheta = \vartheta_D \exp\left\{ \left(-\frac{E_m}{RT} \right) \right\}$ is the vacancy migration frequency, $\vartheta_D = 10^{13}$ s^{-1} is the Debye frequency, $R = 8.314$ J/mol·K is the gas constant, E_m is the vacancy migration energy and T is the absolute temperature, which is taken as the peak temperature of the melt pool as in equations 5.4 and 5.5. ϑ accounts for the number of atomic sites a vacancy jumps per second. $\dot{\epsilon}$ is the LPBF strain rate, which can be estimated via equation 4.5.

The corresponding cellular structure size (d_c) can be estimated via the average LPBF cooling rate (CR) through the empirical equation proposed by Hunt [283]:

$$d_c = B(CR)^{-n}, \tag{5.8}$$

where B and n are material-dependent constants. The average LPBF cooling rate can be approximated via:

$$CR = \dot{\epsilon}\Delta T, \tag{5.9}$$

where, ΔT is the difference between the peak temperature and the powder bed temperature.

Dislocation density variation with thermal strain

The Kocks-Mecking (KM) theory for FCC alloys (equation 5.10) and its modified version for BCC alloys (equation 5.11) have been used [137, 282] to estimate the

166

contribution of dislocation hardening and softening during LPBF:

$$\frac{\mathrm{d}\rho}{\mathrm{d}\epsilon}\bigg|_{FCC} = \frac{k_1}{b}\sqrt{\rho} - f\rho, \tag{5.10}$$

$$\frac{\mathrm{d}\rho}{\mathrm{d}\epsilon}\bigg|_{BCC} = \frac{3k_1}{8b}\sqrt{\rho} - \frac{8}{3}f\rho, \tag{5.11}$$

where k_1 is the dislocation storage coefficient and f is the softening coefficient, accounting for dynamic recovery and/or recrystallization. k_1 can be estimated via $k_1 = (\frac{\mu}{\mu_0})^2\frac{1}{100\alpha}$ [273], where μ_0 is the shear modulus of the material at 0 K.

Thermal strain variation with temperature

The contribution of thermal strain to strengthening is constant for all conditions for a given alloy and depends only on $\alpha_{CTE} = \frac{\mathrm{d}\epsilon}{\mathrm{d}T}$, which values are listed in Table 5.3.

Temperature variation with heat input

Based on equation 2.4, H_n is inversely related to the enthalpy at melting h_s, which can be defined as $h_s = C_p dT + H_m$, where C_p is the heat capacity and H_m is the latent heat of fusion. Therefore, the variation of temperature with heat input can be expressed as:

$$\frac{\mathrm{d}T}{\mathrm{d}H_n} = -\frac{AP}{H_n^2 C_p\sqrt{\pi dv D^3}}. \tag{5.12}$$

5.2.3 Results

$\frac{\mathrm{d}\sigma_Y}{\mathrm{d}H_n}$ is determined for 316L SS, Ti-6Al-4V, and IN718 to identify the variance of yield stress with heat input. Table 5.3 lists all of the material properties used in the calculations, along with their sources, from the literature or ThermoCalc. The contribution of dislocation density in LPBF yield strengthening is determined by the cellular structure and the corresponding dislocation cell size, which is determined by the cooling rate. To calculate the average LPBF cooling rate for the various experimental conditions (E1-E6), the average strain rate is calculated using equation 4.5 and shown in Table 5.4 using the values from Tables 5.2 and 5.3. The average cooling rates of the different experiments are shown in Figure 5.2a, using room temperature as the reference powder bed temperature for all experimental conditions. In the case of 316L SS and IN718 alloys, optimum strength is reached when the cooling rate is at its highest. In Ti-6Al-4V, however, the minimum cooling rate resulted in the highest yield strength. The dislocation cell size is calculated for different process conditions and materials (equation 5.8) and shown in Figure 5.2b using B and n values from Table 5.3. The coarsest d_c resulted in the highest yield strength in Ti-6Al-4V, which is prone to martensitic transformation upon cooling, while the finest d_c resulted in the highest yield strength in non-martensitic alloys (316L SS and IN718). As the dislocation density depends also on ΔS_i, i=FCC, BCC; the variation of ΔS_i with H_n for different alloys is plotted in Figure 5.2c (the values in Tables 5.2 and 5.3 are used for calculations). The variation of ρ with H_n for the given heat inputs are shown in Fig. 5.2d.

As compared to the other two alloys, Ti-6Al-4V has the maximum dislocation entropy and dislocation density. The dislocation density of 316L SS is the lowest. In
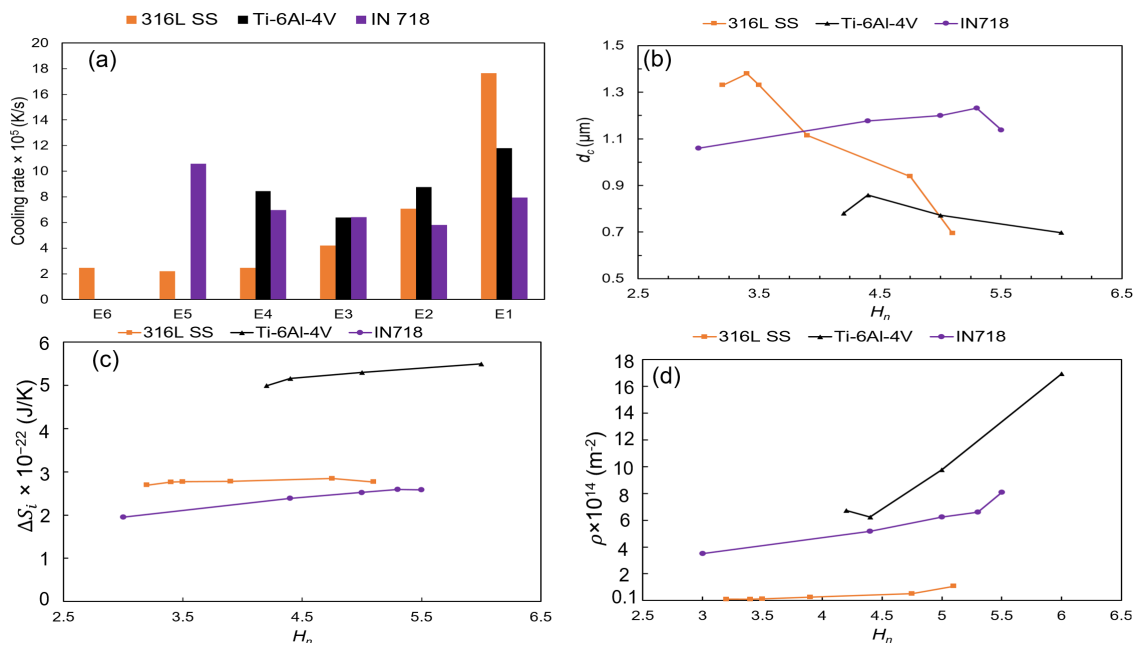
Figure 5.2: (a) Average cooling rate during LPBF of different alloys under various experimental conditions. (b) Variation of dislocation cell size, (c) statistical dislocation entropy and (d) dislocation density with normalised enthalpy in different alloys.

both cases, ρ rises as heat input is increased. Figure 5.3 depicts the contribution of dislocation density to yield strengthening (Taylor strengthening). When comparing the three alloys, it can be seen that Taylor strengthening has the greatest impact on yield strengthening in 316L SS. There is a decrease in the contribution of Taylor strengthening with an increase in heat input in all alloys, indicating that in 316L SS, the lower the Taylor strengthening contribution, the higher yield strength is. In Ti-6Al-4V and IN718 however, optimum yield strength is obtained when Taylor strengthening contributes the most.
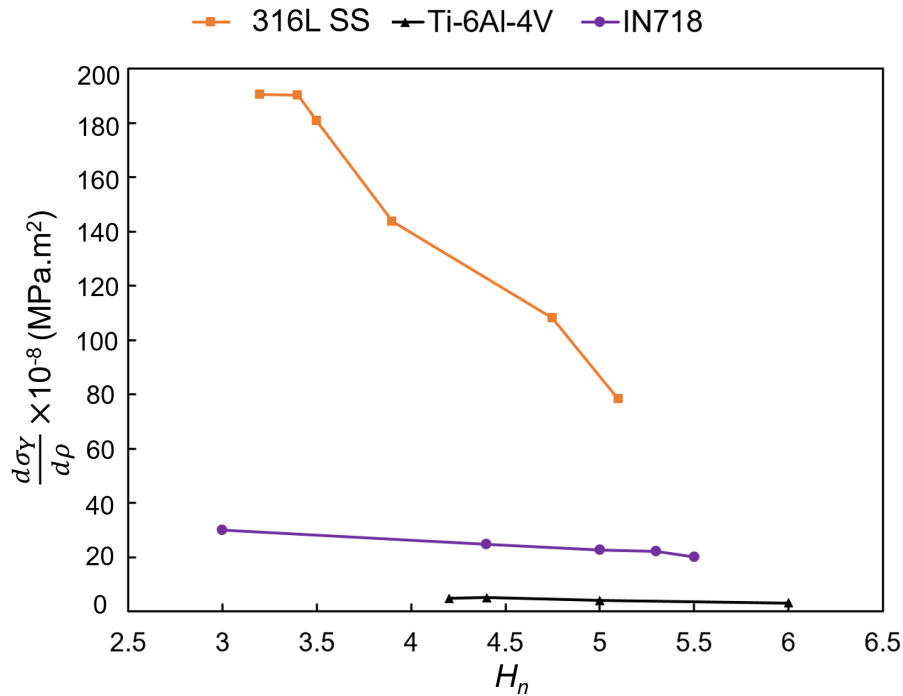
Figure 5.3: Taylor strengthening based on the normalised enthalpy in different alloys.

k_1 and f should be determined to solve the KM equation for the materials studied in this chapter. Process parameters and heat input have no effect on k_1. However, f varies a lot depending on how much heat is put into the process. Table 5.5 shows f values that have been fitted to experiments. When the heat input is increased, the

170

peak temperature rises, which causes f to fall. However, the highest process temperatures increase the rate of recovery and/or recrystallization shown in Table 5.6 as the softening term; this is consistent with the fact that recovery and recrystallization are thermally activated processes, and their occurrence is more likely at higher process temperatures. Table 5.6 shows that rising heat input improves both hardening and softening potential at the same time. Softening is more pronounced in 316L SS than hardening. In this material, the highest strength is obtained when softening exceeds hardening processes due to the other terms in equation 5.1. Hardening, however, dominates softening in Ti-6Al-4V; its maximum yield strength is achieved for low heat inputs, where hardening processes contribute more than softening processes. In IN718, except for the lowest heat input, hardening contributes more to LPBF than softening. As the contribution of softening dominates, however, optimum strength is achieved. Figure 5.4 depicts the combined contribution of dislocation multiplication and annihilation. The higher the yield strength in 316L SS, the more negative the KM equation value is. All of the KM values in Ti-6Al-4V are positive, and the strongest results are obtained when the $\frac{\mathrm{d}\rho}{\mathrm{d}\epsilon}$ value is less positive at lower heat inputs. In IN718 (as in 316L SS), maximum strength is reached when $\frac{\mathrm{d}\rho}{\mathrm{d}\epsilon}$ is negative; but, unlike 316L SS, when the heat input is increased, the $\frac{\mathrm{d}\rho}{\mathrm{d}\epsilon}$ values become positive, reducing yield strength.

Given that the variation of thermal strain with temperature in all cases is primarily determined by α_{CTE}, which is unaffected by H_n, the final contributor to the variation of yield strength with heat input is $\frac{\mathrm{d}T}{\mathrm{d}H_n}$, as shown in Figure 5.5 (using values reported in Tables 5.2 and 5.3). In general, lowering the heat input increases the contribution of temperature variations to yield strength. In comparison to Ti-6Al-4V, temperature
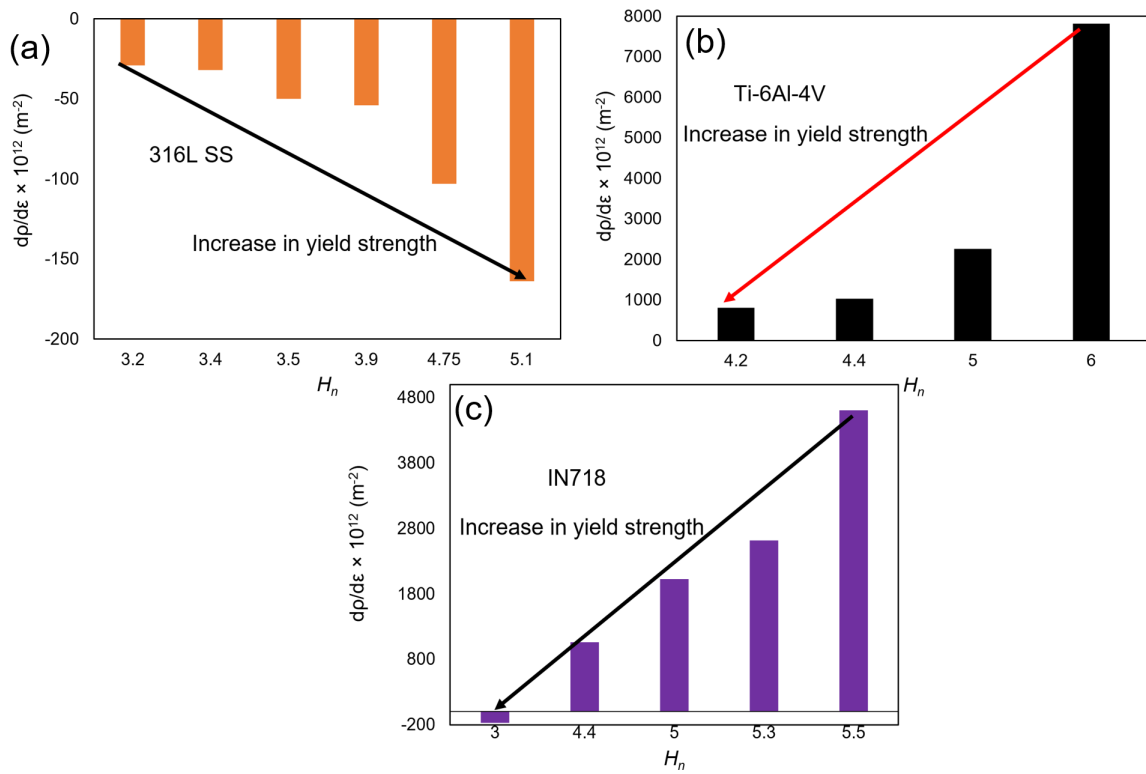
Figure 5.4: Variation of dislocation density with normalised enthalpy for (a) 316L SS, (b) Ti-6Al-4V and (c) IN718.

Table 5.5: The values of k_1 and f used for solving the KM type equations.

Experiment	316L SS		Ti-6Al-4V		IN718	
	k_1	f	k_1	f	k_1	f
E1	0.023	8.38	0.026	2.13	0.028	3.8
E2	0.023	11.59	0.026	2.83	0.028	4.22
E3	0.023	15.39	0.026	3.55	0.028	4.35
E4	0.023	19.39	0.026	3.42	0.028	4.78
E5	0.023	20.38	-	-	0.028	5.8
E6	0.023	20.41	-	-	-	-

Table 5.6: The contribution of hardening and softening during LPBF of different alloys in different processing conditions.

Experiment	Hardening, $\frac{k_1}{b}\sqrt{\rho}$			Softening, $f\rho$		
	316L SS	Ti-6Al-4V	IN718	316L SS	Ti-6Al-4V	IN718
E1	9.799×10^{14}	3.698×10^{15}	3.150×10^{15}	9.815×10^{14}	3.620×10^{15}	3.106×10^{15}
E2	7.082×10^{14}	2.820×10^{15}	2.850×10^{15}	7.093×10^{14}	2.793×10^{15}	2.826×10^{15}
E3	5.332×10^{14}	2.260×10^{15}	2.77×10^{15}	5.337×10^{14}	2.156×10^{15}	2.752×10^{15}
E4	4.234×10^{14}	2.340×10^{15}	2.53×10^{15}	4.239×10^{14}	2.332×10^{15}	2.523×10^{15}
E5	4.025×10^{14}	-	2.095×10^{15}	4.028×10^{14}	-	2.097×10^{15}
E6	4.021×10^{14}	-	-	4.024×10^{14}	-	-

differences with heat input play a larger role in strengthening IN718 and 316L SS.

The numerical values associated with the product of the four terms in equation 5.1 are presented as 'Model' in Figure 5.6 as a proof of concept. In Figure 5.6, the values directly fit from experiments are referred to as 'Experiment', which correspond to the first derivative of the polynomial equations shown in Figure 5.1:

$$\frac{\mathrm{d}\sigma_Y}{\mathrm{d}H_n}\bigg|_{316LSS} = 10H_n + 9, \tag{5.13}$$

$$\frac{\mathrm{d}\sigma_Y}{\mathrm{d}H_n}\bigg|_{Ti-6Al-4V} = -18H_n + 60, \tag{5.14}$$

$$\frac{\mathrm{d}\sigma_Y}{\mathrm{d}H_n}\bigg|_{IN718} = -100H_n + 328. \tag{5.15}$$
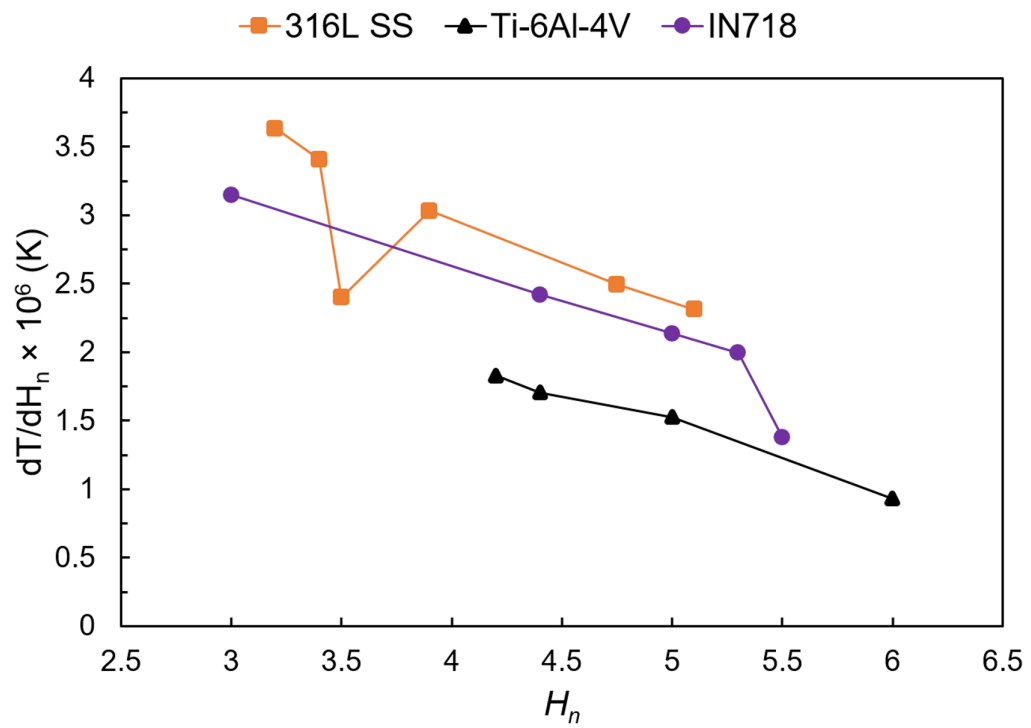
Figure 5.5: The variation of temperature with normalised enthalpy during LPBF of different materials.

In any case, the model and the experiment are a perfect match. Given the near-perfect fit of the slopes of the curves in Figure 5.6, $\frac{d^2\sigma_Y}{dH_n^2}$ can also be numerically extracted, and the entire form of the curves in Figure 5.1 can be precisely determined in support of the validity of equation 5.1.
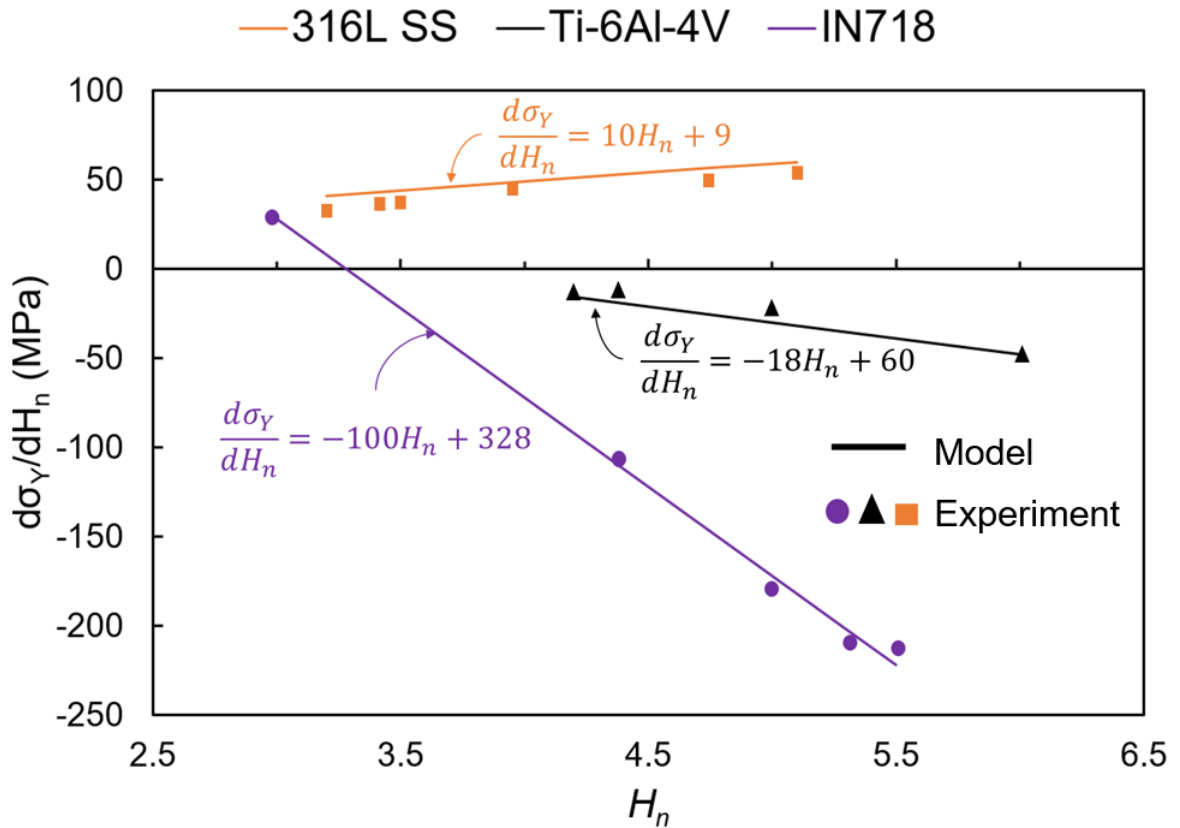
Figure 5.6: Variation of the yield strength with normalised enthalpy, comparing experimental and modelling values. Equations 5.13, 5.14, and 5.15 come from the experimental fitting from Figure 5.1. Model values are the product of the four numerically obtained terms in equation 5.1.

175

5.2.4 Discussion

Variation of yield strength with heat input

In LPBFed alloys, four mechanisms influence yield strength: (i) Taylor strengthening, (ii) Kocks-Mecking contribution, (iii) thermal straining, and (iv) heat dissipation cooling. Process-dependent mechanisms include Taylor strengthening and heat dissipation cooling, while alloy-dependent mechanisms include Kocks-Mecking contribution and thermal straining. The relative contribution of each of these mechanisms to the yield strength of different materials is illustrated in Figure 5.7. We note that the vertical axis in the bar chart is $\ln\left|\frac{d\sigma_Y}{dH_n}\right| = \ln\left|\frac{d\sigma_Y}{d\rho}\right| + \ln\left|\frac{d\rho}{d\epsilon}\right| + \ln\left|\frac{d\epsilon}{dT}\right| + \ln\left|\frac{dT}{dH_n}\right|$ to demonstrate the relative contribution of each term in equation 5.1 in the variation of yield stress with normalised enthalpy. The corresponding fractions of each of the mechanisms contributions are summarised in the pie charts in Figure 5.7 for different alloy families by taking the relative contributions in the bar chart.

Kocks-Mecking contribution

The Kocks-Mecking contribution (Figure 5.7) is the most important strengthening mechanism in all three materials analysed in this chapter, accounting for more than 40% of the yield strength; however, the other mechanisms combined play a similar role. This is in contrast to the belief that the cellular structure is the only factor that contributes to the yield strength of LPBF alloys [17, 11, 13, 141]. As a result, it can be concluded that the dislocation generation coefficient (k_1) and the dynamic recovery coefficient (f) have a major impact on the yield strength of LPBF-produced components. The evolution of dislocations with thermal strain is related to dislocation generation and annihilation, according to equations 5.10 and 5.11. The contribution
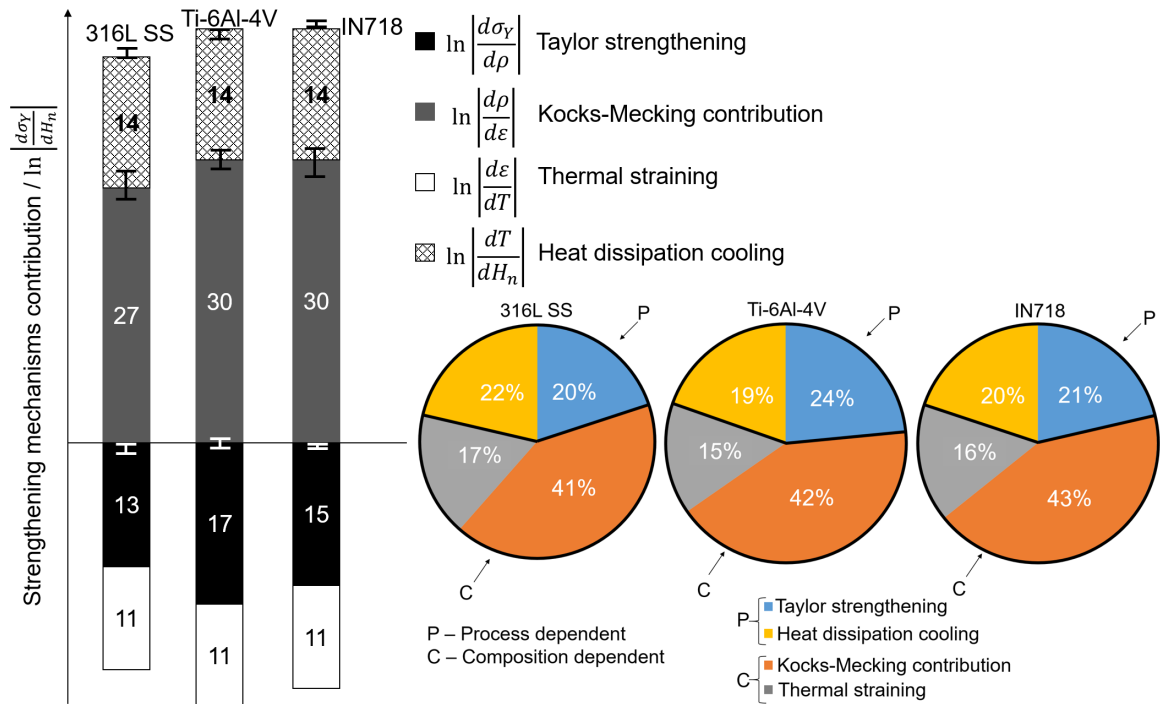
Figure 5.7: Contribution of the four strengthening mechanisms involved during LPBF of different materials in a natural logarithmic scale presented in the bar chart. Error bars represent the ranges within which each term varies with H_n for the corresponding alloy. Pie charts represent the fraction of contribution of each strengthening mechanism in the alloy families produced by LPBF.

of Kocks-Mecking to yield strengthening is depicted in Fig. 5.4. The Kocks-Mecking contribution sensitivity and strain hardening/softening during LPBF are shown in Tables 5.5 and 5.6 in relation to the variations of k_1 and f. A positive and a negative term contribute to dislocation multiplication and annihilation, respectively, in the KM equation. In 316L SS, a softening process (recovery/recrystallization) at high temperatures dominates during LPBF, but hardening dominates in the other alloys (Figure 5.4). Dislocations form as a result of the thermal strain produced during LPBF, and as the thermal straining progresses, dislocations cross-slip and climb. This promotes the formation of more energy favourable dislocation cell structures with LAGBs [284]. This is part of the DRV process, which is thought to be the main softening mechanism in 316L stainless steel (Chapter 4). New dislocation cells will develop as the dislocation population grows, and grain refinement will occur, potentially improving the material's yield strength during tensile testing [285, 284]. The development of dislocation cells during 316L SS LPBF is consistent with previous reports [17, 11], indicating that DRV dominates during 316L SS LPBF. DRX, which is thought to be the key softening mechanism in LPBF of IN718 and Ti-6Al-4V [134, 286], occurs when thermal strain reaches a certain critical value, causing heavily dislocated grains with dislocation cells to nucleate strain-free grains.

According to the data in Table 5.5, the highest dislocation density and maximum strength are reached in 316L SS when f is the lowest (Figure 5.2d). The highest DRV rate is obtained at the highest heat input, as well as the highest contribution of the hardening term, resulting in the maximum yield strength, as shown in Table 5.6. Since thermal strain increases with heat input, a portion of it is relaxed by DRV, while the remainder increases dislocation density, resulting in the highest yield strength.

The behaviour of Ti-6Al-4V is completely different. When f is at its highest, the dislocation density is at its lowest, resulting in maximum strength (Figure 5.2d). The lower the DRX rate (softening in Table 5.6) in Ti-6Al-4V, where DRX is thought to be the key restoration mechanism [287, 288, 289, 290], the higher the propensity for martensite formation. New grains with low dislocation density form when a critical strain for DRX is reached [117]. Therefore, the likelihood of martensite formation during cooling is reduced. The thermal strain generated during LPBF in Ti-6Al-4V is estimated to be about 0.05 ($\epsilon = \alpha_{CTE}\Delta T$) in E3 and E4 conditions, and in these conditions the material has a lower ability for DRX, which leads to more martensite formation upon cooling and a higher subsequent yield strength.

Hardening processes predominate during IN718 LPBF at high and moderate heat inputs, as shown in Figure 5.4c (because the KM equation has a positive value). At low heat inputs, however, $\frac{d\rho}{d\epsilon}$ is negative, indicating that softening is dominant. When a critical strain is reached, IN718 is susceptible to DRX [134]. Interestingly, the highest strength is obtained at the lowest heat input, when softening is predominant. When the heat input is reduced, the f values for IN718 increase. However, at low heat inputs, the dislocation density decreases, resulting in a lower DRX rate (Figure 5.2d). In this material, the lower the DRX rate, the higher the yield strengthening.

At high temperatures, Ti-6Al-4V and IN718 behave similarly (Figure 5.4). At lower heat inputs ($H_n \to 3$), Ti-6Al-4V KM values (Figure 5.4b) are likely to become negative, but due to a lack of data, it can be argued that extrapolation of the current data can lead to similar responses in Ti-6Al-4V and IN718, with both being vulnerable to DRX during LPBF. It can be inferred that DRX-prone materials should be processed in such a way that the DRX rate is slowed by lowering the softening term in

the KM equation. Materials prone to DRV should be subjected to process conditions that result in the highest DRV levels. As shown in Figure 5.1, the yield strength of 316L SS increases with heat input, owing to a higher rate of DRV during processing. The yield strength of Ti-6Al-4V and IN718, on the other hand, is calculated by a balance of DRX softening effects and dislocation multiplication hardening. Thus, the yield strength of these two alloys increases as the DRX rate is reduced at lower heat inputs.

Taylor strengthening

As shown in Figure 5.7, Taylor strengthening is the second most important factor in Ti-6Al-4V and IN718, while heat dissipation cooling is more important in 316L SS. This is primarily due to 316L SS's lower heat capacity (C_p) relative to the other alloys tested, which makes it more vulnerable to heat dissipation during cooling. Despite having the highest Taylor strengthening values, in 316L SS, Taylor strengthening plays a smaller role in yield strengthening than heat dissipation cooling, as shown in Figure 5.7. In Ti-6Al-4V and IN718, the yield strength decreases as the dislocation density increases, as shown in Figure 5.2d. This contradicts a previously held belief that dislocation density has a major influence on yield strength [11, 132]. Furthermore, Figure 5.2b shows that when the largest dislocation cell size is formed during LPBF, the highest yield strength in Ti-6Al-4V is obtained. This also contradicts a previous hypothesis about the importance of dislocation cell size in yield strengthening [17]. Findings of this work demonstrated that dislocation multiplication/annihilation through KM contribution dominates in determining the yield strength in LPBF processed alloys.

It is worth noting that the combination of a very small dislocation cell size and maximum dislocation density (Taylor strengthening) was the third most important contributor to the yield strength of 316L SS. This shows that the role of dislocation density in strengthening is linked to cellular structure, specifically the size of these structures. Therefore, the cellular structure influences the dislocation density in LPBF processed 316L SS, acting as a strengthening mechanism. Dislocation cell size has a direct effect on yield strengthening in IN718, without increasing dislocation density as a result of cell refinement. After LPBF, Ti-6Al-4V usually has a martensitic microstructure; since a very fine cellular structure will inhibit martensite formation, the highest yield strength is obtained when the cellular structure is coarsest, despite the lowest dislocation density.

Heat dissipation cooling and thermal straining

The lowest contribution to strengthening is made by heat dissipation cooling in Ti-6Al-4V and IN718 and thermal straining in all three alloys (Figure 5.7). The fact that 316L SS and IN718 have the highest thermal expansion capability due to thermal strains, as shown in Figure 5.5, indicates that the yield strength of such FCC materials is highly dependent on heat input values. However, martensitic materials such as Ti-6Al-4V have a lower sensitivity to variations in heat input.

Error estimation

Variability in the physical properties used in equation 2.4 (normalised enthalpy) can cause errors in yield strength prediction. The absorptivity is the only parameter whose calculation is sensitive to process parameters, despite the fact that the enthalpy at

melting temperature and the thermal diffusivity have fixed values for a given composition. The LPBF process parameters will adjust the absorptivity values by a factor of two, according to Trapp *et al.* [291]. The following relationship was proposed between absorptivity and process parameters:

$$A = \frac{\Delta H \cdot vP}{l}, \tag{5.16}$$

where ΔH is the enthalpy and l is the total length of the laser track. Equation 5.16 shows that in addition to the process parameters, the enthalpy, which can be calculated via $\Delta H = \int_{T_0}^{T_1} mC_p dT$ (where m is the mass and T_0 and T_1 are the initial and final temperatures, respectively) play a significant role. Due to the difficulty of calculating enthalpy, as well as the effective P and v during LPBF, an average A was used in equation 2.4, which tends to produce reasonable results, at least in the case of keyhole-induced pore and lack of fusion prevention [62]. Furthermore, the two-phase state of powder during solidification in LPBF makes absorptivity measurements more difficult, justifying the use of an average A in equation 2.4.

The error bars in Figure 5.7 display the errors caused by composition changes and process parameters in the four strengthening mechanisms described in this chapter. The error is less than 5% in all situations, indicating that this method can accurately predict yield strength in fully-dense LPBF processed alloys.

Alloy and process design potential

Wrought alloy compositions are currently used in additive manufacturing technologies such as LPBF. However, designing alloys for LPBF to take advantage of its specific thermo-mechanical process features would take a lot of time and effort. The factors

affecting the yield strength of LPBF alloys can be divided into two groups in this study: composition and process based factors. In terms of alloy design, new compositions with optimised k_1 and f values can be produced to improve the yield strength of LPBF manufactured alloys by controlling process parameters to achieve the best dislocation cell sizes, dislocation densities, and heat dissipation during cooling. The thermostatistical approach to describe deformation is particularly suited to the task, as it naturally incorporates the effects of temperature, strain rate and composition [292, 282, 273, 127].

The opportunities for process improvements are illustrated in Figure 5.1, where significant ranges of heat input (H_n) remain unexplored, some of them likely leading to strength improvements such as $H_n < 4.2$ in Ti-6Al-4V or $H_n > 5.1$ in 316L SS.

5.3 Unified Hall-Petch type relationship for yield strength control in LPBF of 316L SS

Based on what has been presented in this chapter, Kocks-Mecking contribution, which is related to restoration mechanisms such as DRX and DRV plays the most important role in strengthening of 316L SS. However, the relationship between normalised enthalpy and yield strength (Figure 5.1) is only valid for fully-dense materials. However, recent publications indicate that porosity may not have adverse effects on mechanical properties, especially on the yield strength [293, 294]. Therefore, the 316L SS samples produced in previous chapter are mechanically tested to investigate the effects of microstructural features revealed in chapter 4 on yield strength. Tensile testing was performed on as-built samples with flat geometry. Room temperature uniaxial tensile

tests were conducted in an Instron 3382 universal testing machine at an initial strain rate of 10^{-4} s^{-1}. Three tests are performed for each experimetal situation that are listed in Table 4.1.

Figure 5.8 shows representative stress-strain curves for as-built samples. Table 5.7 lists the mechanical property values. The process parameters have a significant impact on the yield strength (YS) and ultimate tensile strength (UTS) of the specimens. YS and UTS were higher in S1 with the lowest porosity and recrystallized fraction. However, there is no clear correlation between the YS and the UTS of the samples with porosity content, as S3 with 1.19±0.2% porosity (Table 4.2) has a quite higher YS than S5 with only 0.62±0.2% porosity (Tables 4.2, and 5.7). This demonstrates how microstructure features affect the YS and UTS of LPBF-processed 316L SS. This is in agreement with recent research on the relationship between mechanical properties and porosity content [293, 294]. The presence of pores has no impact on the yield strengthening of LPBF 316L SS, according to Ronnenberg *et al.* [293]; YS is only regulated by microstructural features such as grains and grain boundaries, as well as solidification characteristics. They also discovered that lack of fusion porosity affects only ductility and failure mechanisms. Independency of YS of LPBF 316L SS to the porosity content is also statistically proved by Jost *et al.* [294]. After investigation of 75 LPBF as-built 316L SS samples with various pore size, distribution, and morphology, they concluded that only ductility and strain at ultimate tensile strain are affected by presence of pores. They showed that the critical size of pore that above that size ductility can be affected is about 125 μm. In the as-built samples, it can be seen that YS and UTS increase as the recrystallized fraction decreases and the deformed fraction increases (Tables 4.4 and 5.7). There is also a connection between

the fraction of LAGBs and strength levels, with strength increasing as the fraction of LAGBs increases (Tables 4.5 and 5.7). Surprisingly, porosity content has no effect on ductility, because except from S8, all other samples showed higher elongation to failure values than S1, which has a completely dense structure. This may be attributed to the small size of the pores found in the samples. According to statistical analysis that has been done here, more than 90% of the pores in S2-S8 have a size smaller than 125 μm, which is the crucial pore size for mechanical property deterioration [294]. The lack of correlation between mechanical properties and porosity contents, significant variations in mechanical properties for samples printed with a limited variation in scan speed (S2-S8), and the results of the previous chapter showing that even utilising optimised process parameters to produce fully-dense 316L SS with LPBF can lead to a large variation in mechanical properties, point to the possibility of controlling mechanical properties by optimising microstructural evolution.

Table 5.7: Mechanical properties of the as-built samples.

Sample	Yield strength (MPa)	Ultimate tensile strength (MPa)	Elongation (%)
S1	600±5	707±7	38±1
S2	520±13	645±5	50±4
S3	518±1	644±14	54±4
S4	424±2	585±6	41±1
S5	432±8	596±2	56±6
S6	432±16	596±7	56±6
S7	409±19	561±6	42±2
S8	400±16	543±15	32±3

LAGBs played a significant role in the strengthening of LPBF processed 316L SS, according to the findings of this thesis. For the first time, the yield strength can be quantified in terms of the fraction of LAGBs. In addition to the results of this study, the results of previous studies on LPBF of 316L SS were also used for
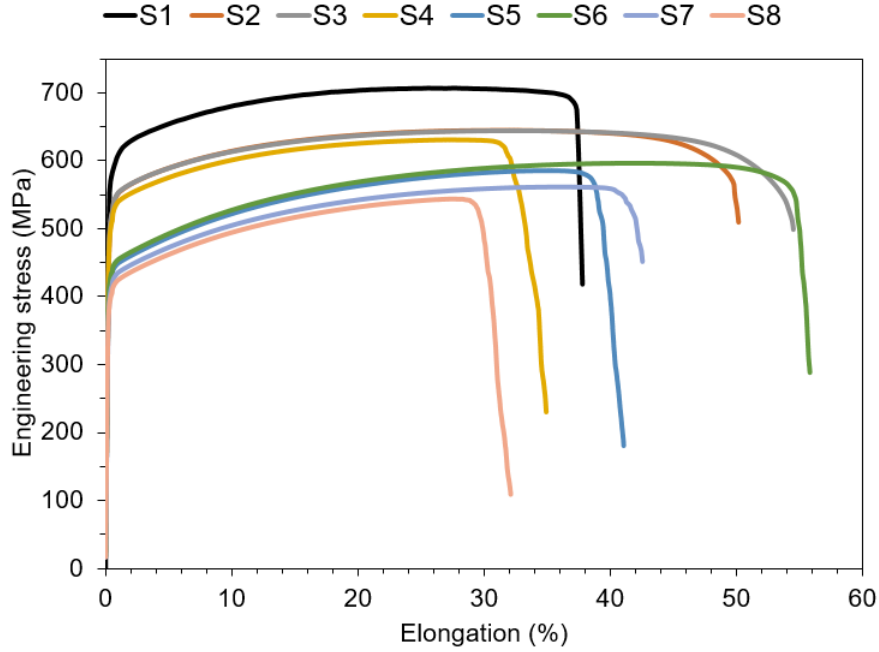
Figure 5.8: Representative engineering tensile stress-strain curves of the as-built samples.

comparison and model verification [295, 296, 297, 298, 299]. Figure 5.9a shows the relationship between the LAGBs fraction (X_{LAGB}) and the yield strength of 316L SS processed with AM. As a result, the LAGBs fraction determines the yield strength of LPBF-processed austenitic SSs that do not undergo phase transformation during processing:

$$\sigma_Y = 725.4 X_{LAGB}^{0.45}.$$ (5.17)

Equation 5.17 represents the yield strength of AM-produced 316L SS with a 4 % estimated error. The error could be caused by porosity and residual stresses generated during LPBF. In LPBF alloys, substructures play a significant role in strengthening, while in wrought materials, both actual grains and substructures contribute to

186
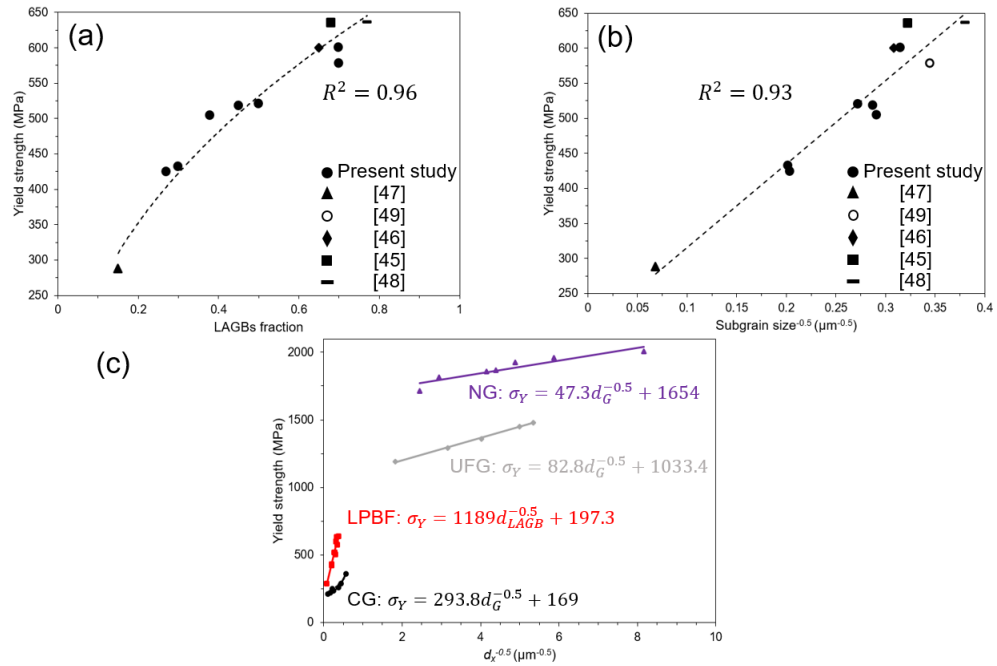
Figure 5.9: (a) Effect of low-angle grain boundaries on the yield strength of 316L SS processed by AM. (b)Yield strength as a function of the inverse square root of subgrain size of LPBF 316L SS reported in the present work and in the literature. (c) Comparison of the Hall-Petch relationships reported for wrought 316L SS with various microstructures (CG: coarse grained, UFG: ultrafine grained and NG: nanograined) [24].

strengthening [144]. In comparison to the common approach for modelling strengthening mechanisms, which includes separate terms for grain boundary, dislocations, and substructure strengthening, this work proposes a unified Hall-Petch-type relationship, which allows processing-microstructure-properties to be linked through grain boundary engineering. The subgrain size (d_{LAGB}), the size of grains with low-angle boundaries) is assumed to be equal to the product of the actual grain size (d_G, only considering HAGBs) and their related fraction (X_{HAGB}):

$$d_{LAGB} = d_G \cdot X_{HAGB} = d_G \cdot [1 - X_{LAGB}]. \tag{5.18}$$

Since the yield strength of LPBF processed 316L SS is greatly influenced by X_{LAGB}, it can be inferred that the yield strength can be interpreted as a Hall-Petch-type relationship when only d_{LAGB} is taken into account. In Fig. 5.9b, the expression for LPBF 316L SS is fitted. The data for the σ_Y, d_G, X_{LAGB}, and X_{HAGB} for modelled conditions are described in Table 5.8. It should be noted that the results of S8 are not taken into account due to its very high porosity contents (more than 2 %).

The Hall-Petch-type equation for LPBF 316L SS based on the subgrain size relationship established in this study (equation 5.18), as shown in Figure 5.9b, agrees very well with the theoretical linear relationship, with a R^2=0.93. For LPBF 316L SS, the Hall-Petch-type equation is as follows:

$$\sigma_Y = 197.3 + 1189 d_{LAGB}^{-0.5}. \tag{5.19}$$

Based on previous research by Yin *et al.* [24], the Hall-Petch equations for nanostructured (NG region), ultrafine grained (UFG region), and coarse grained (CG region) wrought 316L SS are also shown in Figure 5.9c. Table 5.9 shows the values of

Table 5.8: Yield strength (σ_Y), high-angle boundary mean grain size (d_G), LAGBs fraction (X_{LAGB}) and HAGBs fraction (X_{HAGB}) for LPBF 316L SS from this study and literature.

σ_Y (MPa)	d_G (μm)	X_{LAGB}	X_{HAGB}	Reference
600	35	0.7	0.3	Present work
518	22	0.45	0.55	Present work
432	35	0.3	0.7	Present work
504	19	0.38	0.62	Present work
424	33	0.27	0.73	Present work
520	27	0.5	0.5	Present work
635	30	0.68	0.32	[295]
600	29	0.65	0.35	[296]
288	254	0.15	0.85	[297]
637	30	0.77	0.23	[298]
578	28	0.7	0.3	[299]

the Hall-Petch constant and friction stress for wrought and LPBF components. The Hall-Petch constant increased significantly for LPBF 316L SS. The friction stress for LPBF and coarse-grained wrought 316L is quite similar (the slight difference can be attributed to higher N content in LPBF alloys compared to wrought components). A decrease in the actual mean grain size, on the other hand, increased the friction stress significantly. This means that in wrought products, grain refining results in a large increase in dislocation density within grains with HAGBs. Subgrains with LAGBs in LPBF alloys have a high dislocation density around LAGBs, which is consistent with Hong *et al.* [296] microstructural characterisation, as well as the TEM analysis presented in chapter 4 (Figures 4.17 and 4.19). Therefore, as a consequence of LPBF, LAGBs are significantly strengthened. LPBF alloys have Hall-Petch constant that is 4, 15, and 29 times higher than coarse, ultrafine, and nanograined 316L SS, respectively. As opposed to actual grain boundaries in wrought alloys, subgrains in LPBF alloys are much stronger barriers to dislocation movement. Thus, in comparison to

wrought alloys, where actual grain size has the greatest impact on yield strength, sub-grain size (rather than dislocation cell size) plays a critical role in LPBF austenitic SSs strengthening.

Table 5.9: Parameters of Hall-Petch-type equations for LPBF and wrought 316L SS components.

Processing	Hall-Petch constant (MPa μm$^{0.5}$)	Friction stress (MPa)
LPBF	1189	197.3
Wrought (CG)	293.8	169
Wrought (UFG)	82.8	1033.4
Wrought (NG)	47.3	1654

Previous reports in the literature claim that the key contributor to yield strengthening of LPBF FCC alloys is solidification cellular structures [17, 222, 300]. Wang *et al.* [17] claimed that yield strength of the LPBF alloys such as 316L SS is inversely proportional to the size of the cellular structure (d_c) through the following Hall-Petch relationship:

$$\sigma_Y = 183.31 + \frac{253.66}{\sqrt{d_c}}. \tag{5.20}$$

However, the findings of this study show that there is no correlation between d_c and LPBF 316L SS yield strength. When Tables 5.7 and 4.6 are compared, it appears that d_c is not the primary contributor to yield strengthening, as S1 with the highest yield strength has coarser d_c than S2, S3, and even S8, with the lowest yield strength. Moreover, using equation 5.20, the estimated yield strength for samples produced in this work are not close to the experimental results presented in Table 5.7. Comparing our results with the results reported by Wang *et al.* [17] also shows no sense, because despite the similar yield strength of the S1 in our work (600 MPa) and the Concept

machine sample in their work (590 MPa), average d_c in our work is much finer than their sample (0.4 μm for S1 and 0.58 μm for Concept sample), which suggests that there is no Hall-Petch relationship between d_c and yield strength in LPBF alloys. The great differences of the estimated values of yield strength through equation (1) with experimental results also cannot be related to the porosity values, because a reduction of 220 MPa (the predicted yield strength using equation 5.20 for S8 is 620 MPa, but its real yield strength is 400 MPa) in the yield strength (in the case of S8) only because of lack of fusion pores is not reasonable, and such decrease in yield strength due to the presence of pores has not been reported previously. Moreover, the samples in [17] also contained porosity up to 0.8 %, which proves that porosity has no significant influence on the yield strength of LPBF alloys.

The development of DRV has a significant impact on the evolution of LAGBs [301]. Two factors must be controlled to activate DRV during LPBF: (i) process strain rate and (ii) temperature gradients. Controlling the process strain rate, as defined by equation 4.5, can determine the transition between CDRX and DRV, according to the thermostatistical theory of plasticity [127]. The highest LAGBs fraction is obtained when the set of process parameters yields a strain rate nearly equal to $\dot{\epsilon}_c^T$ (equation 2.9), according to the findings of this thesis. Thus, to maximise the yield strength, the following condition should be met:

$$\dot{\epsilon} = \frac{kT_{peak}v}{P} = (\dot{\epsilon}_0 + \vartheta) \exp\left(-\frac{\frac{\lambda}{2}\mu b^3 - \frac{2xl^*}{bk_c}\Delta G_{sys}}{k_B T}\right). \tag{5.21}$$

To increase the LAGBs fraction, at least one thermal cycle, in which DRV can be activated directly is also needed. Hence, temperature gradients and subsequently δ and Δ must be controlled. The present results showed that to get a DRV-based

thermal cycle, it is necessary to minimise δ and maximise Δ (Figure 4.22). Although too large Δ may cause lack of fusion. δ and Δ depend strongly on the layer thickness and the hatch distance, respectively (equations 4.3 and 4.4). Therefore, lower layer thickness and higher hatch distances can increase the strengthening potential of LPBF processed austenitic SSs.

5.4 Conclusions

The yield strength of fully-dense 316L SS, IN718 and Ti-6Al-4V processed by LPBF is linked to the process heat input, leading to the development of a methodology to explain the variation of yield strength with normalised enthalpy. Analytical models are used to interpret the various mechanisms that control LPBF strengthening. The mechanisms governing the superior mechanical properties of LPBF processed alloys include Taylor strengthening, Kocks-Mecking contribution, thermal straining, and heat dissipation cooling. High heat inputs in 316L SS result in optimum strength due to a high recovery rate combined with a higher contribution of dislocation hardening to refine the cellular structure, and subsequently subgrains. However, low heat inputs result in maximum strengths in Ti-6Al-4V and IN718, which can be attributed to a low rate of recrystallization and a positive contribution from dislocation strengthening. The findings show that yield strength in LPBF alloys is governed by dislocation multiplication/annihilation capability, which is strongly influenced by alloy composition. During LPBF, there is a compromise between dislocation multiplication-induced hardening and the activation of softening processes such as dynamic recovery and recrystallization, which scales the yield strength. Findings of this thesis shed light on the mechanisms that contribute to the superior mechanical properties of various

LPBF alloys. The methodology described here can be used as a metric by the AM community to measure yield strength variance as a function of process parameters and alloy families physical properties.

In addition to the fully-dense samples, eight 316L SS samples that produced and analysed in Chapter 4 were mechanically tested. Since samples with very similar grain sizes show different yield strengths, the yield strength of the LPBF as-built samples does not obey the classical Hall-Petch relationship, which implies that grain boundaries are the strongest dislocation movement barriers. Therefore, in LPBF, grain sizes can be divided into two categories: (i) Actual grains (those with HAGBs) and (ii) subgrains (grains with LAGBs). A power law relationship can be used to express the yield strength as a function of fraction of LAGBs. As a result, a unified Hall-Petch-type relationship was established, which relates yield strength to subgrain size rather than the actual high-angle boundary grain size. The relationship allows to control the yield strength of LPBF 316L austenitic SSs through grain boundary engineering. Subgrain size refinement, which is achievable via increasing the fraction of low-angle grain boundaries, is suggested as the main approach for yield strength improvement in LPBF of austenitic stainless steels. The presence of pores and residual stresses could result in deviations from the yield strength estimation. To increase the LAGBs fraction and increase the yield strength of LPBF austenitic SSs, the occurrence of recovery processes should be maximised. Controlling the process strain rate (a criterion is suggested), as well as controlling temperature gradients by decreasing layer thickness and increasing hatch distance, may be used to achieve this.

Chapter 6

Strain hardening modelling of laser powder bed fusion 316L stainless steel

The chapter presents a multiscale dislocation density-based model for strain hardening of LPBF SS builds undergoing TWIP. The physics-based model takes into account the microstructural evolution of twins and dislocations, as well as dynamic recovery/recrystallization during deformation at room temperature. A comparison with conventionally produced TWIP steels is presented, with special emphasis on the evolution of statistically stored and geometrically necessary dislocations. The analysis demonstrates the significance of the TWIP effect at the start of deformation, which is accompanied by a significant increase in the density of geometrically required dislocations. From the middle stages of deformation, dislocation hardening dominates TWIP hardening. At the final stage of deformation, dynamic recrystallization is activated, improving strain hardening capability and accompanied by a dramatic reduction in

the density of statistically stored dislocations, which were the dominant dislocation type in the as-built material. According to the thermostatistical theory of plasticity, strain hardening of LPBFed alloys is primarily controlled by the rate of dislocation recovery [281]. The number of impinging dislocations in LPBFed alloys is shown to be much higher than in conventionally processed alloys, making the strain hardening mechanisms of LPBFed alloys unique. As a result of controlling the rate of dynamic recovery of dislocations, the presented results open up the possibility of producing alloys with superior mechanical properties.

6.1 Introduction

Determining the strain hardening mechanisms of engineering alloys produced through AM is a critical topic in metallurgy. TWIP and transformation-induced plasticity (TRIP) are two of the most important deformation mechanisms for improving strain hardening in low SFE FCC metals and alloys [302, 303]. It was recently discovered that laser powder bed fusion (LPBF) AM can be used to produce low SFE FCC materials with outstanding mechanical properties such as yield strength while maintaining ductility comparable to wrought counterparts [304]. LPBFed 316L SS has been extensively studied among the low SFE austenitic SSs due to its ability to be printed without severe defects such as cracks and porosity (printability), as well as a significant increase in yield strength values in the as-built state [38, 305]. Several models have been developed to predict the yield strength of LPBFed 316L SS [38, 306, 307, 17]. However, there is a lack of a unified strain hardening model that can describe the distinct deformation mechanisms of LPBFed 316L SS.

New experimental studies have revealed that the room temperature deformation

mechanisms of LPBFed 316L SS are dislocation slip, TWIP, and DRX [150, 308, 228, 309], whereas wrought 316L SS is strengthened by dislocation slip, TWIP, and TRIP effects, with no mention of DRX [310, 311]. The austenite stability, which is controlled by dislocation density, accounts for the difference in strain hardening mechanisms. Austenite stability is thought to be related to the material's SFE [311]. TRIP and TWIP effects are commonly observed in FCC metals and alloys with SFE less than 18 mJ/m2 and greater than 22 mJ/m2 [312, 186]. In the previous chapter, it was discovered that the SFE of the LPBFed 316L SS built with various process parameters is approximately 14 ± 5 mJ/m^2, making this alloy susceptible to strain-induced martensitic transformation during room temperature deformation. LPBF processing, in contrast to its wrought counterparts, can suppress TRIP effect in 316L SS due to increased austenite stability as a result of thermal cycling [313].

The cause of LPBFed 316L SS's high ductility has been discussed. There is sufficient evidence that deformation twinning and dislocation slip occur during deformation [149, 314, 315, 295, 316]. It has also been reported that the TWIP effect is the primary cause of such material's high ductility. According to some studies, the interactions between twins and cellular structures that are formed during LPBF due to rapid solidification, control strain hardening [11]. Wang *et al.* [17] reported that solute segregation along cell walls and LAGBs could improve dislocation pinning and promote twin formation during straining. A few previous studies have also reported the presence of deformation-induced DRX grains [150, 308]. For the formation of DRX grains during tensile testing at room temperature in LPBFed 316L SS, lattice rotation and gradual increase in misorientation of LAGBs and their transformation to HAGBs, as well as a deformation twinning-induced DRX mechanism, are proposed

[150, 308]. However, no mention has been made of the role of DRX in the improvement or deterioration of strain hardening. To the best of the author's knowledge, no strain hardening model taking into account the aforementioned phenomena has been reported for LPBFed 316L SS.

During straining, various strain hardening mechanisms can be activated depending on the type of dislocations. There are two types of dislocations: statistically stored dislocations (SSDs) and geometrically necessary dislocations (GNDs) [317]. SSDs form as a result of the random trapping of dislocations in the bulk, and their accumulation usually results in forest hardening [318]. GNDs are formed as a result of crystal lattice geometrical constraints such as grain/subgrain boundaries, dislocation cell walls, and twin boundaries; their pile-ups result in the formation of a back-stress [318]. Despite the fact that investigating them leads to a better understanding of deformation mechanisms in an alloy, no such studies have been conducted in LPBFed alloys. Characterisation of SSDs is difficult, because they have a zero net Burgers vector, but GNDs can be characterised and quantified by EBSD with a resolution in the range of $0.1° - 0.2$ ° and step sizes of $0.5 - 1$ μm [319].

The goal of this chapter is to present a unified modelling approach for quantitatively describing strain hardening mechanisms and microstructural evolution in LPBFed 316L SS. This model incorporates dislocation hardening, the dynamic Hall-Petch effect (via twin obstacles), and DRX. Furthermore, the storage of GNDs and SSDs, as well as their evolution and roles in strain hardening, are investigated.

6.2 Experimental procedure

316L SS flat tensile testing samples that were built in The University of Nottingham were used for characterisation and mechanical testing; the detailed processing parameters and sample geometry were described in a previous study [146]. The initial gas atomised 316L SS powder with a particle size distribution of 15–45 μm and a mean value of around 30 μm was used as feedstock (Figure 6.1a). The particles were spherical, with only a few satellites. Table 3.7 shows the chemical composition of the as-received powder. As shown in Figure 6.1b, the samples for EBSD and TEM characterisation prior to deformation were obtained from the grip of the as-printed tensile testing specimen (the area that had not been strained during tensile testing, blue rectangle). EBSD and TEM samples (EBSD and TEM characterisation were performed in the Beihang University, China, but the analysis was performed by the author of the thesis) after failure were extracted from an area quite close to the fracture surface, as schematically shown in Figure 6.1b (red rectangle).

Mechanical tensile testing was performed at room temperature at an initial strain rate of 10^{-4} s^{-1} using an Instron 3382 universal testing machine. The reported strength and ductility values were the average of 3 tests. Scanning electron microscopy (SEM) observations were conducted in a Tescan Mira 3 LMHP field emission SEM to characterise the powder morphology. EBSD was employed to examine grain orientation, average local misorientation, grain boundary characterisation, and recrystallization determination in a Tescan Mira 3 LMHP field emission SEM equipped with OXFORD instruments symmetry EBSD detector at a scanning step size of 0.8 μm and 0.5 μm prior to and after deformation, respectively. HKL Channel 5 data postprocessing software was used to produce the related EBSD maps. The grain (according

198
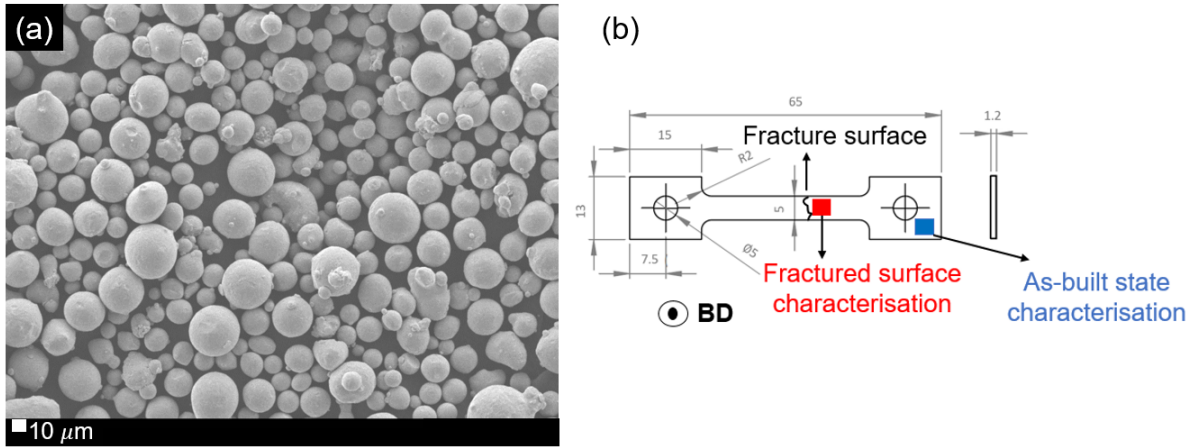
Figure 6.1: (a) SEM images of the particle size distribution of as-received 316L powder. (b) Dimensions of the tensile testing specimen. Build direction (BD) is indicated. Characterisation samples are shown schematically in blue and red rectangles representing the as-built state and fractured state, respectively.

to high-angle grain boundaries, HAGBs) and subgrain (according to LAGBs) size were measured by line intercept method using EBSD grain boundary maps. Grain boundaries are classified according to their misorientation angle into LAGBs ($2° \leq \theta < 15°$) and HAGBs ($15° \leq \theta$). TEM was used for further characterisation of the nanometers scale features such as dislocations, dislocation cells, and deformation twins. Three-mm diameter disks were machined out of the samples, ground to 50 μm thickness, and thinned using Gatan 691 Ion Beam Thinner for TEM using TECNAI G20 at 200 kV.

6.3 Results

6.3.1 Mechanical properties

The true stress-strain curve and strain hardening rate of the LPBFed 316L SS are shown in Figure 6.2a. Table 6.2 shows the average mechanical properties of LPBFed 316L SS. Necking began at a true strain of around 0.33 (the alloy does not follow Considère criterion [320]). The strain hardening rate was constantly decreasing. To gain a better understanding of the deformation mechanisms, the instant strain hardening exponent (n) was plotted as a function of true strain to assess the alloy's strain hardening capability (Figure 6.2b). The value n is given by [321]:

$$n = d(\ln \sigma)/d(\ln \epsilon), \tag{6.1}$$

where σ is the true stress, and ϵ is the true strain. Most metals and alloys have n values ranging between 0.1 to 0.5. In this study, the LPBFed 316L SS exhibits n values between 0.05 and 0.3. These values are higher than the n values reported by Voisin *et al.* [222], they were in the range of 0.05–0.2 for the as-built 316L SS. n values of the present steel are similar to those reported for the LPBFed 316L SS after annealing at 1000 °C for 1h in the same publication [222]. This shows that the strain hardening capability of the present steel is higher than the steel produced in [222], and it is more similar to a LPBFed and recrystallized alloy. At the beginning of plastic deformation, n increases rapidly with increasing strain up to a value of 0.15 (Stage A), then it jumps to higher values of around 0.2, at the strain of about 0.22 (Stage B). n values continue to rise with a significantly higher rate to a maximum value of 0.3 at a strain of 0.27 (Stage C). Finally, n decreases rapidly to 0 by the end of deformation. Abrupt

changes in n values during plastic deformation can be related to various deformation mechanisms during tensile testing. Therefore, strain hardening behaviour of LPBFed 316L SS can be divided into three stages, as indicated in Figure 6.2b by dashed lines.

Table 6.1: Mechanical properties values of LPBFed 316L SS.

True yield strength (MPa)	True ultimate tensile strength (MPa)	Fracture strain
600±5	952±7	0.32±0.01
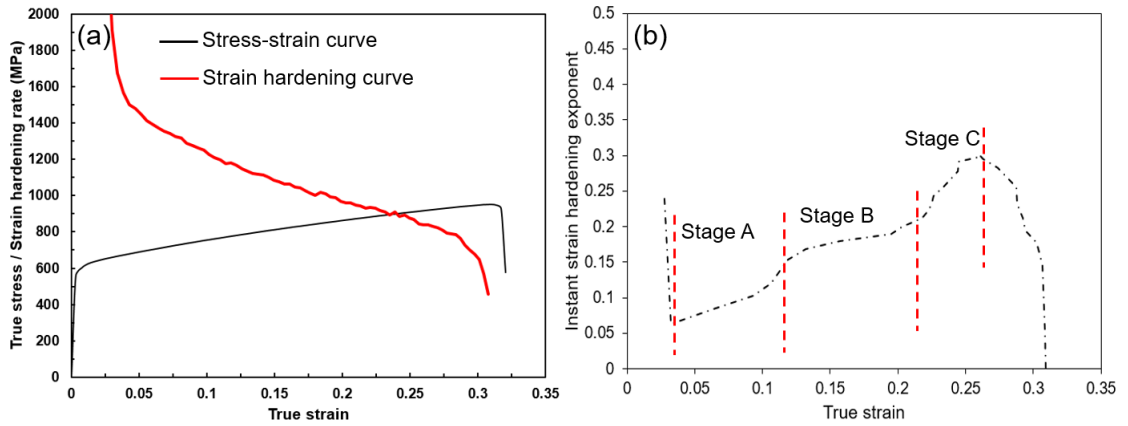
Figure 6.2: (a) Tensile true stress–strain curve of the LPBFed 316L SS and the corresponding strain hardening curve. (b) Instant strain hardening exponent as a function of true strain, indicating the strain hardening capability of the LPBFed 316L SS.

6.3.2 Microstructure

Previous studies of LPBFed 316L SS using various characterisation techniques such as EBSD and TEM revealed the most important aspects of the microstructure of this steel under deformation: grains/subgrains, mechanical twins, dislocation cells, and DRX [304, 308, 322]. Figure 6.3 depicts various microstructural features that can be identified using EBSD after fracture of the current LPBFed 316L SS. Figure 6.3a depicts a representative image quality (IQ) map of the fractured sample with

deformation bands visible in most grains. The post-fracture inverse pole figure (IPF) map from the location shown in Figure 6.1b is shown in Figure 6.3b. HAGBs are indicated in black. The majority of the grains have orientations close to $\langle 101 \rangle$ and $\langle 111 \rangle$, indicated by green- and purple-coloured grains in Figure 6.3b. Variation of the texture in the present study was consistent with earlier reports on LPBFed 316L SS [323, 72, 324]. Deformation bands with two variants close to $\langle 101 \rangle$ and $\langle 100 \rangle$ directions can be recognised. Figure 6.3c shows the twin boundary map of the fractured sample depicting that the characterised deformation bands in Figures 6.3a and 6.3b are mechanical twins. As expected the fractured material was characterised by large deformation twins. Deformation twins are mostly formed in grains with $\langle 101 \rangle$ and $\langle 111 \rangle$ directions, which is consistent with previous reports [304, 324]. The volume fraction of twins based on several EBSD maps is estimated to be 0.28±0.02. Deformation twinning plays an important role in the ductility of materials with low SFE, as twin boundaries act as effective dislocation barriers during deformation. This phenomenon of reducing the dislocation mean free-path is called the dynamic Hall-Petch effect, which will promote the strain hardenability and delays the onset of necking [325]. The distribution of LAGBs and HAGBs in the fractured state is shown in Figure 6.3d, where statistical results show that 60% of the boundaries are high-angle. The distribution of LAGBs and HAGBs of the present steel in the as-built state was reported in Chapter (Figure 4.13a). An increased fraction of HAGBs after fracture from 30% in the LPBF as-built condition to 60% occurred, despite the fact that subgrains (grains with boundaries coloured in yellow) are refined significantly after fracture compared to the as-built state. In addition to a substantial refinement in subgrain size (comparing Figures 6.3d and Figure 4.13a), the transformation of LAGBs to

HAGBs can be recognised. Subgrain size refinement can be related to an increase in both dislocation density and dislocation slip due to plastic deformation. An increase in the misorientation of LAGBs towards becoming HAGBs could be related to the formation of deformation twins.
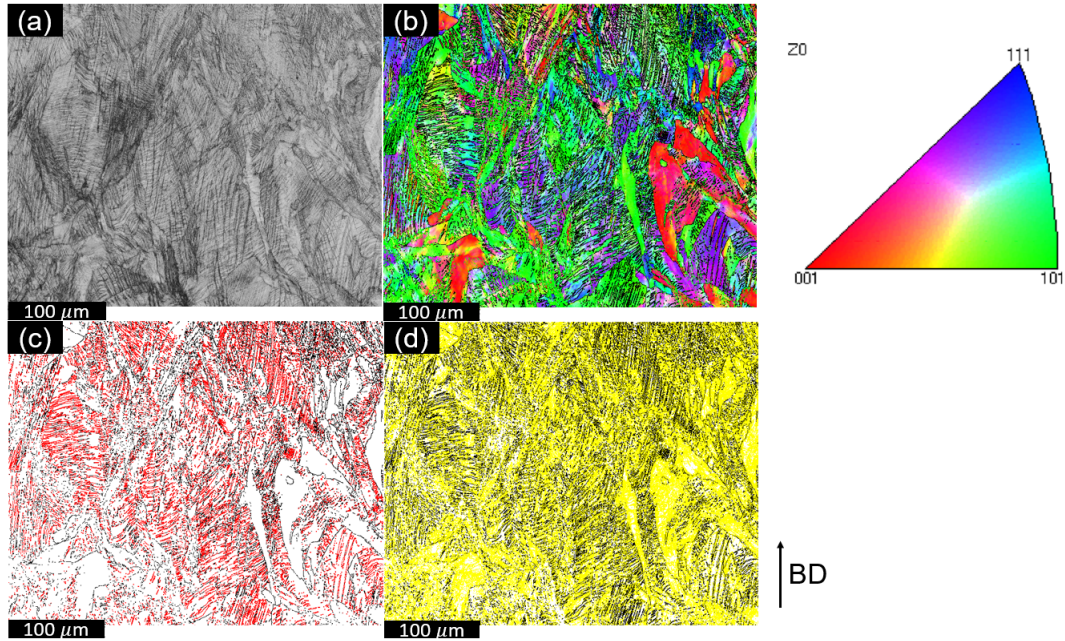
Figure 6.3: (a) EBSD IQ map indicating the fractured microstructure containing several deformation bands. (b) EBSD IPF map showing grain orientation according to the plane parallel to the BD. (c) EBSD twin boundary map showing the distribution of twins in red. (d) EBSD grain boundary map showing HAGBs and LAGBs in black and yellow, respectively.

The kernel average misorientation (KAM) maps (Figures 6.4a and 6.4b) depict local changes in lattice orientations caused by lattice rotation or distortion. Such rotations/distortions are caused by dislocation generation reactions that occur as a result of thermal and residual plastic strains generated during LPBF (Figure 6.4a) and/or during tensile testing (Figure 6.4b). As a result, the local variations in the KAM map can serve as a qualitative representation of both residual stress/strain and

GND density. It should be noted that total dislocation density includes GNDs as well as SSDs. The as-built state showed little local misorientation, as evidenced by the dominance of blue colour (Figure 6.4a), indicating a low overall stress state. Prior to deformation, a heterogeneous dislocation accumulation in the LAGBs is observed (comparing Figure 6.4a with Figure 4.13a), with limited misorientation within the grains/subgrains. Riabov *et al.* [322] demonstrated that strain accumulation occurs around cell boundaries in as-built and deformed LPBFed 316L SS samples. They used a finer EBSD scanning step size than the one used in this study to demonstrate the ability of dislocation cells to pin the dislocations. Regarding the fact that dislocation cell formation is a subprocess for the evolution of LAGBs [306], and that the results of our previous study showed that LAGBs can pin the dislocations at a larger scale, it can be claimed that the current study results are consistent with what has previously been reported about the importance of cell boundaries and, consequently, LAGBs in yield strengthening of LPBFed 316L SS. In contrast with the as-built state, the fractured state showed areas that had a very high local misorientation, due to straining, as well as areas that are strain-free, denoted by blue colour (Figure 6.4b). To confirm the presence of partially/fully recrystallized areas, a recrystallization map of the same area has been generated and shown in Figure 6.4c. It can be seen that the areas that have been characterised as strain-free (blue areas in Figure 6.4b) are also characterised as recrystallized (blue areas in Figure 6.4c) or partially recrystallized (yellow areas in Figure 6.4c). It should be noted that recrystallized, partially recrystallized, and deformed (red in Figure 6.4c) regions are determined by EBSD post processing HKL Channel 5 software based on the internal average misorientation angle inside each grain. If the average misorientation angle within a grain exceeds

the angle threshold of 2°, the grain is classed as deformed. Grains with subgrains of internal misorientation under 2° that the misorientation across subgrains is above 2° are partially recrystallized. The remaining grains, which contain subgrains of misorientations under 2°, and misorientation across subgrains being under 2° are categorised as recrystallized. DRX regions can be observed at the intersections of deformation twins (Comparing Figure 6.4c and Figure 6.3c). Occurrence of DRX during room temperature deformation of LPBFed 316L SS is consistent with the results of previous studies [309, 150]. A thermostatistical-based formulation to estimate the critical strain for the activation of twinning-induced DRX is presented in Chapter 4 (as well as in [308]).
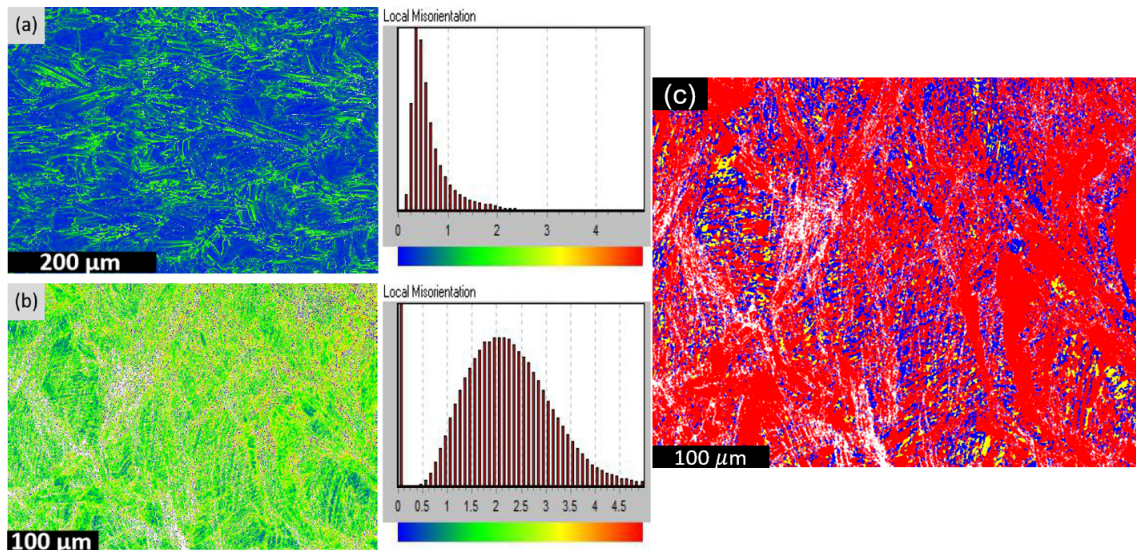
Figure 6.4: (a) Representative EBSD KAM map of the as-built steel. (b) Representative EBSD KAM map of the fractured steel. (c) Representative EBSD recrystallized map, showing recrystallized, partially recrystallized, and deformed regions in blue, yellow, and red, respectively.

Figure 6.5 presents TEM images showing grains exhibiting dislocation cells prior to and after deformation. In the as-built structure, cellular structures that are commonly

observed in LPBFed alloys are present in Figure 6.5a with an average size of 400±80 nm. Cellular walls are observed to be decorated with a higher density of dislocations compared to cell interiors. After deformation, three scenarios are observed for cellular structure evolution: (i) some cells are refined through the pile up of dislocations into their walls (Figure 6.5b). (ii) some cells are cut by LAGBs (Figure 6.5c), and (iii) deformation twins (Figure 6.5d). It can be concluded that most of the existing cellular structures from LPBF as-built state are not strong barriers to dislocation motion, compared to LAGBs and deformation twins. However, their interactions with grains/subgrains and twin boundaries may influence the dislocation mean free path, and subsequently strain hardening capability of the present steel.
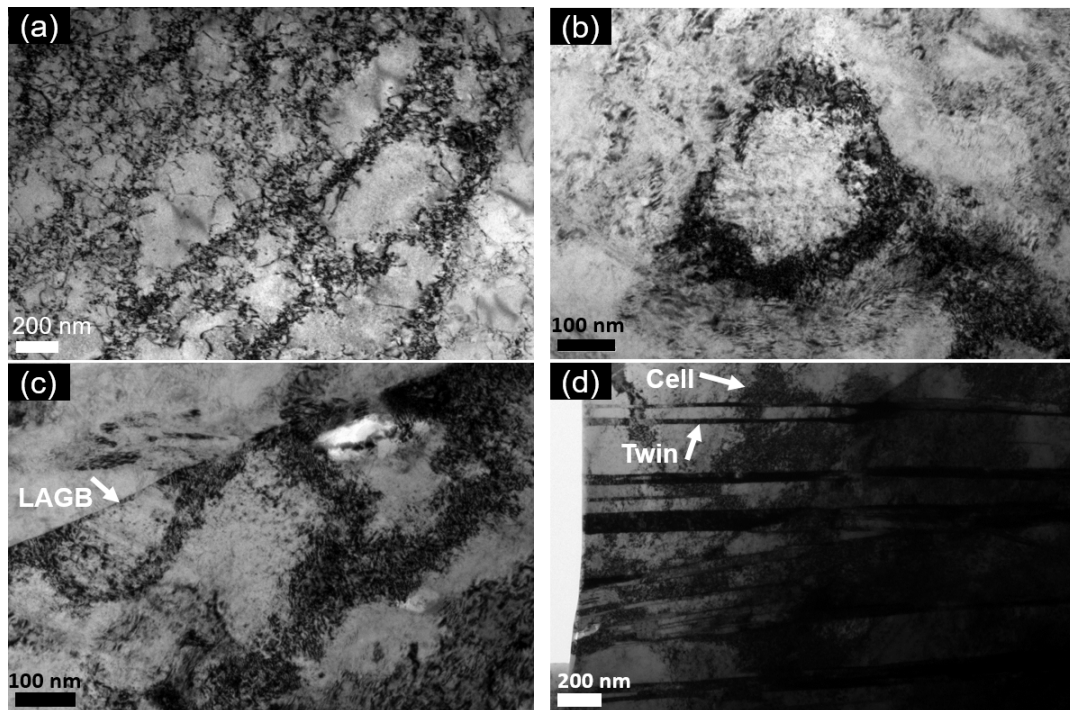
Figure 6.5: Representative bright field TEM images showing (a) the presence of dislocation cells prior to deformation, (b) a dislocation cell after fracture, (c) the dislocation cells that can be cut by LAGBs during deformation, and (d) the growth of deformation twins through the dislocation cells during deformation.

Therefore, our approach to model strain hardening considers a combination of the dislocation slip, deformation twinning, and DRX. Moreover, an analysis regarding the type of dislocations that are evolved during deformation sheds light on recognising which mechanism governs the strain hardening of LPBFed 316L SS.

6.4 Modelling

6.4.1 Flow stress

Evolution of dislocation density, where twinning is also present can be described using a rule of mixtures incorporating both dislocation slip and twinning contributions [326]:

$$d\epsilon = (1 - f_{tw})d\epsilon_{dis} + \epsilon_{tw}df_{tw}, \tag{6.2}$$

where f_{tw} is the volume fraction of twins, $d\epsilon_{dis}$ is the increase in strain as a result of dislocation slip (regarding untwinned area), ϵ_{tw} is the strain induced by formation of twins, and df_{tw} is the increase in twins volume fraction. From equation (6.2), the evolution of dislocation slip contribution with strain $\frac{d\epsilon_{dis}}{d\epsilon}$ can be described as:

$$\frac{d\epsilon_{dis}}{d\epsilon} = \frac{1}{1 - f_{tw}}\left(1 - \epsilon_{tw}\frac{df_{tw}}{d\epsilon}\right). \tag{6.3}$$

It is well-established that the most active twinning system in FCC metals is $\{111\}\langle112\rangle$ [327]. The shear strain for twinning on this system is $\gamma_{tw}=\frac{\sqrt{2}}{2}$. Shear strain is related to the normal strain through the Taylor factor (M): $\epsilon = \gamma/M$. Therefore, equation (6.3) can be rewritten as:

$$\frac{d\epsilon_{dis}}{d\epsilon} = \frac{1}{1 - f_{tw}}\left(1 - \frac{\sqrt{2}}{2M}\frac{df_{tw}}{d\epsilon}\right). \tag{6.4}$$

Dislocation density ρ evolution as a function of true strain can be expressed as:

$$\frac{d\rho}{d\epsilon} = \frac{d\rho}{d\epsilon_{dis}}\frac{d\epsilon_{dis}}{d\epsilon} = \frac{d\rho}{d\epsilon_{dis}}\frac{1}{1 - f_{tw}}\left(1 - \frac{\sqrt{2}}{2M}\frac{df_{tw}}{d\epsilon}\right). \tag{6.5}$$

According to Kocks-Mecking theory for strain hardening, $d\rho/d\epsilon_{dis}$ is a result of the competition between dislocation storage and annihilation due to dynamic recovery and/or recrystallization [137]. Dislocation storage strongly depends on the dislocation mean free path Λ, which is limited by the dislocation forest generation, grain boundaries, and twin boundaries. Previous studies of strengthening mechanisms in LPBFed alloys showed that subgrain boundaries are stronger barriers to dislocation motion, compared to conventional grain boundaries. Thus, in our approach, subgrain size D_s is chosen as the dislocation impedance feature. Λ can be expressed as:

$$\frac{1}{\Lambda} = k_1\sqrt{\rho} + \frac{1}{D_s} + \frac{1}{L}, \tag{6.6}$$

where $k_1 = \frac{1}{30}\left(\frac{\mu}{\mu_0}\right)^2$ is the dislocation storage coefficient, μ is the shear modulus, μ_0 is the shear modulus at 0 K, and $\frac{1}{L}$ represents the reduction in the dislocation mean free path, caused by twin formation and growth [326]:

$$\frac{1}{L} = \frac{1}{2e}\frac{f_{tw}}{1 - f_{tw}}, \tag{6.7}$$

where e is the average twin thickness. The dislocation storage rate $d\rho^+/d\epsilon_{dis} = M/b\Lambda$, where b is the magnitude of the Burgers vector. Therefore the evolution of dislocation density as a result of dislocation slip is expressed as:

$$\frac{d\rho}{d\epsilon_{dis}} = \frac{d\rho^+}{d\epsilon_{dis}} - \frac{d\rho^-}{d\epsilon_{dis}} = M\left(\frac{k_1}{b}\sqrt{\rho} + \frac{1}{bD_s} + \frac{1}{2eb}\frac{f_{tw}}{1-f_{tw}} - (f_{DRV} + f_{DRX})\rho\right), \quad (6.8)$$

where f_{DRV} and f_{DRX} are the dynamic recovery (DRV) and dynamic recrystallization coefficients, respectively. The term $(f_{DRV} + f_{DRX})\rho$ accounts for dislocation annihilation $d\rho^-/d\epsilon_{dis}$. In order to solve equation (6.8), volume fraction of twins and their evolution as a function of strain should be estimated. According to Bouaziz *et al.* [328] twin fraction is related to the strain via:

$$f_{tw} = F_0\left(1 - \exp[-\beta_0(\epsilon - \epsilon_{tw})]\right)^{m^*}, \quad (6.9)$$

where F_0 is the maximum twin fraction, β_0 is the twinning kinetic parameter, ϵ_{tw} is the critical strain for the onset of twinning, and m^* is a fixed exponent. By differentiating equation (6.9) with regard to strain, the evolution of twin fraction with strain is expressed as:

$$\frac{df_{tw}}{d\epsilon} = F_0\beta_0 m \exp\left(-\beta_0(\epsilon - \epsilon_{tw})\right)\left[1 - \exp\left(-\beta_0(\epsilon - \epsilon_T)\right)\right]^{(m-1)}. \quad (6.10)$$

In addition to the contribution of dislocations to the strain hardening, twins also affect strain hardening, as their interactions with the matrix causes back-stress. Back-stress caused by twin formation can be estimated via [25]:

$$\sigma_T = M\mu b\beta\left(\frac{1}{L} + \frac{1}{D_s} + \frac{1}{d_c}\right), \quad (6.11)$$

where d_c is the dislocation cell size, and β is a geometric constant. The term $(1/L + 1/D_s + 1/d_c)$ accounts for dislocation pile-ups at twin and subgrain boundaries, as well as cell walls.

Therefore, the flow stress σ_{flow} of the LPBFed 316L SS can be described as:

$$\sigma_{flow} = \sigma_Y + \sigma_D + \sigma_T = \sigma_Y + \alpha M \mu b \sqrt{\rho} + M \mu b \beta \left(\frac{1}{L^*} + \frac{1}{D_s} + \frac{1}{d_c} \right), \qquad (6.12)$$

where σ_Y is the yield strength, σ_D is the dislocation hardening (comes from Taylor's relationship [137]), and σ_T is the back-stress hardening caused by deformation twin interactions with interfaces.

6.4.2   Dislocation type

Two methods are used to estimate the GNDs density of the present steel. Prior to deformation, EBSD KAM map is used to measure GND density [329]:

$$\rho_{GND} = \frac{\alpha \theta}{bx}, \qquad (6.13)$$

where $\alpha = 2$ is a constant, θ is the KAM angle in radians, and x is the EBSD step size. In order to model the evolution of ρ_{GND} with strain, The Ashby's model has been used [318]:

$$\rho_{GND} = \frac{\epsilon}{4b} \left(\frac{1}{d_s} + \frac{1}{2e} \frac{f_{tw}}{1 - f_{tw}} + \frac{1}{d_c} \right). \qquad (6.14)$$

The term in brackets considers the same dislocation mean free path that has been used to describe the contribution of twinning in strain hardening, as the importance

of the subgrain boundaries and dislocation cell walls in trapping dislocations are well-established in previous studies. Since the total dislocation density (ρ) can be estimated from the Taylor's relationship [137], the SSD density can be approximated by:

$$\rho_{SSD} = \rho - \rho_{GND}. \qquad (6.15)$$

6.5 Analysis

The critical resolved normal stress (σ_T^{crit}) for twin nucleation during deformation can be calculated as [330]:

$$\sigma_T^{crit} = \frac{6 \times SFE}{b_1}, \qquad (6.16)$$

where SFE=14$\pm$5 mJ/m^2 is the SFE of the present steel [308] (measured from TEM observations), and b_1=0.14 nm [330] is the magnitude of the Burgers vector of the twin source. Therefore, σ_T^{crit}=600$\pm$175 MPa. This shows that TWIP effect begins by the onset of plastic deformation in the LPBFed 316L SS. Using equation (6.10), Figure 4.6a shows the evolution of twin volume fraction during tensile deformation. Quantitative measurements from EBSD showed that the volume fraction of the twins after fracture is 0.28$\pm$0.02 (Figure 6.3c); this value has been considered as F_0. The physical parameters used for solving mathematical formulations in this work are listed in Table 6.3. Knowing the final value of the f_{tw} from EBSD analysis, β_0 is fitted to the experimental results, and a value of 20 is obtained for the present steel. This value is significantly larger than the value reported for wrought 304L SS [331] and

Fe-22Mn-0.6C TWIP steel [332] (1.35 and 3, respectively). However, the fitted β_0 values in the present study is similar to wrought Fe-18Mn-0.6C TWIP steel with and without addition of Al (β_0=14–26) with a very fine average grain size (4 μm) [333]. The average thickness of the twins e is taken as 150±68 nm; both micro-twins in Figure 6.3c and nano-twins, which some representatives of them are shown in Figure 6.7 are accounted to measure e. The twin volume fraction increased from the onset of plastic deformation from 0% to ~28%, whereas the intertwin spacing (L^*) decreased gradually during deformation (Figure 6.6b) from 2.1 μm to 770 nm. Thus, the contribution of deformation twins during deformation is plotted in Figure 6.6c. It can be deduced that the direct contribution of deformation twins into flow stress is not significant. σ_T reaches a plateau at a strain of 0.1, which is detected as the end of Stage A in the instant strain hardening exponent (strain hardening capability) (Figure 6.2b).

The evolution of total dislocation density during tensile deformation is modelled and plotted in Figure 6.8a, where it raised from an initial value of 7.8×10^{14} m^{-2} to 1.1×10^{15} m^{-2} at the ultimate tensile stress. The evolution of restoration mechanisms (DRV and DRX) coefficient, which is the representative of the softening ability of the alloy during deformation is fitted to the experimental results and are shown in Figure 6.8b. $f_{DRV} + f_{DRX}$ is significantly increased from an initial value of 0 at the beginning of deformation to a value of 9 at the strain of 0.15, then it gradually decreased to a value of 7.7 at a strain of 0.31, and finally it increased abruptly to a value of 14 until a strain of 0.33. Based on a previous study by the authors, the critical strain to activate DRX at room temperature for the present steel is 0.25±0.01. This means that annihilation processes are mainly controlled by dynamic recovery at the two

Table 6.2: Numerical values of the physical parameters and constants used in various formulations in this work.

Parameter	Value	Source
F_0	0.28±0.02	EBSD analysis
m	2	[331]
e (nm)	150±68	TEM and EBSD analysis
μ (Pa)	(88884.6-37.3T)×10^6	[234]
M	3.06	[137]
b (nm)	0.25	[137]
β	0.24	[25]
V	39×10^{-23}	-
E (Pa)	210×10^9	[334]
ϵ_p	0.14	[146]
ν	0.3	[235]
c (m/s)	5280	[236]
D_s (μm)	10	[306]
d_c (nm)	400	TEM analysis
N_A (atoms)	6.02×10^{23}	-
ρ_b (kg/m^3)	8000	[335]
w_a (g/mol)	55.84	Present work
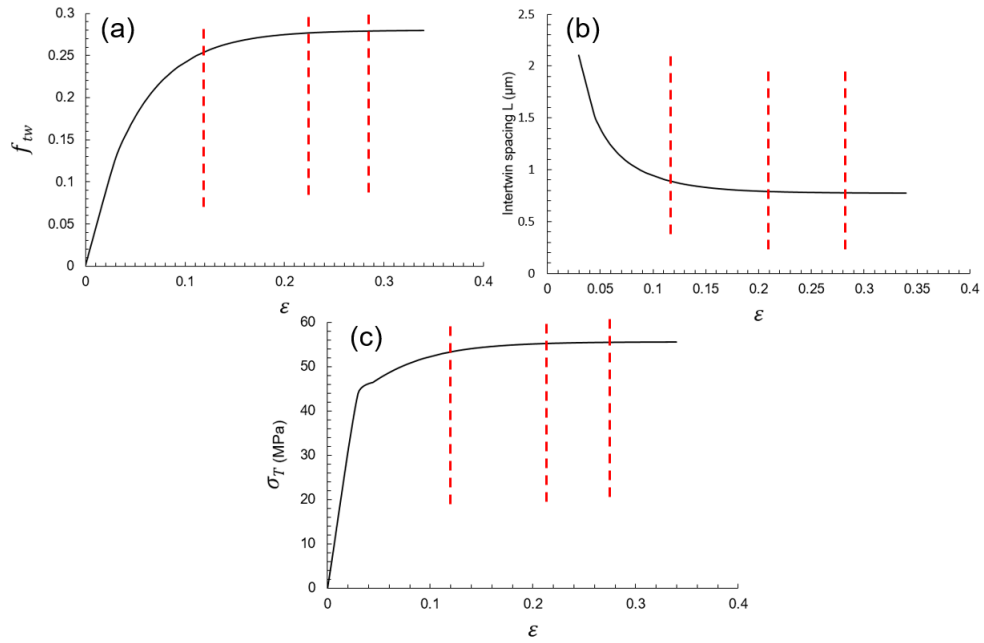
Figure 6.6: (a) Evolution of twin volume fraction f_{tw} with strain. (b) Reduction in intertwin spacing L^* during straining due to formation of more twin obstacles. (c) Contribution of deformation twins in flow stress σ_T during deformation.
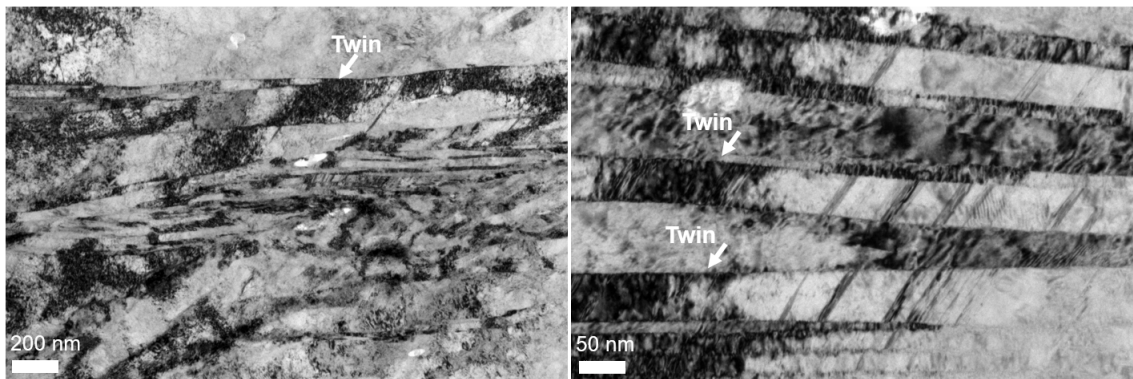
Figure 6.7: Representative bright field TEM images showing thickness of the twins.

first stages of strain hardening. To estimate the dynamic recovery coefficient f_{DRV} evolution, a thermostatistical theory of plastic deformation is used [281]. In order to apply this approach to AM some modifications are made. According to Galindo-Nava *et al.* [273], the annihilation energy barrier for a system consists of a term for formation of dislocations U_{form}, a term for dislocation migration U_{mig}, which initiates dislocation glide towards annihilation, and a term for entropy, which is related to the degree of dislocation disorder at various temperatures. Due to very high residual stress that is already stored in LPBFed alloys, a strain energy term due to deformation U_d must also be added to reduce the energy barrier for annihilation during deformation. The strain energy term due to deformation can be estimated as [336]:
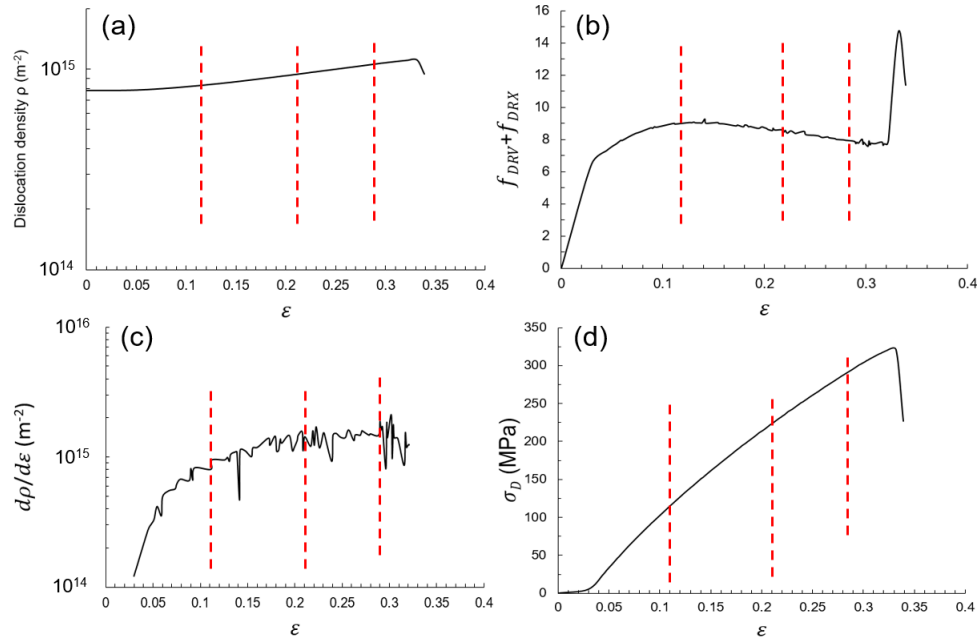
Figure 6.8: Evolution of (a) total dislocation density ρ, (b) DRV and DRX coefficient, (c) rate of dislocation accumulation/annihilation, and (d) contribution of dislocation hardening during deformation.

$$U_d = \frac{1}{2}VE\epsilon_p^2, \tag{6.17}$$

where V is the volume of the system (FCC) per mole, E is the elastic modulus, and ϵ_p^2 is the residual stress stored in the alloy after LPBF. Therefore, the expression for the annihilation energy G^* in LPBFed alloys can be described as:

$$G = U_{form} + U_{mig} - TS - U_d = \frac{1}{2}\mu b^2 l + \sigma_Y A_{act}b^2 l - TS - \frac{1}{2}VE\epsilon_p^2, \tag{6.18}$$

where l is the length of a dislocation segment that undergoes annihilation in a given volume under an applied stress, $A_{act} = \frac{\mu_0 l^*(2+\nu)}{12\pi(1-\nu)SFE}$ [127] is the activation area (the area that the dislocation segment undergoes annihilation), $l^* = 12.5b$ is the dislocation's distortion field length, $S = k_B \ln\left(\frac{\dot{\epsilon}_0}{\dot{\epsilon}}\right)^N$ is the dislocation entropy. N, which accounts for the dislocation's impingement effect, is obtained from $N = 1 + \frac{1}{3}(N_d - 1)$, where N_d is the number of dislocations impinging with the reference dislocation. When $N_d < 1$, N is considered to be 1. Following the mathematical expressions that were published in [273], f_{DRV} for an LPBFed FCC alloy can be defined as:

$$f_{DRV} = \frac{N_A \rho_b b^2 l^*}{w_a} \frac{k_B T \ln\left(\frac{\dot{\epsilon}_0}{\dot{\epsilon}}\right)^N}{\frac{1}{2}\mu b^3 + \sigma_Y A_{act}b^3 - k_B T \ln\left(\frac{\dot{\epsilon}_0}{\dot{\epsilon}}\right)^N - \frac{1}{2}VE\epsilon_p^2}, \tag{6.19}$$

where N_A is the Avogadro's number, ρ_b is the density of the bulk alloy, and w_a is the material's atomic weight. In the absence of impingement (N=1), f_{DRV}=1, which matches the fitted experimental values at the beginning of plastic deformation (Figure 6.8b). f_{DRV} raise with an increase in strain due to dislocation impingement. When the number of impinged dislocations (N_d) increase from 1 to 4, 7, 10, and 13, f_{DRV}

values of 1, 2.9, 4.78, 7.27, and 9.21 are obtained, respectively. This shows that in contrast with their wrought counterparts, FCC LPBFed alloys have more tendency for dislocation annihilation due to their higher impingement probability, which stems from less distance between dislocations in their as-built structures.

The rate of dislocation multiplication/annihilation as a function of strain (using equation 6.8) is also plotted in Figure 6.8c. It shows an increasing rate from the onset of plastic deformation until a strain of about 0.2, where it begins to become stabilised towards the end of deformation. Finally, the contribution of dislocations into the flow stress is shown in Figure 6.8d, where it increases almost linearly towards the ultimate tensile stress.

To better compare the contribution of dislocations and twinning hardening to the flow stress, their contribution in stress increment, which is the difference between the instantaneous flow stress and the yield stress at different strains is plotted in Figure 6.9a. At the very beginning of deformation, twinning dominates the strain hardening till a strain of 0.06. Afterwards, dislocation hardening dominates the total strain hardening mechanisms until fracture. The true stress–true strain curve of the LPBFed 316L SS is plotted again in Figure 6.9b to show the contribution of various mechanisms into flow stress. The initial yield stress is 600 MPa, which is considered as a summation of the friction stress and pre-existing dislocations.

Figure 6.10 shows the evolution of total dislocation density, as well as the density of GNDs and SSDs. The average GND and SSD densities are estimated from equations 6.13 and 6.14, respectively. Figure 6.10 indicates that SSD density varies from 7×10^{14} m^{-2}, which is the major contributor to the toal dislocation density at the beginning of deformation to 6.53×10^{13} m^{-2} at the failure strain. The average value of the
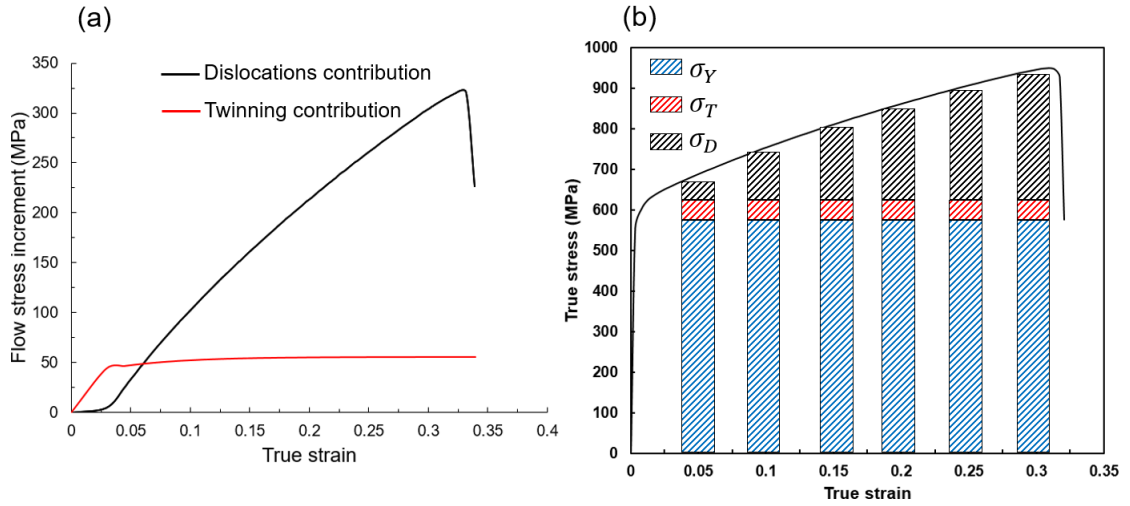
Figure 6.9: Contribution of dislocation and twinning hardening to the stress increment during straining.

GND density increases from 8×10^{13} m^{-2} in the LPBF as-built state to 8.8×10^{14} m^{-2} after fracture. The majority of the total dislocations are the SSDs before about true strain of 0.17, and thereafter the GND density exceeds the density of SSDs. The measured total dislocation density, GNDs and SSDs densities in a wrought high Mn TWIP steel during tensile deformation taken from [25] is also plotted in Figure 6.10 for comparison. At the beginning of deformation (around a strain of 0.06), total dislocation density and SSD density of the LPBFed steel are higher than that in wrought TWIP steel, but the GND density is almost similar for both steels. In contrast with TWIP steel, the SSD density in LPBFed steel decreases constantly till the end of deformation. The trend of GND changes for both steels is ascending, with the LPBFed steel growing with slightly higher values compared to the TWIP steel. The most significant difference of the two steels derives from total dislocation density, which its growth is very slow for the LPBFed steel, while the total dislocation density of the TWIP steel is at least three times higher than the LPBFed steel after a strain of

218

0.33. It can be concluded that strain hardening mechanisms in LPBFed and wrought TWIP steels are fundamentally different, and annihilation processes are more active in the LPBFed alloys.
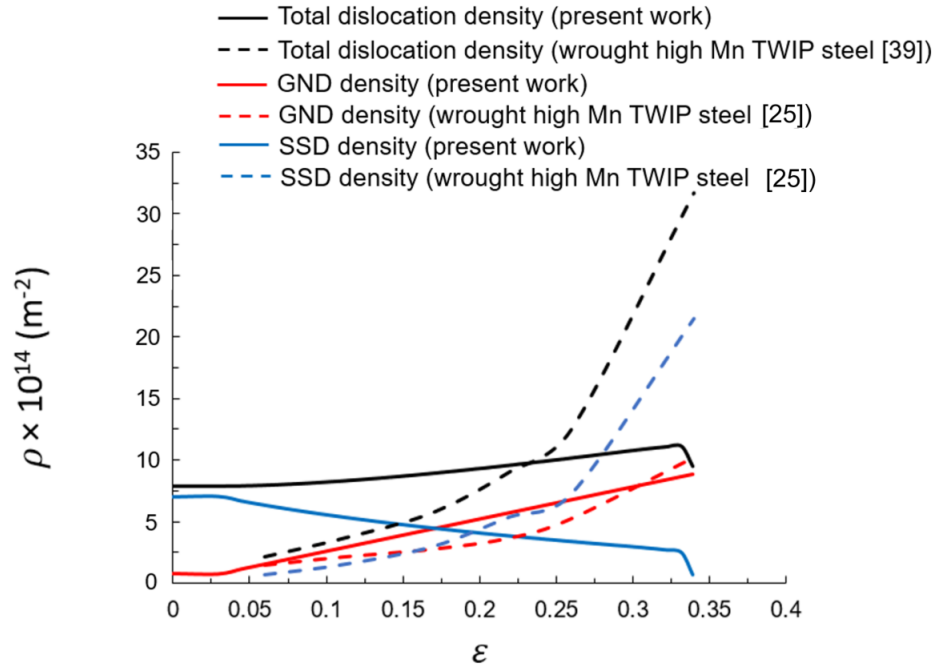
Figure 6.10: Estimated total dislocation density from Taylor's hardening model, measured GND density, and estimated SSD density. Density of total, GNDs and SSDs during deformation of a wrought high Mn TWIP steel is also plotted for comparison [25].

In addition to a wrought TWIP steel, dislocation types in LPBFed as-built structure of the present steel is compared with another 316L SS produced with another set of LPBF processing parameters [305] and a LPBFed FeCoCrNi high-entropy alloy (HEA) [220] in Table 6.4. It can be seen that the density of GNDs and SSDs are very similar in two 316L SSs processed with various processing parameters; HEA exhibit the same trend in the dislocation types with SSDs density dominating the GNDs density in the as-built state. It is worth noting that the total dislocation density is

219

measured using the Taylor's relationship. This shows the consistency of the results of the present work with previous reports on similar low SFE FCC alloys.

Table 6.3: Comparison of the density of different dislocation types in as-built LPBF state in other publications with the present study.

Alloy	ρ_{GND} (m^{-2})	ρ_{SSD} (m^{-2})	ρ (m^{-2})	Source
316L SS	9.84×10^{13}	6.81×10^{14}	7.84×10^{14}	[305]
FeCoCrNi HEA	1.53×10^{14}	5.02×10^{14}	6.55×10^{14}	[220]
316L SS	8×10^{13}	7×10^{14}	7.84×10^{14}	Present work

6.6 Discussion

An integral modelling approach is presented to describe microstructural evolution and strain hardening of LPBFed 316L SS. The model is composed of two important contributions: dislocations and twins. The initial dislocation density after LPBF, subgrain size, and dislocation cell size are input to calculate dislocation forest hardening and TWIP effect. The initial dislocation density, which is estimated from Taylor's relationship, is used for modelling dislocation multiplication/annihilation. The evolution of dislocation density is a competing process between dislocation generation, in which is the result of dislocations interactions ($k_1\sqrt{\rho}$), as well as strain hardening caused by dislocation motion barriers such as subgrain boundaries ($1/D_s$) and twin boundaries ($(1/2e)(f_{tw}/1-f_{tw})$), and dislocation annihilation as a result of DRV and DRX. The latter is mainly governed by DRV at the beginning and middle stages of deformation, and by DRX at the end of deformation as microstructural characterisation proves the dominance of DRX over DRV in the as-fractured state (Figure 6.4c). Therefore, it can be considered that $f_{DRV} + f_{DRX} \sim f_{DRV}$ for stages A and B, but $f_{DRV} + f_{DRX} \sim f_{DRX}$ at stage C for the present steel. As DRV and DRX are usually

considered as thermally activated processes, which are governed by dislocation climb, formulations to estimate f_{DRV} and f_{DRX} at room temperature deformation were currently non-existent, because the dislocation motion is governed by dislocation glide at room temperature, rather than dislocation climb. Therefore, f_{DRV} and f_{DRX} values are fitted to the experimental results. In addition to the untwinned austenitic matrix, dislocation activity can also reduce the intertwin spacing, increasing the strain hardenability of the present steel.

Twinning kinetics $df_{tw}/d\epsilon$ is another key parameter in the present model, as it influences both the dislocation contribution through the evolution of GNDs and the TWIP effect. $df_{tw}/d\epsilon$ is sensitive to the austenite stability, which is determined by SFE, and the twinning kinetics parameter β_0. An increase in SFE values of FCC alloys lead to a decrease in β_0, which can affect other parameters such as F_0, and even f_{DRV} and f_{DRX}. The β_0 value that is obtained for the present steel is 20, which is close to a value of 26 for Fe-18Mn-0.6C TWIP steel reported by Jung and De Cooman [333], with a SFE of around 12 mJ/m^2. The SFE of present steel is measured by direct TEM observations to be 14 ± 5 mJ/m^2. Regarding a higher value of SFE, a lower β_0 value is obtained, which is related to higher austenite stability of the present steel compared to the mentioned high Mn TWIP steel. Another factor that can influence twinning kinetics is the strain rate, which is slow enough in this study to provide enough time for twins to nucleate and grow. As it can be seen in Figure 6.10, the GND density grows significantly during deformation due to rapidly reduced dislocation mean free path caused by twin formation. Simultaneously, the SSD density reduced significantly during deformation due to high DRV and DRX coefficient of the present alloy, increasing the strain hardenability of the material

during straining. This is in contrast with wrought TWIP steels, where the GND and SSD densities grow simultaneously during tensile deformation [25]. This can be related to the very low annihilation rates of the conventionally processed alloys compared to LPBFed alloys.

In order to interpret the higher tendency of the LPBFed alloy for dislocation annihilation during room temperature deformation, equation 6.19 is derived, for the first time in literature to account the influence of the unique feature of LPBFed alloys on DRV coefficient, the residual stress. Interestingly, it has been deduced that the number of impinging dislocations for LPBFed alloy were increasing with an increase in strain, which results in higher ability for annihilation at room temperature. As the main mechanism for dislocation annihilation at room temperature is cross-slip, the distance between partial dislocation, which is controlled by SFE, plays an important role. In wrought alloys, the distance between dislocations is large, which means that dislocation impingement has a negligible effect, leading to a very low value of f_{DRV} during room temperature deformation. However, high residual stress in LPBF as-built state contributes to easier dislocation multiplication, which subsequently increases the dislocation impingement between the strain fields. This can be physically shown by calculating r_{NI} before and after deformation. This shows the importance of dislocation impingement caused by residual stress that is unique to LPBF on strain hardenability of such alloys. In the presence of such high residual stress, the distance between dislocations significantly reduces, making the alloy more prone to annihilation processes, which maintain the ductility of the alloy and prevents the microstructure to be saturated with both GND and SSD types, leading to similar ductility compared to wrought alloys. Therefore, in LPBFed alloys, the decrease in SSDs density during

222

deformation is the key reason for high ductility.

Because of the importance of dislocation cells in yield strengthening of LPBFed 316L SS, their role in strain hardening should also be considered. As is shown in Figure 6.5b, dislocations can pile up to the existing cell walls during deformation, refining their size. The evolution of the cell size with the dislocation density can be modelled via [281]:

$$d_c = \frac{k_c}{\sqrt{\rho}}, \tag{6.20}$$

where $k_c = \frac{12\pi(1-\nu)}{2+\nu}\left(1 + \frac{T\Delta S}{\frac{1}{2}\mu b^3}\right)$. ν=0.3 is the Poisson's ratio, and $\Delta S = k_B \ln\left(\frac{\dot{\epsilon}_0 + \vartheta}{\dot{\epsilon}}\right)$ is the dislocation entropy, where k_B=1.38$\times$10^{-23} J/K is the Boltzmann constant, $\dot{\epsilon}_0$=10^9 s^{-1} is the limiting maximum strain rate [281], and $\vartheta = \vartheta_D \exp\left(-\frac{E_m}{RT}\right)$ is the vacancy migration rate, with ϑ_D=10^{13} s^{-1} is the Debye frequency, E_m=96.5 kJ/mol is the vacancy migration energy [127], and R=8.314 J/mol·K is the universal gas constant. Based on equation (6.17), the d_c at the beginning and end of deformation is 491 nm and 413 nm, respectively, which shows a slight refinement of cell size during tensile deformation. This is consistent with the findings of Riabov et $al.$ [322]. This slight change in the cell size cannot produce large back-stress, thus the contribution of cell size refinement in strain hardening can be ignored during deformation of LPBFed 316L SS. Therefore, cellular structures only contribute in reducing the intertwin spacing, via increasing the GND density through reduction in the dislocation mean free path during tensile deformation.

6.6.1 Strain hardening mechanisms of LPBFed 316L SS

As is plotted in Figure 6.2b, the strain hardening capability of the LPBFed 316L SS can be interpreted in three stages, which are related to the several microstructural evolution phenomena during straining. In Stage A (ϵ=0.03-0.13), deformation twins form quickly, reducing the dislocation mean free path significantly. This leads to an increase in the contribution of both twinning and dislocation slip via deformation twins at this stage. Moreover, f_{DRV} increases abruptly from 0 to 9.25 in Stage A of deformation. This shows that the rate of dislocation annihilation is also very high, which keeps the strain hardenability of the present steel at a low level ($0.07 < n < 0.16$) at Stage A. The formation of twins and heavy dislocation annihilation rate is accompanied with a growth in GNDs density, as well as a drop in SSDs density, respectively. This also shows that strain hardening primarily originates from effective accumulation of GNDs, which concentrate adjacent to high energy sites such as LAGBs, HAGBs, and dislocation cell walls. However, the accumulation of GNDs is slowed by a high rate of dislocation annihilation and large dislocation mean free path at this stage.

Further increasing the strain (Stage B) leads to a saturation in twin formation and dislocation mean free path (Figures 6.6a and 6.6b). The direct contribution of deformation twins to the strain hardening behaviour is very limited and saturated until the end of deformation (around 50 MPa). Thus, at high strains, the strain hardening capability originates from the evolution of total dislocation density. As the dislocation mean free path is at its minimum value due to mechanical twinning during Stage B, the GND density increases constantly, and after a strain of 0.17, GNDs dominate the SSDs in the microstructure of the present steel. As dislocation annihilation rate is still high in Stage B ($7.56 < f_{DRV} < 9.25$), the SSD density

decreases constantly, as well. However, due to a decrease in f_{DRV} values at this stage, the strain hardening capability (n) is higher compared to Stage A.

Finally, at Stage C, microstructural evolution is affected by the activation of DRX; critical strain for the activation of DRX in the present steel at room temperature is calculated to be 0.25±0.01 [308]. DRX activation improved the strain hardening capability of the alloy at this stage, by increasing more HAGBs, which can contribute to the evolution of GNDs density, improving the ability of the alloy to be strain hardened.

6.7 Conclusions

A dislocation-based model for strain hardening in a LPBFed austenitic TWIP SS is presented. The model is based on the contribution of dislocations, as well as twins in strain hardening. The dislocation storage term is enhanced by the presence of LAGBs and twin formation as obstacles that can reduce dislocation mean free path. The dislocation annihilation term is enhanced by DRV and DRX activation during room temperature deformation. The TWIP effect is modelled considering the effects of LAGBs, dislocation cells, and twin-twin interfaces. Moreover, the evolution of GNDs and SSDs during deformation revealed more detailed information about strain hardening mechanisms. The following conclusions are drawn from this study:

i Strain hardening in LPBFed TWIP steels can be divided into three stages. The TWIP effect dominates the strain hardening in Stage A. Using a combination of TEM and EBSD, evolution of twin volume fraction and the dislocation mean free path is modelled. They reach to their saturation levels in Stage A. Because of very

high annihilation rate at this stage, the strain hardening capability is the lowest compared to the next stages of deformation.

ii Significant formation of twins during Stage A of deformation, which stems from very high twinning kinetics parameter (similar to high Mn TWIP steels with similar SFEs), leads to increase in GNDs density, which is in its minimum value before the onset of plastic deformation. High values of DRV coefficient accompanies with a decrease in SSDs density, which is characterised as the main dislocation type of the LPBFed as-built 316L SS.

iii As twin volume fraction is constant at moderate and high strain levels, the direct contribution of TWIP effect remains constant in Stages B and C of deformation. However, twins contribute to strain hardening through increasing GNDs density, as a result of interaction with LAGBs, dislocation cells, and other twins. A drop in DRV coefficient leads to an increase in strain hardening capability values in Stage B. In this stage, GNDs dominate the microstructure of the present steel. The strain hardening in this stage is mainly derived by the total dislocation hardening.

iv DRX activates at Stage C, increasing the strain hardening capability via generating more HAGBs that can lead to more increase in GNDs density. Strain hardening in Stage C is mainly governed by GND hardening.

v A thermostatistical formulation specific to LPBFed alloys is presented to account residual stress to estimate the rate of dislocation annihilation. During room temperature deformation, LPBFed alloys undergo more annihilation processes such as DRV and DRX compared to their wrought counterparts, due to increased dislocation impingement as a result of a much smaller distance between dislocation

partials.

vi The results of the present work strongly suggests that uniform elongation of the LPBFed alloys is controlled primarily by the rate of DRV, which depends strongly on the number of impinging dislocations.

Chapter 7

Concluding remarks

This thesis is focused on providing methodologies to tailor the chemical composition of alloys to become suitable for additive manufacturing (AM) technologies, as well as to control their defect formation and microstructure development. Strategies to maximise the strength of AM alloys are also presented. The main conclusions of this work are as follows:

i Controlling crack and porosity formation during laser powder bed fusion (LPBF) depends on the optimisation of both chemical composition and process parameters. A computational methodology to optimise both chemical composition and processing parameters is presented for 316L stainless steel (SS), 17-4 precipitation hardening (PH) SS, and FORMETRIX alloy. The model was validated for 316L SS, where crack-free, very low porosity specimens were produced via LPBF, exhibiting superior mechanical properties compared to their wrought counterparts.

ii Detailed microstructural evolution and grain refinement mechanisms during LPBF of 316L SS are revealed. Traces of restoration mechanisms such as dynamic re-

crystallization (DRX) and dynamic recovery (DRV) are revealed in the as-built microstructures; they are modelled using two approaches: the classical Zener-Hollomon, and the thermostatistical theory. The presence of deformation nanotwins is reported for the first time in the as-built microstructures. It has been shown that those deformation nanotwins act as promoters for DRX and DRV mechanisms during thermal cycling of LPBF of 316L SS. The conditions under which the activation of discontinuous and continuous DRX mechanisms occur are discussed.

iii Detailed mechanisms governing yield strengthening in LPBF are presented. There is a correlation between the heat input and the yield strength of the fully-dense LPBF alloys from different alloy families (titanium, steels, and nickel). Strengthening mechanisms such as Taylor strengthening, Kocks-Mecking contribution, thermal straining, and heat dissipation cooling contribute to yield strengthening of LPBF alloys. The Kocks-Mecking contribution, which is related to restoration processes such as DRX and DRV, plays the most significant role in controlling yield strength of all the studied alloy families during LPBF.

iv Microstructural features, especially the fraction of low-angle grain boundaries (LAGBs), control the yield strength of LPBFed 316L SS, rather than porosity and defect content. A power law relationship is derived to correlate the yield strength of LPBF as-built 316L SS as a function of LAGB fraction. Then, it is shown that an increase in the LAGB fraction leads to an increase in yield strength.

v A unified Hall-Petch-type relationship is proposed to correlate the yield strength to the size of subgrains, which are defined as grains with LAGBs. This provides

229

insight into the development of LPBF alloys, as the yield strength can be controlled using a grain boundary engineering approach to optimise the occurrence of DRX and DRV during building.

vi An integral dislocation density-based modelling approach was implemented to describe strain hardening behaviour of the LPBFed 316L SS including dislocation hardening, twin formation (twinning induced plasticity (TWIP) effect) and DRX. TWIP effect dominates the strain hardening at the beginning of deformation through introducing barriers against dislocation glide, accompanied with an increase in the geometrically necessary dislocation (GND) density, which is at its minimum level at the beginning of deformation. Due to the high rate of annihilation, statistically stored dislocations (SSD) density is at its maximum in the as-built state, and decreases significantly throughout deformation. Dislocation hardening and DRX dominate the strain hardening at the next stages of deformation. The very high rate of dislocation annihilation during deformation of LPBFed alloys is related to the higher dislocation strain field impingement in such alloys, compared to wrought alloys.

Bibliography

[1] D. Zhang, S. Sun, D. Qiu, M. A. Gibson, M. S. Dargusch, M. Brandt, M. Qian, M. Easton, Metal alloys for fusion-based additive manufacturing, Adv. Eng. Mater. 20 (5) (2018) 1700952.

[2] W. Shi, P. Wang, Y. Liu, G. Han, Experiment of process strategy of selective laser melting forming metal nonhorizontal overhanging structure, Metals 9 (4) (2019) 385.

[3] H. Eskandari Sabzi, P. E. Rivera-Díaz-del Castillo, Defect prevention in selective laser melting components: compositional and process effects, Materials 12 (22) (2019) 3791.

[4] W. E. King, H. D. Barth, V. M. Castillo, G. F. Gallegos, J. W. Gibbs, D. E. Hahn, C. Kamath, A. M. Rubenchik, Observation of keyhole-mode laser melting in laser powder-bed fusion additive manufacturing, J. Mater. Process. Technol. 214 (12) (2014) 2915–2925.

[5] L.-C. Zhang, H. Attar, M. Calin, J. Eckert, Review on manufacture by selective laser melting and properties of titanium based materials for biomedical applications, Mater. Technol. 31 (2) (2016) 66–76.

[6] H. Eskandari Sabzi, Powder bed fusion additive layer manufacturing of titanium alloys, Mater. Sci. Technol. 35 (8) (2019) 875–890.

[7] J. V. Gordon, S. P. Narra, R. W. Cunningham, H. Liu, H. Chen, R. M. Suter, J. L. Beuth, A. D. Rollett, Defect structure process maps for laser powder bed fusion additive manufacturing, Additive Manufacturing 36 (2020) 101552.

[8] L. Johnson, M. Mahmoudi, B. Zhang, R. Seede, X. Huang, J. T. Maier, H. J. Maier, I. Karaman, A. Elwany, R. Arróyave, Assessing printability maps in additive manufacturing of metal alloys, Acta Mater. 176 (2019) 199–210.

[9] A. Deschamps, F. Tancret, I.-E. Benrabah, F. De Geuser, H. P. Van Landeghem, Combinatorial approaches for the design of metallic alloys, Comptes Rendus Physique 19 (8) (2018) 737–754.

[10] G. Cacciamani, et al., An introduction to the calphad method and the compound energy formalism (cef), Tecnologia em Metalurgia, Materiais e Mineração 13 (1) (2016) 16–24.

[11] L. Liu, Q. Ding, Y. Zhong, J. Zou, J. Wu, Y.-L. Chiu, J. Li, Z. Zhang, Q. Yu, Z. Shen, Dislocation network in additive manufactured steel breaks strength–ductility trade-off, Mater. Today. 21 (4) (2018) 354–361.

[12] X. Zhao, S. Li, M. Zhang, Y. Liu, T. B. Sercombe, S. Wang, Y. Hao, R. Yang, L. E. Murr, Comparison of the microstructures and mechanical properties of ti–6al–4v fabricated by selective laser melting and electron beam melting, Mater. Des. 95 (2016) 21–31.

[13] T. G. Gallmeyer, S. Moorthy, B. B. Kappes, M. J. Mills, B. Amin-Ahmadi, A. P. Stebner, Knowledge of process-structure-property relationships to engineer better heat treatments for laser powder bed fusion additive manufactured inconel 718, Addit. Manuf. 31 (2020) 100977.

[14] W. E. Frazier, Metal additive manufacturing: a review, J. Mater. Eng. Perform. 23 (6) (2014) 1917–1928.

[15] A. Hussein, L. Hao, C. Yan, R. Everson, Finite element simulation of the temperature and stress fields in single layers built without-support in selective laser melting, Mater. Des. 52 (2013) 638–647.

[16] V. Manvatkar, A. De, T. DebRoy, Heat transfer and material flow during laser assisted multi-layer additive manufacturing, J. Appl. Phys. 116 (12) (2014) 124905.

[17] Y. M. Wang, T. Voisin, J. T. McKeown, J. Ye, N. P. Calta, Z. Li, Z. Zeng, Y. Zhang, W. Chen, T. T. Roehling, et al., Additively manufactured hierarchical stainless steels with high strength and ductility, Nat. Mater. 17 (1) (2018) 63–71.

[18] A. M. Beese, B. E. Carroll, Review of mechanical properties of ti-6al-4v made by laser-based additive manufacturing using powder feedstock, JOM 68 (3) (2016) 724–734.

[19] Y.-L. Kuo, S. Horikawa, K. Kakehi, The effect of interdendritic δ phase on the mechanical properties of alloy 718 built up by additive manufacturing, Mater. Des. 116 (2017) 411–418.

[20] A. Röttger, K. Geenen, M. Windmann, F. Binner, W. Theisen, Comparison of microstructure and mechanical properties of 316 l austenitic steel processed by selective laser melting with hot-isostatic pressed and cast material, Mater. Sci. Eng. A. 678 (2016) 365–376.

[21] Z. Sun, X. Tan, S. B. Tor, W. Y. Yeong, Selective laser melting of stainless steel 316l with low porosity and high build rates, Mater. Des. 104 (2016) 197–204.

[22] W. Chen, G. Yin, Z. Feng, X. Liao, Effect of powder feedstock on microstructure and mechanical properties of the 316l stainless steel fabricated by selective laser melting, Metals. 8 (9) (2018) 729.

[23] A. Elmesalamy, J. Francis, L. Li, A comparison of residual stresses in multi pass narrow gap laser welds and gas-tungsten arc welds in AISI 316L stainless steel, Int. J. Pressure. Vessels. Piping. 113 (2014) 49–59.

[24] F. Yin, G. J. Cheng, R. Xu, K. Zhao, Q. Li, J. Jian, S. Hu, S. Sun, L. An, Q. Han, Ultrastrong nanocrystalline stainless steel and its Hall-Petch relationship in the nanoscale, Scr. Mater. 155 (2018) 26–31.

[25] H. Zhi, C. Zhang, S. Antonov, H. Yu, T. Guo, Y. Su, Investigations of dislocation-type evolution and strain hardening during mechanical twinning in fe-22mn-0.6 c twinning-induced plasticity steel, Acta Mater. 195 (2020) 371–382.

[26] V. Shankar, T. Gill, S. Mannan, S. Sundaresan, Solidification cracking in austenitic stainless steel welds, Sadhana. 28 (3-4) (2003) 359–382.

[27] I. Toda-Caraballo, P. E. Rivera-Díaz-del Castillo, Modelling solid solution hardening in high entropy alloys, Acta Mater. 85 (2015) 14–23.

[28] F. Cverna, et al., ASM ready reference: thermal properties of metals, ASM International, 2002.

[29] A. Ghobadian, I. Talavera, A. Bhattacharya, V. Kumar, J. A. Garza-Reyes, N. O'regan, Examining legitimatisation of additive manufacturing in the interplay between innovation, lean manufacturing and sustainability, Int. J. Product. Econom. 219 (2020) 457–468.

[30] H. C. Sonar, V. Khanzode, M. Akarte, A conceptual framework on implementing additive manufacturing technology towards firm competitiveness, Int. J. Global Business and Competitiveness 15 (2) (2020) 121–135.

[31] C. Wang, X. Tan, S. B. Tor, C. Lim, Machine learning in additive manufacturing: State-of-the-art and perspectives, Addit. Manuf. (2020) 101538.

[32] S. Ford, M. Despeisse, Additive manufacturing and sustainability: an exploratory study of the advantages and challenges, Journal of cleaner Production 137 (2016) 1573–1587.

[33] S. Terry, H. Lu, I. Fidan, Y. Zhang, K. Tantawi, T. Guo, B. Asiabanpour, The influence of smart manufacturing towards energy conservation: A review, Technologies 8 (2) (2020) 31.

[34] O. Vermesan, P. Friess, Internet of things: converging technologies for smart environments and integrated ecosystems, River publishers, 2013.

[35] A. Bandyopadhyay, S. Bose, Additive manufacturing, CRC press, 2019.

[36] S. Cheruvathur, E. A. Lass, C. E. Campbell, Additive manufacturing of 17-4 PH stainless steel: post-processing heat treatment to achieve uniform reproducible microstructure, JOM 68 (3) (2016) 930–942.

[37] T. DebRoy, H. L. Wei, J. S. Zuback, T. Mukherjee, J. W. Elmer, J. O. Milewski, A. M. Beese, A. d. Wilson-Heid, A. De, W. Zhang, Additive manufacturing of metallic components–process, structure and properties, Prog. Mater. Sci. 92 (2018) 112–224.

[38] H. Eskandari Sabzi, P. E. J. Rivera-Díaz-del Castillo, Composition and process parameter dependence of yield strength in laser powder bed fusion alloys, Mater. Des. (2020) 109024.

[39] J. P. Oliveira, A. LaLonde, J. Ma, Processing parameters in laser powder bed fusion metal additive manufacturing, Mater. Des. 193 (2020) 108762.

[40] J. C. Williams, E. A. Starke Jr, Progress in structural materials for aerospace systems, Acta Mater. 51 (19) (2003) 5775–5799.

[41] Y. Li, C. Yang, H. Zhao, S. Qu, X. Li, Y. Li, New developments of ti-based alloys for biomedical applications, Materials 7 (3) (2014) 1709–1800.

[42] J. Dodson, A. Hunt, H. Parker, Y. Yang, J. Clark, Elemental sustainability: Towards the total recovery of scarce metals, Chem. Eng. Process. Process. Intens. 51 (2012) 69–78.

[43] T. E. Graedel, J. Allwood, J.-P. Birat, M. Buchert, C. Hagelüken, B. K. Reck, S. F. Sibley, G. Sonnemann, What do we know about metal recycling rates?, J. Indust. Ecol. 15 (3) (2011) 355–366.

[44] E. Chauvet, P. Kontis, E. A. Jägle, B. Gault, D. Raabe, C. Tassin, J.-J. Blandin, R. Dendievel, B. Vayre, S. Abed, et al., Hot cracking mechanism affecting a non-weldable ni-based superalloy produced by selective electron beam melting, Acta Mater. 142 (2018) 82–94.

[45] Z. Snow, R. Martukanitz, S. Joshi, On the development of powder spreadability metrics and feedstock requirements for powder bed fusion additive manufacturing, Addit. Manuf. 28 (2019) 78–86.

[46] T. Pollock, A. Clarke, S. Babu, Design and tailoring of alloys for additive manufacturing, Metall. Mater. Trans. A. 51 (12) (2020) 6000–6019.

[47] S. K. Everton, M. Hirsch, P. Stravroulakis, R. K. Leach, A. T. Clare, Review of in-situ process monitoring and in-situ metrology for metal additive manufacturing, Mater. Design. 95 (2016) 431–445.

[48] D. Herzog, V. Seyda, E. Wycisk, C. Emmelmann, Additive manufacturing of metals, Acta Mater. 117 (2016) 371–392.

[49] W. E. King, A. T. Anderson, R. Ferencz, N. Hodge, C. Kamath, S. A. Khairallah, A. M. Rubenchik, Laser powder bed fusion additive manufacturing of metals; physics, computational, and materials challenges, Appl. Phys. Rev. 2 (4) (2015) 041304.

[50] L. E. Criales, Y. M. Arısoy, B. Lane, S. Moylan, A. Donmez, T. Özel, Laser powder bed fusion of nickel alloy 625: experimental investigations of effects of process parameters on melt pool size and shape with spatter analysis, Int. J. Machine Tools Manuf. 121 (2017) 22–36.

[51] C. Wang, X. Tan, E. Liu, S. B. Tor, Process parameter optimization and mechanical properties for additively manufactured stainless steel 316l parts by selective electron beam melting, Mater. Des. 147 (2018) 157–166.

[52] L. E. Murr, S. M. Gaytan, D. A. Ramirez, E. Martinez, J. Hernandez, K. N. Amato, P. W. Shindo, F. R. Medina, R. B. Wicker, Metal fabrication by additive manufacturing using laser and electron beam melting technologies, Mater Sci Tech 28 (2012) 1–14.

[53] S. Ghaoui, Y. Ledoux, F. Vignat, M. Museau, T. H. Vo, F. Villeneuve, A. Ballu, Analysis of geometrical defects in overhang fabrications in electron beam melting based on thermomechanical simulations and experimental validations, Addit. Manuf. 36 (2020) 101557.

[54] F. Spranger, B. Graf, M. Schuch, K. Hilgenberg, M. Rethmeier, Build-up strategies for additive manufacturing of three dimensional ti-6al-4v-parts produced by laser metal deposition, J. Laser Applic. 30 (2) (2018) 022001.

[55] M. J. Matthews, G. Guss, S. A. Khairallah, A. M. Rubenchik, P. J. Depond, W. E. King, Denudation of metal powder layers in laser powder bed fusion processes, Acta Mater. 114 (2016) 33–42.

[56] J. Yin, D. Wang, L. Yang, H. Wei, P. Dong, L. Ke, G. Wang, H. Zhu, X. Zeng, Correlation between forming quality and spatter dynamics in laser powder bed fusion, Addit. Manuf. 31 (2020) 100958.

[57] P. Bidare, I. Bitharas, R. Ward, M. Attallah, A. J. Moore, Fluid and particle dynamics in laser powder bed fusion, Acta Mater. 142 (2018) 107–120.

[58] M.-S. Pham, B. Dovgyy, P. A. Hooper, C. M. Gourlay, A. Piglione, The role of side-branching in microstructure development in laser powder-bed fusion, Nat. Commun. 11 (1) (2020) 1–12.

[59] C. Zhao, K. Fezzaa, R. W. Cunningham, H. Wen, F. Carlo, L. Chen, A. D. Rollett, T. Sun, Sci. Rep. 7 (1) (2017) 3602.

[60] A. A. Martin, N. P. Calta, S. A. Khairallah, J. Wang, P. J. Depond, A. Y. Fong, V. Thampy, G. M. Guss, A. M. Kiss, K. H. Stone, et al., Dynamics of pore formation during laser powder bed fusion additive manufacturing, Nat. Commun. 10 (1) (2019) 1–10.

[61] N. Nadammal, T. Mishurova, T. Fritsch, I. Serrano-Munoz, A. Kromm, C. Haberland, P. D. Portella, G. Bruno, Critical role of scan strategies on the development of microstructure, texture, and residual stresses during laser powder bed fusion additive manufacturing, Addit. Manuf. 38 (2021) 101792.

[62] H. Eskandari Sabzi, S. Maeng, X. Liang, M. Simonelli, N. T. Aboulkhair, P. E. J. Rivera-Díaz-del Castillo, Controlling crack formation and porosity in laser powder bed fusion: alloy design and process optimisation, Addit. Manuf. (2020) 101360.

[63] T. Mukherjee, J. Zuback, A. De, T. DebRoy, Printability of alloys for additive manufacturing, Sci. Rep. 6 (2016) 19717.

[64] H. Hyer, L. Zhou, A. Mehta, S. Park, T. Huynh, S. Song, Y. Bai, K. Cho, B. McWilliams, Y. Sohn, Composition-dependent solidification cracking of

aluminum-silicon alloys during laser powder bed fusion, Acta Mater. 208 (2021) 116698.

[65] B. Böttger, M. Apel, B. Santillana, D. Eskin, Relationship between solidification microstructure and hot cracking susceptibility for continuous casting of low-carbon and high-strength low-alloyed steels: a phase-field study, Metall. Mater. Trans. A. 44 (8) (2013) 3765–3777.

[66] J. Lippold, W. Savage, Solidification of austenitic stainless steel weldments: Part iii–the effect of solidification behavior on hot cracking susceptibility., WELDING J. 61 (12) (1982) 388.

[67] G. Chen, S. Zhao, P. Tan, J. Wang, C. Xiang, H. Tang, A comparative study of ti-6al-4v powders for additive manufacturing by gas atomization, plasma rotating electrode process and plasma atomization, Powder Technol. 333 (2018) 38–46.

[68] V. Prithivirajan, M. D. Sangid, The role of defects and critical pore size analysis in the fatigue response of additively manufactured in718 via crystal plasticity, Mater. Des. 150 (2018) 139–153.

[69] M. Tang, P. C. Pistorius, J. L. Beuth, Prediction of lack-of-fusion porosity for powder bed fusion, Addit. Manuf. 14 (2017) 39–48.

[70] J. Yang, J. Han, H. Yu, J. Yin, M. Gao, Z. Wang, X. Zeng, Role of molten pool mode on formability, microstructure and mechanical properties of selective laser melted ti-6al-4v alloy, Mater. Des. 110 (2016) 558–570.

[71] S. A. Khairallah, A. A. Martin, J. R. Lee, G. Guss, N. P. Calta, J. A. Hammons, M. H. Nielsen, K. Chaput, E. Schwalbach, M. N. Shah, et al., Controlling interdependent meso-nanosecond dynamics and defect generation in metal 3d printing, Science 368 (6491) (2020) 660–665.

[72] H. Choo, K.-L. Sham, J. Bohling, A. Ngo, X. Xiao, Y. Ren, P. J. Depond, M. J. Matthews, E. Garlea, Effect of laser power on defect, texture, and microstructure of a laser powder bed fusion processed 316l stainless steel, Mater. Des. 164 (2019) 107534.

[73] Q. Han, Y. Gu, R. Setchi, F. Lacan, R. Johnston, S. L. Evans, S. Yang, Additive manufacturing of high-strength crack-free ni-based hastelloy x superalloy, Addit. Manuf. 30 (2019) 100919.

[74] M. Iebba, A. Astarita, D. Mistretta, I. Colonna, M. Liberini, F. Scherillo, C. Pirozzi, R. Borrelli, S. Franchitti, A. Squillace, Influence of powder characteristics on formation of porosity in additive manufacturing of ti-6al-4v components, J. Mater. Eng. Perform. 26 (8) (2017) 4138–4147.

[75] A. Thompson, I. Maskery, R. K. Leach, X-ray computed tomography for additive manufacturing: a review, Measurement Science and Technology 27 (7) (2016) 072001.

[76] I. Maskery, N. Aboulkhair, M. Corfield, C. Tuck, A. Clare, R. K. Leach, R. D. Wildman, I. Ashcroft, R. J. Hague, Quantification and characterisation of porosity in selectively laser melted al–si10–mg using x-ray computed tomography, Mater. Charact. 111 (2016) 193–204.

[77] G. Chen, Q. Zhou, S. Zhao, J. Yin, P. Tan, Z. Li, Y. Ge, J. Wang, H. Tang, A pore morphological study of gas-atomized ti-6al-4v powders by scanning electron microscopy and synchrotron x-ray computed tomography, Powder Technol. 330 (2018) 425–430.

[78] R. Cunningham, S. P. Narra, C. Montgomery, J. Beuth, A. Rollett, Synchrotron-based x-ray microtomography characterization of the effect of processing variables on porosity formation in laser power-bed additive manufacturing of ti-6al-4v, JOM 69 (3) (2017) 479–484.

[79] J.-N. Zhu, E. Borisov, X. Liang, E. Farber, M. Hermans, V. Popovich, Predictive analytical modelling and experimental validation of processing maps in additive manufacturing of nitinol alloys, Addit. Manuf. 38 (2021) 101802.

[80] R. Seede, D. Shoukr, B. Zhang, A. Whitt, S. Gibbons, P. Flater, A. Elwany, R. Arroyave, I. Karaman, An ultra-high strength martensitic steel fabricated using selective laser melting additive manufacturing: Densification, microstructure, and mechanical properties, Acta Mater. 186 (2020) 199–214.

[81] D. Hann, J. Iammi, J. Folkes, A simple methodology for predicting laser-weld properties from material and laser parameters, J. Phys. D. Appl. Phys. 44 (44) (2011) 445401.

[82] J. Cherry, H. Davies, S. Mehmood, N. Lavery, S. Brown, J. Sienz, Investigation into the effect of process parameters on microstructural and physical properties of 316l stainless steel parts by selective laser melting, Int. J. Adv. Manuf. Tech. 76 (5-8) (2015) 869–879.

[83] E. Liverani, S. Toschi, L. Ceschini, A. Fortunato, Effect of selective laser melting (slm) process parameters on microstructure and mechanical properties of 316l austenitic stainless steel, J. Mater. Process. Technol. 249 (2017) 255–263.

[84] J. H. Tan, W. L. E. Wong, K. W. Dalgarno, An overview of powder granulometry on feedstock and part performance in the selective laser melting process, Addit. Manuf. 18 (2017) 228–255.

[85] P. Patel, Materials genome initiative and energy, MRS bulletin 36 (12) (2011) 964–966.

[86] C. M. Fonseca, P. J. Fleming, Multiobjective genetic algorithms, in: IEE colloquium on genetic algorithms for control systems engineering, IET, 1993, pp. 6–1.

[87] K. Ohno, K. Esfarjani, Y. Kawazoe, Computational materials science: from ab initio to Monte Carlo methods, Springer, 2018.

[88] P. E. Turchi, I. A. Abrikosov, B. Burton, S. G. Fries, G. Grimvall, L. Kaufman, P. Korzhavyi, V. R. Manga, M. Ohno, A. Pisch, et al., Interface between quantum-mechanical-based approaches, experiments, and calphad methodology, CALPHAD 31 (1) (2007) 4–27.

[89] C. E. Campbell, U. R. Kattner, Z.-K. Liu, The development of phase-based property data using the calphad method and infrastructure needs, Integrating Materials and Manufacturing Innovation 3 (1) (2014) 158–180.

[90] A. Kroupa, Modelling of phase diagrams and thermodynamic properties using calphad method–development of thermodynamic databases, Comput. Mater. Sci. 66 (2013) 3–13.

[91] Z.-K. Liu, First-principles calculations and calphad modeling of thermodynamics, J. Phase Equil. Diffus. 30 (5) (2009) 517–534.

[92] J.-O. Andersson, T. Helander, L. Höglund, P. Shi, B. Sundman, Thermo-calc & DICTRA, computational tools for materials science, CALPHAD 26 (2) (2002) 273–312.

[93] J. S. Aristeidakis, G. N. Haidemenopoulos, Composition and processing design of medium-mn steels based on calphad, sfe modeling, and genetic optimization, Acta Materialia 193 (2020) 291–310.

[94] Q. Lu, S. van der Zwaag, W. Xu, Charting the composition–strengthspace for novel austenitic, martensitic and ferritic creep resistant steels, J. Mater. Sci. Technol. 33 (12) (2017) 1577–1581.

[95] W. Xu, Q. Lu, X. Xu, S. van der Zwaag, The structure of a general materials genome approach to the design of new steel grades for specific properties, Computer Methods in Materials Science 13 (3) (2013) 382–394.

[96] T. T. Molla, J. Liu, G. Schaffer, An icme framework for design of stainless steel for sintering, Integ. Mater. Manuf. Innov. 7 (3) (2018) 136–147.

[97] W. Xu, P. Rivera-Díaz-del Castillo, W. Yan, K. Yang, D. San Martín, L. Kestens, S. Van Der Zwaag, A new ultrahigh-strength stainless steel strength-

ened by various coexisting nanoprecipitates, Acta Mater. 58 (11) (2010) 4067–4075.

[98] W. Xu, P. Rivera-Díaz-del Castillo, S. Van der Zwaag, Designing nanoprecipitation strengthened uhs stainless steels combining genetic algorithms and thermodynamics, Comput. Mater. Sci. 44 (2) (2008) 678–689.

[99] E. Galindo-Nava, W. Rainforth, P. Rivera-Díaz-del Castillo, Predicting microstructure and strength of maraging steels: Elemental optimisation, Acta Materialia 117 (2016) 270–285.

[100] W. Xu, P. Rivera-Díaz-del Castillo, W. Wang, K. Yang, V. Bliznuk, L. Kestens, S. Van der Zwaag, Genetic design and characterization of novel ultra-high-strength stainless steels strengthened by ni3ti intermetallic nanoprecipitates, Acta Mater. 58 (10) (2010) 3582–3593.

[101] W. Xu, P. R. D. del Castillo, S. Van Der Zwaag, A combined optimization of alloy composition and aging temperature in designing new uhs precipitation hardenable stainless steels, Comput. Mater. Sci. 45 (2) (2009) 467–473.

[102] W. Xu, P. Rivera-Díaz-del Castillo, S. Van Der Zwaag, Genetic alloy design based on thermodynamics and kinetics, Philos. Mag. 88 (12) (2008) 1825–1833.

[103] W. Xu, P. Rivera-Díaz-del Castillo, S. Van Der Zwaag, Computational design of uhs maraging stainless steels incorporating composition as well as austenitisation and ageing temperatures as optimisation parameters, Philos. Mag. 89 (20) (2009) 1647–1661.

[104] E. Menou, I. Toda-Caraballo, P. E. J. Rivera-Díaz-del, C. Pineau, E. Bertrand, G. Ramstein, F. Tancret, et al., Evolutionary design of strong and stable high entropy alloys using multi-objective optimisation based on physical models, statistics and thermodynamics, Mater. Des. 143 (2018) 185–195.

[105] S. Gorsse, F. Tancret, Current and emerging practices of calphad toward the development of high entropy alloys and complex concentrated alloys, J. Mater. Res. 33 (19) (2018) 2899–2923.

[106] E. Menou, F. Tancret, I. Toda-Caraballo, G. Ramstein, P. Castany, E. Bertrand, N. Gautier, P. E. J. R. Díaz-Del, et al., Computational design of light and strong high entropy alloys (hea): Obtainment of an extremely high specific solid solution hardening, Scr. Mater. 156 (2018) 120–123.

[107] A. Abu-Odeh, E. Galvan, T. Kirk, H. Mao, Q. Chen, P. Mason, R. Malak, R. Arróyave, Efficient exploration of the high entropy alloy composition-phase space, Acta Mater. 152 (2018) 41–57.

[108] E. Menou, G. Ramstein, E. Bertrand, F. Tancret, Multi-objective constrained design of nickel-base superalloys using data mining-and thermodynamics-driven genetic algorithms, Model. Simul. Mater. Sci. Eng. 24 (5) (2016) 055001.

[109] F. Tancret, Computational thermodynamics, gaussian processes and genetic algorithms: combined tools to design new alloys, Model. Simul. Mater. Sci. Eng. 21 (4) (2013) 045013.

[110] F. Tancret, Computational thermodynamics and genetic algorithms to design affordable γ-strengthened nickel–iron based superalloys, Model. Simul. Mater. Sci. Eng. 20 (4) (2012) 045012.

[111] V. Thampy, A. Y. Fong, N. P. Calta, J. Wang, A. A. Martin, P. J. Depond, A. M. Kiss, G. Guss, Q. Xing, R. T. Ott, et al., Subsurface cooling rates and microstructural response during laser based metal additive manufacturing, Sci. Rep. 10 (1) (2020) 1–9.

[112] M. Galindo-Fernández, K. Mumtaz, P. Rivera-Díaz-del Castillo, E. Galindo-Nava, H. Ghadbeigi, A microstructure sensitive model for deformation of ti-6al-4v describing cast-and-wrought and additive manufacturing morphologies, Mater. Des. 160 (2018) 350–362.

[113] M. Narvan, A. Ghasemi, E. Fereiduni, S. Kendrish, M. Elbestawi, Part deflection and residual stresses in laser powder bed fusion of h13 tool steel, Mater. Des. (2021) 109659.

[114] H. Farnoush, A. Momeni, K. Dehghani, J. A. Mohandesi, H. Keshmiri, Hot deformation characteristics of 2205 duplex stainless steel based on the behavior of constituent phases, Mater. Des. 31 (1) (2010) 220–226.

[115] P. Lin, Z. He, S. Yuan, J. Shen, Tensile deformation behavior of ti–22al–25nb alloy at elevated temperatures, Mater. Sci. Eng. A. 556 (2012) 617–624.

[116] H. McQueen, C. Imbert, Dynamic recrystallization: plasticity enhancing structural development, J. Alloys. Comp. 378 (1-2) (2004) 35–43.

[117] F. J. Humphreys, M. Hatherly, Recrystallization and related annealing phenomena, Elsevier, 2012.

[118] M. El Wahabi, L. Gavard, F. Montheillet, J. M. Cabrera, J. M. Prado, Effect of initial grain size on dynamic recrystallization in high purity austenitic stainless steels, Acta. Mater. 53 (17) (2005) 4605–4612.

[119] M. Tikhonova, R. Kaibyshev, A. Belyakov, Microstructure and mechanical properties of austenitic stainless steels after dynamic and post-dynamic recrystallization treatment, Adv. Eng. Mater. 20 (7) (2018) 1700960.

[120] S. Gourdet, F. Montheillet, A model of continuous dynamic recrystallization, Acta. Mater. 51 (9) (2003) 2685–2699.

[121] P. Bernard, S. Bag, K. Huang, R. E. Logé, A two-site mean field model of discontinuous dynamic recrystallization, Mater. Sci. Eng. A 528 (24) (2011) 7357–7367.

[122] K. A. Babu, Y. H. Mozumder, R. Saha, V. S. Sarma, S. Mandal, Hot-workability of super-304h exhibiting continuous to discontinuous dynamic recrystallization transition, Mater. Sci. Eng. A. 734 (2018) 269–280.

[123] C. Zener, J. H. Hollomon, Effect of strain rate upon plastic flow of steel, J. Appl. Phys. 15 (1) (1944) 22–32.

[124] K. E. Huang, R. E. Logé, A review of dynamic recrystallization phenomena in metallic materials, Mater. Des. 111 (2016) 548–574.

[125] Y. H. Mozumder, K. A. Babu, R. Saha, V. S. Sarma, S. Mandal, Dynamic microstructural evolution and recrystallization mechanism during hot deforma-

tion of intermetallic-hardened duplex lightweight steel, Mater. Sci. Eng. A. 788 (2020) 139613.

[126] X.-g. Liu, L.-g. Zhang, R.-s. Qi, L. Chen, M. Jin, B.-f. Guo, Prediction of critical conditions for dynamic recrystallization in 316LN austenitic steel, J. Iron. Steel Res. Int. 23 (3) (2016) 238–243.

[127] E. Galindo-Nava, P. E. J. Rivera-Díaz-del Castillo, Thermostatistical modelling of hot deformation in fcc metals, Int. J. Plast. 47 (2013) 202–221.

[128] E. Galindo-Nava, P. E. J. Rivera-Díaz-del Castillo, Grain size evolution during discontinuous dynamic recrystallization, Scr. Mater. 72 (2014) 1–4.

[129] F. Caiazzo, V. Alfieri, G. Corrado, P. Argenio, Laser powder-bed fusion of inconel 718 to manufacture turbine blades, Int. J. Adv. Manuf. Technol. 93 (9-12) (2017) 4023–4031.

[130] Q. Zhang, J. Xie, T. London, D. Griffiths, I. Bhamji, V. Oancea, Estimates of the mechanical properties of laser powder bed fusion ti-6al-4v parts using finite element models, Mater. Des. 169 (2019) 107678.

[131] J. Tong, C. Bowen, J. Persson, A. Plummer, Mechanical properties of titanium-based ti–6al–4v alloys manufactured by powder bed additive manufacture, Mater. Sci. Technol. 33 (2) (2017) 138–148.

[132] Z. Li, B. He, Q. Guo, Strengthening and hardening mechanisms of additively manufactured stainless steels: The role of cell sizes, Scr. Mater. 177 (2020) 17–21.

[133] E. I. Samuel, B. Choudhary, K. B. S. Rao, Influence of temperature and strain rate on tensile work hardening behaviour of type 316 ln austenitic stainless steel, Scr. Mater. 46 (7) (2002) 507–512.

[134] M. Azarbarmas, M. Aghaie-Khafri, J. Cabrera, J. Calvo, Dynamic recrystallization mechanisms and twining evolution during hot deformation of inconel 718, Mater. Sci. Eng. A. 678 (2016) 137–152.

[135] Y. Fan, P. Cheng, Y. L. Yao, Z. Yang, K. Egland, Effect of phase transformations on laser forming of ti–6al–4v alloy, J. Appl. Phys. 98 (1) (2005) 013518.

[136] N. Hansen, Hall–Petch relation and boundary strengthening, Scr. Mater. 51 (8) (2004) 801–806.

[137] U. F. Kocks, H. Mecking, Physics and phenomenology of strain hardening: the FCC case, Prog. Mater. Sci. 48 (3) (2003) 171–273.

[138] A. Hadadzadeh, C. Baxter, B. S. Amirkhiz, M. Mohammadi, Strengthening mechanisms in direct metal laser sintered AlSi10Mg: Comparison between virgin and recycled powders, Addit. Manuf. 23 (2018) 108–120.

[139] R. Li, M. Wang, Z. Li, P. Cao, T. Yuan, H. Zhu, Developing a high-strength Al-Mg-Si-Sc-Zr alloy for selective laser melting: crack-inhibiting and multiple strengthening mechanisms, Acta. Mater. (2020).

[140] A. Hadadzadeh, A. Shahriari, B. S. Amirkhiz, J. Li, M. Mohammadi, Additive manufacturing of an Fe–Cr–Ni–Al maraging stainless steel: Microstructure evolution, heat treatment, and strengthening mechanisms, Mater. Sci. Eng. A. (2020) 139470.

[141] Z. G. Zhu, Q. B. Nguyen, F. L. Ng, X. H. An, X. Z. Liao, P. K. Liaw, S. M. L. Nai, J. Wei, Hierarchical microstructure and strengthening mechanisms of a CoCrFeNiMn high entropy alloy additively manufactured by selective laser melting, Scr. Mater. 154 (2018) 20–24.

[142] J. A. Gonzalez, J. Mireles, S. Stafford, M. A. Perez, C. A. Terrazas, R. B. Wicker, Characterization of Inconel 625 fabricated using powder-bed-based additive manufacturing technologies, J. Mater. Process. Technol. 264 (2019) 200–210.

[143] Q. Jia, P. Rometsch, P. Kürnsteiner, Q. Chao, A. Huang, M. Weyland, L. Bourgeois, X. Wu, Selective laser melting of a high strength AlMnSc alloy: Alloy design and strengthening mechanisms, Acta. Mater. 171 (2019) 108–118.

[144] Z. Yanushkevich, S. V. Dobatkin, A. Belyakov, R. Kaibyshev, Hall-Petch relationship for austenitic stainless steels processed by large strain warm rolling, Acta Mater. 136 (2017) 39–48.

[145] T. Kurzynowski, K. Gruber, W. Stopyra, B. Kuźnicka, E. Chlebus, Correlation between process parameters, microstructure and properties of 316L stainless steel processed by selective laser melting, Mater. Sci. Eng. A. 718 (2018) 64–73.

[146] H. Eskandari Sabzi, N. T. Aboulkhair, X. Liang, X.-H. Li, M. Simonelli, H. Fu, P. E. J. Rivera-Díaz-del Castillo, Grain refinement in laser powder bed fusion: The influence of dynamic recrystallization and recovery, Mater. Des. (2020) 109181.

[147] T. Sakai, A. Belyakov, R. Kaibyshev, H. Miura, J. J. Jonas, Dynamic and post-dynamic recrystallization under hot, cold and severe plastic deformation conditions, Prog. Mater. Sci. 60 (2014) 130–207.

[148] Y. Estrin, A. Vinogradov, Extreme grain refinement by severe plastic deformation: A wealth of challenging science, Acta Mater. 61 (3) (2013) 782–817.

[149] D. Kong, C. Dong, X. Ni, Z. Liang, C. Man, X. Li, Hetero-deformation-induced stress in additively manufactured 316l stainless steel, Mater. Res. Lett. 8 (10) (2020) 390–397.

[150] A. Heidarzadeh, J. Zavašnik, R. Shabadi, R. T. Mousavian, Dynamic recrystallization's role in strength-ductility trade-off in polycrystalline fe–cr–ni stainless steels produced by laser powder bed fusion, Mater. Sci. Eng. A. 814 (2021) 141214.

[151] F. C. Campbell, Elements of metallurgy and engineering alloys, ASM International, 2008.

[152] T. Soysal, S. Kou, A simple test for assessing solidification cracking susceptibility and checking validity of susceptibility prediction, Acta Mater. 143 (2018) 181–197.

[153] J. Yu, M. Rombouts, G. Maes, Cracking behavior and mechanical properties of austenitic stainless steel parts produced by laser metal deposition, Mater. Des. 45 (2013) 228–235.

[154] R. Saluja, K. Moeed, The emphasis of phase transformations and alloying constituents on hot cracking susceptibility of type 304l and 316l stainless steel welds, Int. J. Eng. Sci. Technol. 4 (5) (2012) 2206–2216.

[155] K. Gruber, R. Dziedzic, B. Kuźnicka, B. Madejski, M. Malicki, Impact of high temperature stress relieving on final properties of inconel 718 processed by laser powder bed fusion, Mater. Sci. Eng. A. (2021) 141111.

[156] J. Hunt, F. Derguti, I. Todd, Selection of steels suitable for additive layer manufacturing, Ironmak. Steelmak. 41 (4) (2014) 254–256.

[157] F. Hull, Delta ferrite and martnesite formation in stainless steels, Weld. J. 52 (5) (1973) 193.

[158] K.-H. Tseng, C.-Y. Hsu, Performance of activated tig process in austenitic stainless steel welds, J. Mater. Process. Technol. 211 (3) (2011) 503–512.

[159] T. Zhou, R. J. Omalley, H. S. Zurob, Study of grain-growth kinetics in delta-ferrite and austenite with application to thin-slab cast direct-rolling microalloyed steels, Metall. Mater. Trans. A. 41 (8) (2010) 2112–2120.

[160] R. Faulkner, J. Williams, E. G. Sanchez, A. Marshall, Influence of co, cu and w on microstructure of 9% cr steel weld metals, Mater. Sci. Technol. 19 (3) (2003) 347–354.

[161] J. Elmer, S. Allen, T. Eagar, Microstructural development during solidification of stainless steel alloys, Metall. Trans. A. 20 (10) (1989) 2117–2131.

[162] U. S. Bertoli, B. E. MacDonald, J. M. Schoenung, Stability of cellular microstructure in laser powder bed fusion of 316L stainless steel, Mater. Sci. Eng. A. 739 (2019) 109–117.

[163] C. Elangeswaran, A. Cutolo, G. K. Muralidharan, C. de Formanoir, F. Berto, K. Vanmeensel, B. Van Hooreweder, Effect of post-treatments on the fatigue behaviour of 316l stainless steel manufactured by laser powder bed fusion, Int. J. Fatigue. 123 (2019) 31–39.

[164] M. A. Obeidi, E. McCarthy, B. OConnell, I. Ul Ahad, D. Brabazon, Laser polishing of additive manufactured 316l stainless steel synthesized by selective laser melting, Materials. 12 (6) (2019) 991.

[165] R. Shrestha, J. Simsiriwong, N. Shamsaei, Addit. Manuf. 28 (2019) 23–38.

[166] Y. Yang, Y. Zhu, M. Khonsari, H. Yang, Wear anisotropy of selective laser melted 316l stainless steel, Wear. 428 (2019) 376–386.

[167] Y. Yin, J. Sun, J. Guo, X. Kan, D. Yang, Mater. Sci. Eng. A. 744 (2019) 773–777.

[168] W. Harun, R. Asri, F. Romlay, S. Sharif, N. Jan, F. Tsumori, Surface characterisation and corrosion behaviour of oxide layer for slmed-316l stainless steel, J. Alloys Compd. 748 (2018) 1044–1052.

[169] M. H. Kunkel, A. Gebhardt, K. Mpofu, S. Kallweit, Statistical assessment of mechanical properties of selective laser melted specimens of stainless steel, Int. J. Adv. Manuf. Tech. 98 (5-8) (2018) 1409–1431.

[170] M. Lodhi, K. Deen, W. Haider, Corrosion behavior of additively manufactured 316l stainless steel in acidic media, Materialia. 2 (2018) 111–121.

[171] F. Yan, W. Xiong, E. Faierson, G. B. Olson, Characterization of nano-scale oxides in austenitic stainless steel processed by powder bed fusion, Scr. Mater. 155 (2018) 104–108.

[172] S. M. Yusuf, M. Nie, Y. Chen, S. Yang, N. Gao, Microstructure and corrosion performance of 316l stainless steel fabricated by selective laser melting and processed through high-pressure torsion, J. Alloys Compd. 763 (2018) 360–375.

[173] R. Masumura, P. Hazzledine, C. Pande, Yield stress of fine grained materials, Acta Mater. 46 (13) (1998) 4527–4534.

[174] I. Toda-Caraballo, E. I. Galindo-Nava, P. E. Rivera-Díaz-del Castillo, Unravelling the materials genome: symmetry relationships in alloy properties, J. Alloys Compd. 566 (2013) 217–228.

[175] P. Promoppatum, S.-C. Yao, P. C. Pistorius, A. D. Rollett, A comprehensive comparison of the analytical and numerical prediction of the thermal history and solidification microstructure of inconel 718 products made by laser powder-bed fusion, Engineering. 3 (5) (2017) 685–694.

[176] A. M. Rubenchik, W. E. King, S. S. Wu, Scaling laws for the additive manufacturing, J. Mater. Process. Technol. 257 (2018) 234–243.

[177] T. Mukherjee, J. S. Zuback, A. De, T. DebRoy, Printability of alloys for additive manufacturing, Sci. Rep. 6 (1) (2016) 19717.

[178] J. C. Ion, H. R. Shercliff, M. F. Ashby, Diagrams for laser materials processing, Acta Metallurgica et Materialia 40 (7) (1992) 1539–1551.

[179] I. 52921, Standard terminology for additive manufacturing–coordinate systems and test methodologies (2013).

[180] C. A. Schneider, W. S. Rasband, K. W. Eliceiri, NIH image to ImageJ: 25 years of image analysis, Nat. Methods. 9 (7) (2012) 671.

[181] ASTM, ASTM E8 (2008).

[182] U. S. Bertoli, A. J. Wolfer, M. J. Matthews, J.-P. R. Delplanque, J. M. Schoenung, On the limitations of volumetric energy density as a design parameter for selective laser melting, Mater Design. 113 (2017) 331–340.

[183] H. Fayazfar, M. Salarian, A. Rogalsky, D. Sarker, P. Russo, V. Paserin, E. Toyserkani, A critical review of powder-based additive manufacturing of ferrous alloys: Process parameters, microstructure and mechanical properties, Mater Design. 144 (2018) 98–128.

[184] P. R. Anderson, M. M. Benjamin, Effect of silicon on the crystallization and adsorption properties of ferric oxides, Environmental science & technology 19 (11) (1985) 1048–1053.

[185] D. Wang, C. Song, Y. Yang, Y. Bai, Investigation of crystal growth mechanism during selective laser melting and mechanical property characterization of 316L stainless steel parts, Mater. Des. 100 (2016) 291–299.

[186] H. E. Sabzi, A. Z. Hanzaki, H. Abedi, R. Soltani, A. Mateo, J. Roa, The effects of bimodal grain size distributions on the work hardening behavior of a

transformation-twinning induced plasticity steel, Mater. Sci. Eng. A. 678 (2016) 23–32.

[187] Z. Sun, X. Tan, S. B. Tor, C. K. Chua, Simultaneously enhanced strength and ductility for 3d-printed stainless steel 316l by selective laser melting, NPG Asia Mater. 10 (4) (2018) 127.

[188] J. Nowacki, Weldability of 17-4 PH stainless steel in centrifugal compressor impeller applications, J. Mater. Process. Technol. 157 (2004) 578–583.

[189] I. Mutlu, E. Oktay, Characterization of 17-4 PH stainless steel foam for biomedical applications in simulated body fluid and artificial saliva environments, Mater. Sci. Eng. C. 33 (3) (2013) 1125–1131.

[190] C. F. Arisoy, G. Başman, M. K. Şeşen, Failure of a 17-4 PH stainless steel sailboat propeller shaft, Eng. Fail. Analysis. 10 (6) (2003) 711–717.

[191] C. Hsiao, C. Chiou, J. Yang, Aging reactions in a 17-4 PH stainless steel, Mater. Chemist. Phys. 74 (2) (2002) 134–142.

[192] H. K. Rafi, D. Pal, N. Patil, T. L. Starr, B. E. Stucker, Microstructure and mechanical behavior of 17-4 precipitation hardenable steel processed by selective laser melting, J. Mater. Eng. Perform. 23 (12) (2014) 4421–4428.

[193] S. Vunnam, A. Saboo, C. Sudbrack, T. L. Starr, Effect of powder chemical composition on the as-built microstructure of 17-4 PH stainless steel processed by selective laser melting, Addit. Manuf. 30 (2019) 100876.

[194] L. E. Murr, E. Martinez, K. N. Amato, S. M. Gaytan, J. Hernandez, D. A. Ramirez, P. W. Shindo, F. Medina, R. B. Wicker, Fabrication of metal and

alloy components by additive manufacturing: examples of 3d materials science, J. Mater. Res. Technol. 1 (1) (2012) 42–54.

[195] A. Yadollahi, N. Shamsaei, S. M. Thompson, A. Elwany, L. Bian, Effects of building orientation and heat treatment on fatigue behavior of selective laser melted 17-4 PH stainless steel, Int. J. Fatigue 94 (2017) 218–235.

[196] M. Mahmoudi, A. Elwany, A. Yadollahi, S. M. Thompson, L. Bian, N. Shamsaei, Mechanical properties and microstructural characterization of selective laser melted 17-4 ph stainless steel, Rapid Prototyping Journal 23 (2) (2017) 280–294.

[197] R. Rashid, S. Masood, D. Ruan, S. Palanisamy, R. R. Rashid, M. Brandt, Effect of scan strategy on density and metallurgical properties of 17-4 PH parts printed by selective laser melting (slm), J. Mater. Process. Technol. 249 (2017) 502–511.

[198] S. M. Yusuf, N. Gao, Influence of energy density on metallurgy and properties in metal additive manufacturing, Mater. Sci. Technol. 33 (11) (2017) 1269–1289.

[199] S. Pasebani, M. Ghayoor, S. Badwe, H. Irrinki, S. V. Atre, Effects of atomizing media and post processing on mechanical properties of 17-4 PH stainless steel manufactured via selective laser melting, Addit. Manuf. 22 (2018) 127–137.

[200] T. LeBrun, T. Nakamoto, K. Horikawa, H. Kobayashi, Effect of retained austenite on subsequent thermal processing and resultant mechanical properties of selective laser melted 17–4 PH stainless steel, Mater. Des. 81 (2015) 44–53.

[201] Y. Sun, R. J. Hebert, M. Aindow, Effect of heat treatments on microstructural evolution of additively manufactured and wrought 17-4ph stainless steel, Mater. Des. 156 (2018) 429–440.

[202] J.-Y. Park, Y.-S. Park, The effects of heat-treatment parameters on corrosion resistance and phase transformations of 14cr–3mo martensitic stainless steel, Mater. Sci. Eng. A. 449 (2007) 1131–1134.

[203] A. Kudzal, B. McWilliams, C. Hofmeister, F. Kellogg, J. Yu, J. Taggart-Scarff, J. Liang, Effect of scan pattern on the microstructure and mechanical properties of powder bed fusion additive manufactured 17-4 stainless steel, Mater. Des. 133 (2017) 205–215.

[204] G. Tapia, A. Elwany, H. Sang, Prediction of porosity in metal-based additive manufacturing using spatial gaussian process models, Addit. Manuf. 12 (2016) 282–290.

[205] C. D. Tuffile, H. Lemke, 3d printable hard ferrous metallic alloys for powder bed fusion, uS Patent 10,953,465 (Mar. 23 2021).

[206] C. Campbell, G. B. Olson, Systems design of high performance stainless steels I. conceptual and computational design, J. Computer-Aided Mater. Des. 7 (3) (2000) 145–170.

[207] K. Ishida, Calculation of the effect of alloying elements on the ms temperature in steels, J. Alloys. Comp. 220 (1-2) (1995) 126–131.

[208] M. Alnajjar, F. Christien, K. Wolski, C. Bosch, Evidence of austenite by-passing in a stainless steel obtained from laser melting additive manufacturing, Addit. Manuf. 25 (2019) 187–195.

[209] Y. Sun, R. J. Hebert, M. Aindow, Non-metallic inclusions in 17-4 PH stainless steel parts produced by selective laser melting, Mater. Des. 140 (2018) 153–162.

[210] M. Averyanova, P. Bertrand, B. Verquin, Studying the influence of initial powder characteristics on the properties of final parts manufactured by the selective laser melting technology: a detailed study on the influence of the initial properties of various martensitic stainless steel powders on the final microstructures and mechanical properties of parts manufactured using an optimized SLM process is reported in this paper, Virtual and Physical Prototyping 6 (4) (2011) 215–223.

[211] C. Das, H. Dey, G. Srinivasan, S. Albert, A. Bhaduri, A. Dasgupta, Weldability of 17-4 PH stainless steel in overaged heat treated condition, Science and Technology of Welding and Joining 11 (5) (2006) 502–508.

[212] J. W. Christian, The theory of transformations in metals and alloys, Newnes, 2002.

[213] M. Salandre, S. Garabedian, G. Gaillard, T. Williamson, T. Joffre, Development of a new tooling steel (l40) for laser powder bed fusion: Influence of particles size distribution and powder atomization on mechanical performances, Adv. Eng. Mater. (2021).

[214] E. Mirkoohi, H.-C. Tran, Y.-L. Lo, Y.-C. Chang, H.-Y. Lin, S. Y. Liang, Analytical mechanics modeling of residual stress in laser powder bed considering flow hardening and softening, Int. J. Adv. Manuf. Technol. 107 (9) (2020) 4159–4172.

[215] W. M. Tucho, V. H. Lysne, H. Austbø, A. Sjolyst-Kverneland, V. Hansen, Investigation of effects of process parameters on microstructure and hardness of slm manufactured SS316L, J. Alloys Comp. 740 (2018) 910–925.

[216] A. Kreitcberg, V. Brailovski, S. Turenne, Effect of heat treatment and hot isostatic pressing on the microstructure and mechanical properties of inconel 625 alloy processed by laser powder bed fusion, Mater. Sci. Eng. A. 689 (2017) 1–10.

[217] L. Chen, B. Richter, X. Zhang, K. B. Bertsch, D. J. Thoma, F. E. Pfefferkorn, Effect of laser polishing on the microstructure and mechanical properties of stainless steel 316l fabricated by laser powder bed fusion, Mater. Sci. Eng. A. 802 (2021) 140579.

[218] Z. Yanushkevich, A. Belyakov, R. Kaibyshev, Microstructural evolution of a 304-type austenitic stainless steel during rolling at temperatures of 773–1273 K, Acta Mater. 82 (2015) 244–254.

[219] S. Gourdet, F. Montheillet, An experimental study of the recrystallization mechanism during hot deformation of aluminium, Mater. Sci. Eng. A. 283 (1-2) (2000) 274–288.

[220] D. Lin, L. Xu, H. Jing, Y. Han, L. Zhao, F. Minami, Effects of annealing on the structure and mechanical properties of FeCoCrNi high-entropy alloy fabricated via selective laser melting, Addit. Manuf. 32 (2020) 101058.

[221] R. Doherty, D. Hughes, F. Humphreys, J. J. Jonas, D. J. Jensen, M. Kassner, W. King, T. McNelley, H. McQueen, A. Rollett, Current issues in recrystallization: a review, Mater. Sci. Eng. A. 238 (2) (1997) 219–274.

[222] T. Voisin, J.-B. Forien, A. Perron, S. Aubry, N. Bertin, A. Samanta, A. Baker, Y. M. Wang, New insights on cellular structures strengthening mechanisms and thermal stability of an austenitic stainless steel fabricated by laser powder-bed-fusion, Acta Mater. 203 (2021) 116476.

[223] M. Shamsujjoha, S. R. Agnew, J. M. Fitz-Gerald, W. R. Moore, T. A. Newman, High strength and ductility of additively manufactured 316L stainless steel explained, Metall. Mater. Trans. A. 49 (7) (2018) 3011–3027.

[224] M. Eskandari, A. Najafizadeh, A. Kermanpur, Effect of strain-induced martensite on the formation of nanocrystalline 316l stainless steel after cold rolling and annealing, Mater. Sci. Eng. A. 519 (1-2) (2009) 46–50.

[225] J. Li, B. Gao, Z. Huang, H. Zhou, Q. Mao, Y. Li, Design for strength-ductility synergy of 316l stainless steel with heterogeneous lamella structure through medium cold rolling and annealing, Vacuum 157 (2018) 128–135.

[226] S. Wang, T. Jozaghi, I. Karaman, R. Arroyave, Y. Chumlyakov, Hierarchical evolution and thermal stability of microstructure with deformation twins in 316 stainless steel, Mater. Sci. Eng. A. 694 (2017) 121–131.

[227] O. Bouaziz, D. Barbier, Strain-hardening in nano-structured single phase steels: mechanisms and control, J. Nanosci. Nanotechnol. 12 (11) (2012) 8732–8734.

[228] S. Gao, Z. Hu, M. Duchamp, P. S. R. Krishnan, S. Tekumalla, X. Song, M. Seita, Recrystallization-based grain boundary engineering of 316l stainless steel produced via selective laser melting, Acta Mater. 200 (2020) 366–377.

[229] R. Li, P. Niu, T. Yuan, P. Cao, C. Chen, K. Zhou, Selective laser melting of an equiatomic cocrfemnni high-entropy alloy: Processability, non-equilibrium microstructure and mechanical property, J. Alloys. Comp. 746 (2018) 125–134.

[230] I. Karaman, G. Yapici, Y. Chumlyakov, I. Kireeva, Deformation twinning in difficult-to-work alloys during severe plastic deformation, Mater. Sci. Eng. A. 410 (2005) 243–247.

[231] Q. Xue, X. Liao, Y. Zhu, G. Gray Iii, Formation mechanisms of nanostructures in stainless steel during high-strain-rate severe plastic deformation, Mater. Sci. Eng. A. 410 (2005) 252–256.

[232] P. Liu, X. Cui, J. Deng, S. Li, Z. Li, L. Chen, Investigation of thermal responses during metallic additive manufacturing using a tri-prism finite element method, Int. J. Thermal. Sci. 136 (2019) 217–229.

[233] R. Puli, G. J. Ram, Dynamic recrystallization in friction surfaced austenitic stainless steel coatings, Mater. Charact. 74 (2012) 49–54.

[234] E. Puchi Cabrera, High temperature deformation of 316L stainless steel, Mater. Sci. Technol. 17 (2) (2001) 155–161.

[235] C. Robertson, M. Fivel, A. Fissolo, Dislocation substructure in 316L stainless steel under thermal fatigue up to 650 K, Mater. Sci. Eng. A. 315 (1-2) (2001) 47–57.

[236] L. M. Headings, K. Kotian, M. J. Dapino, Speed of sound measurement in solids using polyvinylidene fluoride (PVDF) sensors, in: Smart Materials, Adaptive Structures and Intelligent Systems, Vol. 56031, American Society of Mechanical Engineers, 2013, p. V001T04A012.

[237] R. E. Smallman, R. J. Bishop, Elsevier, 1999.

[238] G. Krauss, Martensite in steel: strength and structure, Mater. Sci. Eng. A. 273 (1999) 40–57.

[239] E. Moin, L. Murr, Interactive effects of shock loading parameters on the substructure and mechanical properties of nickel and stainless steel, Mater. Sci. Eng. 37 (3) (1979) 249–269.

[240] H. Idrissi, K. Renard, D. Schryvers, P. Jacques, Tem investigation of the formation mechanism of deformation twins in fe–mn–si–al twip steels, Philosophical Magazine 93 (35) (2013) 4378–4391.

[241] J. Venables, On dislocation pole models for twinning, Philos. Mag. 30 (5) (1974) 1165–1169.

[242] J. Cohen, J. Weertman, A dislocation model for twinning in fcc metals, Acta. Metall. 11 (8) (1963) 996–998.

[243] T. Mori, H. Fujita, Dislocation reactions during deformation twinning in cu-11at.% al single crystals, Acta Metallurgica 28 (6) (1980) 771–776.

[244] S. Mahajan, G. Chin, Formation of deformation twins in fcc crystals, Acta. Metall. 21 (10) (1973) 1353–1363.

[245] E. El-Danaf, S. R. Kalidindi, R. D. Doherty, Influence of grain size and stacking-fault energy on deformation twinning in fcc metals, Metall. Mater. Trans. A. 30 (5) (1999) 1223–1233.

[246] R. C. Reed, The superalloys: fundamentals and applications, Cambridge university press, 2008.

[247] G. Liu, N. Tao, K. Lu, 316l austenite stainless steels strengthened by means of nano-scale twins, J. Mater. Sci.Technol. 26 (4) (2010) 289–292.

[248] J. Huang, Y. Wu, H. Ye, Deformation structures in ball milled copper, Acta Mater. 44 (3) (1996) 1211–1221.

[249] W. Jiang, Y. Zhang, W. Woo, Using heat sink technology to decrease residual stress in 316L stainless steel welding joint: Finite element simulation, Int. J. Pressure. Vessels. Piping. 92 (2012) 56–62.

[250] J. C. Tan, M. J. Tan, Dynamic continuous recrystallization characteristics in two stage deformation of Mg–3Al–1Zn alloy sheet, Mater. Sci. Eng. A. 339 (1-2) (2003) 124–132.

[251] A. Hadadzadeh, B. S. Amirkhiz, A. Odeshi, J. Li, M. Mohammadi, Role of hierarchical microstructure of additively manufactured alsi10mg on dynamic loading behavior, Addit. Manuf. 28 (2019) 1–13.

[252] M. Masoomi, S. M. Thompson, N. Shamsaei, Laser powder bed fusion of ti-6al-4v parts: Thermal modeling and mechanical implications, Int. J. Machine Tools. Manuf. 118 (2017) 73–90.

[253] H. Eskandari Sabzi, P. E. J. Rivera-Díaz-del Castillo, Materials 12 (22) (2019) 3791.

[254] H. Ali, H. Ghadbeigi, K. Mumtaz, Processing parameter effects on residual stress and mechanical properties of selective laser melted ti6al4v, J. Mater. Eng. Perform. 27 (8) (2018) 4059–4068.

[255] M. Aydinöz, F. Brenne, M. Schaper, C. Schaak, W. Tillmann, J. Nellesen, T. Niendorf, On the microstructural and mechanical properties of post-treated additively manufactured inconel 718 superalloy under quasi-static and cyclic loading, Mater. Sci. Eng. A. 669 (2016) 246–258.

[256] V. Popovich, E. Borisov, A. Popovich, V. S. Sufiiarov, D. Masaylo, L. Alzina, Impact of heat treatment on mechanical behaviour of Inconel 718 processed with tailored microstructure by selective laser melting, Mater. Des. 131 (2017) 12–22.

[257] H. T. Tran, Q. Chen, J. Mohan, A. C. To, A new method for predicting cracking at the interface between solid and lattice support during laser powder bed fusion additive manufacturing, Addit. Manuf. 32 (2020) 101050.

[258] Q. Lu, N. Nguyen, A. Hum, T. Tran, C. Wong, Optical in-situ monitoring and correlation of density and mechanical properties of stainless steel parts

produced by selective laser melting process based on varied energy density, J. Mater. Process. Technol. 271 (2019) 520–531.

[259] A. Wilson-Heid, T. Novak, A. Beese, Characterization of the effects of internal pores on tensile properties of additively manufactured austenitic stainless steel 316l, Experiment. Mech. 59 (6) (2019) 793–804.

[260] C. Pauzon, P. Forêt, E. Hryha, T. Arunprasad, L. Nyborg, Argon-helium mixtures as laser-powder bed fusion atmospheres: Towards increased build rate of ti-6al-4v, J. Mater. Process. Technol. 279 (2020) 116555.

[261] O. Salman, F. Brenne, T. Niendorf, J. Eckert, K. Prashanth, T. He, S. Scudino, Impact of the scanning strategy on the mechanical behavior of 316l steel synthesized by selective laser melting, J. Manuf. Process. 45 (2019) 255–261.

[262] A. Mertens, S. Reginster, H. Paydas, Q. Contrepois, T. Dormal, O. Lemaire, J. Lecomte-Beckers, Mechanical properties of alloy ti–6al–4v and of stainless steel 316l processed by selective laser melting: influence of out-of-equilibrium microstructures, Powder Metall. 57 (3) (2014) 184–189.

[263] K. Karayagiz, A. Elwany, G. Tapia, B. Franco, L. Johnson, J. Ma, I. Karaman, R. Arróyave, Numerical and experimental analysis of heat distribution in the laser powder bed fusion of ti-6al-4v, IISE Transactions 51 (2) (2019) 136–152.

[264] E. Soylemez, High deposition rate approach of selective laser melting through defocused single bead experiments and thermal finite element analysis for ti-6al-4v, Addit. Manuf. 31 (2020) 100984.

[265] P. Liu, Z. Wang, Y. Xiao, M. F. Horstemeyer, X. Cui, L. Chen, Insight into the mechanisms of columnar to equiaxed grain transition during metallic additive manufacturing, Addit. Manuf. 26 (2019) 22–29.

[266] P. Follansbee, G. Gray, An analysis of the low temperature, low and high strain-rate deformation of Ti- 6Al- 4V, Metall. Trans. A. 20 (5) (1989) 863–874.

[267] A. Thomas, M. El-Wahabi, J. Cabrera, J. Prado, High temperature deformation of Inconel 718, J. Mater Process. Tech. 177 (1-3) (2006) 469–472.

[268] M. Fisk, J. C. Ion, L.-E. Lindgren, Flow stress model for IN718 accounting for evolution of strengthening precipitates during thermal treatment, Comput. Mater. Sci. 82 (2014) 531–539.

[269] M. Labudovic, R. Kovacevic, I. Kmecko, T. Khan, D. Blecic, Z. Blecic, Mechanism of surface modification of the Ti-6Al-4V alloy using a gas tungsten arc heat source, Metall. Mater. Trans. A. 30 (6) (1999) 1597–1603.

[270] S. J. Wolff, Z. Gan, S. Lin, J. L. Bennett, W. Yan, G. Hyatt, K. F. Ehmann, G. J. Wagner, W. K. Liu, J. Cao, Experimentally validated predictions of thermal history and microhardness in laser-deposited Inconel 718 on carbon steel, Addit. Manuf. 27 (2019) 540–551.

[271] D. T. Queheillalt, H. N. Wadley, B. W. Choi, D. S. Schwartz, Creep expansion of porous Ti-6Al-4V sandwich structures, Metall. Mater. Trans. A. 31 (1) (2000) 261–273.

[272] D. Dye, K. Conlon, R. Reed, Characterization and modeling of quenching-induced residual stresses in the nickel-based superalloy IN718, Metall. Mater. Trans. A. 35 (6) (2004) 1703–1713.

[273] E. Galindo-Nava, J. Sietsma, P. Rivera-Díaz-del Castillo, Dislocation annihilation in plastic deformation: II. kocks–mecking analysis, Acta Mater. 60 (6-7) (2012) 2615–2624.

[274] P. Nandwana, Y. Lee, Influence of scan strategy on porosity and microstructure of Ti-6Al-4V fabricated by electron beam powder bed fusion, Mater. Today. Commun. (2020) 100962.

[275] S. Li, H. Xiao, K. Liu, W. Xiao, Y. Li, X. Han, J. Mazumder, L. Song, Melt-pool motion, temperature variation and dendritic morphology of Inconel 718 during pulsed-and continuous-wave laser additive manufacturing: A comparative study, Mater. Des. 119 (2017) 351–360.

[276] Y. Estrin, L. Toth, A. Molinari, Y. Bréchet, A dislocation-based model for all hardening stages in large strain deformation, Acta. Mater. 46 (15) (1998) 5509–5522.

[277] O. Le Bacq, F. Willaime, A. Pasturel, Unrelaxed vacancy formation energies in group-iv elements calculated by the full-potential linear muffin-tin orbital method: Invariance with crystal structure, Phys. Rev. B. 59 (13) (1999) 8508.

[278] R. W. Cahn, P. Haasen, Physical metallurgy (1983).

[279] R. Madec, B. Devincre, L. P. Kubin, From dislocation junctions to forest hardening, Phys. Rev. Lett. 89 (25) (2002) 255508.

[280] F. Roters, D. Raabe, G. Gottstein, Work hardening in heterogeneous alloysa microstructural approach based on three internal state variables, Acta Mater. 48 (17) (2000) 4181–4189.

[281] E. Galindo-Nava, P. E. J. Rivera-Díaz-del Castillo, A thermodynamic theory for dislocation cell formation and misorientation in metals, Acta Mater. 60 (11) (2012) 4370–4378.

[282] E. I. Galindo-Nava, P. E. J. Rivera-Díaz-del Castillo, Modelling plastic deformation in BCC metals: dynamic recovery and cell formation effects, Mater. Sci. Eng. A. 558 (2012) 641–648.

[283] J. Hunt, Solidification and casting of metals, The Metal Society, London 3 (1979).

[284] R. Hossain, F. Pahlevani, V. Sahajwalla, Revealing the mechanism of extraordinary hardness without compensating the toughness in a low alloyed high carbon steel, Sci. Rep. 10 (1) (2020) 1–13.

[285] N. Ohno, J.-D. Wang, Kinematic hardening rules with critical state of dynamic recovery, part I: formulation and basic features for ratchetting behavior, Int. J. Plast. 9 (3) (1993) 375–390.

[286] H. Matsumoto, L. Bin, S.-H. Lee, Y. Li, Y. Ono, A. Chiba, Frequent occurrence of discontinuous dynamic recrystallization in Ti-6Al-4V alloy with α martensite starting microstructure, Metall. Mater. Trans. A. 44 (7) (2013) 3245–3260.

[287] R. Ding, Z. Guo, Microstructural evolution of a Ti–6Al–4V alloy during β-phase processing: experimental and simulative investigations, Mater. Sci. Eng. A. 365 (1-2) (2004) 172–179.

[288] R. Ding, Z. Guo, A. Wilson, Microstructural evolution of a Ti–6Al–4V alloy during thermomechanical processing, Mater. Sci. Eng. A. 327 (2) (2002) 233–245.

[289] C. Chen, J. Coyne, Deformation characteristics of Ti-6Al-4V alloy under isothermal forging conditions, Metall. Trans. A. 7 (12) (1976) 1931–1941.

[290] X. Wang, L. Wang, L. Luo, X. Liu, Y. Tang, X. Li, R. Chen, Y. Su, J. Guo, H. Fu, Hot deformation behavior and dynamic recrystallization of melt hydrogenated Ti-6Al-4V alloy, J. Alloys. Comp. 728 (2017) 709–718.

[291] J. Trapp, A. M. Rubenchik, G. Guss, M. J. Matthews, In situ absorptivity measurements of metallic powders during laser powder-bed fusion additive manufacturing, Appl. Mater. Today. 9 (2017) 341–349.

[292] P. E. J. Rivera-Díaz-del Castillo, K. Hayashi, E. I. Galindo-Nava, Computational design of nanostructured steels employing irreversible thermodynamics, Mater. Sci. Tech. 29 (10) (2013) 1206–1211.

[293] T. Ronneberg, C. M. Davies, P. A. Hooper, Revealing relationships between porosity, microstructure and mechanical properties of laser powder bed fusion 316l stainless steel through heat treatment, Mater. Des. 189 (2020) 108481.

[294] E. W. Jost, J. C. Miers, A. Robbins, D. G. Moore, C. Saldana, Effects of spatial energy distribution-induced porosity on mechanical properties of laser powder bed fusion 316l stainless steel, Addit. Manuf. 39 (2021) 101875.

[295] Z. Li, T. Voisin, J. T. McKeown, J. Ye, T. Braun, C. Kamath, W. E. King, Y. M. Wang, Tensile properties, strain rate sensitivity, and activation volume of additively manufactured 316L stainless steels, Int. J. Plast. 120 (2019) 395–410.

[296] Y. Hong, C. Zhou, Y. Zheng, L. Zhang, J. Zheng, X. Chen, B. An, Formation of strain-induced martensite in selective laser melting austenitic stainless steel, Mater. Sci. Eng. A. 740 (2019) 420–426.

[297] F. Khodabakhshi, M. Farshidianfar, A. Gerlich, M. Nosko, V. Trembošová, A. Khajepour, Effects of laser additive manufacturing on microstructure and crystallographic texture of austenitic and martensitic stainless steels, Addit. Manuf. 31 (2020) 100915.

[298] D. Kong, C. Dong, X. Ni, L. Zhang, J. Yao, C. Man, X. Cheng, K. Xiao, X. Li, Mechanical properties and corrosion behavior of selective laser melted 316L stainless steel after different heat treatment processes, J. Mater. Sci. Technol. 35 (7) (2019) 1499–1507.

[299] Y. Hong, C. Zhou, Y. Zheng, L. Zhang, J. Zheng, The cellular boundary with high density of dislocations governed the strengthening mechanism in selective laser melted 316L stainless steel, Mater. Sci. Eng. A. (2020) 140279.

[300] D. Kong, C. Dong, S. Wei, X. Ni, L. Zhang, R. Li, L. Wang, C. Man, X. Li, About metastable cellular structure in additively manufactured austenitic stainless steels, Addit. Manuf. 38 (2021) 101804.

[301] C. Pithan, T. Hashimoto, M. Kawazoe, J. Nagahora, K. Higashi, Microstructure and texture evolution in ECAE processed A5056, Mater. Sci. Eng. A. 280 (1) (2000) 62–68.

[302] H. Beladi, I. Timokhina, Y. Estrin, J. Kim, B. De Cooman, S. Kim, Orientation dependence of twinning and strain hardening behaviour of a high manganese twinning induced plasticity steel with polycrystalline structure, Acta Mater. 59 (20) (2011) 7787–7799.

[303] A. Vinogradov, A. Lazarev, M. Linderov, A. Weidner, H. Biermann, Kinetics of deformation processes in high-alloyed cast transformation-induced plasticity/twinning-induced plasticity steels determined by acoustic emission and scanning electron microscopy: Influence of austenite stability on deformation mechanisms, Acta Mater. 61 (7) (2013) 2434–2449.

[304] X. Wang, J. A. Muniz-Lerma, M. A. Shandiz, O. Sanchez-Mata, M. Brochu, Crystallographic-orientation-dependent tensile behaviours of stainless steel 316l fabricated by laser powder bed fusion, Mater. Sci. Eng. A. 766 (2019) 138395.

[305] J. Fu, S. Qu, J. Ding, X. Song, M. Fu, Comparison of the microstructure, mechanical properties and distortion of stainless steel 316 l fabricated by micro and conventional laser powder bed fusion, Addit. Manuf. 44 (2021) 102067.

[306] H. Eskandari Sabzi, E. Hernandez-Nava, X.-H. Li, H. Fu, D. San-Martín, P. E. J. Rivera-Díaz-del Castillo, Strengthening control in laser powder bed fusion of austenitic stainless steels via grain boundary engineering, Mater. Des. 212 (2021) 110246.

[307] S. Afkhami, M. Dabiri, H. Piili, T. Björk, Effects of manufacturing parameters and mechanical post-processing on stainless steel 316l processed by laser powder bed fusion, Mater. Sci. Eng. A. 802 (2021) 140660.

[308] H. Eskandari Sabzi, X.-H. Li, C. Zhang, H. Fu, D. San-Martín, P. E. J. Rivera-Díaz-del Castillo, Deformation twinning-induced dynamic recrystallization during laser powder bed fusion, Scr. Mater. 207 (2022) 114307.

[309] X. Wang, J. Muñiz-Lerma, O. Sanchez-Mata, M. A. Shandiz, N. Brodusch, R. Gauvin, M. Brochu, Characterization of single crystalline austenitic stainless steel thin struts processed by laser powder bed fusion, Scr. Mater. 163 (2019) 51–56.

[310] S. Scheriau, Z. Zhang, S. Kleber, R. Pippan, Deformation mechanisms of a modified 316l austenitic steel subjected to high pressure torsion, Mater. Sci. Eng. A. 528 (6) (2011) 2776–2786.

[311] S. G. Chowdhury, S. Das, P. De, Cold rolling behaviour and textural evolution in aisi 316l austenitic stainless steel, Acta Mater. 53 (14) (2005) 3951–3959.

[312] A. Saeed-Akbari, A. Schwedt, W. Bleck, Low stacking fault energy steels in the context of manganese-rich iron-based alloys, Scr. Mater. 66 (12) (2012) 1024–1029.

[313] C. Wang, X. Lin, L. Wang, S. Zhang, W. Huang, Cryogenic mechanical properties of 316l stainless steel fabricated by selective laser melting, Mater. Sci. Eng. A. 815 (2021) 141317.

[314] Q. Liu, G. Wang, C. Qiu, On the role of dynamic grain movement in deformation and mechanical anisotropy development in a selectively laser melted stainless steel, Addit. Manuf. 35 (2020) 101329.

[315] J. Li, M. Yi, H. Wu, Q. Fang, Y. Liu, B. Liu, K. Zhou, P. K. Liaw, Fine-grain-embedded dislocation-cell structures for high strength and ductility in additively manufactured steels, Mater. Sci. Eng. A. 790 (2020) 139736.

[316] C. Qiu, M. Al Kindi, A. S. Aladawi, I. Al Hatmi, A comprehensive study on microstructure and tensile behaviour of a selectively laser melted stainless steel, Scientific reports 8 (1) (2018) 1–16.

[317] A. Arsenlis, D. Parks, Crystallographic aspects of geometrically-necessary and statistically-stored dislocation density, Acta Mater. 47 (5) (1999) 1597–1611.

[318] M. Ashby, The deformation of plastically non-homogeneous materials, Philos. Mag. 21 (170) (1970) 399–424.

[319] A. Kundu, D. P. Field, Influence of microstructural heterogeneity and plastic strain on geometrically necessary dislocation structure evolution in single-phase and two-phase alloys, Mater. Charact. 170 (2020) 110690.

[320] I. S. Yasnikov, A. Vinogradov, Y. Estrin, Revisiting the considère criterion from the viewpoint of dislocation theory fundamentals, Scr. Mater. 76 (2014) 37–40.

[321] J. H. Hollomon, Tensile deformation, Aime Trans 12 (4) (1945) 1–22.

[322] D. Riabov, A. Leicht, J. Ahlström, E. Hryha, Investigation of the strengthening mechanism in 316l stainless steel produced with laser powder bed fusion, Mater. Sci. Eng. A. 822 (2021) 141699.

[323] D. Kumar, G. Shankar, K. Prashanth, S. Suwas, Texture dependent strain hardening in additively manufactured stainless steel 316l, Mater. Sci. Eng. A. (2021) 141483.

[324] X. Wang, J. A. Muniz-Lerma, O. Sánchez-Mata, M. A. Shandiz, M. Brochu, Microstructure and mechanical properties of stainless steel 316l vertical struts manufactured by laser powder bed fusion process, Mater. Sci. Eng. 736 (2018) 27–40.

[325] J. G. Sevillano, An alternative model for the strain hardening of fcc alloys that twin, validated for twinning-induced plasticity steel, Scr. Mater. 60 (5) (2009) 336–339.

[326] E. Galindo-Nava, P. E. J. Rivera-Díaz-del Castillo, Understanding martensite and twin formation in austenitic steels: A model describing trip and twip effects, Acta Mater. 128 (2017) 120–134.

[327] G. Chin, W. Hosford, D. Mendorf, Accommodation of constrained deformation in fcc metals by slip and twinning, Proceedings of the Royal Society of London. A. Mathematical and Physical Sciences 309 (1499) (1969) 433–456.

[328] O. Bouaziz, S. Allain, C. Scott, Effect of grain and twin boundaries on the hardening mechanisms of twinning-induced plasticity steels, Scr. Mater. 58 (6) (2008) 484–487.

[329] M. Calcagnotto, D. Ponge, E. Demir, D. Raabe, Orientation gradients and geometrically necessary dislocations in ultrafine grained dual-phase steels studied by 2d and 3d ebsd, Mater. Sci. Eng. A. 527 (10-11) (2010) 2738–2746.

[330] B. C. De Cooman, Y. Estrin, S. K. Kim, Twinning-induced plasticity (twip) steels, Acta Mater. 142 (2018) 283–362.

[331] O. Bouaziz, N. Guelton, Modelling of twip effect on work-hardening, Mater. Sci. Eng. A. 319 (2001) 246–249.

[332] D. R. Steinmetz, T. Jäpel, B. Wietbrock, P. Eisenlohr, I. Gutierrez-Urrutia, A. Saeed-Akbari, T. Hickel, F. Roters, D. Raabe, Revealing the strain-hardening behavior of twinning-induced plasticity steels: Theory, simulations, experiments, Acta Mater. 61 (2) (2013) 494–510.

[333] I.-C. Jung, B. C. De Cooman, Temperature dependence of the flow stress of fe–18mn–0.6 c–xal twinning-induced plasticity steel, Acta Mater. 61 (18) (2013) 6724–6735.

[334] J. Čapek, M. Machová, M. Fousová, J. Kubásek, D. Vojtěch, J. Fojt, E. Jablonská, J. Lipov, T. Ruml, Highly porous, low elastic modulus 316l stainless steel scaffold prepared by selective laser melting, Mater. Sci. Eng. C 69 (2016) 631–639.

[335] A. Ascari, A. H. Lutey, E. Liverani, A. Fortunato, Laser directed energy deposition of bulk 316l stainless steel, Lasers Manuf. Mater. Process. 7 (4) (2020) 426–448.

[336] J. Lee, M. Yoo, Elastic strain energy of deformation twinning in tetragonal crystals, Metall. Trans. A. 21 (9) (1990) 2521–2530.